THERMAL HYDRAULIC INVESTIGATIONS ON TOTAL INSTANTANEOUS BLOCKAGE IN A FUEL SUBASSEMBLY OF FAST REACTOR

By

RAVI L

(ENGG02201104031)

Indira Gandhi Centre for Atomic Research, Kalpakkam

A thesis submitted to the Board of Studies in Engineering Sciences

In partial fulfillment of requirements

for the Degree of

DOCTOR OF PHILOSOPHY

of

HOMI BHABHA NATIONAL INSTITUTE

April, 2017

HOMI BHABHA NATIONAL INSTITUTE

Recommendations of the Viva Voce Committee

As members of the Viva Voce Committee, we certify that we have read the dissertation prepared by **Mr. Ravi L** entitled **"Thermal Hydraulic Investigations on Total Instantaneous Blockage in a Fuel Subassembly of Fast Reactor"** and recommend that it may be accepted as fulfilling the thesis requirement for the award of Degree of Doctor of Philosophy.

BPCRao — **Date:** 13/4/2017
Chairman: **Dr. B.P.C. Rao**

C. V — **Date:** 13/4/2017
Guide/Convener: **Dr. K. Velusamy**

T. Sundarajan — **Date:** 13.04.17
External Examiner: **Dr. T. Sundarajan**

B. K. Panigrahi — **Date:** 13/4/17
Member 1: **Dr. B. K. Panigrahi**

K. Devan — **Date:** 13/4/17
Member 2: **Dr. K. Devan**

Final approval and acceptance of this thesis is contingent upon the candidate's submission of the final copies of the thesis to HBNI.

I hereby certify that I have read this thesis prepared under my direction and recommend that it may be accepted as fulfilling the thesis requirement.

Date: 13/4/2017

Place: Indira Gandhi Centre for Atomic Research (IGCAR) (Kalpakkam

C. V

Dr.K. Velusamy
(Guide)

STATEMENT BY AUTHOR

This dissertation has been submitted in partial fulfillment of requirements for an advanced degree at Homi Bhabha National Institute (HBNI) and is deposited in the Library to be made available to borrowers under rules of the HBNI.

Brief quotations from this dissertation are allowable without special permission, provided that accurate acknowledgement of source is made. Requests for permission for extended quotation from or reproduction of this manuscript in whole or in part may be granted by the Competent Authority of HBNI when in his or her judgment the proposed use of the material is in the interests of scholarship. In all other instances, however, permission must be obtained from the author.

Ravi. L

DECLARATION

I, hereby declare that the investigation presented in the thesis has been carried out by me. The work is original and has not been submitted earlier as a whole or in part for a degree / diploma at this or any other Institution / University.

Ravi. L

LIST OF PUBLICATIONS

JOURNAL

1. **Ravi, L**., Velusamy, K., Chellapandi, P., A Robust Thermal Model to Investigate Radial Propagation of Core Damage due to Total Instantaneous Blockage in SFR Fuel Subassembly, *Annals of Nuclear Ene*rgy, **2013**, *62*, 342-356.

2. **Ravi, L**., Velusamy, K., Chellapandi, P., 2015, Investigation of Natural Convection in Heat Generating Molten Nuclear Fuel and Assessment of Damage Propagation in the Core, *ASME Journal of Thermal Science and Engineering Application*, **2015**, *7(3)*, 031009-031009-10, DOI:10.1115/1.4030248.

3. **Ravi, L**., Velusamy, K., Chellapandi, P., Conjugate Heat Transfer Investigation of Core Damage Propagation during Total Instantaneous Blockage in SFR Fuel Subassembly, *Annals of Nuclear Energy*, **2016**, *90*, 371-388.

4. **Ravi, L**., Velusamy, Investigation of TIB in an SFR Fuel Subassembly by an Intergraded Thermal Hydraulics Model, *Nuclear Engineering and Design*, **2016** (Under preparation).

CONFERENCE PROCEEDINGS

1. **Ravi, L**., Velusamy, K., Chellapandi, P., 2013, Investigation of Natural Convection in Heat Generating Molten Nuclear Fuel and Assessment of Damage Propagation in the Core, *Proceedings of the 22nd National and 11th International ISHMT-ASME Heat and Mass Transfer Conference*, December 28-31, **2013**, IIT-Kharagpur, India.

2. **Ravi, L**., Velusamy, K., Chellapandi, P., Transient Natural Convection in a Heat Generating Fuel Pool and Damage Propagation in Core During Flow Blockage in a Single Fuel Subassembly, *Proceedings of the 5th International & 41st National Conference of Fluid Mechanics and Fluid Power*, December 12-14, **2014**, IIT-Kanpur, India.

3. **Ravi, L**., Velusamy, K., Chellapandi, P., Numerical Investigation of Damage Propagation Within a Nuclear Fuel Subassembly Due to Flow Blockage, *Proceedings of International Conference on Computational Methods in Engineering and Health Science*, December 17-19, **2014**, Manipal Institute of Technology, Manipal, India.

4. **Ravi, L**., Velusamy, K., Investigation of Core Damage Progression during Total Instantaneous Blockage in SFR Fuel Subassembly, *Proceedings of the CANDU Safety Association for Sustainability and New Horizons in Nuclear Reactor Thermal-Hydraulics and Safety*, December 8-11, **2015**, Anushaktinagar, Mumbai, India.

5. **Ravi, L**., Velusamy, K., Numerical Investigation of Heat Transfer and Damage Progression During Total Instantaneous Blockage in a Nuclear Fuel Subassembly, *Proceedings of the 23rd National Heat and Mass Transfer Conference and 1st International ISHMT-ASTFE Heat and Mass Transfer Conference*, December 17-20, **2015**, ISRO, Thiruvananthapuram, India.

(**RAVI. L**)

DEDICATED

TO

MY PARENTS

ACKNOWLEDGEMENT

I take this opportunity to express my thanks to the people who have been very helpful to me during the time it took me to complete this thesis.

First and foremost I acknowledge my Guide **Dr. K. Velusamy**, *Head, Mechanics and Hydraulics Division, Reactor Design Group (RDG), IGCAR* for his persistent encouragement, caring, constant motivation, everlasting patience and insightful guidance in all the ways leading to the completion of my Ph.D work. The joy and enthusiasm he has for his research was contagious and motivational for me, even during tough times.

I am highly grateful to my *Doctoral Committee (DC) members* (**Dr. B.P.C Rao, Dr. B. K. Panigrahi and Dr. K. Devan),** for their valuable inputs, continuous monitoring of my progress and valuable support throughout the course of my research.

I sincerely thank **Shri G. Srinivasan,** *Director, RDG* for his perpetual support and encouragement throughout my research period. I thank **Dr. S.A.V. Satya Murty,** *Director, IGCAR,* **Dr. R. B. Grover,** *Director, HBNI, Mumbai and* **Dr. B. K. Dutta,** *Dean, HBNI, Mumbai* for allowing me to continue my research work. I thank **Shri P. Selvaraj,** Associate *Director, RAG* for his kind support and encouragement throughout my research period. I sincerely thank our guardian **Dr. M. Sai Baba,** Associate *Director, RMG* for his care and support from day one.

I would like to express my deep thanks to **Shri M. Asokkumar**, *SO* (*G*), *THS* for his suggestions, advices, caring and moral support throughout the thesis period.

My special thanks are due to the officers of Thermal Hydraulics Section **S/Shri R. Gajapathy, U. Partha Sarathy, K. Natesan** and **R. Arulbaskar** for sharing their knowledge and support during my thesis work. I sincerely appreciate **Mr. M. Rajendra Kumar, Mr. Juby Abraham** and **Mr. Ram Kumar Maity** for their kind help and sharing their scientific and technical knowledge.

I acknowledge the support of **Mr. S. Saravanan** *DM/D, RAS,* **Mr. S. Jaisankar**, *DM/D, CES* and **Mr. S.P. Sundarlingam**, *Tech./C, CES* during the thesis work.

I would like to acknowledge **Smt. R.Vijayashree, Mr. P.A Sasidhran** and **Mr. B. Madhavan** for providing advanced computational facility (SAMDO LAB). I also acknowledge

the support of **Mr. A. Sivakumar**, *DM/D, THS and* **Mrs. M. Banumathi**, *Streno Gr-II* during the thesis work.

My special thanks are due to my friends, **Mr. Siva Srinivas Kolukula, Mr. Ashutosh Mishra, Mr. Srijan babu, Mr. Varun Hassija, Mr. M. Naveen Raj, Ms. Sumathi, Mr. Anuj Dubey, Mr. Ronit Panda, Mr. Bala Sundaram, Mr. Chandan Reddy** and **Mr. Balagani Nagendra** for their support and care during my stay at Kalpakkam. I thank all the research scholars and the training school staff.

I thank all my family members and friends who were with me during the ups and downs of my life. Last but not the least, I thank the Almighty for his blessings that led to the completion of this thesis.

CONTENTS

Title		Page No.
SYNOPSIS		**i**
LIST OF FIGURES		**iii**
LIST OF TABLES		**viii**
CHAPTER 1	**INTRODUCTION**	**1-10**
1.0	FOREWORD	2
1.1	FLOW BLOCKAGE IN FUEL SUBASSEMBLY	5
1.2	MOTIVATION FOR THE PRESENT STUDY	8
1.3	OBJECTIVES AND SCOPE OF THE THESIS WORK	9
1.4	ORGANISATION OF THE THESIS	9
CHAPTER 2	**LITERATURE REVIEW**	**12-28**
2.0	INTRODUCTION	12
2.1	EXPERIMENTAL STUDIES	13
2.2	THEORETICAL STUDIES	20
2.3	CONCLUSIONS	28
CHAPTER 3	**DEVELOPMENT OF A 1-D MODEL AND INVESTIGATION OF DAMAGE PROGRESSION**	**30-67**
3.0	INTRODUCTION	30
3.1	MAJOR ASSUMPTIONS	31
3.2	MATHEMATICAL MODELING	32
	3.2.1 STAGE-I	33
	3.2.2 STAGE-II	43
	3.2.3 STAGE-III	46
3.3	VALIDATION STUDIES	48
3.4	RESULTS AND DISCUSSION	50
	3.4.1 STAGE-I	50
	3.4.2 STAGE-II	54

3.4.3 STAGE-III..... 57
3.4.4 EFFECT OF REACTOR POWER..... 60
3.4.5 EFFECT OF HEXCAN THICKNESS..... 63
3.4.6 EFFECT OF THERMAL CONDUCTIVITY OF HEXCAN MATERIAL..... 65
3.4.7 EFFECT OF THERMOCOUPLE RESPONSE TIME..... 66
3.5 CLOSURE..... 67
CHAPTER 4 NATURAL CONVECTION IN FUEL POOL AND ITS IMPACT ON DAMAGE PROGRESSION..... **69-92**
4.0 INTRODUCTION..... 69
4.1 MODELING..... 70
4.1.1 PHYSICAL MODEL AND THE COORDINATE SYSTEM..... 70
4.1.2 MATHEMATICAL MODEL..... 74
4.2 SOLUTION METHOD AND VALIDATION..... 77
4.2.1 STEP-1..... 77
4.2.2 STEP-2..... 79
4.3 RESULTS AND DISCUSSION..... 80
4.3.1 STEP-1: DETERMINATION OF THE EQUIVALENT THERMAL CONDUCTIVITY..... 80
4.3.2 STEP-2: INVESTIGATION OF HEXCAN MELTING..... 88
4.4 CLOSURE..... 91
CHAPTER 5 DEVELOPMENT OF INTEGRATED 2-D MODEL AND INVESTIGATION OF DAMAGE PROGRESSION..... **94-134**
5.0 INTRODUCTION..... 94
5.1 MODELING..... 95
5.1.1 GEOMETRIC MODELING..... 95
5.1.2 MATHEMATICAL MODELING..... 99
5.2 CODE VALIDATION..... 105
5.2.1 GRID SENSITIVITY STUDY..... 105
5.2.2 ACADEMIC BENCHMARK..... 106
5.2.3 APPLICATION BENCHMARK..... 109
5.3 RESULTS AND DISCUSSION..... 117

5.3.1 STEADY STATE ANALYSIS……..…..... 117

5.3.2 TRANSIENT ANALYSIS……..…… 121

5.4 CONCLUSIONS……..... 133

CHAPTER 6 CONCLUSIONS AND SCOPE FOR FUTURE RESEARCH..... 136-138

6.0 CONCLUSIONS……..... 136

6.0.1 DEVELOPMENT OF A 1-D MODEL AND INVESTIGATION OF DAMAGE PROGRESSION……..….. 136

6.0.2 NATURAL CONVECTION IN FUEL POOL AND ITS IMPACT ON DAMAGE PROGRESSION……...…….. 137

6.0.3 DEVELOPMENT OF INTEGRATED 2-D MODEL AND INVESTIGATION OF DAMAGE PROGRESSION……..…...……. 138

6.1 SCOPE FOR FUTURE STUDIES..... 138

APPENDIX..... 140-142

REFERENCES..... 143-150

NOMENCLATURE..... 151-158

SYNOPSIS

Sodium cooled Fast Reactors (SFRs) form the second stage of the Indian nuclear power program. Safe operation of these reactors is of prime importance and for which reactor safety analysis is carried out. The heat generating fuel pins in SFR are arranged in a tightly packed triangular pitch within a hexagonal sheath forming a fuel subassembly (SA). Due to compact design and large power density, continuous flow of coolant in the SA is essential for safe reactor operation. Because of the miniature gap between fuel pins, there is a finite chance for formation of local flow blockage inside the SA. Possible reasons for development of blockages include, (i) flow area reduction due to excessive fuel/clad swelling, (ii) damaged spacer wires clogging the sub-channels, and (iii) deposition of corrosion/erosion products in sub-channels. Such blockages are expected to grow gradually and the core monitoring thermocouples which are located at the top of the SA are capable of detecting these blockages at their infancy. But, large size blockages may not be detected by the thermocouples due to low velocity of sodium issuing from the blocked subassembly. The extent of damage propagation before reactor shuts down depends on the size of the blockage and its rate of growth. Total instantaneous blockage (TIB) at the inlet of a SA is a serious event which may be considered as a theoretical envelope of all smaller blockages. During a TIB, continuous rise in the temperatures of fuel, clad and sodium in the blocked subassembly takes place. As a consequence of this, coolant boiling takes place, followed by clad and fuel melting. During these transient phenomena, there is inter-subassembly heat transfer from the blocked SA to neighboring SA. Monitoring the sodium outlet temperature of the neighboring SA and initiating safety actions once the measured thermocouple reading exceeds the specified threshold value is one of the means to detect the blockage in the subassembly. Such detection depends on many parameters, including (i) sodium flow rate in the neighboring subassemblies, (ii) reactor power, (iii) thermocouple response time, (iv) hexcan (or) wrapper thickness, and (v) sequence of damages in the blocked subassembly, viz., sodium

boiling, clad melting, fuel melting and hexcan melting. The rate and the extent of damage progression depends strongly on radial heat flux emerging from the blocked SA which in turn depends on the various modes of heat transfer taking place during this transient phenomenon. The thermal hydraulics phenomena involved during damage progression are very complex, involving phase change heat transfer with moving solid-liquid interfaces.

The present thesis attempts to understand the thermal hydraulics of the damage progression and to investigate i) the sequence of damage progression, ii) possibility of TIB detection by online monitoring of the sodium outlet temperature from the neighboring SA and iii) determination of number of SA that are likely to get damaged severely before reactor shutdown, which is an important parameter to define the thermal load on the core-catcher. Towards this a transient enthalpy based thermal hydraulic model has been developed. The transient model considering multi-material and multi-phase flow features adopts an explicit finite difference method employing Voller's algorithm for interface tracking. The model has been validated against published benchmark data. Natural convection within the fuel pool due to inter subassembly heat transfer has been predicted by developing a code. The axi-symmetric transient CFD code is based on finite volume method employing k-ε turbulence model, wherein the pressure-velocity coupling is resolved by the SIMPLE algorithm. The code has been validated against the standard benchmark solutions for natural convection. Finally the enthalpy based thermal hydraulics code is linked with CFD code for a coupled thermal hydraulics investigation of TIB event.

It is established that TIB can be detected by core temperature monitoring thermocouples of six adjacent SA. The number of SA that are likely to get damaged during a TIB event is only 7.

LIST OF FIGURES

Figure No	Figure Title	Page No
1.1	Indian three stage nuclear power programme.	2
1.2	Flow sheet of typical pool type fast reactor.	4
1.3	Primary circuit assembly of pool type fast breeder reactor.	4
1.4	Typical fuel subassembly of medium size fast breeder reactor.	6
2.1	Overall framework of the SIMMER-III and SIMMER-IV codes.	24
3.1	Sketch showing TIB event progression: Normal condition, stage-I: transients within blocked SA before hexcan failure, stage-II: molten fuel attacking blocked SA hexcan and stage-III: molten fuel attacking neighboring hexcan.	34
3.2	Cross section of a fuel SA showing partition of inner and outer regions.	34
3.3a	Representative inner fuel pin and associated sodium.	35
3.3b	Representative outer fuel pin and associated sodium.	35
3.3c	Heat conduction in hollow cylinder.	37
3.3d	Heat conduction in inner fuel pin.	38
3.3e	Heat conduction in outer fuel pin.	39
3.3f	Heat conduction in inner and outer sodium.	39
3.3g	Heat conduction in outer sodium and blocked SA hexcan.	40
3.4	Blocked SA with molten pool and neighboring SA during stage-II	44
3.5	Geometric modeling during stage-II.	44
3.6	Sectional view of blocked SA with molten fuel pool and neighboring SA with plugged inter-wrapper region.	47
3.7	Geometric modeling during stage-III.	48
3.8	Time dependent temperature rise of sodium from neighboring SA outlet during TIB in a fuel subassembly.	49
3.9	Temperature evolution in inner and outer sodium during stage-I.	51
3.10	Temperature evolution in the cladding during stage-I.	52

3.11	Temperature evolution in the fuel pellet during stage-I.	53
3.12	Temperature evolution of blocked SA hexcan, inter-wrapper sodium and neighboring SA hexcan during stage-I.	53
3.13	Temperature evolution of fuel elements (F-366 to F-370) and hexcan elements (H-1 to H-20) during stage-II.	55
3.14	Temperature evolution of inter-wrapper sodium during stage-II.	56
3.15a	Temperature evolution of affected SA fuel and neighboring SA hexcan elements at nodal points during stage-III.	58
3.15b	Temperature evolution of affected SA fuel and neighboring SA hexcan elements at nodal points during the initial stage of stage –III.	58
3.16	Time dependent temperature rise of neighboring SA sodium with corresponding thermocouple reading and melted thickness of neighboring hexcan during stage-III at 8MW power (time = 0 s refers to commencement of stage-III).	59
3.17	Evolution of neighboring SA thermocouple reading during all the three stages of TIB in a single fuel SA with 8 MW (time = 0 s refers to start of TIB).	60
3.18	Evolution of neighboring SA thermocouple reading during TIB in single fuel SA at different powers levels.	62
3.19	Residual thickness of neighboring SA hexcan with time for different SA power.	62
3.20	Instantaneous melting speed of neighboring SA hexcan as a function of hexcan thickness.	64
3.21	Temperature rise of neighboring SA sodium during TIB with the corresponding residual thickness of neighboring hexcan.	64
3.22	Temperature rise of neighboring SA sodium during TIB as a function of thermal conductivity of hexacn with the corresponding residual thickness of neighboring hexcan.	65
3.23	Evolution of neighboring SA thermocouple reading as a function of thermocouple time constant.	66
4.1	TIB event progression: (a) Normal condition, (b) Molten fuel attacking neighboring subassembly during stage-III and (c) Fuel pool details.	71
4.2	Physical model with boundary conditions.	72
4.3	Physical model of neighboring subassembly hexcan melting during stage-III for step-2 calculation.	73

4.4	Comparison of stream function and isotherms for a square cavity at $Ra_E = 10^6$ and $Ra_I = 10^7$ against the results of Acharya and Goldstein (1985).	78
4.5	Flow and temperature fields in the cavity for $Ra_I = 3\times10^7$ and A= 5: (a) Isotherms with pure conduction, (b) Isotherms with natural convection, (c) Natural convection velocity and (d) Natural convection stream function.	83
4.6	Dimensionless temperature variation along the centerline of the pool.	84
4.7	Dimensionless temperature variation along the centerline of the pool for different values of aspect ratios.	84
4.8a	Dimensionless local heat flux variation along the hexcan wall with different values of aspect ratios of the pool for A = 1.	85
4.8b	Dimensionless local heat flux variation along the hexcan wall with different values of aspect ratios of the pool for A = 2.	85
4.9	Variation of dimensionless bulk temperature of pool with Ra_I for different values of aspect ratio.	86
4.10	Equivalent conductivity factor for various values of aspect ratio.	87
4.11a	Evolution of affected SA fuel and neighboring SA hexcan temperatures during molten fuel attack for CF = 1.	89
4.11b	Evolution of affected SA fuel and neighboring SA hexcan temperatures during molten fuel attack for CF = 4.	89
4.12	Time dependent temperature rise of neighboring subassembly sodium during molten fuel attack as a function of conductivity factor.	90
5.1	Structure of the code for integrated study with various stages and interface conditions (q'' wall heat flux).	96
5.2	Sectional view of central (blocked) SA and one of the six neighboring SA.	98
5.3	Geometrical model with mesh for central (blocked) SA with neighboring SA.	98
5.4	Power variation along the active length of the fuel pin.	99
5.5	Effect of grids on time of occurrence of principal events during TIB.	106
5.6	Comparison of stream function and isotherm for a square cavity at $Ra_E = 10^5$ and $Ra_I = 10^7$ against results of Shim and Hyun, (1997).	108
5.7	Temporal variation in the neighboring SA thermocouple reading (t = 4 s) during TIB in a fuel SA.	110

5.8	Sectional view of SCRABEE BE+3 test arrangement.	111
5.9	Geometric model of SCRABEE BE+3 test arrangement.	112
5.10	Comparison of calculated sodium temperature distribution along the axial direction with the experimental data.	113
5.11	Comparison of calculated cladding temperature distribution along axial direction with the experimental data.	114
5.12	Comparison of calculated temperature of sodium and cladding in third ring with the experimental data.	116
5.13	Comparison of calculated TH1 wall temperature with the experimental data.	116
5.14	Initial temperature variation of sodium along the axial direction of the active region before TIB.	117
5.15	Initial temperature variation along axial direction of the cladding before TIB.	119
5.16	Initial temperature variation along axial direction of the fuel pellet before TIB.	119
5.17	Initial temperature variation in the hexcan and inter-wrapper sodium along the axial direction of the active region before TIB.	120
5.18	Temperature evolution of fuel, clad and sodium in the center region of the central (blocked) SA along the axial direction of the active region before TIB and 2 s after TIB.	122
5.19	Temperature evolution of central (blocked) SA hexcan, inter-wrapper sodium and the neighboring SA hexcan along the axial direction of the active region before TIB and 2 s after TIB.	122
5.20	Temperature evolution in sodium at different planes of the blocked SA during TIB.	123
5.21	Temperature evolution in clad at mid-plane of the blocked SA during TIB.	124
5.22	Temperature evolution in fuel at mid-plane of the blocked SA during TIB.	125
5.23	Temperature evolution of blocked SA hexcan at various axial positions during TIB.	125
5.24	Instantaneous (a) temperature field and (b) material distribution during molten fuel attacking neighboring SA hexcan (at t = 26.3 s).	127
5.25a	Temperature and material distributions (see, the legend of Fig. 5.24b) during TIB before fuel pool formation (height of the fuel pin is	128

ordinate and radial distance from center of the SA is abscissa).

5.25b Temperature and material distributions (see, the legend of Fig. 5.24b) during fuel pool formation (height of the fuel pin is ordinate and radial distance from center of the SA is abscissa). 129

5.26 Evolution of neighboring SA thermocouple reading as a function of thermocouple time constant and residual thickness of neighboring hexcan during TIB. 131

5.27 Comparison of conduction model with convection model for time dependent temperature rise of thermocouple (time constant = 8 s) and corresponding residual thickness of the neighboring SA hexcan. 132

LIST OF TABLES

Table No	Table Title	Page No
2.1	Test matrix of SCRABEE-N experiment program showing details of various tests performed under six different test groups	15
3.1	Comparison of instants when different processes take place.	50
4.1	Comparison of predicted peak temperature in the cavity with Shim and Hyun (1997) and Acharya and Goldstein (1985).	79
4.2	Comparison of predicted average Nusselt number on hot sidewall of the rectangular cavity with Shim and Hyun (1997).	79
4.3	Values of a and b for laminar and turbulent regimes.	87
5.1	Geometric parameters of the fuel subassembly.	97
5.2	Comparison of predicted non-dimensional peak temperature in the square cavity at $Ra_E = 10^5$ and $Ra_I = 10^7$ with Shim and Hyun, (1997).	108
5.3	Instants of occurrence of various events during a TIB..	109
5.4	Power details of the SCRABEE BE+3 test setup.	111
5.5	Flow details of the SCRABEE BE+3 test setup.	111
5.6	Comparison of calculated steady state results with 3-D Computational Fluid Dynamic results (Naveen and Velusamy, 2016).	118

CHAPTER 1

INTRODUCTION 1

1.0 FOREWORD

Energy is a vital ingredient for economic development of a country. In developing countries like India with growing population and rapid industrialization, the energy consumption rate is growing at a faster pace creating a large energy deficit. To meet this energy demand, new energy sources and technologies are being developed. Among these energy generation methods, the non-conventional and renewable sources of energy which are environment friendly are preferred globally. Nuclear energy is considered to be one of the clean and sustainable sources of non-conventional energy. For a judicial utilization of nominal amount of uranium and a vast amount of thorium, India has formulated the well known three-stage nuclear power program as depicted in Fig. 1.1(Kakodkar, 2008).

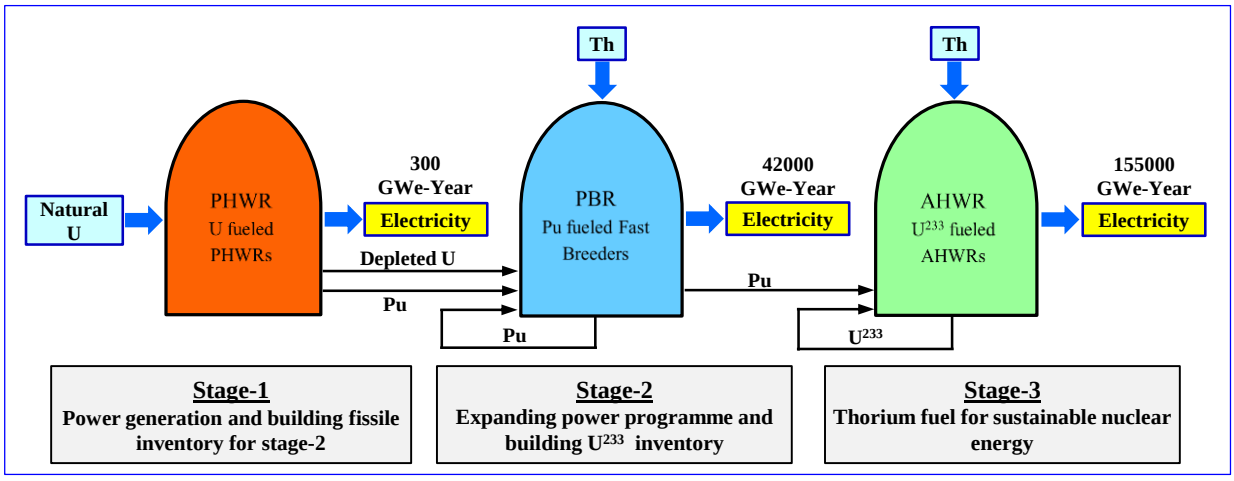

Fig. 1.1. Indian three stage nuclear power programme.

The first-stage programme was based on Pressurized Heavy Water Reactors (PHWRs), which use natural uranium as fuel containing only 0.7% of the fissile isotope of uranium (U^{235}). In the

second-stage of nuclear programme, the energy potential of natural uranium can be increased to about 3,00,000 MW in the coming years through Fast Breeder Reactors (FBRs) which can utilize depleted uranium (U^{238}) and plutonium obtained from recycled spent fuel of the first stage. By adopting Th^{232}-U^{233} cycle in the 3rd stage, the energy potential for sustainable electricity generation is substantially increased that would last for a few centuries.

Towards development of the second stage of nuclear programme, a 40 MW thermal capacity loop type Fast Breeder Test Reactor (FBTR) was constructed at Kalpakkam, India in the year 1985 (Srinivasan et al., 2006). As a follow up to FBTR, a 500MW electric power Prototype Fast Breeder Reactor (PFBR) was designed and presently it is in an advanced state of commissioning in Kalpakkam, India (Chetal et al., 2006, 2011). The flow sheet of a typical pool type fast breeder reactor is depicted in Fig. 1.2. A typical fast breeder reactor consists of three circuits, viz., two sodium circuits to transfer the nuclear heat generated in the core to the steam-water system and power plant circuit to produce steam to run the turbine. The two sodium circuits are known as primary and secondary circuits. Among these two circuits, the primary circuit is entirely inside the pool of sodium. An expanded view of primary circuit assembly is depicted in Fig. 1.3. In these reactors, all the primary system components are housed inside a main vessel which is surrounded by a safety vessel. Main vessel houses the hot primary sodium pool (820 K) and cold primary sodium pool (670 K), inner vessel which separates these pools, control plug, primary sodium pumps, Intermediate Heat Exchanger etc. The nuclear heat produced in the core is transported to the secondary circuit through the Intermediate Heat Exchangers (IHX). Also, the Safety Grade Decay Heat Removal (SGDHR) system operates between hot primary sodium and atmospheric air to remove the decay heat produced during the reactor shut down condition. In the case of PFBR, there are two secondary circuits with 4 IHX and eight numbers of steam generators. The steam exit from the turbine is cooled by a condenser.

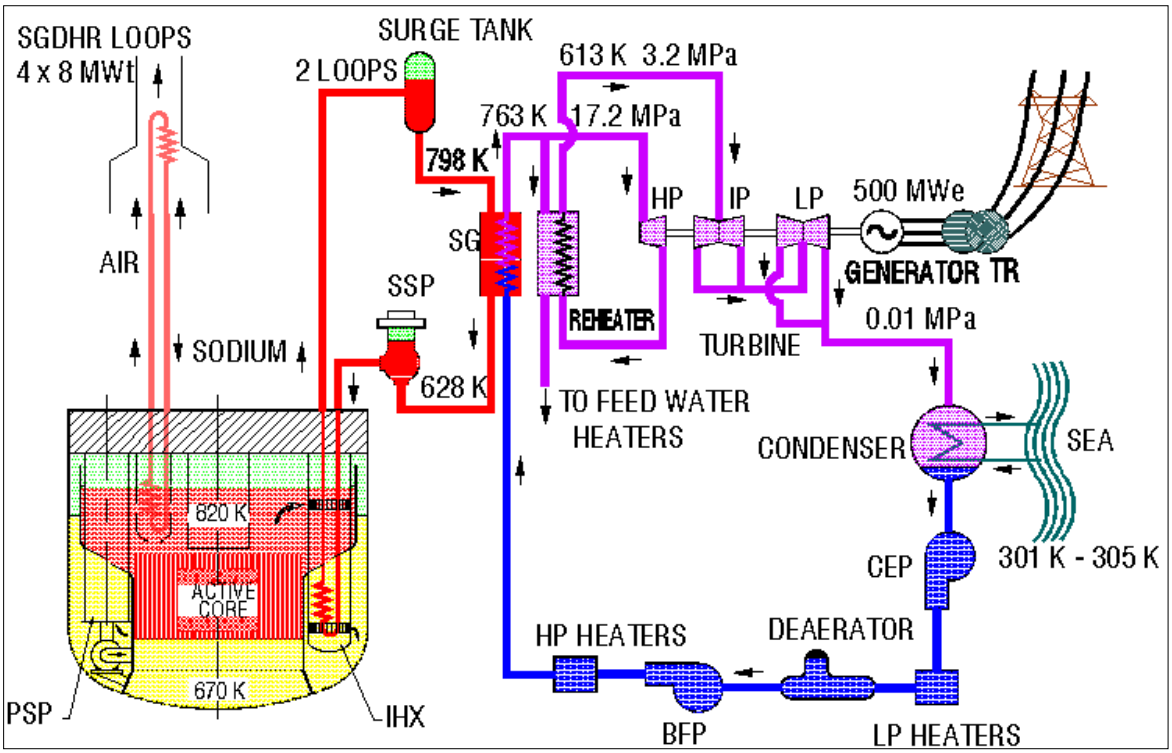

Fig. 1.2. Flow sheet of typical pool type fast reactor.

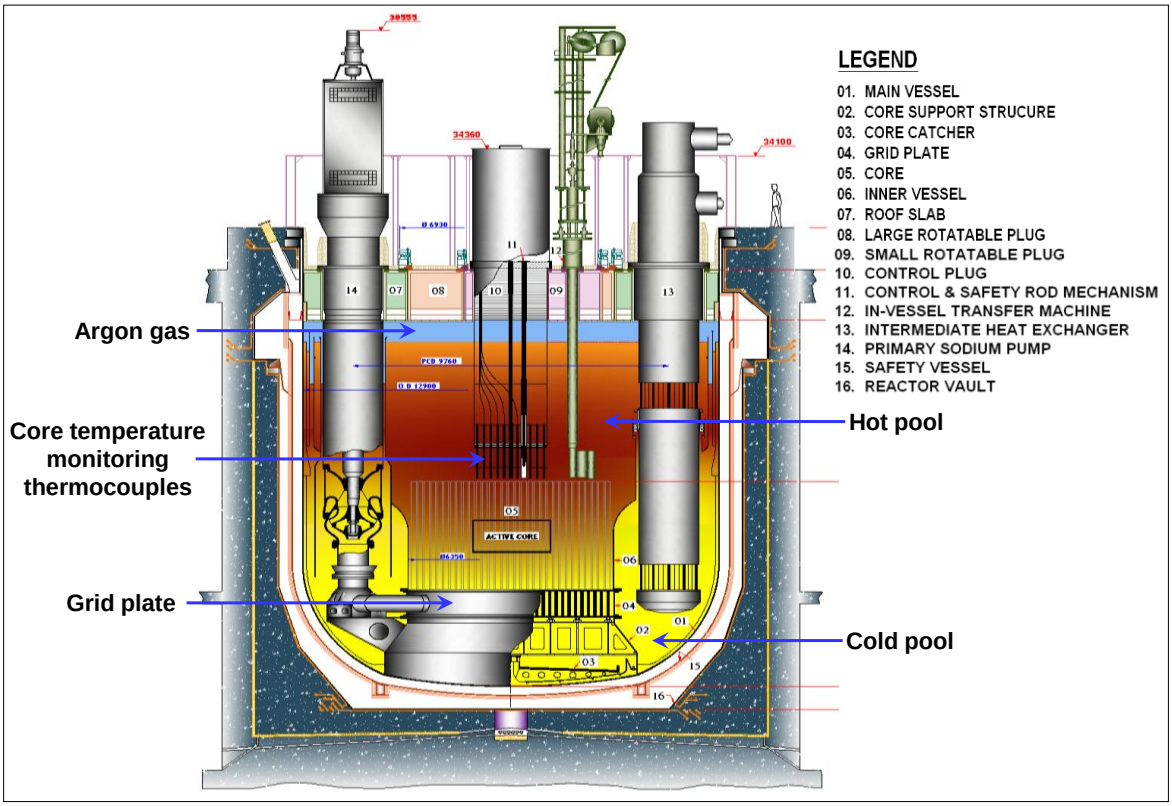

Fig. 1.3. Primary circuit assembly of pool type fast breeder reactor.

Safe operation of the reactor is of prime importance for which detailed reactor safety analysis is carried out. With the advancement of numerical methods and computing technology in the recent past, Computational Fluid Dynamics (CFD) has been harnessed to address and solve many of the thermal hydraulic challenges in the design and safety evaluation of FBRs. This is evident from the published work of Tenchine, (2010) for French FBRs and Velusamy et al., (2010 and 2015) for Indian FBRs.

1.1 FLOW BLOCKAGE IN FUEL SUBASSEMBLY

FBR fuel pins are arranged in a tightly packed triangular pitch and are housed in a hexagonal sheath forming a subassembly (SA). A typical fuel SA of 8 MW thermal power with 217 fuel pins is depicted in Fig. 1.4. FBR core is very compact with large power density and hence the peak heat flux in the fuel pins is ~2 MW/m^2. To extract this large heat flux with small temperature difference between coolant and clad surface, liquid sodium is chosen as the coolant. It has a large heat transfer coefficient due to its large thermal conductivity (~70W/m-K) and it also has a high boiling point (~1153 K) at atmospheric pressure. Due to compact design and large power density, continuous flow of coolant in the SA is essential for safe reactor operation. Because of the miniature gap between fuel pins, there is a finite chance for the formation of local blockage in a coolant sub-channel. This local or partial blockage may be caused by (i) deformation of cladding due to severe swelling, (ii) spacer wire loosening or breaking, (iii) foreign materials left during construction, (iv) fragments from failed fuel and (v) corrosion product deposition in the flow channels. However, such blockages are expected to grow gradually and the core monitoring thermocouples are capable of detecting these slow growing blockages at their infancy. But, large size blockages may not be detected by the thermocouples due to low velocity of sodium issuing from the blocked subassembly and the strong masking effect from the neighboring streams.

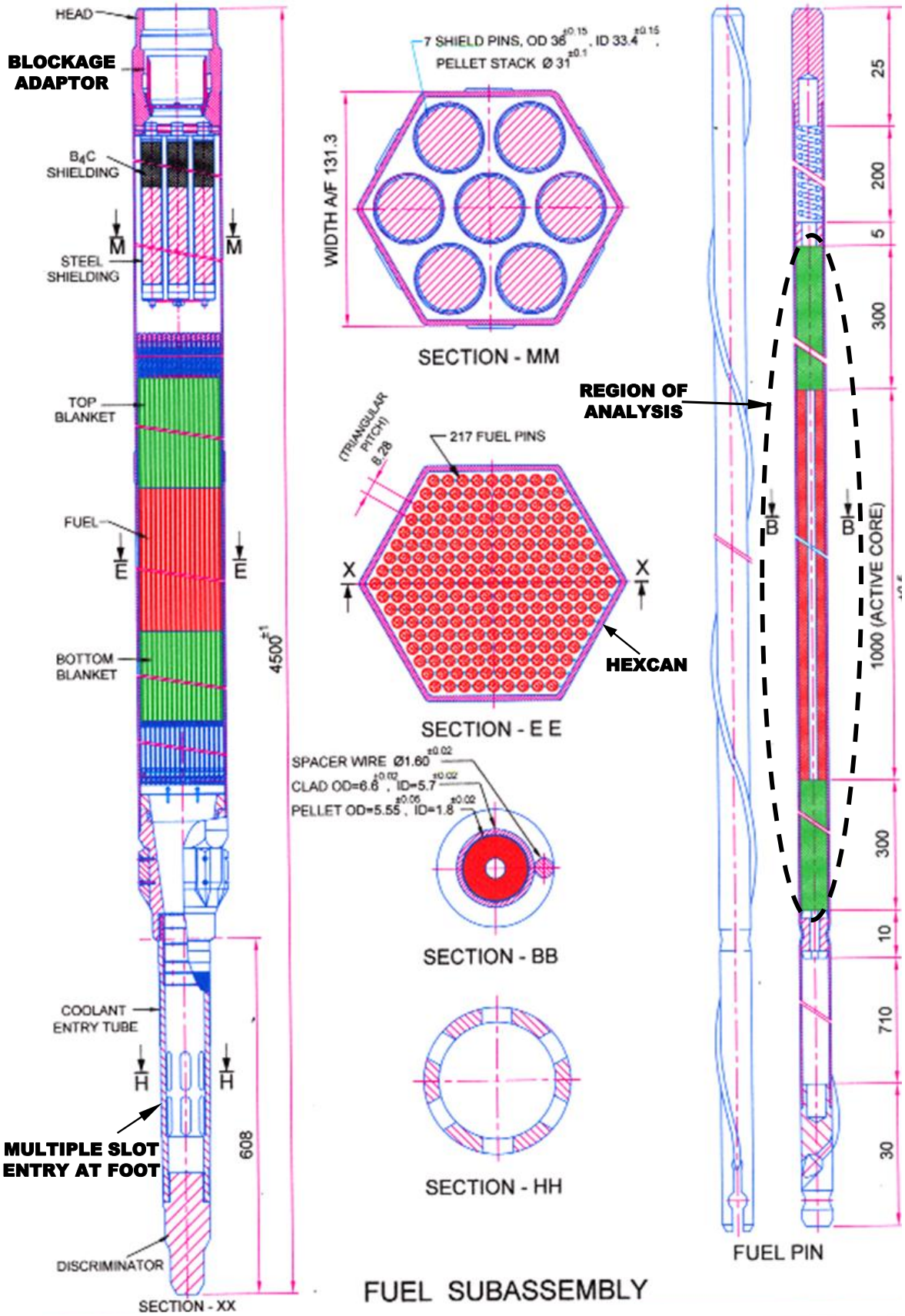

Fig. 1.4. Typical fuel subassembly of medium size fast breeder reactor.

The extent of damage propagation before reactor shut down depends up on the size of the blockage. The probable initiating events for these accident scenarios are different kinds of subassembly blockages. But, total instantaneous blockage (TIB) at the inlet of a SA may be considered as a theoretical envelope of all smaller possible blockages (Mayer-Heine et al., 1986). Since the heat removal rate during a TIB is less than the heat generated, continuous rise in the temperatures of fuel, clad and sodium is expected in the blocked subassembly (Chang et al., 2011). Due to this temperature rise, inter-subassembly heat transfer from blocked subassembly to neighboring subassembly takes place. One of the means to detect the blockage in the subassembly is by monitoring the sodium outlet temperature of the neighboring subassemblies and initiating safety actions, viz., alarm / reactor shutdown when the measured thermocouple reading exceeds its specified threshold values (Kayser et al., 1998 and Paumel et al., 2013). For a typical medium size fast reactor, the alarm threshold for the core temperature monitoring system is fixed as 5 K and shut down threshold is fixed as 10 K (Natesan et al., 2012). Such detection depends on many parameters, including (i) sodium flow rate in the neighboring subassemblies, (ii) reactor power, (iii) thermocouple response time, (iv) hexcan (or) wrapper thickness, and (v) sequence of damages in the blocked subassembly, viz., sodium boiling, clad melting, fuel melting and hexcan melting.

Total instantaneous blockage in a fuel subassembly is a serious event in FBR, due to large power density. Provisions of (i) multiple slots to feed the subassembly at the foot and (ii) a blockage adaptor at the head with multiple radial holes in the wrapper sheath (Fig. 1.4) make this event a Beyond Design Basis Event in FBR. During this event, the blocked fuel subassembly and a few of the neighboring subassemblies are expected to undergo severe damage, generating fragmented core debris. To accommodate and cool the core debris maintaining them in a subcritical state as well as to guard the reactor main vessel from the heat generating debris, a core catcher is provided at the bottom of the reactor assembly beneath the core, as an engineered

safety feature (Fig. 1.3). The magnitude of thermal load on the core catcher is an important parameter that decides the core catcher design. On the other hand, the thermal load depends on the number of subassemblies that get damaged as a consequence of TIB in one subassembly. The knowledge of (i) sequence of damages taking place in the blocked subassembly, (ii) radial propagation of heat and damage to the neighboring subassemblies and (iii) eventual shutdown of the reactor by core temperature monitoring system are very essential for safety evaluation of the reactor, which forms the basis for this thesis work.

1.2 MOTIVATION FOR THE PRESENT STUDY

From detailed literature survey presented in the next Chapter, it was found that most of the TIB studies were experimental based or by using complex numerical models. Out of pile experimental studies provide important input data for mathematical model development. However, many a times, it is difficult to directly extrapolate such experiments to the reactor conditions. Moreover, the findings of such studies are very sensitive to the SA design that varies from reactor to reactor, constraining extrapolation of the results of one reactor to the other. On the other hand, various thermal hydraulic phenomena taking place during radial propagation of damage arising out of a TIB in a fuel subassembly are very complex, involving phase-change heat transfer, moving solid-liquid interfaces and progressive changes in the geometrical configurations of the blocked subassembly as a consequence of melting of fuel, clad and wrapper. Comprehensive investigation of sequence of the event progression requires detailed multi-phase thermo-mechanical modeling adopting complex codes such as SIMMER-III (Maschek et al., 2003). But for elaborate parametric studies, simplified and robust models that capture the essential features of the event progression are preferable. To the best knowledge of this author, no robust thermal hydraulics model has been reported in open literature for TIB

analysis of FBR fuel subassembly. Development of such a robust and adequately accurate model and investigation of TIB event in FBR fuel subassembly forms the motivation for this research work.

1.3 OBJECTIVES AND SCOPE OF THE THESIS WORK

In the present work, a transient, multiphase, multi-material enthalpy based computational model has been developed to carry out detailed thermal hydraulic investigation of damage progression during TIB at the inlet of sodium cooled FBR fuel subassembly. Important phenomena, viz., fuel relocation, molten pool formation, natural convection within the molten pool and hexcan failure are investigated through the developed code which is validated against the published experimental data. The focus of the investigation has been:

i) Determination of sequence and the time of occurrence of principal events during TIB in a fuel SA.

ii) Detection of blockage by online monitoring of sodium outlet temperature from the neighboring subassembly.

iii) Determination of number of subassemblies that are likely to get damaged severely before reactor shuts down, which is an important parameter to define the thermal load on the core-catcher.

iv) Bringing out the effects of various parameters that influence damage progression to neighboring SA.

1.4 ORGANISATION OF THE THESIS

Present thesis is divided into three major parts. The first part comprises of two Chapters with introduction of the problem in Chapter-1 and critical review of literature in Chapter-2. The

second part comprises of three Chapters dealing with development of a robust 1-D model and assessment of damage progression in Chapter-3 and investigation of natural convection in fuel pool and its impact on damage progression and development of integrated 2-D model in Chapters 4 and 5 respectively. The final part of the thesis (Chapter-6) focuses on the summary of the major findings of this thesis and future scope of the work.

CHAPTER 2

LITERATURE REVIEW 2

2.0 INTRODUCTION

The sodium cooled pool type fast reactors have specific favorable safety features, such as operation at low pressure and high thermal inertia. However, the general safety concerns of these reactors require serious attention because some potential accident may lead to reactivity insertion and power increase. Therefore, extensive studies have been carried out on reactivity-sensitivity phenomena like loss of coolant flow in the core and flow blockage or total core meltdown, with great care through large experimental programs and theoretical developments. The probable initiating events for these accident scenarios are the different kinds of SA blockages, which are dangerous enough to present potential risk. The local SA blockages are expected to grow gradually and core monitoring thermocouples are capable of detecting them at their infancy (Di Piazza et al., 2014). But, large size blockages may not be detected by the thermocouple due to low velocity of sodium issuing from the blocked SA and the strong masking effect from the neighboring streams (Maity et al., 2013). Hence, total instantaneous blockage at the inlet of the SA is considered as the most severe of all imaginable blockages and is a theoretical envelope of all smaller possible blockages (Meyer-Hein et al., 1986). The flow blockage accident in a fuel subassembly of a fast reactor was first reported in Fermi-1 reactor in 1966 at Michigan (Scott, 1971 and Alexanderson, 1979). In this incident, two of the loose crumpled Zircaly plates at the bottom of the core were swept away by the flowing coolant. Further the plate floated to different locations to partially or completely block the inlet of the nozzle of various fuel subassemblies during the multiple shutdowns and startups. As a consequence of this, fuel melting was reported

in two adjacent fuel subassemblies and a geometrical change in another subassembly was also observed. Towards establishing the current level of understanding on the consequences of TIB in a fuel SA of fast reactor, a comprehensive literature survey has been carried out encompassing experimental and numerical studies reported in the open literature.. Apart from the TIB studies, other tests which aim at investigating similar accidents such as unprotected loss-of-flow (ULOF), unprotected transient-overpower (UTOP) or basic phenomena in core disruptive accidents (CDA), also provide valuable experience and data for the TIB study. Some of the significant literatures related to these fields are discussed elaborately in this Chapter.

2.1 EXPERIMENTAL STUDIES

The SCARABEE-N (Livolant et al., 1990 and Kayser et al., 1998) was an in-pile experimental test program evolved from general safety concerns for sodium cooled fast reactors. This experimental program was carried out in the SURA facility of Cadarache in France. The objective of this program was to understand the consequences of TIB accident in liquid-metal reactor subassembly. Besides this major objective, attention was also focused on understanding the physics of meltdown and progression processes, which may be encountered in other severe accidents. The size of the experimental devices was small when compared to the scale at which the phenomena evolve in a reactor. Due to this reason, no integral test was possible to understand the complete accident scenario of the TIB. Therefore, three test groups were defined to study the different phenomena of the TIB scenario separately. The first group known as BE+ group concentrated on events inside the blocked SA. The second group known as PI group concentrated on the propagation in the inter-subassembly gaps and the third group, viz., PV group concentrated on the damage progression to the neighboring SA. However, the experimental scenario does not exactly reflect the real behavior of the reactor. Extrapolation had

to be made taking into account the difference in size with the combined use of experimental results, code, analytical calculations and engineering judgment. For this purpose, physical understanding of the relevant phenomena was necessary where the importance of size was concerned. Towards this, three more test groups were formed namely: BF test, APL test and BE test. These test groups focused on physical understanding of the specific phenomenon that occurs at various stages of the TIB scenario. The BF test group focused on understanding the heat transfer in molten and boiling pool formed in the core during accident scenario. The APL test group focused on phenomena inside an under-cooled SA resulting from a slow pump coast-down without SCRAM, which has similarity with the resulting phenomena with those of the TIB accident. The BE test focused on studying the situation that occurs during TIB at entrance of the SA before reactor startup. Totally 14 tests were conducted under six different test groups of the SCRABEE-N experimental program, whose details are tabulated in Table 2.1, as detailed in (Kayser et al., 1998). Some of these tests of the SCRABEE-N experimental program were directly concentrated on specific events of TIB scenario. The important conclusions of this program are: (i) no violent, energetic fuel-coolant interactions takes place, (ii) almost no fuel is ejected out of the fissile zone, (iii) the melt penetration into the neighboring subassemblies proceeds rapidly, (iv) no steel pressure buildup takes place and (v) the occurrence of TIB can be detected during rapid damage progress to neighboring SA by DND system. However, other detection system and SCRAM possibilities may exist during this accident scenario, such as reactivity effects due to molten material movements and temperature rise at the outlet of the neighboring subassemblies.

The CABRI (Dadillon et al., 1979 and 1982) is an experimental facility developed at Cadarache in France with joint collaboration of German, UK and US. This program had 32 tests to simulate the various core disruptive accident conditions in sodium cooled fast reactors to understand different phenomena that occur during the accident.

Table. 2.1. Test matrix of SCRABEE-N experiment program showing details of various tests performed under six different test groups (Kayser et al., 1998).

Test Names		Geometry of Test Setup	Objectives of Test	Characteristics
TIB	**BE+**	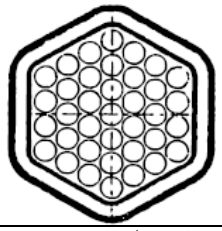	Evolution of scenario inside the blocked subassembly such as sodium boiling, clad/fuel melting and molten fuel pool formation.	No. pins in SA: BE+1: 19 pins BE+2: 19 pins BE+3: 37 pins BE+3bis: 37 pins BTI-Cabri: 1pin coolant: sodium
	PI-A	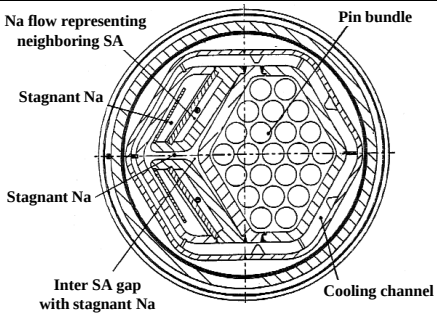	Melt-through of the blocked SA hexcan wall due to molten fuel attack. Propagation of the melt into the inter-subassembly gaps.	No. pins in SA: 23 coolant: sodium
	PV-A	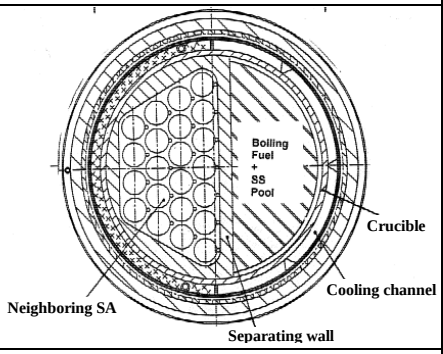	Melt-through of the neighboring SA hexcan wall. Propagation of the melt into the neighboring subassembly.	pool: boiling UO_2+SS mass of UO_2 = 4 kg mass of SS = 0.6kg heating rate of pool = 140 W/g No. pins in neighboring SA = 22 pins
BF		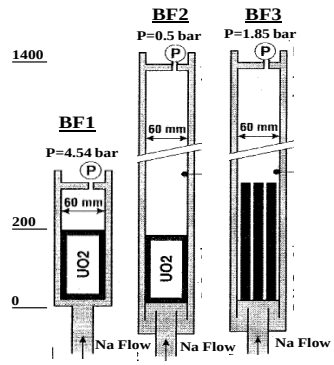	Thermal hydraulics of molten and boiling, heat generating fuel and steel pools. Heat transfer in the pools with respect to flux concentration, pressurization by the steel and heat transfer correlations.	BF1 (pool: molten UO_2) mass of UO_2 = 5 kg heating rate = 17W/g BF2 (pool: boiling UO_2) mass of UO_2 = 6 kg heating rate (max) = 93.4W/g BF3 (pool: boiling UO_2 +SS) mass of UO_2 = 6 kg mass of SS = 2 kg heating rate (max) = 81.2W/g
APL		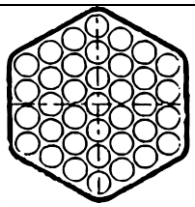	Evolution of scenario inside an under cooled subassembly resulting from slow pump coastdown	No. pins in SA: APL1 = 19 pins APL2 = 37 pins APL3 = 37 pins
BE		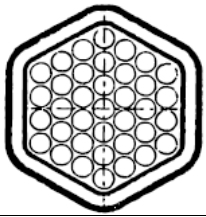	Thermal hydraulics of blockage in the fuel SA before power start-up	No. pins in SA: 37

The main objective of this experiment was to investigate the behavior of fuel pins of FBR when subjected to fast power transients with and without flow coast-down from representative steady state conditions. The results of the study were used to check and improve the theoretical models developed for core disruptive accident analysis.

The Mol 7C/6 is an experimental program (Aberle et al., 1994) carried out in the Belgian BR-2 reactor to investigate the consequences of local faults in irradiated fuel subassembly and response of detection system to such faults. It was found that local subassembly faults in high burn up fuel subassemblies are not self-limiting and need active system to prevent damage propagation.

The dynamics of molten material motion during TIB and other CDAs play a crucial role in determining the courses and consequences of accident progression in FBRs (Kondo, 1994). The coolant voiding and melting and relocation of the core fuel and clad have relatively strong reactivity effects. The resulting re-criticality potential and the energetics are the major concerns for the safety evaluation of SFRs. Towards this, a number of in-pile and out-of-pile experimental programs have been conducted to improve phenomenological understandings on key physical processes of material motion during CDAs and to evaluate the safety margin of the plant. Some of these experiments are discussed subsequently.

The hexcan wall failure in-pile experiment test was conducted under the EAGLE program to study recriticality issues associated with the molten fuel pool formation during hypothetical core disruptive accidents in FBR core (Konishi et al., 2007). In this experiment molten steel-fuel pool was formed by melting 2 kg of uranium dioxide fuel-pins by nuclear heating in the IGR (Impulse Graphite Reactor). The stainless steel wall was strongly heated by the molten pool, leading to wall failure. The result suggests that molten core materials formed in hypothetical core disruptive accidents have a certain potential to destroy stainless steel-wall boundaries early in the accident phase, thereby providing fuel escape paths from the core region.

The early establishment of such fuel escape paths is regarded as a favorable characteristic in eliminating the possibility of severe re-criticality events. The failure mechanism of stainless steel hexcan wall due to molten oxide attack during subassembly melt propagation accident in SFRs was experimentally investigated in the SCRABEE BE+3 in-pile test by Kayser and Stansfield, (1994). This experiment suggested four different hexcan failure mechanisms. CAMEL C6 and C7 out-of-pile tests (Spencer et .al., 1985) were carried out to examine the discharge/relocation mechanisms of reactor materials from disrupted core through various available pathways of U.S Clinch River Breeder Reactor (CRBR). This experiment also simulated the fuel discharge mechanism through the Control Rod Guide Tube (CRGT) in CRBR. Hossain et al. (2009) carried out experiments to understand the fundamental mechanisms of penetration and freezing behavior of molten metal flowing through a seven-pin channel. These authors conducted a series of simulant experiments that focused on the fuel-pin-bundle geometry under various thermal conditions of the molten metal and pins, and produced data for the fundamental verification of the safety analysis code SIMMER-III. The liquid penetration length and the solidified frozen metal in the flow channel were also investigated in these experiments. A non-radioactive out-of-pile experimental program called SIMBATH was carried out in Germany to investigate the material motion, relocation and SA hexcan failure during fast reactor accident (Kaiser et al., 1994). In these simulation experiments, the behavior of single pin, 7-pin, 19-pin and 37-pin bundles undergoing melt-down was investigated. Non-radioactive material thermite ($Al+Fe_2O_3$) filled tubes of 7.6 mm diameter were used as fuel pin simulators and exothermal heat from thermite reaction simulated the nuclear heat. The energy produced by the fuel pins was large enough to generate high temperature melt to simulate the mild Unprotected Transient Overpower Accident (UTOPA) or Unprotected Loss of Flow Accident (ULOFA). The results of the study were used to validate the computer codes like SIMMER. Series of experiments were conducted to study ability of the molten fuel to penetrate unblocked flow paths and material relocation

phenomena in seven-pin-bundle structures at the THEFIS (Thermite Freezing In Structures) facility in Germany (Fieg et al., 1992). The alumina and alumina-iron melts were used as stimulants to study the melt penetration and freezing behavior in different structures. The SIGELCO experiment was conducted in France (CEA) to study freezing phenomena of various simulant materials such as HITCH, Woods's metal and tin in different geometries, viz., tubes, pin bundle, etc. (Duret and Bonnard, 1988). Freezing of pure UO_2 melt and condensing of boiling steel over tubes and pin bundles were also investigated by conducting series of tests under GEYSER Programme at CEA France (Berthoude and Duret, 1989). Edwards et al. (1992) carried out Sodium Entry Series (SES) out-of-pile experiments at Molten Fuel Test Facility (MFTF) in UK to investigate the extent of penetration of molten fuel oxide in a test sections representing full scale geometries of a fast reactor fuel subassembly. In these experiments, the test sections initially filled with sodium at 773 K was injected with thermite-generated molten uranium dioxide. The results of the study highlighted that the presence of sodium has little effect on molten fuel penetration in initially intact SA geometries and it also indicated that Molten Fuel Coolant Interaction (MFCI) was completely absent in all of the SES experiments. Seven in-pile experiments were performed on fresh and irradiated seven pin fuel bundle (oxide fuel) in the Transient Reactor Test (TREAT) Facility at USA to simulate, fast reactor severe accident conditions (Doerner et al., 1992). The major objectives of these tests were to measure post failure fuel motion and to determine the underlying dispersive mechanisms.

Molten fuel pool formed in the reactor core during severe accident leads to re-criticality risk in a reactor. Fuel discharge from the core is very essential to decrease reactivity. The molten fuel damages the structure such as hexcan wall enclosing the molten fuel or the control rod guide tube in order to access the fuel discharge paths. The heat transfer within fuel pool under decay heat condition is a key process that controls the pool behavior. Towards this, several studies on

heat transfer characteristics of the fuel pool are reported in the literature. Some of the important works are discussed below:

Experiment was carried out by Alvarez et al. (1986) to investigate the thermal hydraulic characteristics of natural convection in heat generating molten pool and a few heat transfer correlations were proposed for cylindrical and rectangular cavities. Experimental and theoretical studies on convective heat transfer from a heat generating fluid confined to a closed volume were reviewed by Bol'shov et al. (2001). They identified four basic and one asymptotic regimes of heat transfer depending on the heat generation rate. Limiting heat transfer distribution patterns were found for the lower boundary. Also heat transfer in a quasi-two-dimensional geometry was analyzed. They also compared various heat transfer correlations proposed from various studies. Series of out-of-pile tests were carried out in the SEBULON experimental program at France (CEA) to study the thermal hydraulic behavior of salt added boiling pool of water (Bede et al., 1993). The melt-through of neighboring SA hexcan wall due to molten fuel attack was investigated in PV-A test under SCRABEE experimental program (Schwarz et al., 1994). In this test a boiling pool was created from the compressed fuel and stainless steel mass through power ramp. Several tests were carried out in BF series of SCRABEE- N experimental program to study the radial heat transfer in a molten and boiling heat generating pools (Seiler et al., 1994). Under this test series, BF-2 test was carried out to investigate the heat transfer in an oscillating boiling pool of pure UO_2 and a heat transfer correlation was proposed. Based on the study carried out on boiling UO_2 plus steel pool in BF-3 test, two important observations were noted a) The steel in the molten boiling pool gets segregated out of the pool and deposits on the walls of the hexcan and it does not participate in the heat exchange. Then, the boiling pool behaves like pure UO_2 and b) Steel concentration in the boundary layer enhances the heat transfer coefficient by a factor of 5 compared to what would be calculated for a homogeneous fuel/steel mixture. Gabor et al. (1980) carried out experimental work to study the heat transfer from internally

heated $ZnSO_4$-H_2O pools to curved surfaces. The effect of curvature on heat transfer from the boiling pool was investigated. An experiment was carried by Park et al. (1999) to investigate the effect of crust formation in molten metal pool on natural convection heat transfer. The study indicated that the crust formation reduces the heat transfer rate in the pool as the crust serves as a thermal barrier. A correlation between the Nusselt number and Rayleigh number in the molten metal pool with crust formation was also proposed. The fuel-to-steel heat transfer characteristics within a molten fuel/steel mixture system were investigated in the TPA2 test of the CABRI-RAFT program (Yamano et al., 2009). In this test, a test capsule containing fresh 12.3%-enriched UO_2 pellets with embedded stainless steel balls was subjected to transient over power in French CABRI reactor, which resulted in fuel melting and steel vaporization. The observed steel vapor pressure buildup was quite low, which suggested the presence of a mechanism that significantly reduced the fuel-to-steel heat transfer.

2.2 THEORETICAL STUDIES

The sizes of the experimental devices are smaller than the scale at which various phenomena evolve in a reactor. Due to this, no integral tests are possible to study the complete accident scenario of the TIB. Therefore many separate effect tests are conducted to study the different phenomena that occur during a TIB scenario. However, the experimental scenario does not numerically reflect the real behavior of the reactor. Hence, extrapolation must be made to the reactor conditions through mathematical model taking into account the difference in size with combined use of in-pile and out-of -pile experimental data. Towards this, many experimental models such as MULTICANA, MOWGLI, THEBES, CALICO, BUCOGEL PROPAGEL PLUGM, etc., and codes such as QUASAR, PHYSURA-GRAPPE, SURFASS, SAS4A,

SIMMER, AFDM, SABENA, SABRE, etc., have been developed for analyzing the accident scenario.

QUASAR is a simple analytical code, which was developed in Japan by Kasahara and Endo (1992) to analyze the phenomena related to severe subassembly accidents, such as TIB at the inlet of the fuel subassembly. The code can model the affected and neighboring subassemblies, mainly focusing on the thermal consequences and the propagation potential of the accidents without neutronic coupling. The phase change phenomena like sodium boiling and clad/fuel melting/freezing are modeled using enthalpy formulation without solving the momentum equations. The enthalpy values of these SA components (to decide their respective phase changes) are adjusted using the SCRABBE experimental data. The code validation with the experimental results was found to be successful for the initial stages of the accidents. The code is found to be suitable for studying the event sequence of TIB scenario and accident termination potentials.

SURFASS (SURete Fusion ASSemblage) code was developed in the Technology Research Institute of CEA to study TIB in a fuel SA of a fast reactor (Anzieu et al., 1986 and Anzieu and Van Dorsselaere, 1990). It is a 2-D multi-material, multi-phase code which can describe various events of the TIB from the very start to final coolable state of the TIB scenario. The code has undergone various stages of development starting from SURFASS 1A followed by SURFASS 1C, SURFASS 1D, SURFASS 1F, SURFASS 2, etc., and it has been validated with the help of SCRABEE-N experimental data. Various key phenomena such as sodium boiling, fuel break up, molten material relocation, fuel crust stability, etc., are modeled in this code based on data from SCRABEE experiment.

Advanced Fluid Dynamics Model (AFDM) is a computer code that investigates new approaches simulating the multiphase fluid dynamics aspects of severe accidents in fast reactors (Bohl and Wilhelm, 1992 and Bohl et al., 1990). The partner countries in the AFDM program

were Germany, Japan, Italy and U.S. The initial purpose of the AFDM project was to understand fluid dynamics problems encountered in using the SIMMER-II code. The AFDM is a three-velocity-field, two-dimensional, multiphase, Eulerian, fluid dynamics code. Its formalism starts with differential equations similar to those in the SIMMER-II code. These equations are modified to treat three velocity fields and supplemented with a variety of new models. It has 12 topologies describing the possible material contacts depending on the presence or absence of a given material in a computational cell. The AFDM is limited to unrestricted flow, and channel geometry has not been modeled. Melted fast reactor fuel is expected to boil because of decay heat and/or transient neutronic events. Four flow regimes viz., bubbly, churn, cellular, and dispersed flow are modeled in different parts of the pool. The development and implementation of AFDM in SIMMER-II calculations resulted in overcoming various difficulties associated with numerical stability.

SABENA is a two-fluid model subchannel code developed in Japan (PNC) for simulation of the sodium boiling transient and fuel pin heat transfer in an FBR fuel subassembly under various transient and accident conditions (Ninokata and Okano, 1990). This code has options for approximating a subassembly in one and two dimensions as well as in subchannel formulation. With the use of relatively simple but reasonable constitutive models, the SABENA code has been applied to and validated against many multi-pin sodium boiling problems. The numerical method is a reliable and efficient in solving a wide spectrum of problems, including low-pressure sodium boiling.

SABRE is a transient, subchannel based computational tool for calculating multiphase fluid flow and heat transfer in fuel pin bundles. It can not only deal with unperturbed fuel pin bundles, but also can deal with distorted geometries which may occur during reactor operation such as rod bowing, and with accident situations in which such events as blockages, coolant boiling and natural convection might occur (Macdougall and Lillington, 1984). The code has

been used to analyze the blockage situations and analysis of natural convection within the cluster.

SAS4A is a transient analysis code developed at Argonne National Laboratory to analyze a severe core disruptive accident in sodium cooled fast reactor resulting from under cooling or overpower initiating conditions (Cahalan et al., 1990). It contains detailed, mechanistic models of transient thermal hydraulic, neutronic, and mechanical phenomena to describe the response of the reactor core, its coolant, fuel elements, and structural members to accident conditions. The core models in SAS4A provide the capability to analyze the initial phase of core disruptive accidents, through coolant heat up and boiling, fuel element failure, clad melting and relocation, and fuel melting and relocation. The code can analyze oxide fuel clad with stainless steel, as well as metallic fuel with advanced, low swelling cladding alloys. In space, each SAS4A channel represents one or more subassemblies with either a single pin model or a multiple pin model. Many channels are employed for a whole-core representation. Heat transfer in each pin is modeled with a two-dimensional heat conduction equation. Single and two-phase coolant thermal-hydraulics are simulated with a unique, one-dimensional (axial) multiple-bubble liquid metal boiling model. Fuel and cladding melting and subsequent relocation are described with multiple-component fluid dynamics models, with material motions driven by pressures from coolant vaporization, fission gas liberation, and fuel and cladding vaporization. Numerical models used in the code modules range from semi-implicit to explicit. The coupling of modules in time is semi-explicit within a multiple-level time step framework (Cahalan et al.,1994).

SIMMER is a versatile and flexible tool, applicable for the safety analysis of various reactor types with different neutron spectra, fuels and coolants up to new accelerator driven systems (ADS) for waste transmutation and molten salt reactors (Maschek et al., 2003). It has undergone various stages of improvement. The different versions of the SIMMER code are: SIMMER-I, SIMMER-II, SIMMER-III and SIMMER-IV. The SIMMER-III and SIMMER-IV

versions are developed by Japan in cooperation with other countries France, Germany, Switzerland etc. SIMMER-III is a two-dimensional, and SIMMER-IV is a three-dimensional, three-velocity-field, multi-phase, multi-component, Eulerian, fluid-dynamics code coupled with a structure model including fuel-pins, hexcans, etc., and a space-time energy-dependent neutron kinetics model. A conceptual overall framework of SIMMER-III and SIMMER-IV codes is depicted in Fig. 2.1 (Maschek et al., 2003). The SIMMER code models the basic FBR core materials: fuel, steel, coolant and fission gas. A material can exist in different physical states. For example, fuel needs to be represented by fabricated pin fuel, liquid fuel, a crust refrozen on structure, solid particles and fuel vapor, while fission gas exists only in the gaseous state. Thus, the material mass distributions are modeled by 27 density components in SIMMER-III. The energy distributions are modeled by 16 energy components since some density components are assigned to the same energy component. SIMMER code has three space discretization levels (fluid-dynamics, neutronics and, pin/structure) and 3 time levels. Depending on the application, model packages can be linked into the code.

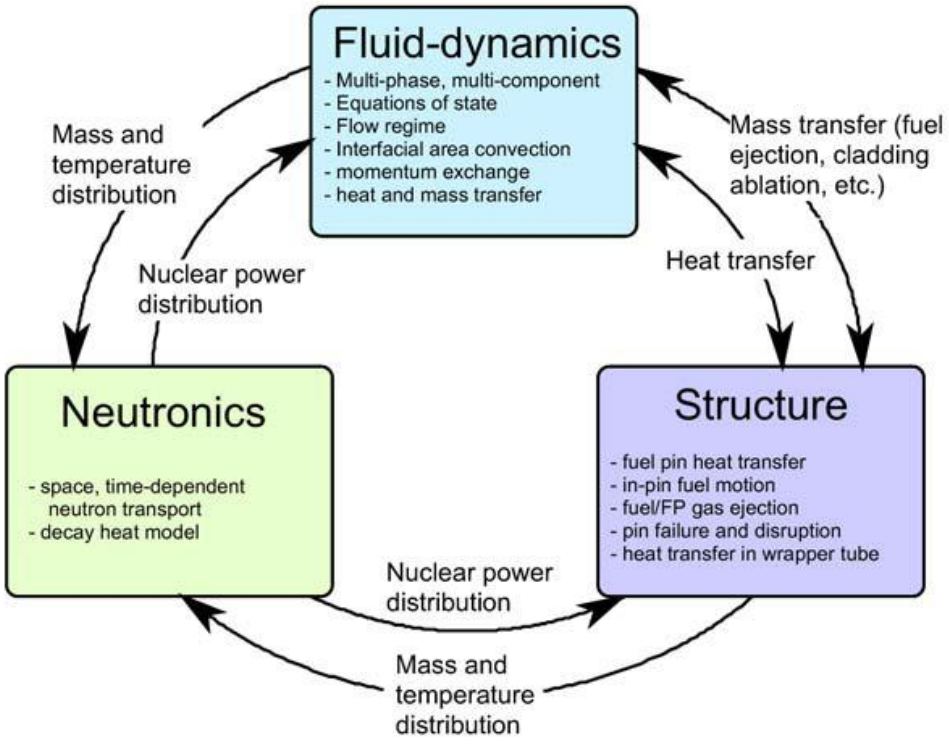

Fig. 2.1. Overall framework of the SIMMER-III and SIMMER-IV codes (Maschek et al., 2003).

Many theoretical studies carried out to analyze whole or partial events of the TIB and other severe accident scenarios in SFRs using various codes and models are reported in the open literature. Some of them are discussed below:

The beyond design basis study to investigate the phenomena involved in a hypothetical bounding case of the TIB in a SA for CREYS MALVILLE (Superphenix) reactor was carried out by Murin et al. (1982). This theoretical study indicated that the TIB detection is possible before damage propagates beyond the neighboring six SA by monitoring neighboring SA sodium outlet temperature. Wang and Cao, (2007) carried out TIB study for Chinese Experimental Fast Reactor (CEFR) using SIMMER code to investigate the sequence of occurrence of various key events and concluded that the damage propagation is limited to neighboring six subassemblies. The accident scenario initiated by a TIB in the Phenix reactor was evaluated by Cadiou and Louvet, (2006). This study concluded that TIB detection by delay neutron detection system is possible before onset of structural melting in the neighboring subassemblies. Detailed analysis for understanding the various phenomena in core disruptive accidents of SFR was carried out by Morita et al. (2011) using COMPASS code. Yamano and Tobita, (2014) carried out theoretical studies to analyze wall failure and fuel discharge/relocation behavior noticed in SCRABEE BE+3 and CAMEL C6 experiments by simulation using SIMMER-III/IV code. A multidimensional, multi-phase, sub-channel analysis code KAMUI was used to simulate the TIB accident experiment SCRABEE BE+1 (Kasahara and Ninokata, 2000). The study highlighted the significance of radial heat loss through the hexcan wall and its influence on boiling evolution and dynamic behavior of coolant and clad motion. They also indicated that a multi-dimensional analysis is essential for evaluating the hypothetical SA accidents including large size local blockage and complete inlet blockage. Sawada et al. (1995) carried out the calculations of the 7-pin bundle SIMBATH core destructive accident experiment using the SIMMER-II code. In this theoretical study, the phenomena such as the propagation of void region, fuel pin disintegration,

molten materials relocation and final materials redistribution were very well reproduced by the SIMMER code. In order to achieve the safety objectives of a 400MWth European Facility for Industrial Transmutation (EFIT) accelerator driven transmuter, various protected and unprotected design basis conditions and design extension conditions were analyzed by Liu et al. (2010) using the SIMMER-III code. Kriventsev et al. (2014) theoretically investigated the unprotected blockage accident scenarios in the 94 MWth FAst Spectrum Transmutation Experimental Facility (FASTEF) subcritical core (proposed core for the MYRRHA reactor). In this study, several hypothetical blockage events in a single fuel SA, starting from 50% blockage of the nominal coolant flow rate to total blockage were simulated using SIMMER-IV code. The analysis concluded that the no pin failure occurs if the flow rate is reduced by 70-75% from the nominal level. And in 85-100% blockage case, the damage is limited to blocked and neighboring SAs. Chen et al. (2015) had proposed a macroscopic continuum differential model for the CFD simulation of pin bundle flow. In this model the flow through pin bundle is treated as a porous medium flow, where the flow and the structure are smeared over the whole space. Instead of their detailed geometrical formation, only their effective parameters, e.g., the volume fractions, the wetted area and the pressure drop, are explicitly modeled. This approximation is suitable especially for one SA. This model is implemented in the SIMMER-III code and is applied for blockage analysis in MYRRHA reactor. Local fuel-coolant interactions observed in molten fuel pool experiment were numerically simulated using SIMMER-III code (Cheng et al., 2015). The interaction characteristics including the pressure buildup as well as mechanical energy release and its conversion efficiency during interaction of water and low-melting-point alloy were investigated. The total instantaneous flow blockage at the inlet of the fuel SA of Japanese prototype fast reactor (MONJU) was investigated by Fukano (2015) using SAS4A code. The results of the study highlighted that the consequences of TIB at inlet of fuel SA were much less severe than that of the ULOF events which represent the most severe accidents in MONJU

reactor. Therefore, it was concluded that all the consequences of local faults in MONJU can be found among the consequences of ULOF and this evaluation method would be also applicable to enveloping safety assessments of local faults in generic SFRs. The limitations in modeling fuel SAs by a simplified average single pin model over a multi-pin model in a severe accident analysis was investigated by Guyot et al. (2014). Detailed analyses by these authors indicated that averaged single pin model can affect voiding and melting patterns which in turn may influence reactivity insertions and power history. It is further indicated that the single-pin hypothesis may introduce important biases in the prediction of hexcan thermal ablation and also the radial propagation of the degradation and subsequent accident consequences may thus be affected. To overcome these issues, the authors have suggested adopting a multiple-pin model. Further, a two-node radial meshing of the subassembly was suggested for treating the peripheral ring of fuel pins separately from the rest of the pins. Suresh et al. (2005) carried out 3-dimensional numerical study to investigate the heat transfer due to natural convection during total blockage in FBTR and PFBR fuel SAs. The objective of their work was to predict the maximum SA power that can be removed by inter-subassembly heat transfer before sodium starts boiling.

Apart from the traditional methodology of demonstrating FBR safety by adopting the 'Bounding' accidental scenarios and simulating with very complex multi-physical codes, such as SIMMER, a new physico-statistical approach has been developed by CAE under its Generation IV Sodium Fast Reactors R&D program (Marie et al., 2015). As a preliminary evaluation of the efficiency and relevance of such a physico-statistical tool, these authors have chosen the accident initiated by TIB of a SA during nominal conditions in the SPX reactor core with fresh fuel for demonstration purpose. This approach involves fast-running description of extended accident sequences, coupling analytical models for various physical phenomena in combination with advanced statistical analysis techniques. Towards establishment of these physical models

describing the TIB phenomenology, 27 uncertain input parameters and their associated probability density functions were identified and adopted. A propagation of these input parameter uncertainties was performed via a Monte-Carlo sampling, providing probability distribution of TIB outputs. A quantification of safety margin was also deduced. A neural network based strategy for detecting TIB in a sodium cooled fast reactor was proposed by Martinez-Martinez et al, (2015). Abnormal rise in temperature of SAs neighboring the blocked SA was considered as a parameter for detecting the TIB. Here, two strategies were proposed depending on whether the measurement sensors of the suspected assembly are reliable or not. The proposed methodology is implemented with a time-lagged feed forward neutral (TLFFN) network to predict the one-step-ahead temperature of a given subassembly.

2.3 CONCLUSIONS

From above literature survey, it is clear that the amount of literature dealing with TIB study is limited. Also, most of the literature deal with experimental investigations or use complex numerical models. Apparently, no robust thermal hydraulics model has been reported in open literature for TIB analysis of FBR fuel subassembly. Moreover, the findings of such studies are very sensitive to the SA design that varies from reactor to reactor, constraining extrapolation of the results of one reactor to other. Comprehensive investigation of sequence of the event progression requires detailed multi-phase thermo-mechanical modeling adopting complex 3-D codes such as SIMMER-III (Maschek et al., 2003). But for elaborate parametric studies, simplified and robust models that capture the essential features of the event progression are preferable. Development of such a robust and adequately accurate model and investigation of TIB event in FBR fuel subassembly form the motivation for the present research work.

CHAPTER 3

DEVELOPMENT OF A 1-D MODEL AND INVESTIGATION OF DAMAGE PROGRESSION

3

3.0 INTRODUCTION

As already mentioned, the various thermal hydraulic phenomena taking place during radial propagation of damage arising out of TIB in a fuel subassembly are very complex, involving phase-change heat transfer, moving solid-liquid interfaces and progressive changes in the geometrical configurations of the blocked subassembly as a consequence of melting of fuel, clad and wrapper. A comprehensive investigation of sequence of the event progression requires detailed multi-phase thermo-mechanical modeling adopting complex codes such as SIMMER-III (Yamano et al., 2003). But for elaborate parametric studies, simplified and robust models that capture the essential features of the event progression are preferable. Development of such a robust 1-dimensional transient model and investigation of TIB event in the fuel subassembly are the prime objectives of the present research work. With these objectives, the model developed attempts to (i) describe the duration of the various phenomena that occur during a TIB, (ii) estimate the extent of damage propagation (i.e., the number of subassembly rows that get damaged) and (iii) speed of damage propagation before neighboring SA thermocouple senses the temperature rise leading to reactor shutdown.

Detailed discussion on development of the robust model, its validation and implementation for the analysis are presented in this Chapter. Further, the effect of various

parameters such as SA power, hexcan thickness, thermal conductivity of hexcan material, thermocouple time constant, inter SA heat transfer and damage progression are discussed in this Chapter.

3.1 MAJOR ASSUMPTIONS

Various assumptions are made in the present work towards simplifying the analysis of complex phenomena involved in the TIB event without sacrificing the essential physics. The major assumptions invoked are as follows:

i) In the present model variations in core reactivity during the phenomena such as sodium voiding, clad and fuel relocation and pool formation are not accounted. Hence, the volumetric heat generation rate of fuel in solid and liquid phase is maintained constant. This is acceptable for power reactors due to the presence of a large number of subassemblies (see, for example, a study carried by Cadiou and Louvet, (2006) on power generation in a SA block during TIB in Phenix reactor).

ii) It may be highlighted that based on preliminary computations, it was found that that sodium boiling, clad melting and fuel melting follow in sequence. This sequence is implicitly assumed while formulating the governing equations.

iii) The natural convection of sodium during boiling is not considered in the present formulation, because the hydraulic diameter of the sub-channel is very small (~3 mm). Further, the pin bundle is provided with helically wound spacer wires. These features offer significant resistance for flow. Such an approach is also essential to retain simplicity of the model.

iv) The enthalpy based 1-D transient model discussed in this Chapter is a simplified model based on uniform axial fuel power distribution in the pin which is found to be effective to carry out detailed parametric studies. However, to capture the realistic effect of axial

variation in temperature of fuel, clad and sodium, the Cosine profile power distribution along the fuel pin axis with peaking at the center of the core is considered in the integrated 2-D model discussed in Chapter-5.

v) The heat generating molten fuel pool formed in the core during TIB sets up natural convection within the pool which enhances the heat transfer and damage progression rate. This effect is not accounted in the 1-D model discussed in this Chapter. However to bring out the realistic effect, a transient natural convection model is incorporated in the integrated 2-D model discussed in Chapter-5.

vi) The high heat flux and temperature on the hexcan and other SA components during TIB accident reduces their mechanical resistance and may lead to early mechanical failure rather than failure due to melting. Thus, structural failure by thermal effect alone is considered in the present study. Effect of creep and internal pressure are not considered in the present study to decide structural failure.

vii) The molten material relocation (draining down) during clad and fuel melting is modeled in the present study by adopting a simplified technique of detaching the molten element by dynamic node deletion from the computational domain.

viii) It is reported in BE +3 and BE+3bis test results that slight azimuthal asymmetries will prevent the occurrence of coherent failure of all the six sides of the hexcan. However, towards simplifying the analysis, the core damage progression in radial direction is assumed to be symmetric in the present study.

3.2 MATHEMATICAL MODELING

With the objectives stated in Section-3.0, a mathematical model is developed that is suitable for prediction of evolution of various phenomena within the blocked SA, thermal interaction between the blocked SA and its neighboring SA, damage propagation to neighboring

SA and subsequent response of the neighboring SA thermocouples. The event progression is divided in to the following three stages as depicted in Fig. 3.1:

Stage-I: Evolution of the scenario and transients before blocked SA hexcan melting.

Stage-II: Transients and consequences during blocked SA hexcan melting.

Stage-III: Transients and consequences during neighboring SA hexcan melting.

3.2.1 STAGE-I

Stage-I is focused to investigate the fundamental thermo-hydraulics inside the blocked SA before its hexcan gets damaged. In the case of a medium sized, 500 MWe, fast reactor (Chetal et al., 2006) the subassembly consists of 217 pins arranged in a tight triangular pitch having 8 rows. The peripheral row consists of 48 pins, which is termed as outer region, while the interior 169 pins are termed as inner region (Fig. 3.2). Each of these two regions is represented by a single fuel pin. The fuel pellets are hollow which aids in fuel squirting phenomena during a Transient Over Power Accident. The pellet diameter is 5.7 mm and the central hole diameter is 1.8 mm. Thickness of the clad is 0.45 mm and its inner diameter is 5.7 mm. The width across flats of the hexcan is 131.3 mm with hexcan thickness of 3.4 mm. The sodium surrounding the clad is assumed to be an annular cylindrical column. The sodium surrounding inner clad is known as inner sodium and that surrounding outer clad is known as outer sodium (see, Fig. 3.3a and Fig. 3.3b). The amount of sodium that surrounds the clad outer surface is calculated from volumetric considerations dividing the total volume of sodium present in the inner/outer regions. The height of active fuel zone prior to fuel melting is 1 m, assuming uniform power generation in all the 217 pins. It may be mentioned that this Chapter deals with lumped parameter approach to understand the TIB event. In this case axial variation is not considered. Further sodium, clad and fuel are modeled as single zones. However, detailed grid independence studies have been carried out for the integrated model (See, Fig. 5.5).

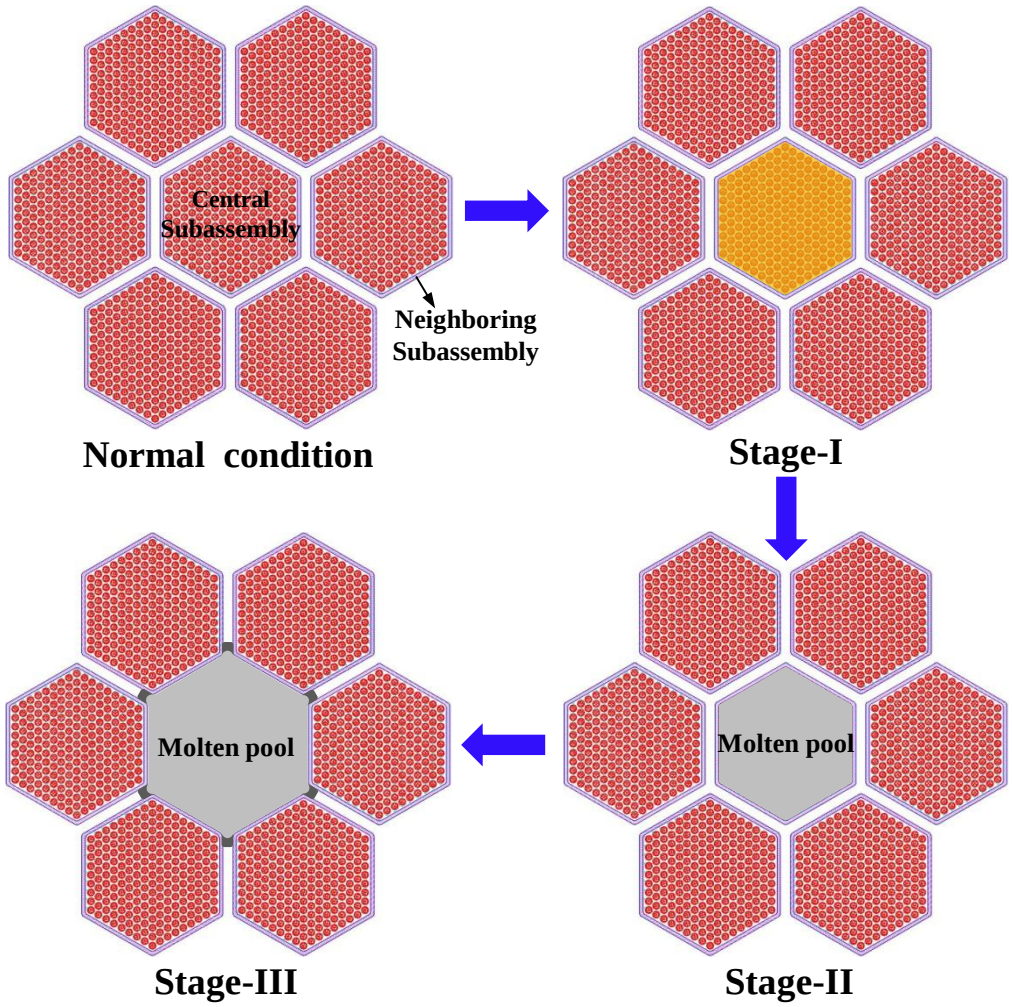

Fig. 3.1. Sketch showing TIB event progression: Normal condition, stage-I: transients within blocked SA before hexcan failure, stage-II: molten fuel attacking blocked SA hexcan and stage-III: molten fuel attacking neighboring hexcan.

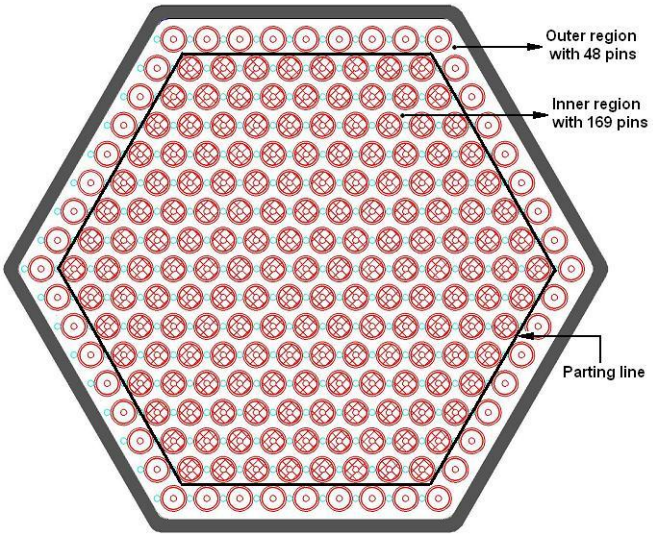

Fig. 3.2. Cross section of a fuel SA showing partition of inner and outer regions.

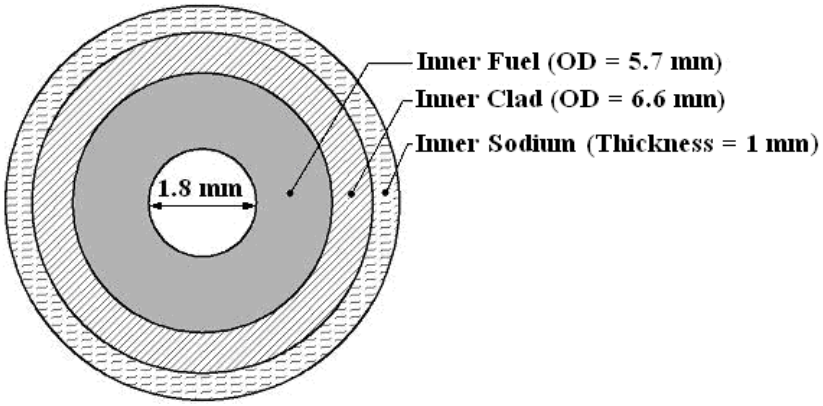

Fig. 3.3a. Representative inner fuel pin and associated sodium.

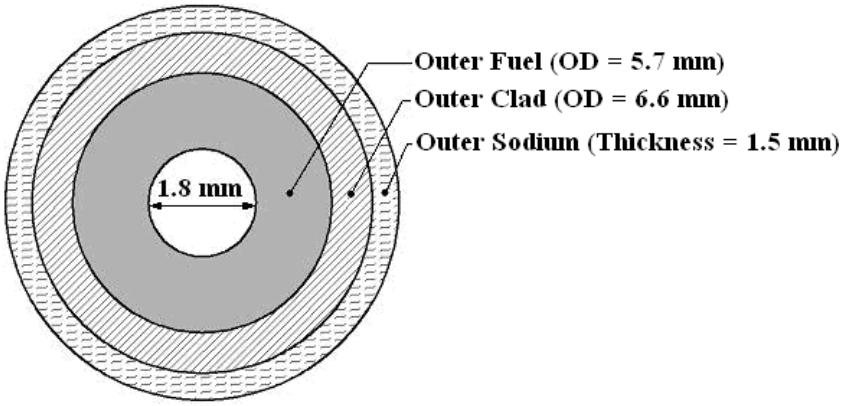

Fig. 3.3b. Representative outer fuel pin and associated sodium.

During a TIB accident scenario, the radial heat transfer from blocked SA to neighboring SA takes place through multiple paths. The transient heat balance equations for (i) fuel, clad and sodium representing both inner and outer regions as well as hexcan of blocked SA, (ii) inter-wrapper sodium and (iii) hexcan of neighboring SA are derived. These are non-linear, inter-linked ordinary differential equations for different parts of blocked and neighboring SA as follows:

Inner fuel:

$$\frac{d}{dt}(H_{fi}) = q_{fi} - (1-\theta_{ci})G_{fci}(T_{fi} - T_{ci}) \tag{3.1}$$

Inner clad:

$$\frac{d}{dt}(H_{ci}) = (1-\theta_{ci})G_{fci}(T_{fi}-T_{ci}) - (1-\theta_{si})G_{csi}(T_{ci}-T_{si}) \tag{3.2}$$

Inner sodium:

$$\frac{d}{dt}(H_{si}) = (1-\theta_{si})G_{csi}(T_{ci}-T_{si}) - (1-\theta_{si})G_{sio}(T_{si}-T_{so}) \tag{3.3}$$

Outer sodium:

$$\frac{d}{dt}(H_{so}) = (1-\theta_{si})G_{sio}(T_{si}-T_{so}) + (1-\theta_{so})G_{cso}(T_{co}-T_{so}) - (1-\theta_{so})G_{sxo}(T_{so}-T_{xb}) \tag{3.4}$$

Outer clad:

$$\frac{d}{dt}(H_{co}) = (1-\theta_{co})G_{fco}(T_{fo}-T_{co}) - (1-\theta_{so})G_{cso}(T_{co}-T_{so}) - \left[\frac{\theta_{so}(1-\theta_{co})\sigma\ (T_{co}^4-T_{xb}^4)}{\frac{1-e_{co}}{a_{co}e_{co}}+\frac{1-e_{xb}}{a_{xb}e_{xb}}+\frac{1}{a_{co}F_{cxo}}}\right] \tag{3.5}$$

Outer fuel:

$$\frac{d}{dt}(H_{fo}) = q_{fo} - (1-\theta_{co})G_{fco}(T_{fo}-T_{co}) - \theta_{co}\left[\frac{\sigma\ (T_{fo}^4-T_{xb}^4)}{\frac{1-e_{fo}}{a_{fo}e_{fo}}+\frac{1-e_{xb}}{a_{xb}e_{xb}}+\frac{1}{a_{fo}F_{fxo}}}\right] \tag{3.6}$$

Blocked subassembly hexcan:

$$\frac{d}{dt}(H_{xb}) = (1-\theta_{so})G_{sxo}(T_{so}-T_{xb}) - (1-\theta_{sr})G_{sxr}(T_{xb}-T_{sr}) + \theta_{so}(1-\theta_{co})\left[\frac{\sigma\ (T_{co}^4-T_{xb}^4)}{\frac{1-e_{co}}{a_{co}e_{co}}+\frac{1-e_{xb}}{a_{xb}e_{xb}}+\frac{1}{a_{co}F_{cxo}}}\right]$$
$$+\theta_{co}\left[\frac{\sigma\ (T_{fo}^4-T_{xb}^4)}{\frac{1-e_{fo}}{a_{fo}e_{fo}}+\frac{1-e_{xb}}{a_{xb}e_{xb}}+\frac{1}{a_{fo}F_{fxo}}}\right] - \theta_{sr}\left[\frac{\sigma\ (T_{xb}^4-T_{xn}^4)}{\frac{1-e_{xb}}{a_{xb}e_{xb}}+\frac{1-e_{xn}}{a_{xn}e_{xn}}+\frac{1}{a_{xb}F_{xbn}}}\right] \tag{3.7}$$

Inter-wrapper sodium:

$$\frac{d}{dt}(H_{sr}) = (1-\theta_{sr})G_{sxr}(T_{xb}-T_{sr}) - (1-\theta_{sr})G_{sxr}(T_{sr}-T_{xn}) \tag{3.8}$$

Neighboring hexcan:

$$\frac{d}{dt}(H_{xn}) = (1-\theta_{sr})G_{sxr}(T_{sr}-T_{xn}) - G_{sxn}(T_{xn}-T_{sn}) + \theta_{sr}\left[\frac{\sigma\,(T_{xb}^4 - T_{xn}^4)}{\frac{1-e_{xb}}{a_{xb}e_{xb}} + \frac{1-e_{xn}}{a_{xn}e_{xn}} + \frac{1}{a_{xb}F_{xbn}}}\right] \tag{3.9}$$

Where, $\theta_{si,}$ $\theta_{so,}$ $\theta_{ci,}$ θ_{co} and θ_{sr} are equal to 0 before their respective phase change and equal to 1 after the phase change. Other symbols are explained in Nomenclature. Some of these equations can also be found in Chen et al., (1979). It may be highlighted that based on preliminary computations, it was found that that sodium boiling, clad melting and fuel melting follow in sequence. This sequence is implicitly assumed while formulating the governing equations.

Calculation of effective thermal Conductance

The effective thermal conductance values between the nodal points of fuel and clad (both inner and outer regions of SA) are calculated using the general expression for radial heat flow across a hallow cylinder (see, Fig. 3.3c).

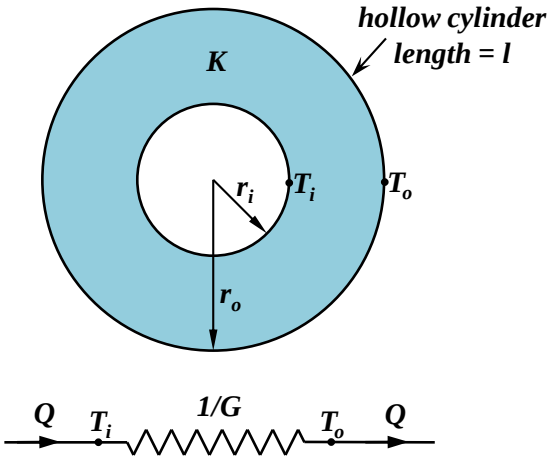

Fig. 3.3c. Heat conduction in hollow cylinder.

$$G = \left[\frac{1}{2\ \pi\ K\ l} \log\left(\frac{r_o}{r_i} \right) \right]^{-1} \tag{3.10}$$

Fuel pellet is a hollow cylindrical heat generating body housed in cylindrical cladding. The overall thermal conductance between nodal points of fuel and clad (G_{fci}) is calculated by considering the individual thermal resistance between the nodal point and interface. G_{fci} is mathematically expressed as (see, Fig 3.3d):

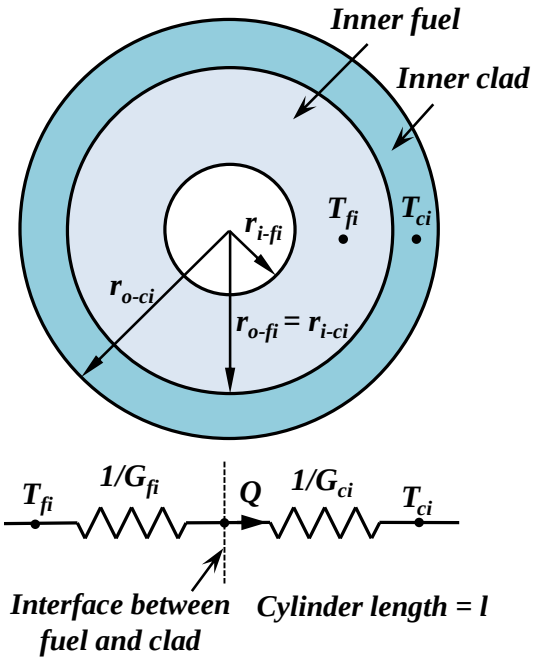

Fig. 3.3d. Heat conduction in inner fuel pin.

$$G_{fci} = \left[\frac{1}{G_{fi}} + \frac{1}{G_{ci}} \right]^{-1} = \left[\frac{1}{2\pi\ K_f l_f} \log\left(\frac{2\ r_{o-fi}}{r_{o-fi} + r_{i-fi}} \right) + \frac{1}{2\pi\ K_c l_c} \log\left(\frac{r_{o-ci} + r_{i-ci}}{2\ r_{i-ci}} \right) \right]^{-1} \tag{3.11}$$

Similarly, the effective conductance between the fuel and clad at outer region of blocked SA is expressed as (see, Fig 3.3e):

$$G_{fco} = \left[\frac{1}{G_{fo}} + \frac{1}{G_{co}} \right]^{-1} = \left[\frac{1}{2\pi\ K_f l_f} \log\left(\frac{2 r_{o-fo}}{r_{o-fo} + r_{i-fo}} \right) + \frac{1}{2\pi\ K_c l_c} \log\left(\frac{r_{o-co} + r_{i-co}}{2\ r_{i-co}} \right) \right]^{-1} \tag{3.12}$$

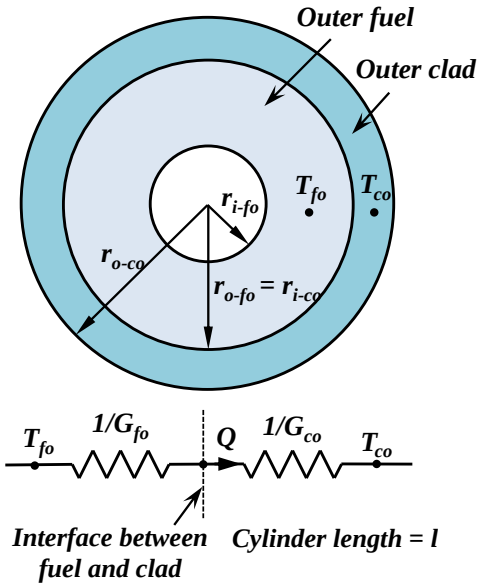

Fig. 3.3e. Heat conduction in outer fuel pin.

$$G_{fco} = \left[\frac{1}{G_{fo}} + \frac{1}{G_{co}}\right]^{-1} = \left[\frac{1}{2\pi K_f l_f}\log\left(\frac{2r_{o-fo}}{r_{o-fo} + r_{i-fo}}\right) + \frac{1}{2\pi K_c l_c}\log\left(\frac{r_{o-co} + r_{i-co}}{2\,r_{i-co}}\right)\right]^{-1} \tag{3.12}$$

The sodium column surrounding the fuel cladding is treated as hollow cylindrical body and hence the effective conductance between clad and sodium is calculated by an analogous procedure. The effective thermal conductance between the inner and outer sodium columns is expressed as (see, Fig. 3.3f):

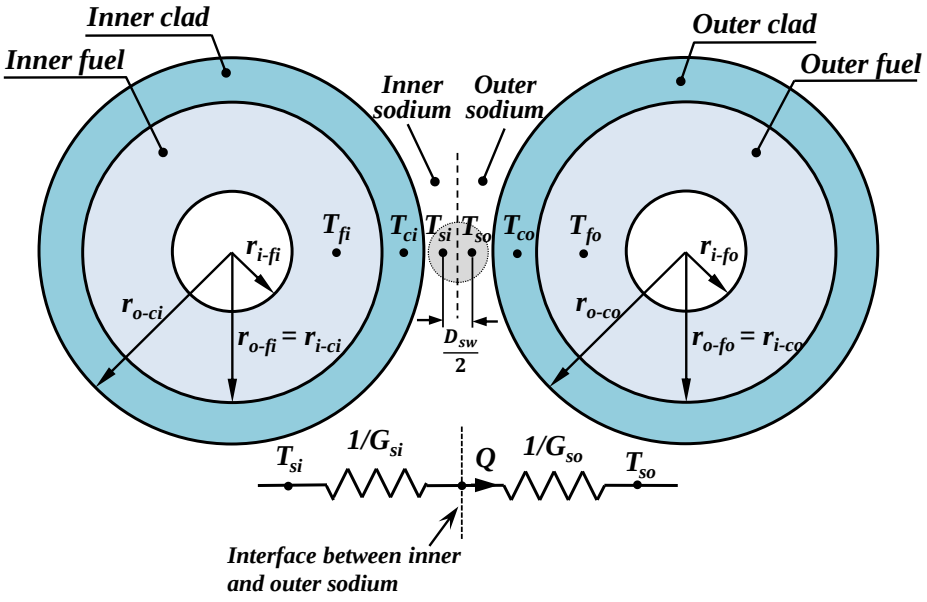

Fig. 3.3f. Heat conduction in inner and outer sodium.

$$G_{sio} = \frac{2K_s a_{sio}}{D_{sw}} \tag{3.13}$$

The nodal points of outer sodium column and blocked SA hexcan are separated by a distance equal to the radius of spacer wire. Therefore effective thermal conductance between them is expressed as (see, Fig. 3.3g):

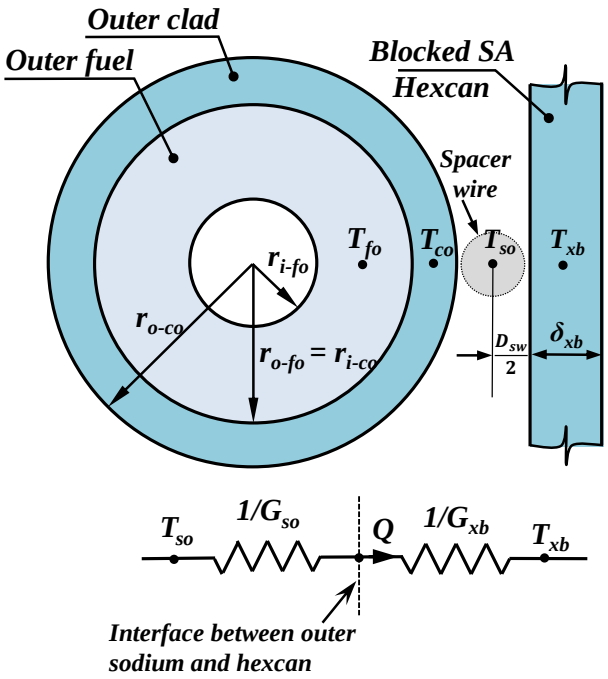

Fig. 3.3g. Heat conduction in outer sodium and blocked SA hexcan.

$$G_{sxo} = \left[\frac{1}{G_{so}} + \frac{1}{G_{xb}}\right]^{-1} = \frac{a_{sxo}}{\frac{D_{sw}}{2K_s} + \frac{\delta_{xb}}{2K_{xb}}} \tag{3.14}$$

The effective thermal conductance between the neighboring hexcan and neighboring SA sodium flow is evaluated by considering individual thermal resistance of neighboring hexcan wall thickness and surface convective resistance at inner surface of neighboring hexcan as:

$$G_{sxn} = \frac{a_{sxn}}{\frac{\delta_{xn}}{2K_{xn}} + \frac{1}{h_{sxn}}} \tag{3.15}$$

The heat transfer coefficient on the inner surface of neighboring hexcan due to forced sodium flow (h_{sxn}) is calculated using the correlation proposed by Kazimi and Carelli (1976),

$$Nu = 4 + 0.33\left(\frac{P_t}{D_c}\right)^{3.8}\left(\frac{Pe}{100}\right)^{0.86} + 0.16\left(\frac{P_t}{D_c}\right)^{5}, \text{ for } 1.15 \le \frac{P_t}{D_c} \le 1.3 \text{ and } 10 \le Pe \le 5000 \qquad (3.16)$$

where, P_t is triangular pitch, D_c is diameter of clad, Pe is Peclet number of sodium flow.

Various parts of SA undergo temperature and phase changes during the transient. For sodium, the enthalpy formulation is adopted to model the sodium boiling, which is best suited for phase change heat transfer. The hydraulic diameter of the sub-channel is very small (~3 mm). Further, the pin bundle is provided with helically wound spacer wires. These features offer significant resistance for flow and hence, natural convection of sodium during boiling is not considered in the present formulation. Such an approach is also essential to retain simplicity of the model. The boiling point for sodium is taken as 1156 K and enthalpy is related to temperature by:

$$T = \begin{bmatrix} H_{spe}/C_{lp},\ if\ \ H_{spe} < C_{lp}T_{bp},\ (Liquid\ Phase) \\ T_{bp},\ if\ \ C_{lp}T_{bp} \le H_{spe} \le C_{lp}T_{bp} + L_{va},\ (Boiling) \\ T_{bp} + \ (H_{spe} - (C_{lp}T_{bp} + L_{va}))/\,C_{vp},\ if\ \ H_{spe} > C_{lp}T_{bp} + L_{va},\ (Vapor\ Phase) \end{bmatrix} \qquad (3.17)$$

Temperature of clad, fuel and hexcan materials at various phases is determined as follows:

a) For materials with fixed melting point:

$$T = \begin{bmatrix} H_{spe}/C_{sp},\ if\ \ H_{spe} < C_{sp}T_{mp},\ (Solid\ Phase) \\ T_{mp},\ if\ \ C_{sp}T_{mp} \le H_{spe} \le C_{sp}T_{mp} + L_{fu},\ (Melting) \\ T_{mp} + (H_{spe} - (C_{sp}T_{mp} + L_{fu}))/C_{lp},\ if\ \ H_{spe} > C_{sp}T_{mp} + L_{fu},\ (Liquid\ Phase) \end{bmatrix} \qquad (3.18)$$

b) For materials which melt between solidus and liquidus points:

$$T = \begin{bmatrix} H_{spe}/C_{sp},\ if\ \ H_{spe} < C_{sp}T_{Sol},\ (Solid\ Phase) \\ T_{Sol} + (T_{Liq} - T_{Sol})(H_{spe} - C_{sp}T_{Sol})/L_{fu},\ if\ \ C_{sp}T_{Sol} \le H_{spe} \le C_{sp}T_{Sol} + L_{fu},\ (Melting) \\ T_{Liq} + (H_{spe} - (C_{sp}T_{Sol} + \ L_{fu}))/C_{lp},\ if\ \ H_{spe} > C_{sp}T_{Sol} + L_{fu},\ (Liquid\ Phase) \end{bmatrix} \qquad (3.19)$$

The meanings of various subscripts are given in Nomenclature. The variation in the thermophysical properties of sodium, steel and fuel material due to temperature changes is taken into account by using the correlations given by Chawla et al., (1984).

Sodium outlet temperature from neighboring SA and thermocouple response

During TIB in a fuel SA, the radial heat emerging from the blocked SA is transferred to neighboring SA. Taking this into account, the sodium outlet temperature from neighboring SA is evaluated from,

$$T_{sno} = T_{sni} + \frac{G_{sxn}(T_{xn} - T_{sn})}{m_s C_s} \tag{3.20}$$

It shall be mentioned that core monitoring thermocouples are located at 100 mm above the SA outlet to monitor the sodium temperature. Above the active core (see, Fig. 1.4) there are axial blanket, mixing plenum, steel/B_4C shielding and blockage adopter. These provisions offer ample scope for mixing of sodium from varies subassemblies. Considering these points, sodium from neighboring subassembly is assumed to be well mixed. Prediction of sodium outlet temperature distribution, calls for transient, 3-D CFD analysis of neighboring SA flow characteristics. This is taken as scope for future research. Thus, the measured temperature can be considered to be mass averaged temperature.

But these thermocouples do not read the instantaneous sodium temperature due to the presence of finite response time. Typical value of thermocouple response time is 8 s. Taking this into account, the instantaneous thermocouple reading due to sodium temperature change at SA exit is determined by:

$$T_{tr}^{j+1} = \frac{(T_{tr}^{j} / \Delta t) + (T_{sno}^{j+1} / \tau)}{(1/\Delta t) + (1/\tau)} \tag{3.21}$$

where, T_{tr}^{j+1} is the thermocouple reading at $(j+1)^{th}$ time step, T_{tr}^{j} is the thermocouple reading at j^{th} time step, Δt is the time step, τ is the thermocouple response time and T_{sno}^{j+1} is the instantaneous sodium outlet temperature from neighboring SA.

During stage-I, sodium boiling occurs, followed by clad and fuel melting. It is understood from the BE+ test series of SCARABEE_N experimental program that during clad melting, the upward sodium vapor flow is not strong enough to entrain the molten steel. The liquid steel drains downward and creates a steel blockage around the still intact fuel pins at the level of the solidus temperature of the cladding. The molten steel due to clad melting starts accumulating over a steel blockage forming a molten steel pool around the intact fuel pins. Then, the fuel pins above the molten steel pool break up and collapse, forming a molten fuel pool displacing the steel pool. It is reported that due to material motion and blockage formation, a very little or no fuel is ejected out of the fissile zone early in the transient (Kayser et al., 1998).

3.2.2 STAGE-II

Stage-II is focused to examine the thermal transients in various parts of blocked SA as well as inter-wrapper sodium and neighboring SA hexcan. Further, it is required to estimate the time taken for complete melting of blocked SA hexcan and the corresponding temperature rise in neighboring SA sodium outlet towards an early detection of the event. Reported estimation of melting and solidification rates using analytical methods is limited to semi infinite regions and constant material properties (Epstein, 1973). In the present study finite thickness and variable material properties of both fuel and hexcan are taken into account during their melting/solidification process. In stage-II, the molten fuel of blocked SA in a bottled-up condition forms a liquid column with effective height determined based on the quantity of fuel material in fissile zone. The heat loss in the axial direction is neglected due to formation of

adiabatic atmosphere by sodium vapor over top and bottom surfaces of molten pool blockage. Heat transfer takes place predominantly in the radial direction from the molten pool to the six faces of the hexcan. The molten pool in the SA is divided into 6 sectors and one sector is considered for the analysis as shown in the Fig. 3.4. The single equilateral triangular fuel sector is divided into ~370 elements. The blocked SA hexcan wall is divided into 20 elements. The stagnant inter-wrapper sodium is represented by a single element and the neighboring hexcan is also considered as a single element (Fig. 3.5).

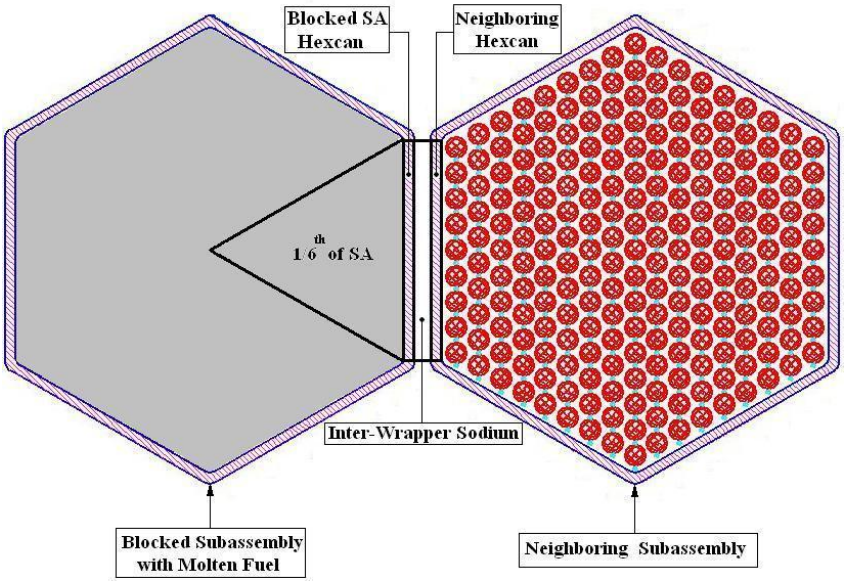

Fig. 3.4. Blocked SA with molten pool and neighboring SA during stage-II.

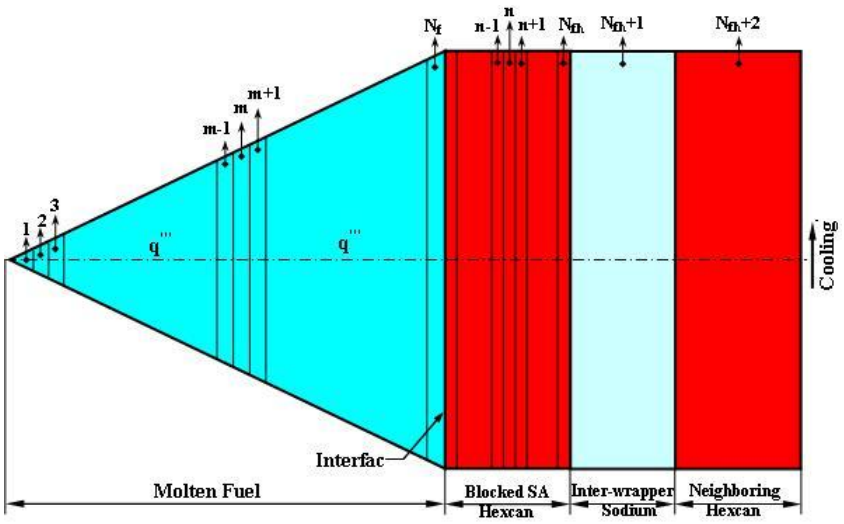

Fig. 3.5. Geometric modeling during stage-II.

During this stage, the hexcan of blocked SA in contact with the molten fuel starts melting layer by layer from inner side and its outer surface is exposed to inter-wrapper sodium. Heat flux leaving the outer surface of hexcan is affected by thermal resistance of hexcan which decreases with time due to reduction in its thickness by melting. In general, the temperature of fuel and hexcan elements at any instant depends upon the heat generation rate of fuel, their thermal resistances and external cooling rate. One of the difficulties associated with phase change heat transfer is the moving solid-liquid interface, popularly known as 'Stefan problem'. There are a number of numerical techniques available to tackle the above problem. In the present work, enthalpy based method is implemented which is one of the robust and efficient methods, which does not require to satisfy the condition of moving boundary and instead is based on fixed domain solution. However, this method is associated with the mild oscillations in the temperature field. This has been overcome by implementing a technique based on fixed space grid but a variable time step keeping phase front always on a node point, known as 'node-Jumping scheme' (Voller, 1987). This scheme is implemented by making suitable modifications in the governing equations to incorporate the heat source term and establishing proper connectivity for heat transfer between dissimilar materials at the interface of melting front.

General enthalpy formulation is expressed as:

$$\rho \frac{\partial H_{spe}}{\partial t} = \nabla \left[K(\nabla T) \right] + q''' \tag{3.22}$$

The heat balance equation for m^{th} fuel element is expressed as:

$$\frac{d(H_{fe})_m}{dt} = (q_{fe})_m + (G_{fe})_{m-1,m} \left[(T_{fe})_{m-1} - (T_{fe})_m \right] - (G_{fe})_{m,m+1} \left[(T_{fe})_m - (T_{fe})_{m+1} \right] \tag{3.23}$$

Similarly, the heat balance equation for n^{th} hexcan element is expressed as:

$$\frac{d(H_{xe})_n}{dt} = (G_{xe})_{n-1,n} \left[(T_{xe})_{n-1} - (T_{xe})_n \right] - (G_{xe})_{n,n+1} \left[(T_{xe})_n - (T_{xe})_{n+1} \right] \tag{3.24}$$

The first element of hexcan in contact with molten pool gets heated up and attains the melting point before any other element. As soon as the hexcan element melts completely, it gets detached from the neighboring element and floats over the molten fuel due to its low density (Kayser et al., 1998). Then the melting front advances forward in the radial direction and comes in contact with second hexcan element, which also eventually melts. Hence, the melting front keeps on progressing in radial direction until entire hexcan melts completely or gets stabilized at some point with a finite residual thickness of hexcan whose thermal resistance is less enough to balance the radial heat flux emerging from the molten pool with external cooling. Elimination of melted steel element from the fuel-steel interface and maintaining the advancement of melting front are mathematically modeled in the present work by dynamically deleting the node of molten steel element from the domain and bringing the next node of steel element to interface, retaining the melting front at same position. However, the natural convection effect within the fuel pool is neglected. The detailed study on natural convection in the fuel pool and its effect on inter-subassembly heat transfer and damage progression are discussed in the next Chapter. Selection of proper grid size is found essential to avoid temperature oscillation due to dynamic node deletion.

3.2.3 STAGE-III

At the end of stage-II, the blocked SA hexcan completely melts down due to the molten fuel attack and the melt front further advances towards the neighboring SA. The BE+3 test of SCARABEE-N experimental program conforms that no significant amount of fuel will escape through the inter-wrapper gap and the specially designed PI-A test showed that the molten steel coming from the melting hexcan will enter into inter wrapper gaps and plug them. Thus, a tight blockage of fuel pool is formed which is surrounded by 6 neighboring SA, whose hexcan are attacked (see, Fig. 3.6).

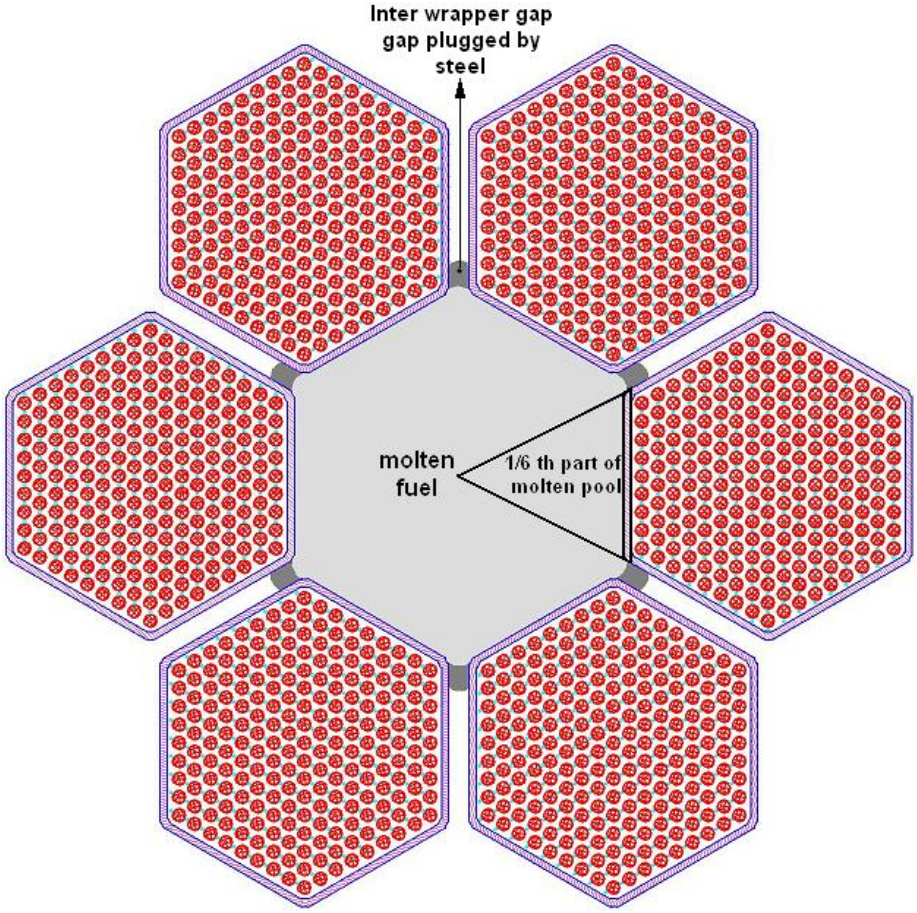

Fig. 3.6. Sectional view of blocked SA with molten fuel pool and neighboring SA with plugged inter-wrapper region.

The objective of stage-III is to study the expected temperature rise in the thermocouple reading of the neighboring SA when its hexcan undergoes melting on outer side and cooled by sodium on inside. Another primary objective of this stage is determination of residual thickness of neighboring SA hexcan wall at the time of reactor trip. In this stage also, the fuel pool surrounded by neighboring SA is divided in to six equal sectors, and one symmetry sector is considered for the analysis. The single sector is further divided into ~ 370 elements. The neighboring hexcan of 3.4 mm thick is divided into 20 equal elements (Fig. 3.7). The initial temperature distribution for starting this stage of calculation is taken from the end of Stage-II.

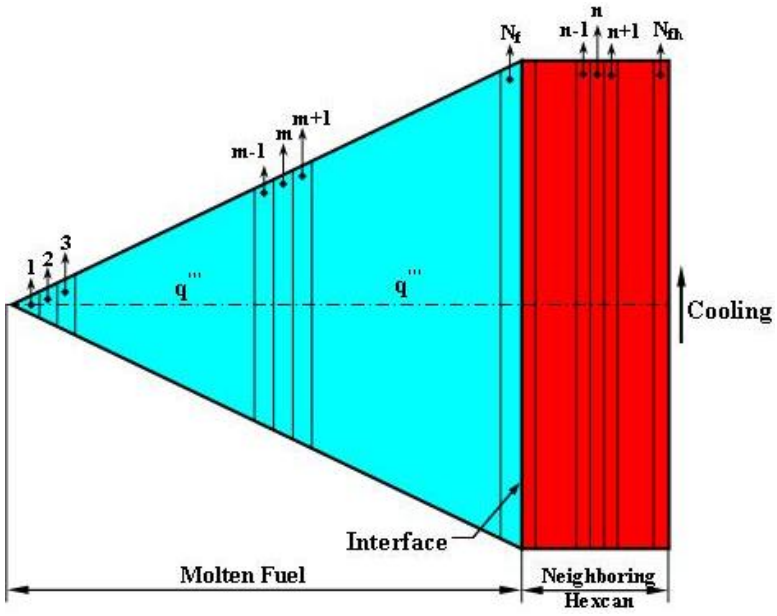

Fig. 3.7. Geometric modeling during stage-III

3.3 VALIDATION STUDIES

The results of present calculations are compared with the related SCARABEE tests (Kayser et al., 1998) and also with the TIB calculations of Phenix reactor (Cadiou and Louvet, 2006), Superphenix reactor (Murin et al., 1982) and CEFR (Wang and Cao, 2007).

The temperature rise at the outlet of adjacent SA, calculated in the present TIB study is compared with Superphenix reactor calculations (Murin et al., 1982) in Fig. 3.8. Rise in neighboring SA sodium outlet temperature is very gradual till the blocked SA melting is completed which lasts for about 20 s. Subsequent to this, the heat transfer between the molten fuel and the neighboring hexcan is intensive, leading to a sharp rise in the sodium outlet temperature. The intensity of heat transfer is a strong function of thermal conductivity of molten fuel and presence of natural convection within the molten fuel pool. The natural convection in the molten fuel pool enhances the rate of heat transfer to neighboring subassembly. But in the present 1-D model, the pool is assumed to be stagnant where the conduction heat transfer alone is considered. This is the reason behind slow temperature rise. However, detailed study on

natural convection in fuel pool is carried out in Chapters 4 and 5 to predict realistic heat transfer and damage progression rates.

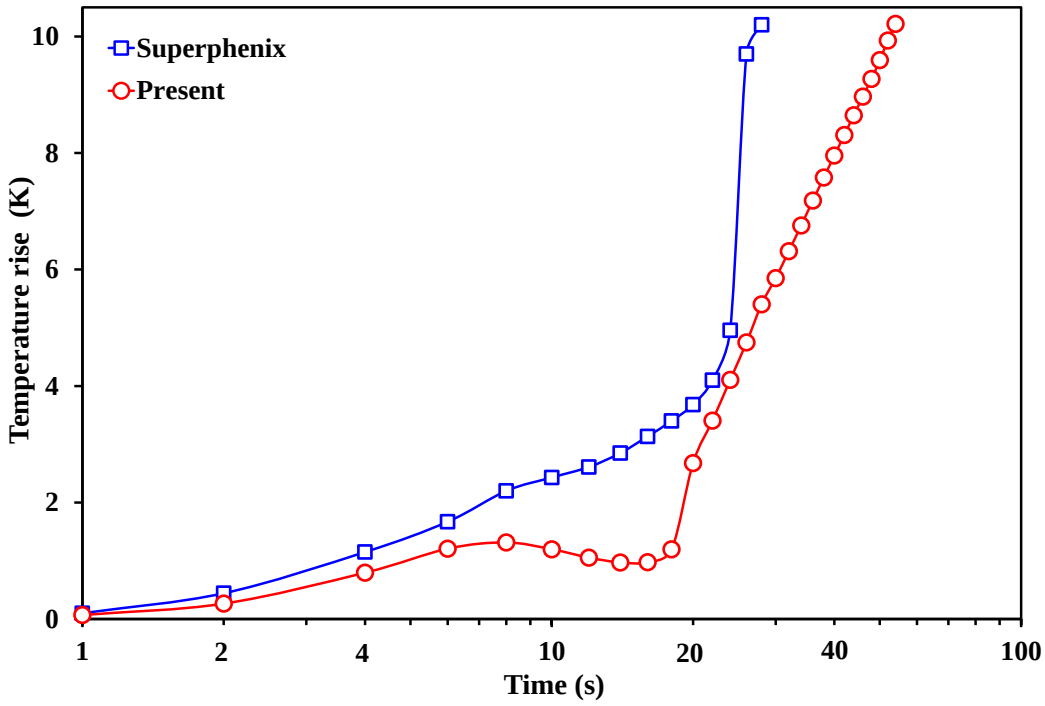

Fig. 3.8. Time dependent temperature rise of sodium from neighboring SA outlet during TIB in a fuel subassembly.

It may be noted that the present results compare well with that of Superphenix up to ~8 s. Beyond 8 s, the present results indicate a dip in thermocouple reading, while such an explicit dip is not obvious in Superphenix results. It may be highlighted that once sodium is completely evaporated in the blocked SA, the heat transfer from clad to hexcan reduces initially. As a consequence of this, the clad and fuel temperatures increase. Due to this, radiation heat exchange between clad and hexcan picks-up. This is the reason for a non-monotonic heat transfer from affected SA to neighboring SA and the consequent sodium temperature rise in the neighboring SA.

The sequence and time of occurrence of principal events during TIB accident scenario reported in open literature are compared with the present calculations. Table-3.1 compares the instants when various principal processes occur in a totally blocked SA with SCARABEE test

(Kayser et al., 1998). Also shown in the same Table are the reported results of Phenix (Cadiou and Louvet, 2006) and CEFR reactor (Wang and Cao, 2007) subassemblies. It is clear that the time predicted by the present robust model is in line with that reported for other reactors, demonstrating the acceptability of the present model.

Table 3.1 Comparison of instants when different processes take place

Process	Time (s)					
	PFBR (Present)	Phenix	CEFR	SCRABEE BE+ Tests		
				BE+1	BE+2	BE+3
Start of TIB	0.0	0.0	0.0	0.0	0.0	0.0
Start of sodium boiling	1.9	0.5	1.0	3.0	2.0	-
End of sodium boiling	6.2	5.0	2.5	-	3.0	-
Start of clad melting	8.5	6.0	5.2	6.0	5.5	-
End of clad melting	10.0	9.2	6.0	-	-	-
End of fuel melting	17.8	-	15.0	-	-	-
End of affected hexcan melting	19.0	18.5	16.5	-	-	21.0

3.4 RESULTS AND DISCUSSION

3.4.1 STAGE-I

Having established satisfactory comparison of results from the present model with the published data, detailed investigations of TIB accident scenario in a single fuel SA of medium size FBR fuel SA (Chetal et al., 2006) is carried out. During full power operation, the thermal power rating of central fuel SA is 8MW. Sodium mass flow rate in the SA is 35.8 kg/s with sodium temperatures at fuel SA inlet/outlet are 673 and 833 K respectively. When the SA sodium flow is blocked suddenly, temperature of the SA starts rising, followed by sodium

boiling in the inner region first at 2 s and then in outer region of the SA nearly at the same time (Fig. 3.9). Temperature of both inner and outer sodium remains nearly identical during boiling and the sodium volume fraction in the blocked SA keeps reducing. Sodium boiling ends in the inner region first at ~6 s and later in outer region at 7.5 s, resulting in complete sodium dry out.

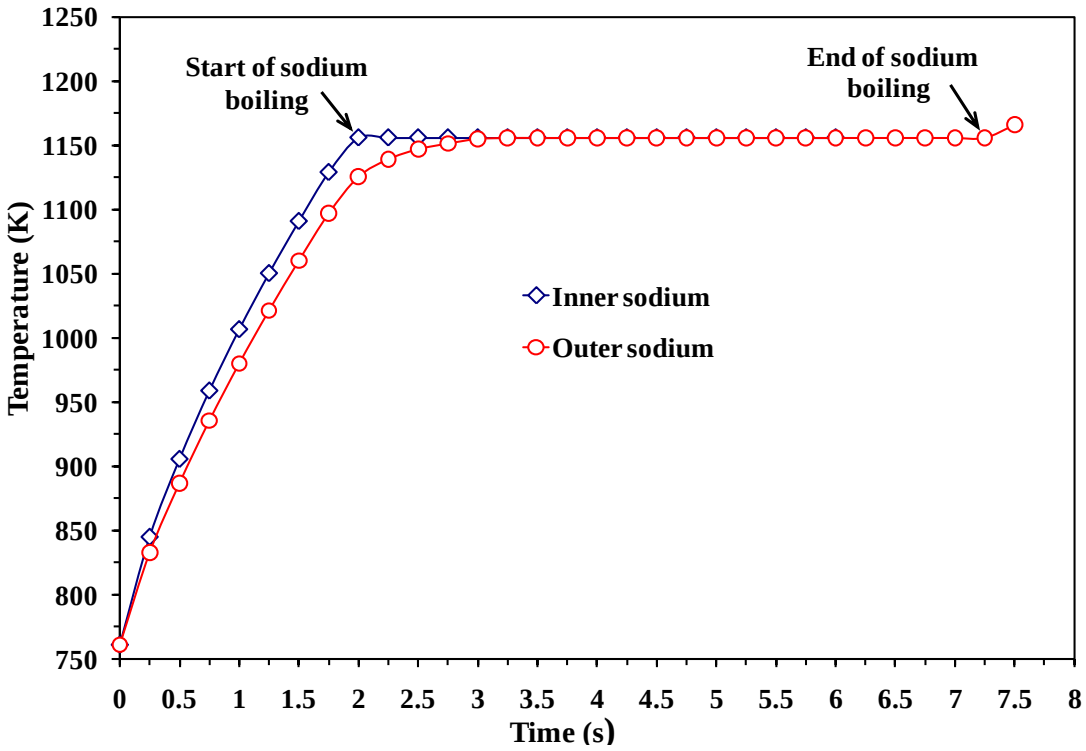

Fig. 3.9. Temperature evolution in inner and outer sodium during stage-I.

Sodium dry out in SA creates an adiabatic environment around the cladding surface, causing a sudden rise in cladding temperature as depicted in Fig. 3.10. Clad melting starts in the inner region as well as in the outer region of SA nearly at the same time at about 8.5 s and it ends in both the regions at ~10 s after start of TIB. The clad temperature is seen to be very close to that of sodium, during the interval when sodium boiling occurs. This is due to the large boiling heat transfer coefficient of sodium.

Based upon the reported experience from BE+ test series of SCARABEE experimental program, it is assumed that the liquid steel coming out due to clad melting, drains downward and settles at the bottom of active zone, forming a steel blockage around the bare fuel pin.

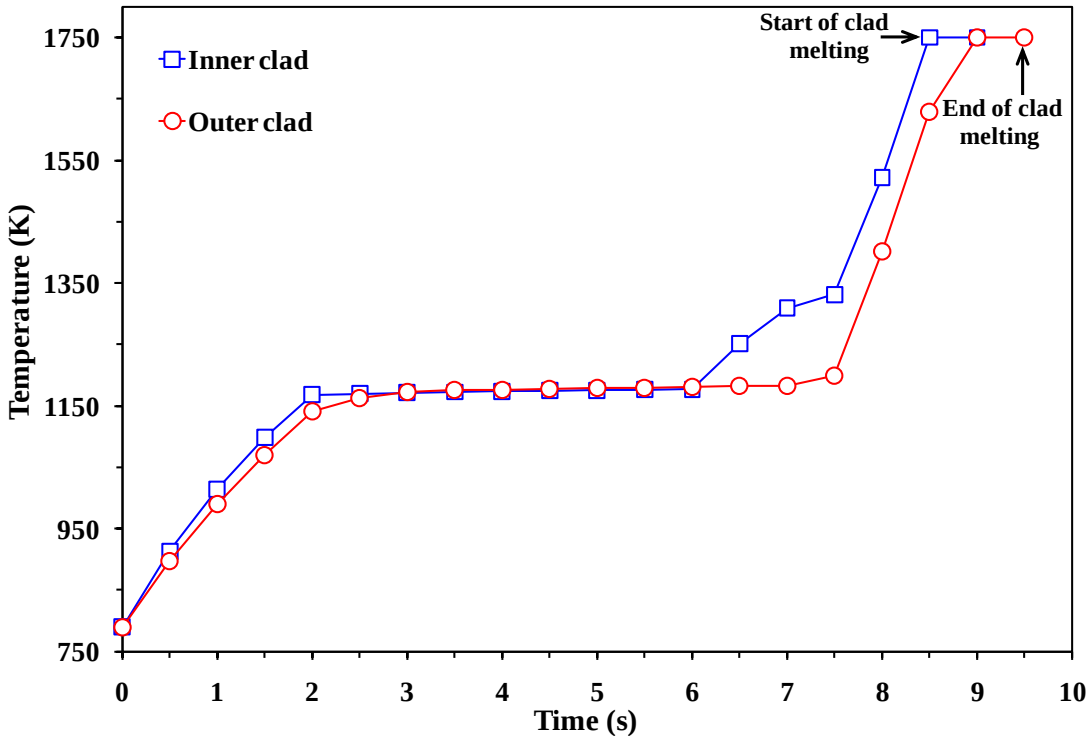

Fig. 3.10. Temperature evolution in the cladding during stage-I.

The fuel melting starts first at inner region followed by outer region of the SA at about 14 s and 15.5 s respectively after start of TIB as can be seen in Fig. 3.11. It takes only ~4 s for complete fuel melting in both the regions, culminating in fuel pool formation at ~18 s after the initiation of TIB. Fuel temperature rise is very gradual up to ~8 s, where there is intense heat exchange between fuel and boiling sodium through the clad. At the end of sodium vaporization and complete clad melting, the fuel temperature increases at a faster rate.

The hexcan wall, whose inner surface is exposed to blocked SA sodium and outer surface to inter-wrapper sodium, experiences a non-monotonic temperature rise (Fig. 3.12). As soon as TIB starts inside the SA, temperature of liquid sodium within the SA rises allowing effective heat transfer between fuel pin and hexcan surface leading to inter-wrapper sodium temperature rise. Later at ~7.5 s (from the commencement of TIB), the hexcan temperature starts decreasing. This is because of sodium dry out in the SA which retards the heat transfer to hexcan from clad through sodium. However, hexcan temperature starts rising later as a result of increasing

temperature difference between the isolated clad and hexcan surface, which gives rise to radiation heat transfer

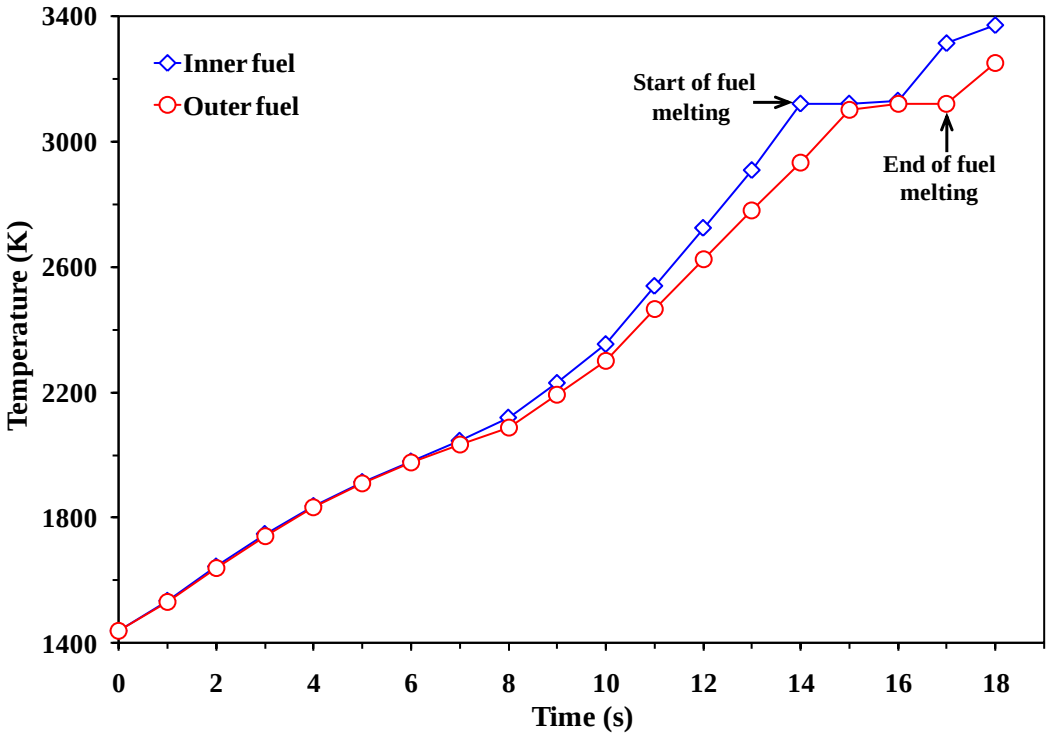

Fig. 3.11. Temperature evolution in the fuel pellet during stage-I.

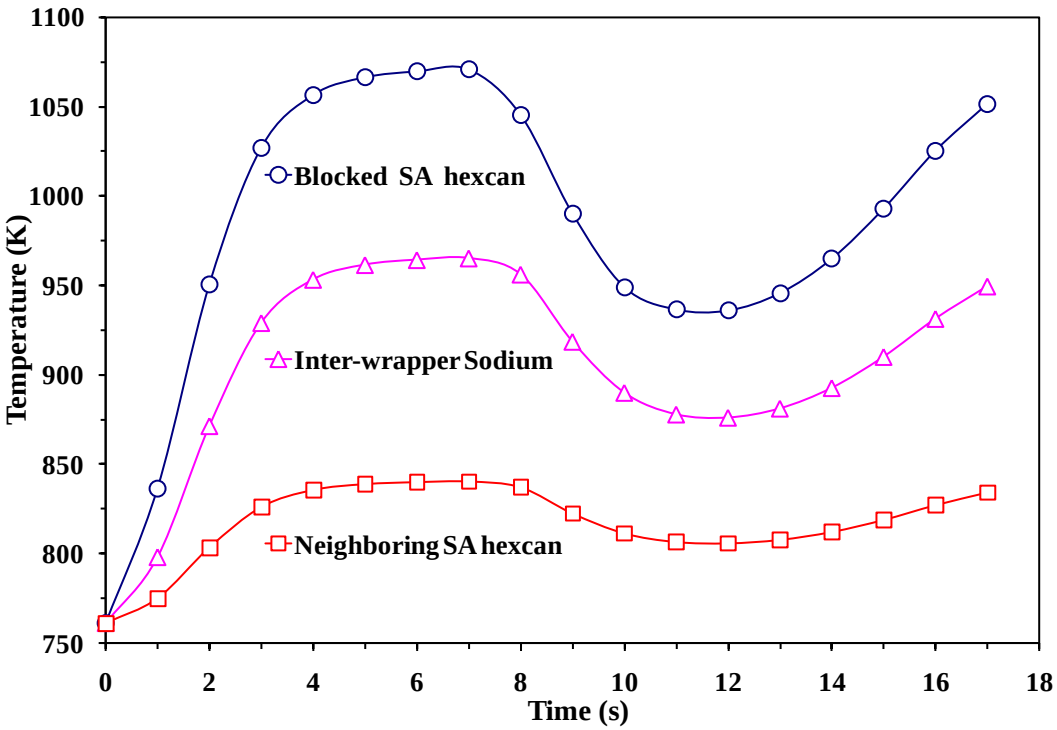

Fig. 3.12. Temperature evolution of blocked SA hexcan, inter-wrapper sodium and neighboring SA hexcan during stage-I.

It is clear from the Fig. 3.12 that the integrity of hexcan is not of much concern during stage-I because its peak temperature during this stage is well below its melting point. The inter-wrapper sodium and neighboring SA hexcan also experience only mild temperature variations with peak values less than the respective phase change temperatures.

The maximum temperature rise in neighboring SA sodium due to radial heat emerging from blocked SA during stage-I is found to be only 2 K, which is well below the SCRAM threshold of 10 K. Hence, it is to be noted that TIB occurrence in the SA is not detected by the core temperature monitoring system during stage-I when fuel pins melt down completely forming a fuel pool in the SA.

3.4.2 STAGE-II

In general, the damage propagation rate in SA at any instant depends upon various parameters influencing the heat transfer and material property variation due to phase change. Predicted temperature evolution during stage-II in fuel and hexcan of the blocked SA is depicted in Fig. 3.13. It is seen that the hexcan melts down completely within 1.2 s after the molten fuel attack. Adjacent elements of fuel and hexcan exhibit large temperature changes on contact with each other. For example, the temperature of fuel element (F-370) bordering hexcan reduces from ~3300 K (before interaction) to ~1820 K within a short time after the interaction. On the other hand, the temperature of hexcan element (H-1) bordering fuel increases from ~920 K to 1820 K within the same interval. The fuel element temperatures bordering hexcan indicate that a significant part of the fuel freezes due to intense heat transfer to hexcan.

It may be recalled that in the present model, the molten hexcan elements are dynamically removed, since the density of steel is less than that of fuel and molten fuel and steel are immiscible.

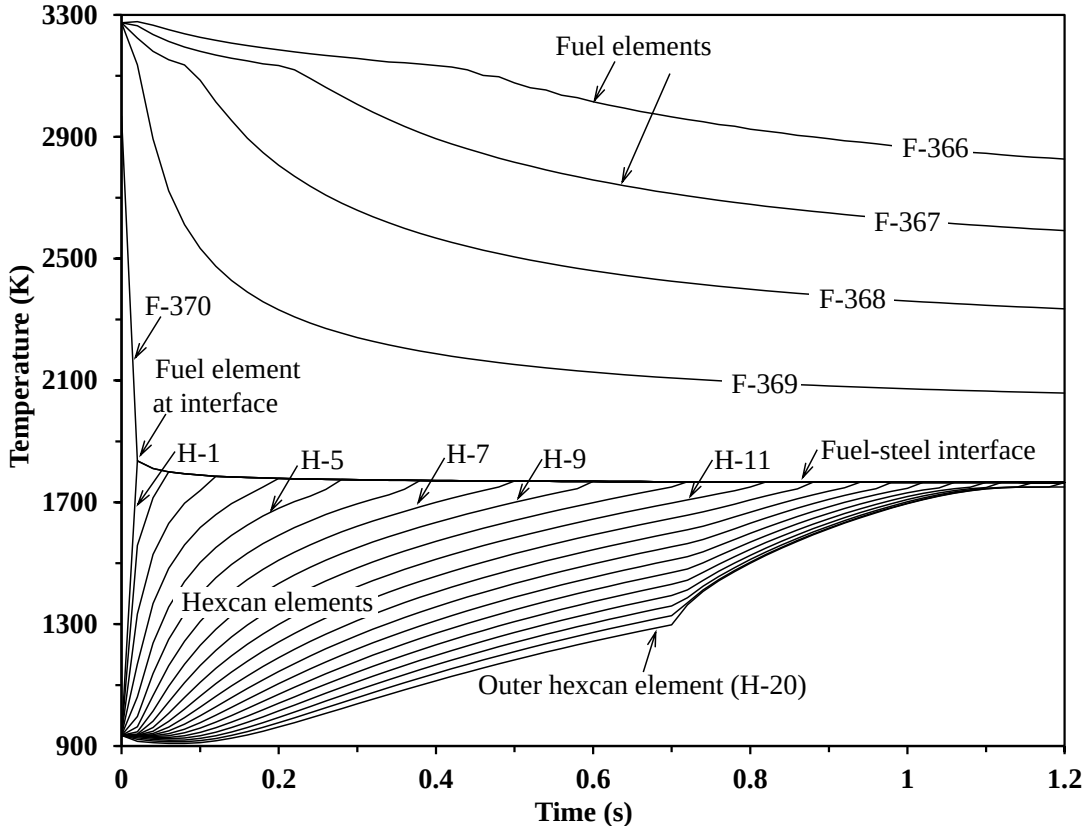

Fig. 3.13. Temperature evolution of fuel elements (F-366 to F-370) and hexcan elements (H-1 to H-20) during stage-II.

This dynamic node removal establishes fresh hexcan element to come into contact with molten fuel, effectively reducing the thickness of the hexcan during the transient. The reduction in hexcan thickness leads to enhanced heat transfer from hexcan to inter-wrapper sodium. As a result of this the melting speed of the hexcan reduces with time upto ~0.7 s. After this instant, the inter-wrapper sodium completely vaporizes leading to reduction in heat loss from the hexcan. As a consequence of this phenomenon, the hexcan melting rate increases leading to complete melting of hexcan within another 0.5 s. Thus the inter-wrapper sodium which controls heat absorption from hexcan outer surface plays a major role in deciding the melting speed of hexcan. The temperature variation of inter-wrapper sodium during stage-II is shown in the Fig. 3.14. It is observed that the sodium temperature continuously increases, during its liquid phase, remains at boiling point during evaporation and again increases during superheating. The bulk temperature

of neighboring SA hexcan almost remains unaffected but decreases after inter-wrapper sodium has completely evaporated. This is due to reduction in heat flux arriving from blocked SA and continuous cooling on the inner side of hexcan by neighboring SA sodium flow.

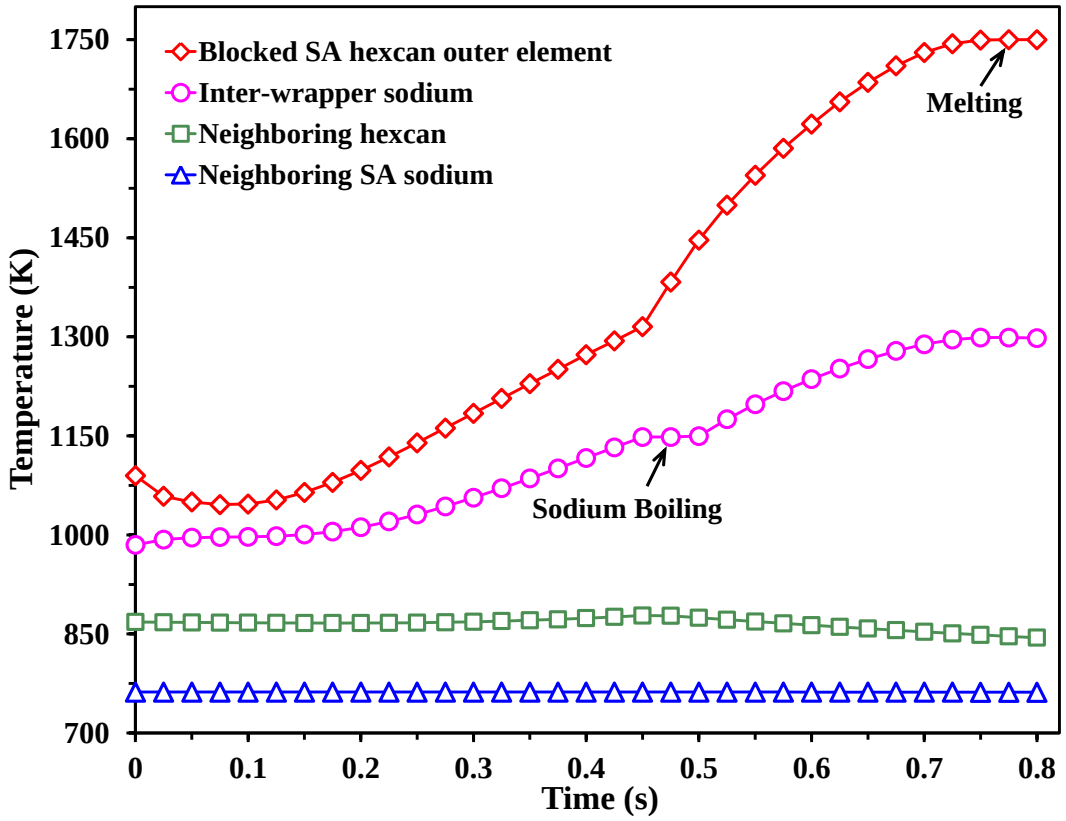

Fig. 3.14. Temperature evolution of inter-wrapper sodium during stage-II.

These results are found to be qualitatively similar to the numerical study carried out on interaction of molten UO_2 with stainless steel cladding under Transient Over Power (TOP) accident by Jones et al. (1978). No appreciable increase was noticed in the neighboring SA sodium outlet temperature due to relatively low heat transfer from boiling pool in the blocked SA during this stage. Hence, it is to be noted that TIB occurrence in the SA is not detected by core temperature monitoring system before blocked SA hexcan melting. Pool of fuel formed by melting of fuel and hexcan at the end of stage-II attacks the neighboring SA hexcan, which is discussed in stage-III.

3.4.3 STAGE-III

In stage-III, the melting speed of neighboring hexcan is slow at the beginning of molten fuel attack, because the melting front advances towards neighboring hexcan after melting the blocked subassembly hexcan at the expense of its internal energy. This results in sufficient cooling and solidification of fuel layers by the time it approaches the neighboring hexcan. It is observed in Fig. 3.15a that a time duration of several seconds is required for the interface temperature to rise before start of hexcan melting. This is due to poor thermal diffusivity of fuel and continuous cooling of hexcan on the inner side by sodium flow. The initial temperature of frozen fuel element at the interface is 1630 K and it falls rapidly to 1326 K before rising gradually later (Fig.3.15b). The initial temperature of neighboring hexcan element bordering the fuel is 844 K and the first element completes melting by 8.8 s (Fig. 3.15a) after initiation of stage-III. There is a continuous rise in the temperature of fuel elements at interface even after start of hexcan melting. But, the speed of hexcan melting is found to decrease mainly due to enhanced heat absorption by the flowing sodium consequent to continuous reduction in hexcan thickness. The neighboring SA sodium temperature rise is rapid at the beginning of fuel attack; for example, the SA sodium temperature rises by ~5 K in 2 s at 8 MW power level (Fig. 3.16). This is due to high heat flux at outer face of hexcan by sudden heating of hexcan on initial contact with fuel elements. However, the rate of rise reduces due to freezing of the fuel front. Following these, a gradual increase in sodium outlet temperature is observed from the neighboring SA.

Expected thermocouple reading of the neighboring SA due to temperature rise in SA sodium during stage-III is calculated considering a thermocouple time constant of 8 s. It is seen that the thermocouple temperature rise crosses 10 K at about 38 s after the neighboring hexcan came into contact with molten fuel. Hence, it is to be noted that TIB occurrence in the SA can be detected by monitoring the SA outlet temperature. The residual thickness of hexcan at the time of reactor SCRAM is 51%.

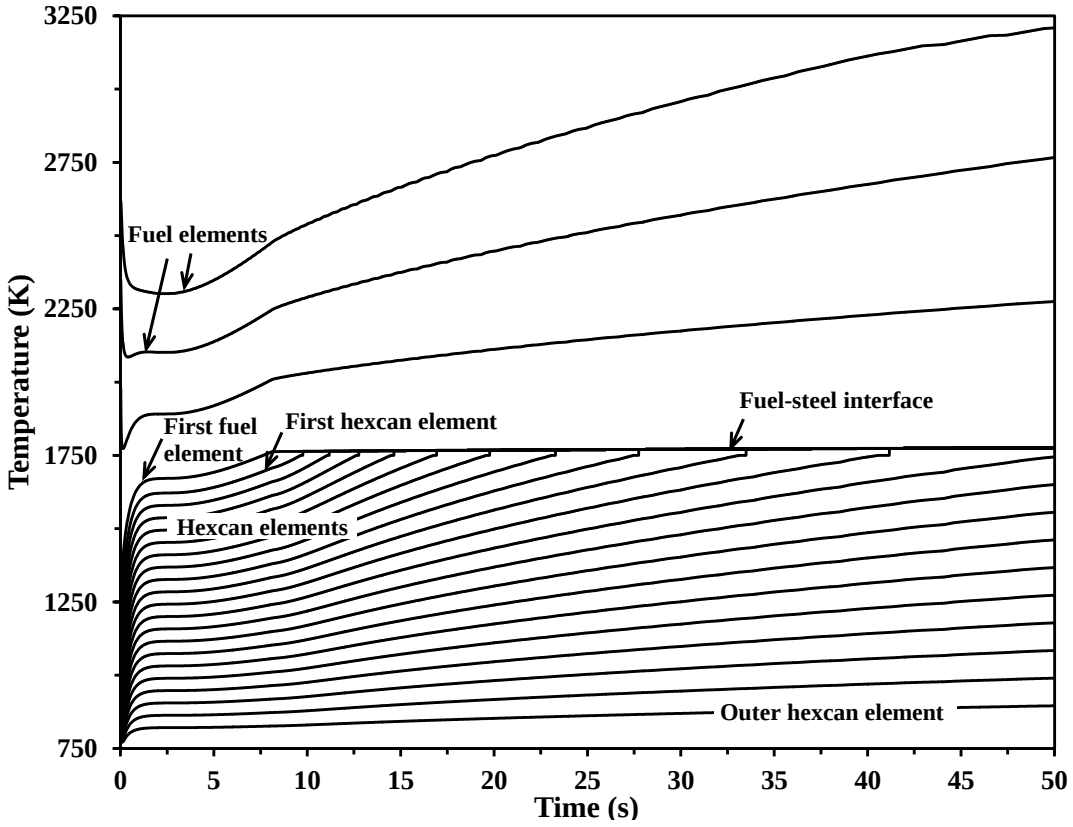

Fig. 3.15a. Temperature evolution of affected SA fuel and neighboring SA hexcan elements at nodal points during stage-III.

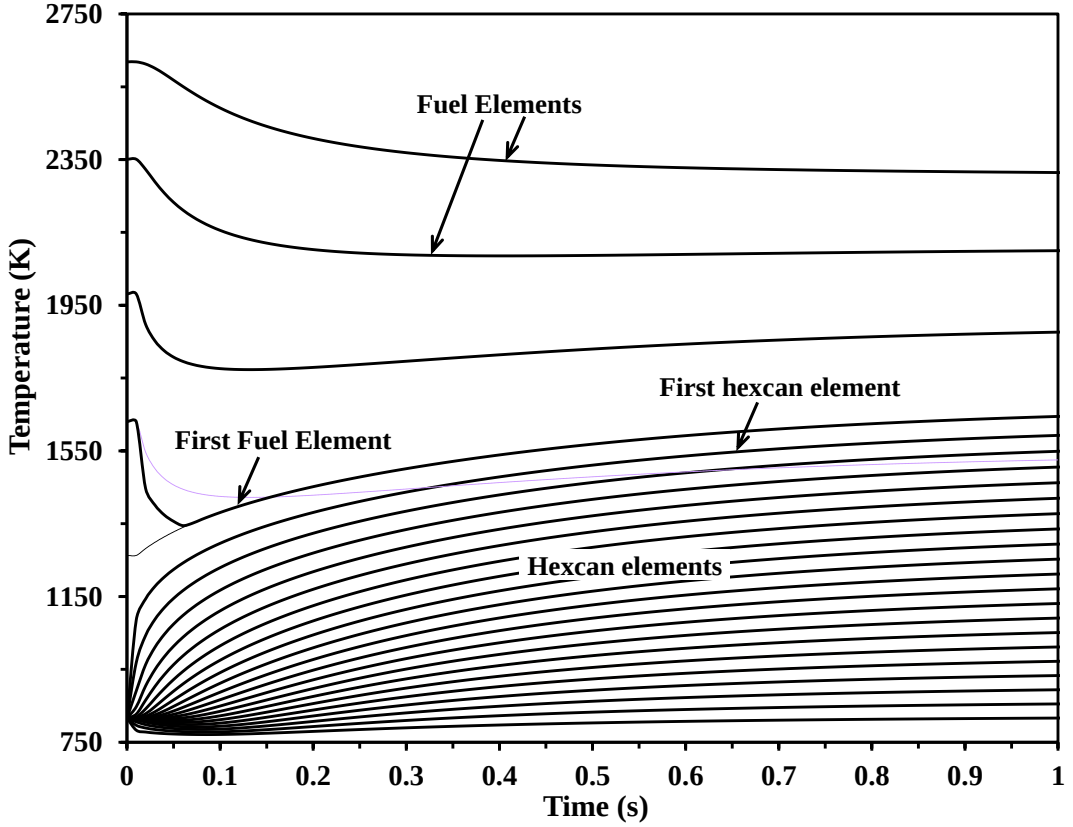

Fig. 3.15b. Temperature evolution of affected SA fuel and neighboring SA hexcan elements at nodal points during the initial stage of stage –III.

It shall be highlighted that structural failure by thermal effect alone is considered in the present study. Effect of creep and internal pressure are not considered in the present study to decide structural failure.

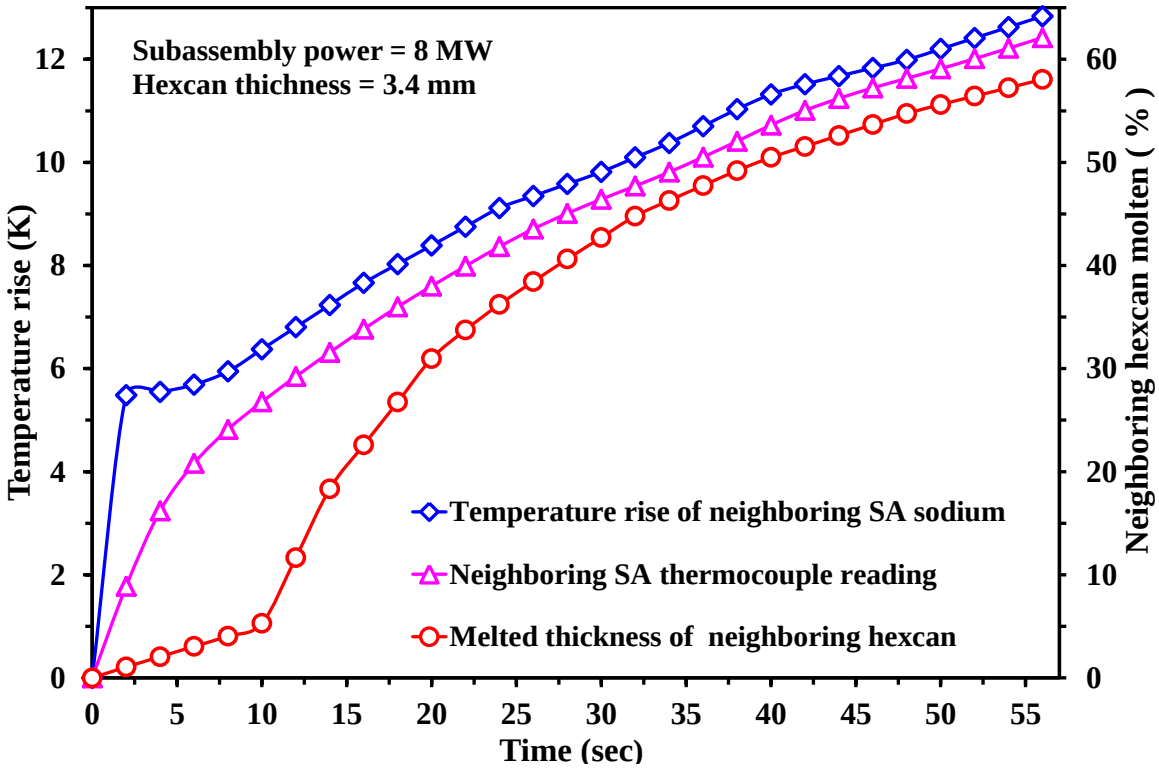

Fig. 3.16. Time dependent temperature rise of neighboring SA sodium with corresponding thermocouple reading and melted thickness of neighboring hexcan during stage-III at 8MW power (time = 0 s refers to commencement of stage-III).

From the point of view of detection of this event, the thermocouple reading of the neighboring SA sodium outlet is an important parameter. Evolution of this reading as a function of time since the initiation of TIB is depicted in Fig. 3.17. The sequence of various processes is also shown in the same figure, wherein the thermocouple time constant is 8 s and the SA power is 8 MW. As already discussed, it is evident that sodium boiling in the blocked SA completes 7.6 s after start of TIB. Following this, the blocked SA clad melting ends by ~10 s. Subsequent to this, fuel melting completes by 18 s, after start of TIB. However, significant temperature rise is not observed in neighboring SA sodium. After fuel melting and material relocation to form

molten fuel pool, neighboring SA sodium temperature starts rising due to molten fuel attack on blocked SA hexcan, leading to its complete melting. After 55 s from start of TIB, the temperature rise recorded by neighboring thermocouple is 10 K.

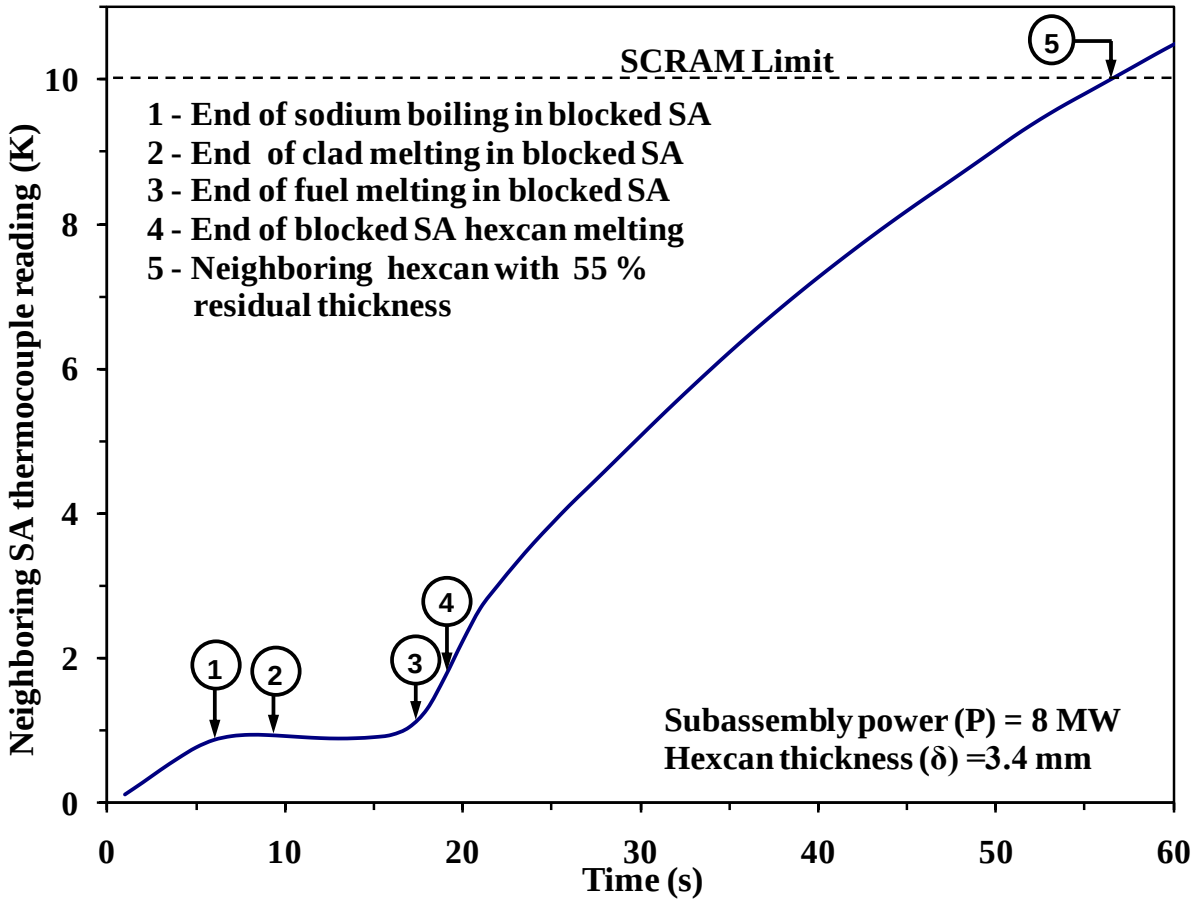

Fig. 3.17. Evolution of neighboring SA thermocouple reading during all the three stages of TIB in a single fuel SA with 8 MW (time = 0 s refers to start of TIB).

3.4.4 EFFECT OF REACTOR POWER

It is essential to know as how the reactor power influences the sequence of various phenomena that take place during a TIB. Hence, further study is carried out for three different values of SA power to understand the progression of TIB accident in terms of damage propagation and also to check for an early detection of TIB. The three cases studied are 4 MW, 2 MW and 1 MW. The SA sodium flow rate is assumed to be proportional to SA power.

The evolutionary sequence of various processes when the SA power is 4 MW (ie., 50 % reactor power) is depicted in Fig. 3.18 along with the predicted reading of the neighboring SA thermocouple. The sequence of events is found to be similar to that of 8 MW case but significant variations are noticed in time duration for completion of each event, which leads to an overall increase in detection time. It is observed that stage-I (viz., fuel melting) completes by ~40 s which is almost double the time taken in 8 MW case (~18 s). However, stage-II (viz., blocked SA hexcan melting) takes nearly the same time as that of 8 MW case. But stage-III has significant variation both in time as well as in temperature rise. An increase in reading of 10 K is recorded by the neighboring SA thermocouple at ~90 s after TIB is initiated. It can be seen that immediately after the end of sodium boiling in the blocked SA the heat transfer rate to the neighboring SA decreases, since the heat transfer from clad to blocked hexcan is only by radiation. The residual thickness of hexcan at the time of SCRAM is found to be 93% which is higher than the 8 MW case where the residual thickness of neighboring SA hexcan is about 55 %. The corresponding results for 2 MW and 1 MW power are also depicted in Fig. 3.18, wherein conditions highly favorable for early detection are noticed. No melting of hexcan of the neighboring SA is noticed for 1 MW power when SCRAM by the temperature monitoring system was initiated. In fact, SCRAM takes place even before sodium boiling in the blocked SA. Therefore, it is clear that detection of TIB is more likely at low power condition of the reactor. This is due to fact that irrespective of power rating of the SA, the fuel and steel have to attain molten temperature before attacking SA hexcan. This leads to the fact that nearly similar amount of heat flux emerges out of pool in all the cases, However, the subassembly with low power rating is associated with low sodium mass flow rate in neighboring SA, which eventually leads to large rise in sodium outlet temperature.

The neighboring SA hexcan residual thickness with respect to time during stage-III for different SA power ratings is shown in Fig. 3.19.

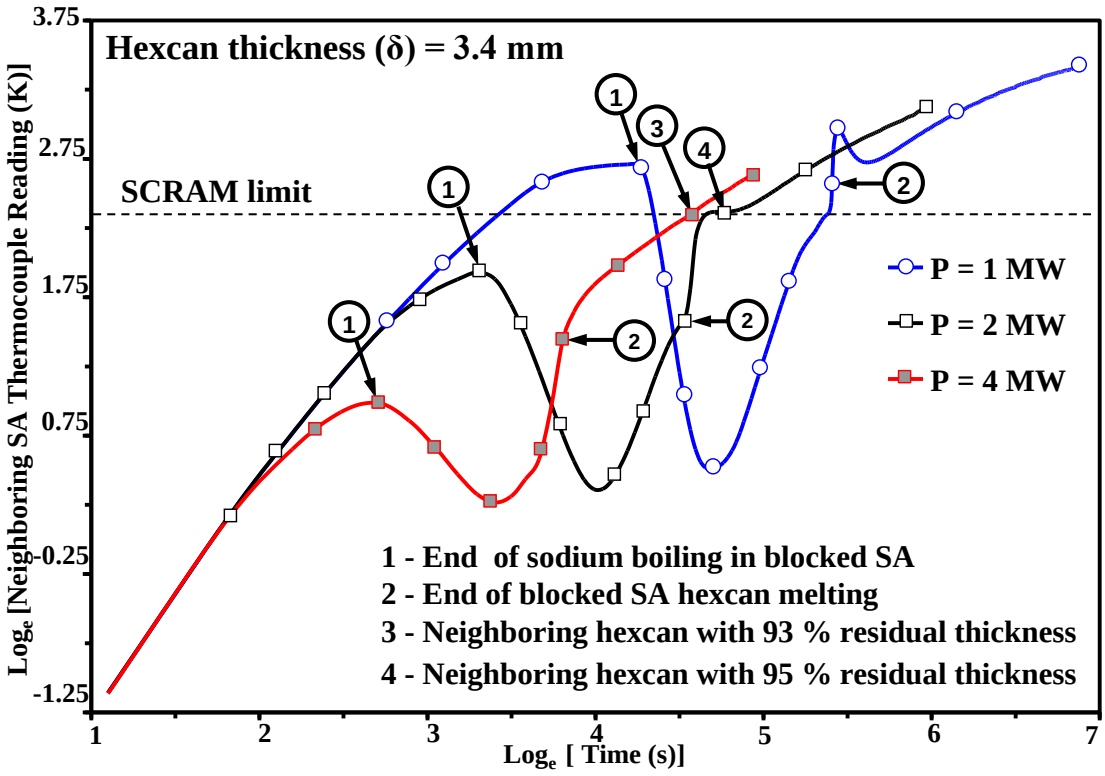

Fig. 3.18. Evolution of neighboring SA thermocouple reading during TIB in single fuel SA at different powers levels.

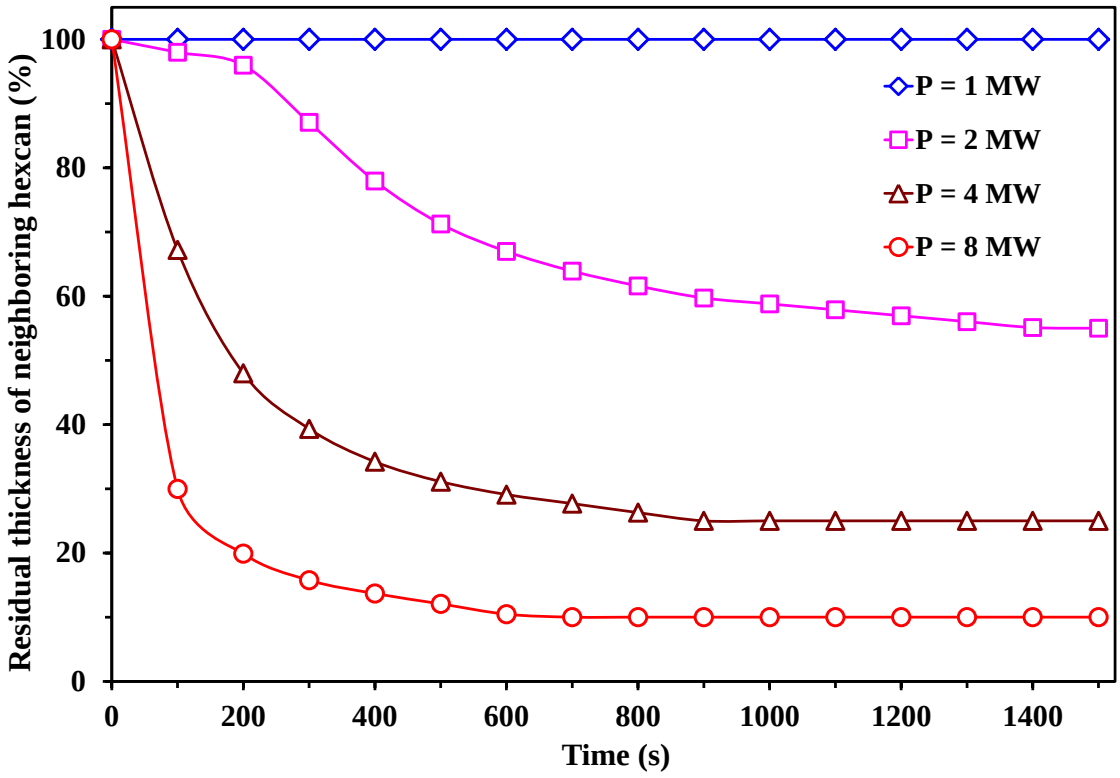

Fig. 3.19. Residual thickness of neighboring SA hexcan with time for different SA power.

It is seen that in SA with 8 MW power rating, the residual thickness stabilizes at 10%. The stabilized residual thickness for 4 MW and 2 MW are 25% and 55% respectively. However no melting is seen for 1 MW case. Therefore, it is evident that subassembly power plays an important role in deciding the extent of damage propagation during TIB accident. It is observed that the SA with low power rating has less damage propagation rate.

3.4.5 EFFECT OF HEXCAN THICKNESS

In order to understand the role of hexcan thickness on event progression, two additional thickness values are studied for subassembly power of 8 MW. The thickness values of hexcan studied are one with twice the thickness of existing hexcan (6.8 mm) and another with half of existing hexcan thickness (1.7 mm). The stage-I and stage-II results for these two hexcan thicknesses did not show any appreciable changes compared to 3.4 mm thickness. However, a few changes are noticed during neighboring SA hexcan melting (stage-III). It is observed that the SA with thicker hexcan has high melting speed at the beginning, as seen in see Fig. 3.20. The increase in thermal resistance of SA hexan due to increase in its wall thickness reduces the radial heat transfer from the molten pool to neighboring SA which in turn increases the heat accumulation and temperature of molten pool. Therefore SA with thicker hexcan has high molten fuel temperature compared to SA with thinner hexcan before attacking the neighboring hexcan. This is found to be the prime cause for the variation in melting speed of neighboring hexcan in SA with different hexcan thickness. However, these variations do not make any appreciable support for early detection of TIB, because the residual thicknesses at the instant of SCRAM are found to be almost independent of initial hexcan thickness (Fig. 3.21). Hence, it can be concluded that for the same SA power rating, increasing the SA hexcan thickness does not help in early detection of TIB.

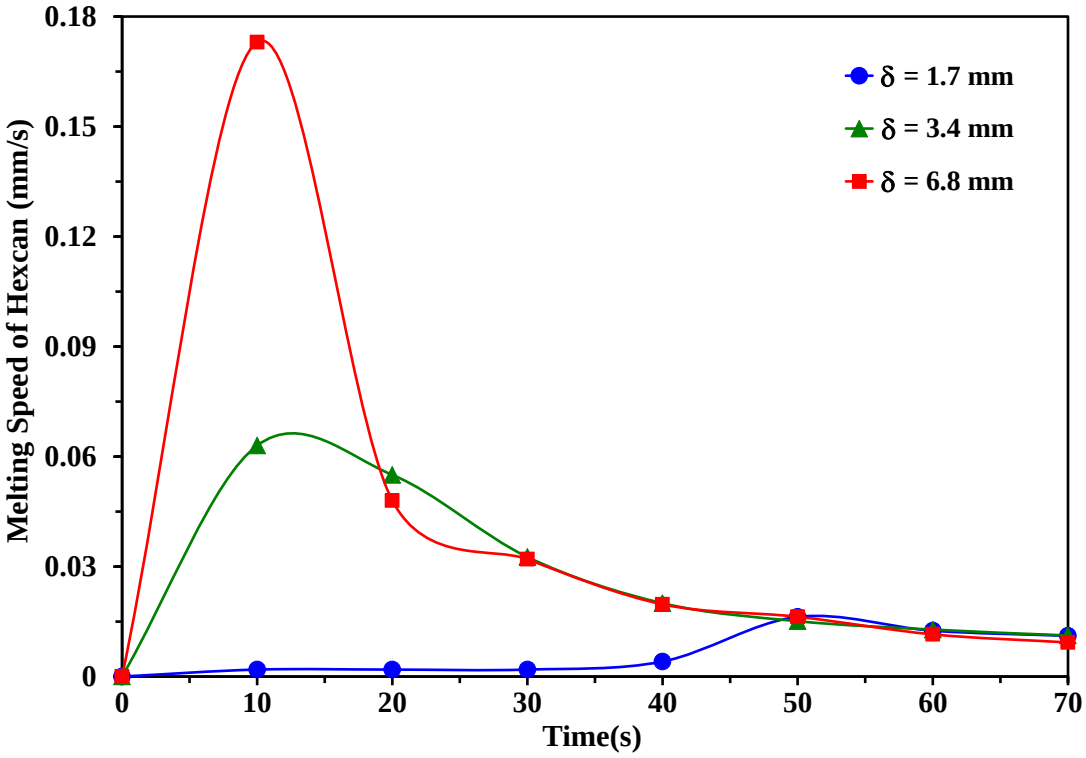

Fig. 3.20. Instantaneous melting speed of neighboring SA hexcan as a function of hexcan thickness.

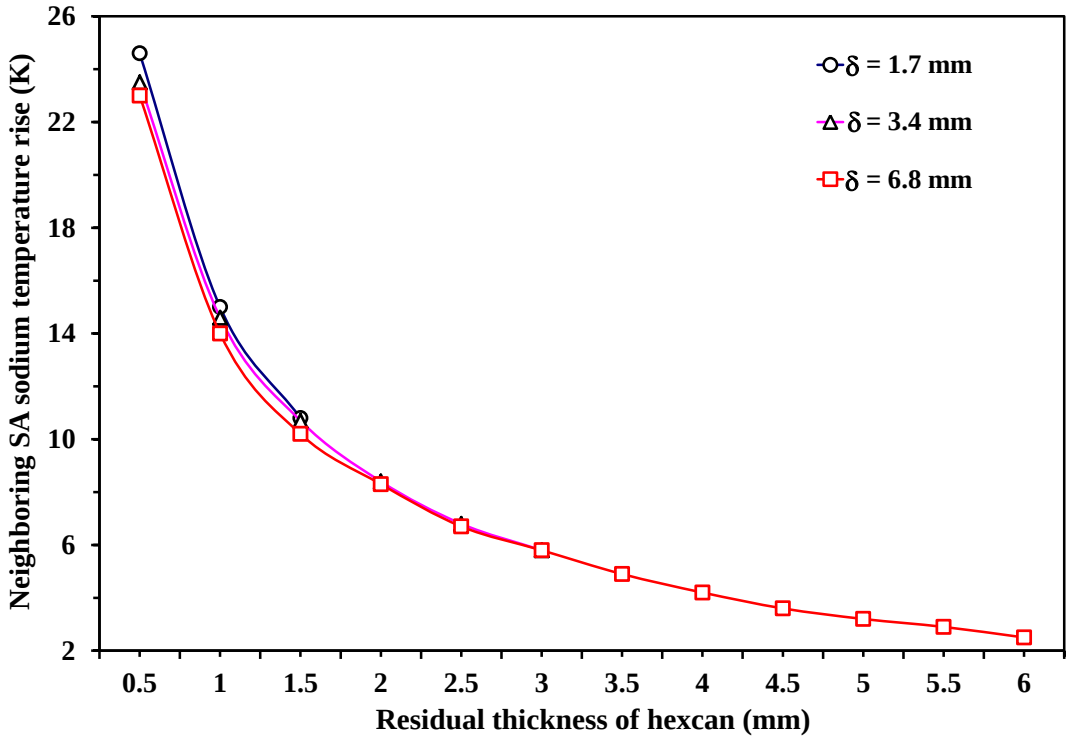

Fig. 3.21. Temperature rise of neighboring SA sodium during TIB with the corresponding residual thickness of neighboring hexcan.

3.4.6 EFFECT OF THERMAL CONDUCTIVITY OF HEXCAN MATERIAL

Thermal conductivity of hexcan material is an important parameter that affects heat transfer from fuel pool to sodium. To understand this, 4 different values of thermal conductivity have been considered. The stage-I and stage-II results on these thermal conductivities did not show any appreciable changes. But, considerable changes were noticed during neighboring SA hexcan melting (stage-III). From Fig. 3.22, it is clear that nominal thermal conductivity has the residual thickness of only 0.9 mm for 10 K temperature rise in neighboring SA sodium. But hexcan with twice the nominal conductivity has a residual thickness of 3.2 mm. From this it can be concluded that the thermal conductivity of hexcan material plays an important role in early detection of TIB.

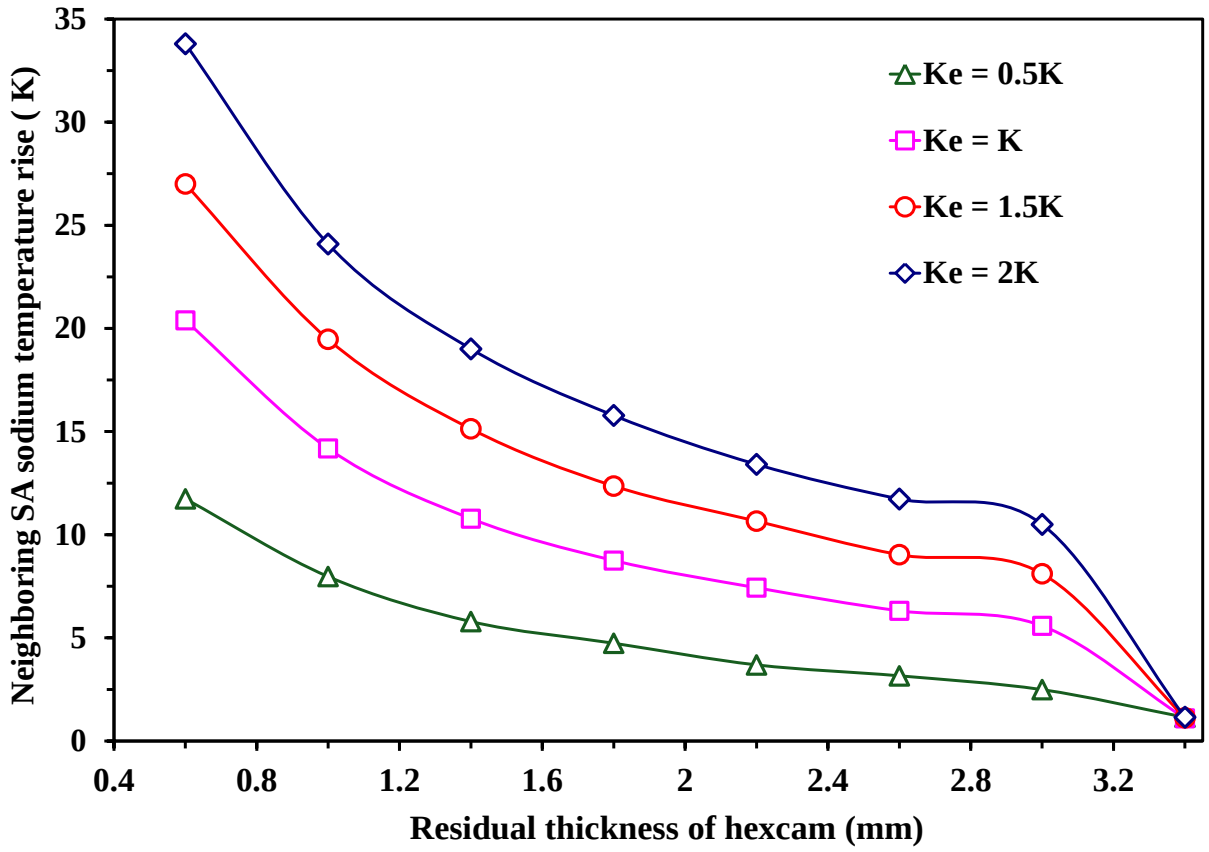

Fig. 3.22. Temperature rise of neighboring SA sodium during TIB as a function of thermal conductivity of hexacn with the corresponding residual thickness of neighboring hexcan.

3.4.7 EFFECT OF THERMOCOUPLE RESPONSE TIME

The thermocouples located at SA outlet to monitor the sodium temperature, have a finite response time as explained earlier (Section 3.2.1). The effect of thermocouple response time on early detection of TIB is analyzed in this section. Study was carried out at SA power of 8 MW for five different thermocouple time constants, viz., 0, 2, 4, 6 and 8 s. For 0 s response time, neighboring SA thermocouple reading showed a temperature rise of 10 K at about ~49 s after start of TIB and the residual thickness of neighboring hexcan at that instant is ~58%. These results are similar to the corresponding data of 55 s and 51% respectively for 8 s response time, demonstrating that no significant improvement can be achieved in early detection of TIB by having a thermocouple with low response time (Fig. 3.23).

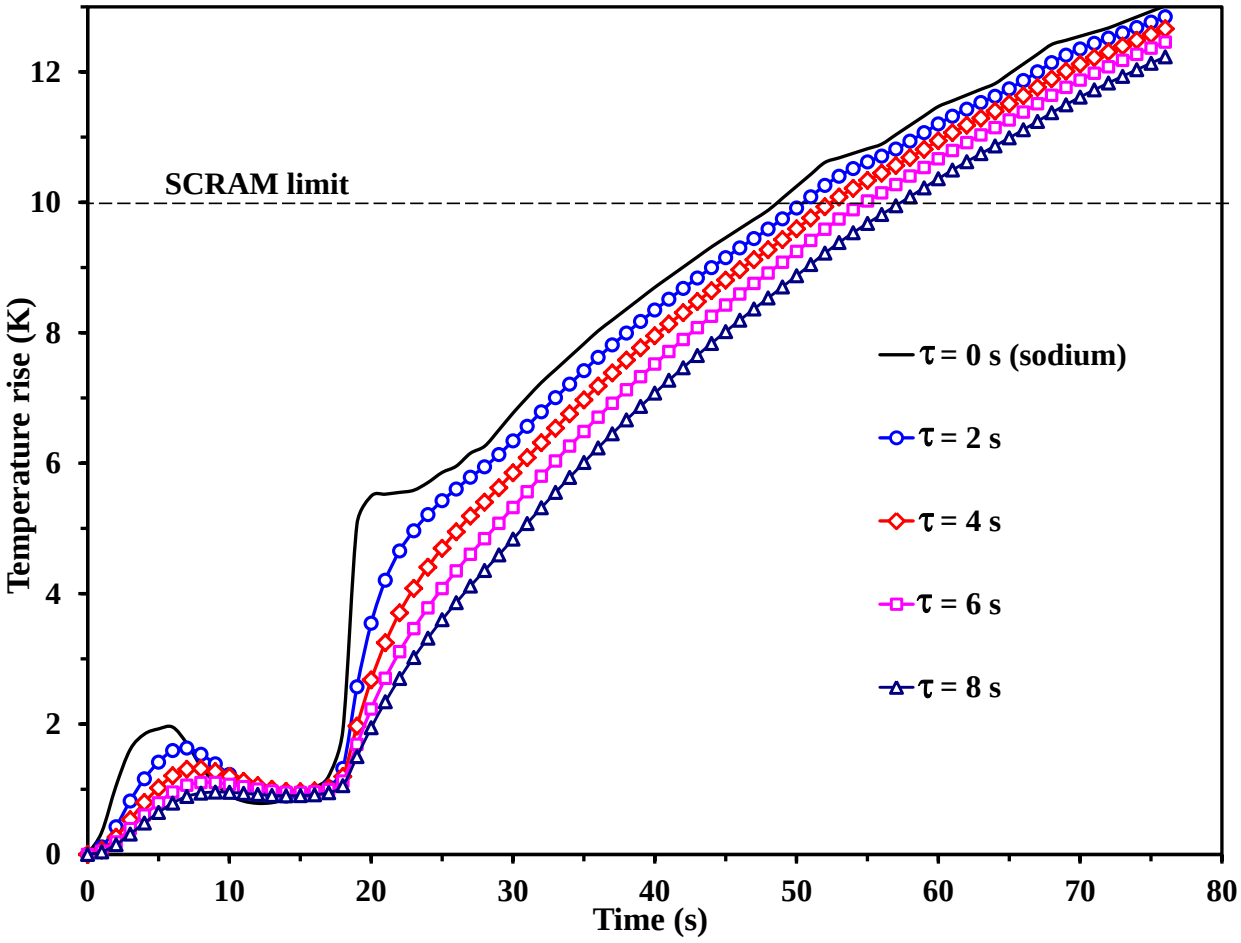

Fig. 3.23. Evolution of neighboring SA thermocouple reading as a function of thermocouple time constant.

3.5 CLOSURE

It is found that during nominal power condition, thermal damage propagates to only one row of SA indicating that the associated thermal load on core-catcher during the event is decay power of seven SA. Complete melting of the blocked SA occurs within ~20 s. Further, reactor SCRAM from neighboring SA thermocouple takes place at 55 s after the TIB and the residual thickness of hexcan wall at the time of reactor SCRAM is 51%. At low power conditions of the reactor (and hence at low SA power ratings) detection capability improves and the residual thickness of neighboring hexcan during reactor SCRAM also increases. Detailed parametric studies lead to the following conclusions:

- Thicker hexcan does not enhance early detection.
- Increase in thermal conductivity of hexcan material enhances early detection of the event and improves the residual thickness at the time of SCRAM.
- Reduction in time constant of thermocouple does not significantly help in early detection of TIB event.

CHAPTER 4

NATURAL CONVECTION IN FUEL POOL AND ITS IMPACT ON DAMAGE PROGRESSION

4

4.0 INTRODUCTION

The fuel pool formed during stage-III of the TIB results in heat transfer to sodium flowing in the six neighboring subassemblies. Thus, a large temperature difference develops between the central and peripheral zones of the fuel pool. As a consequence of this, natural convection sets-in within the pool, which augments the radial heat transfer from the pool to the neighboring subassemblies. The extent of damage depends strongly on the strength of the natural convection that takes place within the fuel pool. Considering only conduction heat transfer in the fuel pool may result in under estimation of heat transfer rate. For a realistic estimate of heat flux on the neighboring SA hexcan, natural convection in the heat generating molten fuel pool is to be considered. Unlike the convection driven by non-isothermal side walls, the convection generated by internal heat source exhibits a wide class of convection flows and interesting temperature/heat flux distributions. Further, natural convection in heat generating fluids is found in other nuclear applications such as cooling of core catcher during post-accident decay heat removal in a nuclear reactor. Hence, knowledge of natural convection heat transfer characteristics form heat generating fuel pool is essential.

The rate of propagation of damage and the temperature rise in neighboring SA sodium due to heat transfer from fuel pool through hexcan wall are investigated by a two-step mathematical approach. In the first step natural convection in the fuel pool is studied by a 2-D axi-symmetric computational fluid dynamic model and correlations for effective thermal

conductivity, as a function of internal Rayleigh number and aspect ratio, have been developed. In the second step, the rate of damage propagation to the hexcan wall and sodium temperature rise are predicted by a 1-D transient enthalpy model.

4.1 MODELING

4.1.1 PHYSICAL MODEL AND THE COORDINATE SYSTEM

As discussed earlier, it is clear that during a TIB in one fuel subassembly, the blocked subassembly hexcan completely melts down due to the molten fuel attack and the melt front further advances towards the neighboring subassembly. The SCARABEE-R experimental program (Kayser et al., 1998) confirms that no significant amount of fuel will escape through the inter-wrapper gap and the molten steel from the melting hexcan will enter into inter-wrapper gaps to plug the gaps. Thus, a tight blockage of fuel pool is formed which is surrounded by six neighboring subassemblies, whose hexcan are attacked (Fig. 4.1).

To understand the strength of natural convection in the fuel pool, its influence on damage propagation and eventual temperature rise in sodium outlet of the neighboring subassemblies (which is the basis for safety action), the two-step computational procedure is adopted. In the first step, natural convection in heat generating cylindrical fuel pool is studied, considering the aspect ratio of the pool and heat generating rate as parameters. The bulk temperature of the pool subjected to internal convection is estimated. The same problem is re-analyzed considering a stagnant pool. The thermal conductivity of the stagnant pool is treated as a parameter in this conduction calculation. The thermal conductivity value that gives a bulk pool temperature same as that under natural convection is determined, which is known as the equivalent thermal conductivity. By a detailed parametric study, suitable correlations are developed for equivalent thermal conductivity, for ready use in the second step.

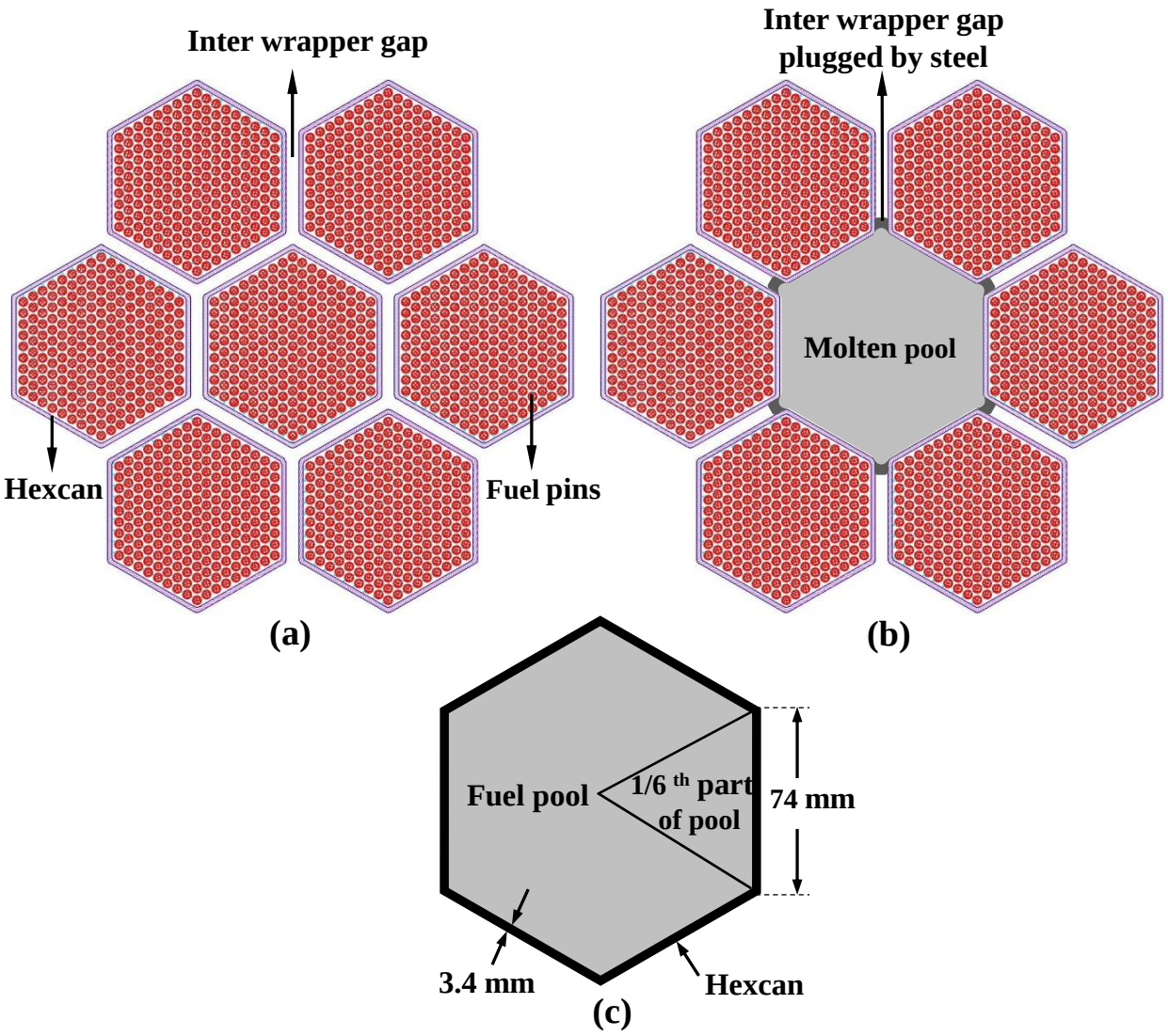

Fig. 4.1. TIB event progression: (a) Normal condition, (b) Molten fuel attacking neighboring subassembly during stage-III and (c) Fuel pool details.

In the second step, heat transfer features of the fuel pool and hexcan wall are determined by an enthalpy based melting/freezing model. The focus of this transient study is to determine the residual thickness of hexcan wall as a function of time and temperature rise in the neighboring subassembly sodium outlet temperature. The answer being sought is, ‘what is the residual thickness of hexcan wall when sodium outlet temperature increases by 10 K. It may be recalled that 10 K is the trip threshold.

Natural convection in the fuel pool is modeled as a volumetric heat generating fluid enclosed in a cylindrical enclosure with side wall maintained isothermally equal to the melting point of hexcan (T_w) and top as well as bottom walls with adiabatic boundary condition. The geometry considered for the first step of the study is represented by a 2-D cylindrical enclosure as depicted in the Fig. 4.2. The radius and height of the enclosure are denoted by r_{pol} and z_{pol} respectively. The aspect ratio of the enclosure (A) is defined as the ratio of height to radius of the pool ($A = z_{pol}/r_{pol}$).

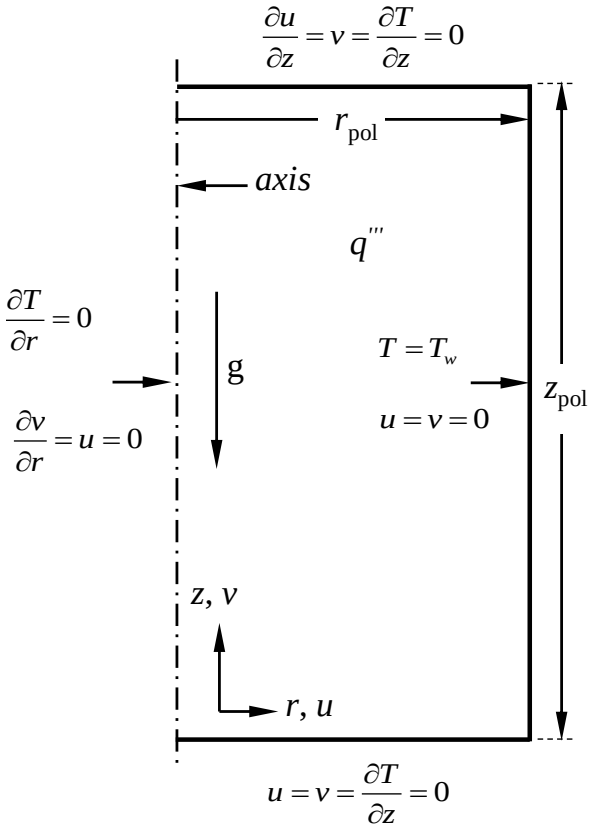

Fig. 4.2. Physical model with boundary conditions

It shall be highlighted that for simulation of natural convection in heat generating fuel pool, an axi-symmetric model has been adopted, instead of a 30° ($1/6^{\text{th}}$) symmetric sector of the hexcan. This is to reduce the computational effort. However, in the axi-symmetric model, the volume of the heat generating fuel pool is preserved which is very important from the point of

view of amount of heat that has to be dissipated. The difference in the hydraulic diameters of hexagonal duct and the volume preserved circular duct is ~5%. It is known that the forced convective heat transfer coefficient in ducts is proportional to (Hydraulic diameter)$^{-0.2}$. Hence, the possible error in the heat transfer rate is only ~1%. Considering the significant computational advantage of the axi-symmetric model, the same has been adopted in the present work.

The physical model for the second step of the study is modeled similar to stage-III in the previous Chapter, wherein a conduction model with equivalent thermal conductivity for the fuel pool is adopted as depicted in Fig. 4.3. The molten fuel pool surrounded by neighboring subassemblies is divided into six equal sectors (Fig. 4.1c) and one symmetry sector is considered for the analysis. The single equilateral triangular fuel sector is further divided into ~ 370 elements based on grid independence study. The neighboring subassembly hexcan wall (3.4 mm thick) is divided into 20 equal elements (Fig. 4.3).

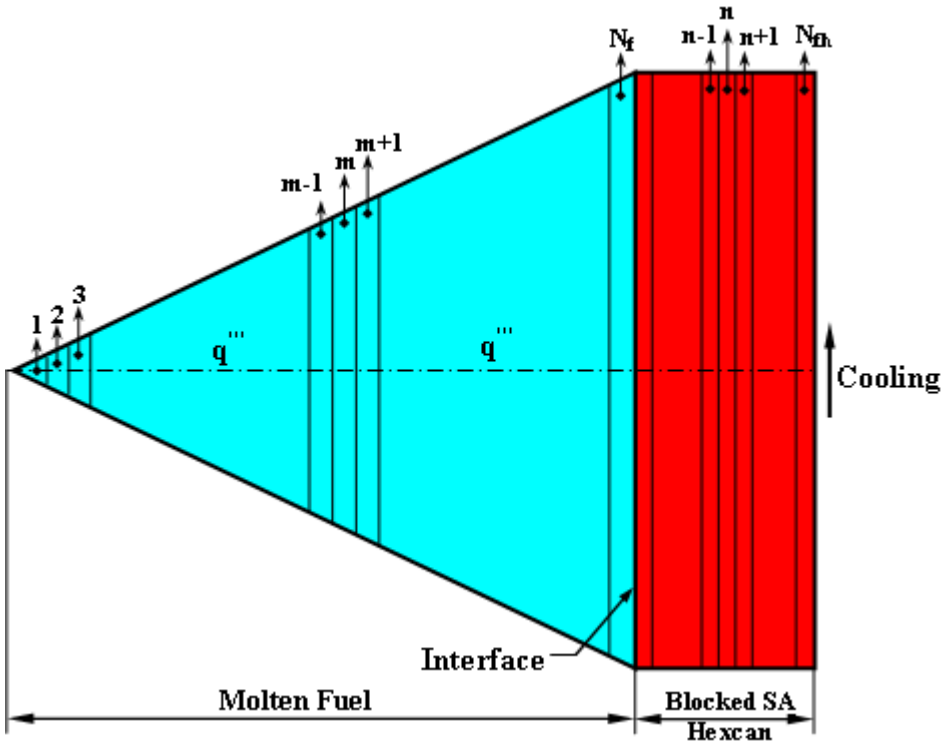

Fig. 4.3. Physical model of neighboring subassembly hexcan melting during stage-III for step-2 calculation.

4.1.2 MATHEMATICAL MODEL

Step-1

The flow and associated heat transfer due to volumetric heat generation of the fluid (q''') are characterized by the internal Rayleigh number and the Prandtl number, which are evaluated from:

$$Ra_I = \frac{g\,\beta\,q'''\,r_{pol}^5}{\upsilon\,\alpha\,K} \text{ and } Pr = \frac{\upsilon}{\alpha} \tag{4.1}$$

The dependent and independent variables are nondimensionalized as defined below:

$$r^* = \frac{r}{r_{pol}},\ z^* = \frac{z}{r_{pol}},\ u^* = \frac{u\,r_{pol}}{\alpha},\ v^* = \frac{v\,r_{pol}}{\alpha},\ p^* = \frac{p\,r_{pol}^2}{\rho\,\alpha^2},\ T^* = \frac{(T\text{-}T_w)K}{r_{pol}^2 q'''},\ \varepsilon^* = \frac{\varepsilon\,r_{pol}^4}{\alpha^3}$$

$$k^* = \frac{k\,r_{pol}^2}{\alpha^2} \tag{4.2}$$

The fluid is assumed to be Newtonian and incompressible with constant thermo-physical properties except for the density in the buoyancy term, which follows the Boussinesq approximation. The melting point of fuel is 3070 K and its boiling point is 3300 K. Thus the temperature variation in fuel pool (ΔT) is 230 K. The value of β for liquid fuel is 0.000105 K^{-1} (see Appendix for thermo-physical properties of materials). Thus the product of $\beta \times \Delta T$ is 0.02415, which is less than the limiting value of 0.1. Hence Boussinesq approximation is justified. Turbulence is modeled by Reynolds Averaged Navier Stokes (RANS) equations based on standard k-ε model. The steady state mass, momentum, energy, turbulent kinetic energy (k) and turbulent dissipation rate (ε) equations that govern the flow and heat transfer are:

Continuity

$$\frac{1}{r^*}\frac{\partial(r^*u^*)}{\partial r^*} + \frac{\partial v^*}{\partial z^*} = 0 \tag{4.3}$$

Radial momentum

$$\left(u^{*}\frac{\partial u^{*}}{\partial r^{*}}+v^{*}\frac{\partial u^{*}}{\partial z^{*}}\right)=-\frac{\partial p^{*}}{\partial r^{*}}+\frac{1}{r^{*}}\frac{\partial}{\partial r^{*}}\left(r^{*}\,Pr_{eff}\frac{\partial u^{*}}{\partial r^{*}}\right)+\frac{\partial}{\partial z^{*}}\left(Pr_{eff}\frac{\partial u^{*}}{\partial z^{*}}\right)\text{-}Pr_{eff}\frac{u^{*}}{r^{*2}} \tag{4.4}$$

Axial momentum

$$\left(u^{*}\frac{\partial v^{*}}{\partial r^{*}}+v^{*}\frac{\partial v^{*}}{\partial z^{*}}\right)=-\frac{\partial p^{*}}{\partial z^{*}}+\frac{1}{r^{*}}\frac{\partial}{\partial r^{*}}\left(r^{*}\,Pr_{eff}\frac{\partial v^{*}}{\partial r^{*}}\right)+\frac{\partial}{\partial z^{*}}\left(Pr_{eff}\frac{\partial v^{*}}{\partial z^{*}}\right)+Pr\,Ra\,(T^{*}\text{-}T_{ref}^{*}) \tag{4.5}$$

Energy

$$\left(u^{*}\frac{\partial T^{*}}{\partial r^{*}}+v^{*}\frac{\partial T^{*}}{\partial z^{*}}\right)=1+\frac{1}{r^{*}}\frac{\partial}{\partial r^{*}}\left[r^{*}\left(1+\frac{Pr_{t}}{\sigma_{t}}\right)\frac{\partial T^{*}}{\partial r^{*}}\right]+\frac{\partial}{\partial z^{*}}\left[\left(1+\frac{Pr_{t}}{\sigma_{t}}\right)\frac{\partial T^{*}}{\partial z^{*}}\right] \tag{4.6}$$

Turbulent kinetic energy

$$\frac{\partial(u^{*}k^{*})}{\partial r^{*}}+\frac{\partial(v^{*}k^{*})}{\partial z^{*}}=\frac{1}{r^{*}}\frac{\partial}{\partial r^{*}}\left[r^{*}\left(Pr+\frac{Pr_{t}}{\sigma_{k}}\right)\frac{\partial k^{*}}{\partial r^{*}}\right]+\frac{\partial}{\partial z^{*}}\left[\left(Pr+\frac{Pr_{t}}{\sigma_{k}}\right)\frac{\partial k^{*}}{\partial z^{*}}\right]+P_{k}+B_{k}^{*}\text{-}\,\varepsilon^{*} \tag{4.7}$$

Turbulent dissipation rate

$$\begin{aligned}\frac{\partial(u^{*}\varepsilon^{*})}{\partial r^{*}}+\frac{\partial(v^{*}\varepsilon^{*})}{\partial z^{*}}=&\frac{1}{r^{*}}\frac{\partial}{\partial r^{*}}\left[r^{*}\left(Pr+\frac{Pr_{t}}{\sigma_{\varepsilon}}\right)\frac{\partial\varepsilon^{*}}{\partial r^{*}}\right]\\&+\frac{\partial}{\partial z^{*}}\left[\left(Pr+\frac{Pr_{t}}{\sigma_{\varepsilon}}\right)\frac{\partial\varepsilon^{*}}{\partial z^{*}}\right]+\left[C_{\varepsilon1}(P_{k}+C_{\varepsilon3}B_{k}^{*})-C_{\varepsilon2}\varepsilon^{*}\right]\frac{\varepsilon^{*}}{k^{*}}\end{aligned} \tag{4.8}$$

Where

$$P_{k}^{*}=Pr_{t}\left[2\left(\frac{\partial u^{*}}{\partial r^{*}}\right)^{2}+2\left(\frac{\partial v^{*}}{\partial z^{*}}\right)^{2}+\left(\frac{\partial u^{*}}{\partial z^{*}}+\frac{\partial v^{*}}{\partial r^{*}}\right)^{2}+2\left(\frac{u^{*}}{r^{*}}\right)^{2}\right] \tag{4.9}$$

$$B_{k}^{*}=\text{-}Pr\,Ra_{I}\frac{Pr_{t}}{\sigma_{T}}\frac{\partial T^{*}}{\partial z^{*}} \tag{4.10}$$

$$Pr_{eff}=Pr+Pr_{t} \tag{4.11}$$

$$Pr_t = C_\mu \frac{k^{*2}}{\varepsilon^*} \tag{4.12}$$

The values of turbulence model constants used are:

$\sigma_\varepsilon = 1.3$, $\sigma_T = 0.9$, $\sigma_k = 1.0$, $C_{\varepsilon 1} = 1.44$, $C_{\varepsilon 2} = 1.92$, $C_{\varepsilon 3} = \tanh(v^*/u^*)$ and $C_\mu = 0.09$.

Step-2

During molten fuel attack, the hexcan (made of stainless steel) in contact with the molten fuel starts melting, layer by layer, from inner side and its outer surface is exposed to flowing sodium. At any instant, the heat flux leaving outer surface of melting hexcan is a function of natural convection within the fuel pool, thermal resistance of the hexcan wall and external cooling. The melting and freezing phenomena during molten fuel attack on neighboring subassembly hexcan are modeled by employing enthalpy based transient energy equation (similar to stage-III discussed in Chapter-3). The general enthalpy formulation is expressed as:

$$\rho \frac{\partial H_{spe}}{\partial t} = \nabla\left[K(\nabla T)\right] + q''' \tag{4.13}$$

In the present work, above formulation is implemented by making suitable modification in the governing equations to incorporate the heat source term and establishing proper connectivity for heat transfer between dissimilar materials at the interface of melting front. The effect of natural convection in fuel pool is accounted by employing the equivalent thermal conductivity of the fuel pool determined in step-1. The heat balance equation for m^{th} fuel element is expressed as (refer Eq. (3.23)):

$$\frac{d(H_m)}{dt} = q_m + G_{m-1,m}\left(T_{m-1} - T_m\right) - G_{m,m+1}\left(T_m - T_{m+1}\right) \tag{4.14}$$

Similarly, the heat balance equation for n^{th} hexcan element is expressed as (refer Eq. (3.24)):

$$\frac{d(H_n)}{dt} = G_{n-1,n}\left(T_{n-1} - T_n\right) - G_{n,n+1}\left(T_n - T_{n+1}\right) \tag{4.15}$$

4.2 SOLUTION METHOD AND VALIDATION

4.2.1 STEP-1

The solution to flow and heat transfer equations used in the present natural convection study is obtained numerically by using a Finite Volume Method (FVM). A non-uniform structured staggered grid is employed. The size of the grid is taken fine enough at the boundary and coarse away from the wall, such that the first grid from the boundary wall lies within the viscous sub-layer during turbulent flow. The pressure–velocity coupling is resolved by using the SIMPLE algorithm proposed by Patankar and Spalding (1972). The buoyancy force in the vertical momentum equation due to change in the density of the fluid is taken in to account by employing the Boussinesq approximation. The present computational model is used to predict natural convection in a 2-dimensional cavity with heat generating fluid. The predicted results are compared against the benchmark numerical results of Acharya and Goldstein (1985). The internal Rayleigh number (Ra_I) and external Rayleigh number (Ra_E) for the square cavity are evaluated as:

$$Ra_I = \frac{g\,\beta\,q'''\,z_{cav}^5}{\upsilon\alpha K},\ Ra_E = \frac{g\beta\,\Delta T\,z_{cav}^3}{\upsilon\alpha} \tag{4.16}$$

where, ΔT denotes the imposed temperature difference between the two vertical walls, z_{cav} is the height of the cavity, β is the volumetric expansion coefficient of fluid, g is the acceleration due gravity, v and α are kinematic viscosity and thermal diffusivity of the fluid respectively. The authors have carried out the study for both the Rayleigh numbers Ra_E and Ra_I up to $10^7$with Pr = 0.7. In the present validation study, Ra_E is varied as a function of temperature difference between the vertical hot and cold walls of the cavity, whereas Ra_I is varied by changing the volumetric heat generation rate of the fluid. The top and bottom walls of the cavity are assumed to adiabatic while the vertical hot and cold walls are maintained at temperatures T_{hot} (ϕ = 0.5) and T_{cold} (ϕ = -0.5) respectively, where ϕ is a dimensionless temperature of cavity defined as:

$$\phi = \frac{T - (T_{hot} + T_{cold})/2}{(T_{hot} - T_{cold})} \tag{4.17}$$

The stream lines and isotherms predicted by the present model for Ra_E = 10^6 and Ra_I = $10^7$are depicted in Fig. 4.4. Also shown in the same figure are the results of the Acharya and Goldstein (1985). It is clear that the present results compare well with the benchmark results.

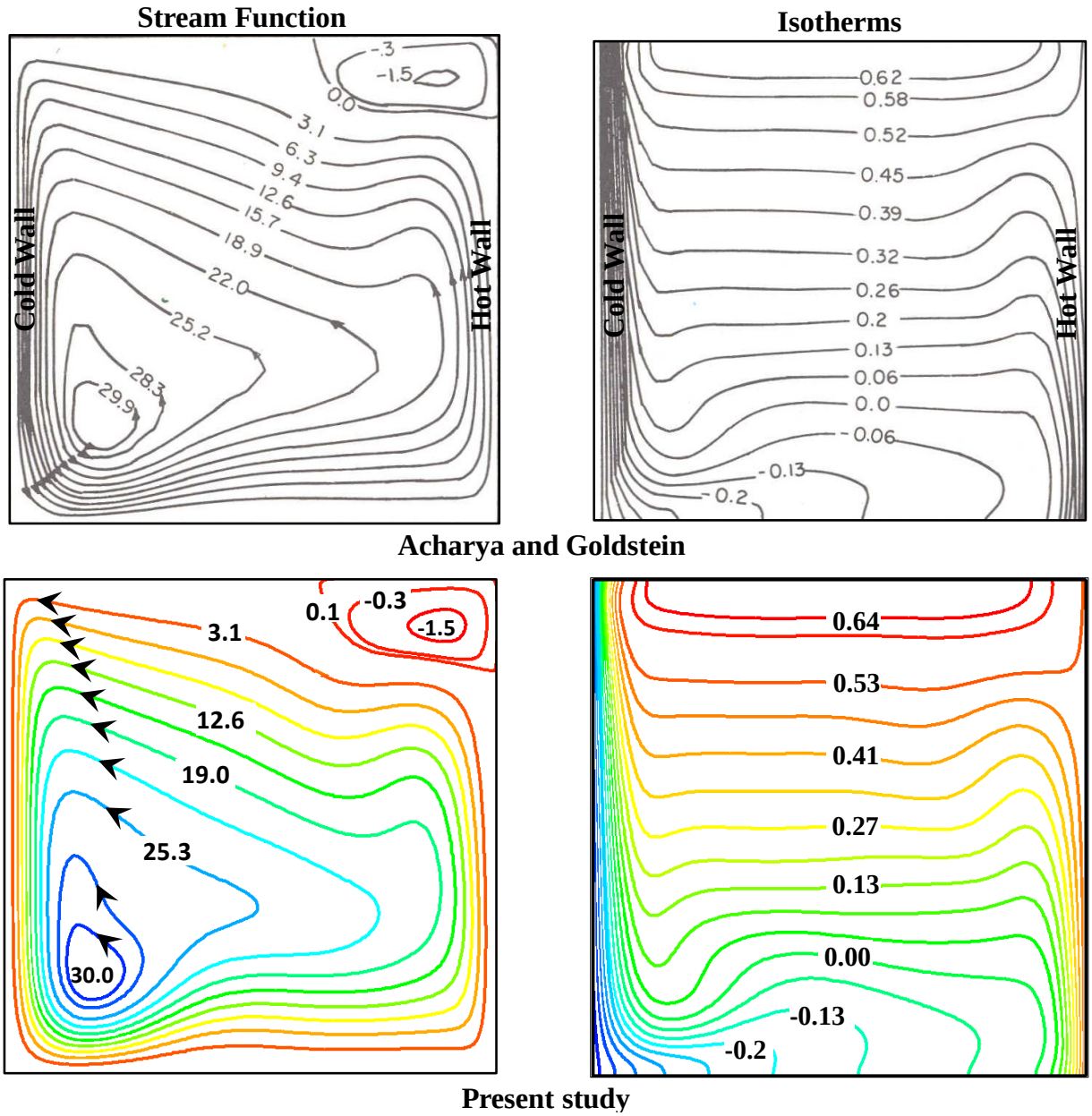

Fig. 4.4. Comparison of stream function and isotherms for a square cavity at Ra_E = $10^6$and Ra_I =10^7 against the results of Acharya and Goldstein (1985).

The steady state peak temperatures of the fluid in the cavity are compared against the published data of Shim and Hyun (1997) and Acharya and Goldstein (1985) in Table 4.1 and found to be in good agreement. The average Nusselt number on the hot sidewall of the cavity corresponding to different set of Ra_E and Ra_I are compared against the published data of Shim and Hyun (1997) in Table 4.2 and are again found to be in good agreement.

Table 4.1. Comparison of predicted peak temperature in the cavity with Shim and Hyun (1997) and Acharya and Goldstein (1985).

Ra_E	Ra_I	Temperature (ϕ_{max})		
		Present	Shim and Hyun (1997)	Acharya and Goldstein (1985)
10^5	10^6	0.89	0.87	-
10^5	10^7	5.62	5.54	-
10^6	10^7	0.64	-	0.62

Table 4.2. Comparison of predicted average Nusselt number on hot sidewall of the rectangular cavity with Shim and Hyun (1997).

Ra_E	Ra_I	Average Nusselt number	
		Present	Shim and Hyun (1997)
10^5	10^5	6.1	6.2
10^5	10^6	-0.26	-0.15
10^5	10^7	-67.1	-66.0
10^5	10^8	-762.0	-760.1

4.2.2 STEP-2

As discussed in pervious Chapter (i.e., Chapter-3), during stage-III, the molten fuel attacking the neighboring SA hexcan is associated with problems such as moving solid-liquid interface and unrealistic oscillation of temperature. These complex problems have been overcome by implementing enthalpy based Voller's algorithm (Voller, 1987).

4.3 RESULTS AND DISCUSSION

The study on natural convection in the cylindrical cavity is carried out for different aspect ratios of the fuel pool ranging from 1 to 5. The value of Ra_I, is varied from 10^3 to 10^7 for evaluating the enhancement in total heat transfer from the pool to neighboring subassembly by natural convection compared to that by conduction. Then a correlation expressing equivalent conductivity factor (*CF*) as a function of Ra_I is developed. The equivalent conductivity factor *CF* is the ratio of equivalent thermal conductivity (K_e) to the nominal conductivity of the fluid (K). Using this correlation, rate of melting of the hexagonal sheath that contains the fuel pool and temperature rise in sodium outlet from neighboring subassemblies are determined.

4.3.1 STEP-1: DETERMINATION OF THE EQUIVALENT THERMAL CONDUCTIVITY

The determination of equivalent thermal conductivity (K_e) of the fuel pool during natural convection is based on the heat conduction equation of a solid cylinder with volumetric heat source, defined as:

$$Q = K\,S\,(T_{bulk} - T_w) \tag{4.18}$$

Where, Q is total heat transfer rate, K is liquid thermal conductivity, S is conduction shape factor for cylinder equal to $8\times\pi\times z_{pol}$, T_{bulk} is volume averaged bulk temperature and T_w is wall temperature (equal to melting point of hexcan material).

To determine the equivalent thermal conductivity (K_e), the following procedure is adopted:

(i) For the given values of Ra_I and A, natural convection within the pool is predicted and bulk temperature of the pool ($T_{bulk,conv}$) is determined.

(ii) For the same volumetric heat source (q''') and pool radius (r_{pol}), the bulk temperature of the pool ($T_{bulk,conv}$) obtained from the previous step is substituted in the following equation to obtain the equivalent thermal conductivity (K_e).

$$K_e = \frac{q''' r_{pol}^2}{8(T_{bulk,conv} - T_w)} \tag{4.19}$$

Then the equivalent conductivity factor *CF* is defined as:

$$CF = \frac{K_e}{K} \tag{4.20}$$

The role of convection comes in to play only when the Ra_I exceeds a critical value Ra_c. In Eqn. (4.20), $K_e \approx K$ and $CF \approx 1$ when $Ra_I < Ra_c$, because heat transfer in the pool is predominantly by conduction.

The results of isotherms and natural convection velocity field inside cylindrical pool with internal heat source considering free convection and without free convection (pure conduction) for $Ra_I = 3\times10^7$ and $A = 5$ are depicted in Fig. 4.5. It is observed that during pure conduction the peak temperature of the pool occurs at the central line and there is no temperature variation in the axial direction of the pool (Fig. 4.5a) as expected. On other hand, by considering natural convection the peak temperature of the pool is concentrated at the top region of the pool (Fig. 4.5b). It is also observed that the peak temperature of the pool falls with onset of natural convection within the pool. The velocity vector plot and stream lines in the cavity are depicted in Figs. 4.5c and 4.5d respectively.

The temperature distribution along the centerline of the fuel pool for various values of Ra_I is depicted in Fig. 4.6 for aspect ratio of 5. At low Ra_I values there is no significant temperature variation along the height due to weak convection currents and a conduction dominated heat transfer. However, at large Ra_I values, significant thermal stratification effects can be seen in the pool, with hot liquid settling at the top.

The peak value of non-dimensional temperature is low if Ra_I is large due to enhanced convection. The influence of aspect ratio on centerline temperature is depicted in Fig. 4.7 for a fixed value of Ra_I. It is clear that thermal stratification effect is more if the pool height is larger. This is exhibited by the large value of non-dimensional temperature at the top of the pool. In short pools, mixing is better, which is evident from the nearly uniform temperature in the case of low aspect ratios.

The non-dimensional local heat flux along the hexcan wall is evaluated from,

$$q''^{*} = \left(\frac{q''}{T_{mpf} - T_{mph}} \right) \frac{r_{pol}}{K} \qquad (4.21)$$

The relative effects of Ra_I and aspect ratio on local heat flux are depicted in Figs. 4.8a and 4.8b. For A = 1, at low Ra_I no significant variation in the local heat flux along the hexcan wall is noticed in Fig. 4.8a. This is due to weak buoyancy driven flow circulation and diffusion dominant heat transfer. With increasing values of Ra_I, the local heat flux increases along the pool height. The heat flux at the top of the hexcan wall is high compared to that at the bottom. This is due to the buoyancy driven circulation, which intensifies with increase in Ra_I, promoting hot fluid to rise along the pool center and sink along the hexcan wall (see, Fig. 4. 5c). As a consequence of this, a thermal boundary layer develops along the hexcan wall. The leading edge of this boundary layer is located at the top of hexcan wall. Hence, the heat transfer coefficient and hence the heat flux are high at the top of the hexcan wall where the boundary layer thickness is minimum. The heat flux reduces towards the bottom of the hexcan, as boundary layer thickness increases. The impact of the aspect ratio on heat flux distribution is depicted in Fig. 4.8b. Comparing Figs. 4.8a and 4.8b, it is clear that the heat flux does not exhibit significant dependence on pool aspect ratio. However, a mild dip in the peak value of the heat flux is noticed, which is due to the increase in the thermal stratification of the fluid caused by the increase in height of the pool.

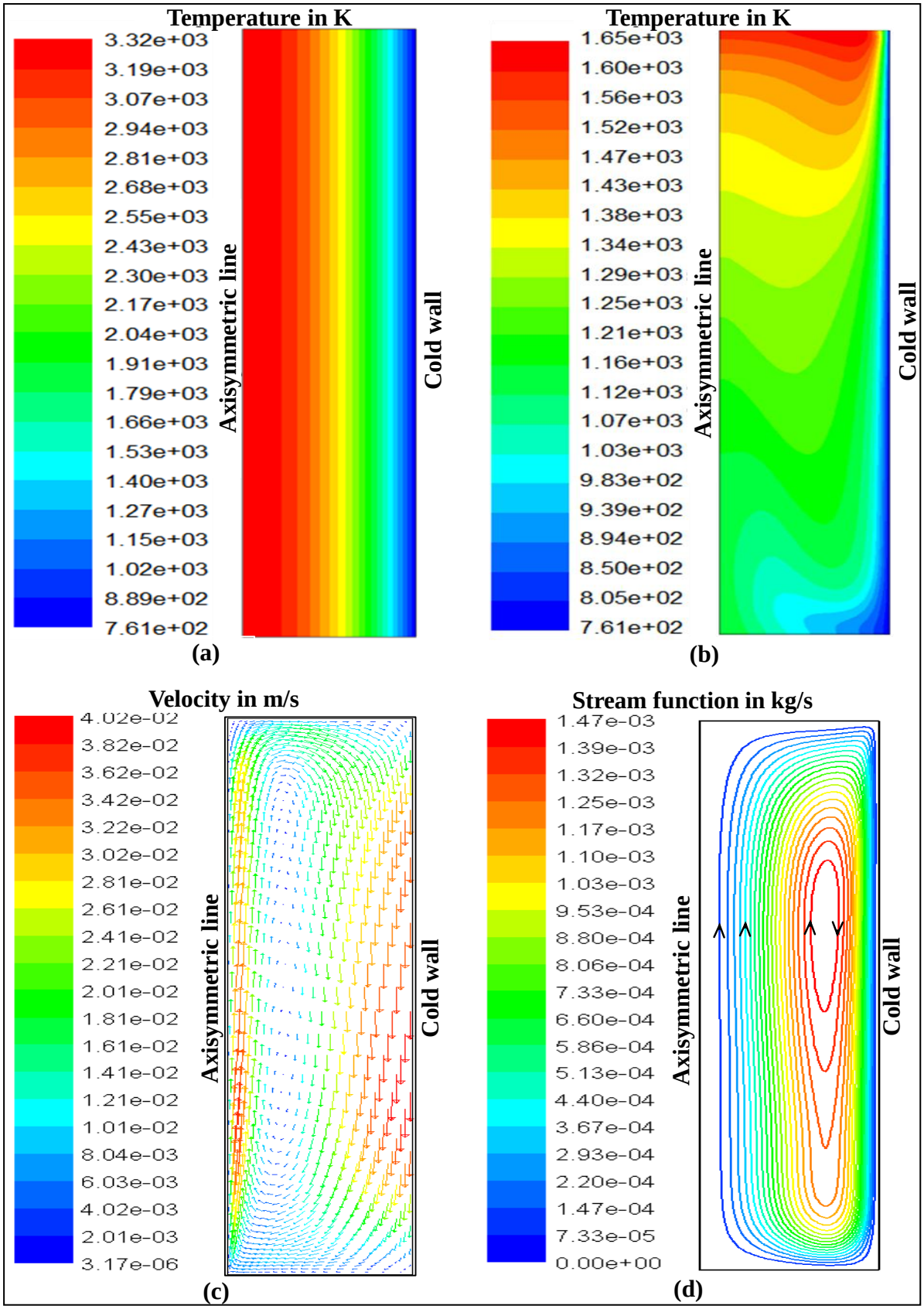

Fig. 4.5. Flow and temperature fields in the cavity for $Ra_I = 3\times10^7$ and A= 5: (a) Isotherms with pure conduction, (b) Isotherms with natural convection, (c) Natural convection velocity and (d) Natural convection stream function.

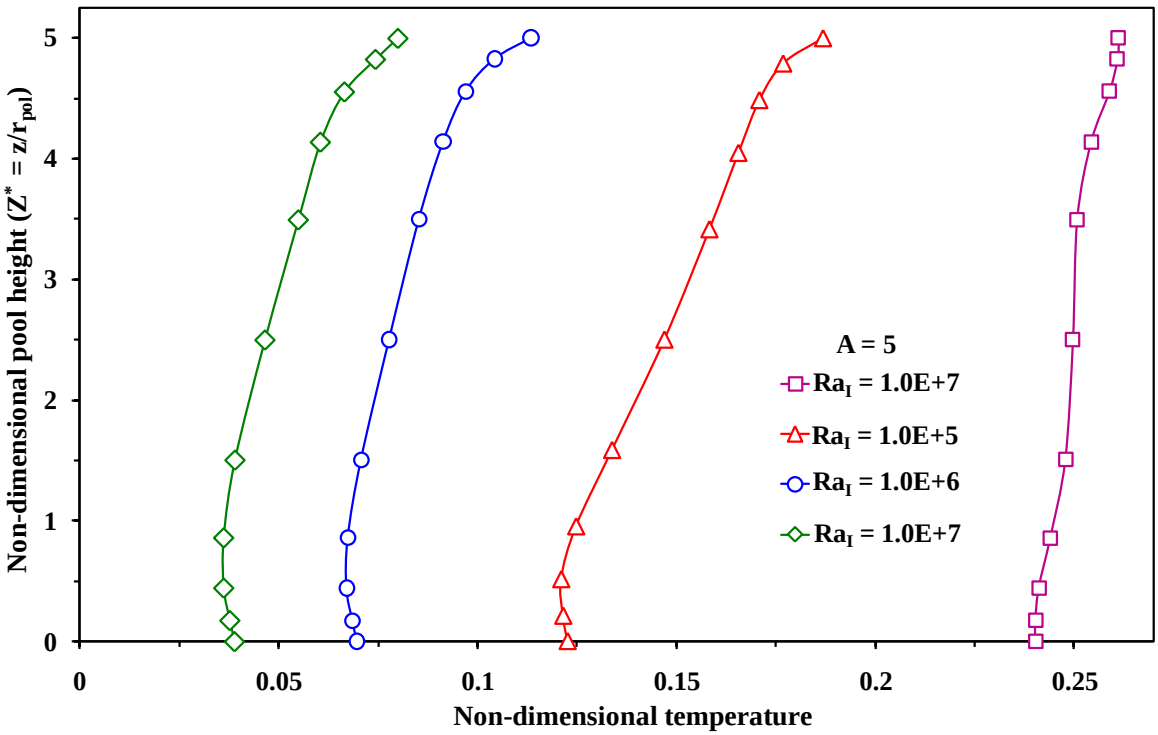

Fig. 4.6. Dimensionless temperature variation along the centerline of the pool.

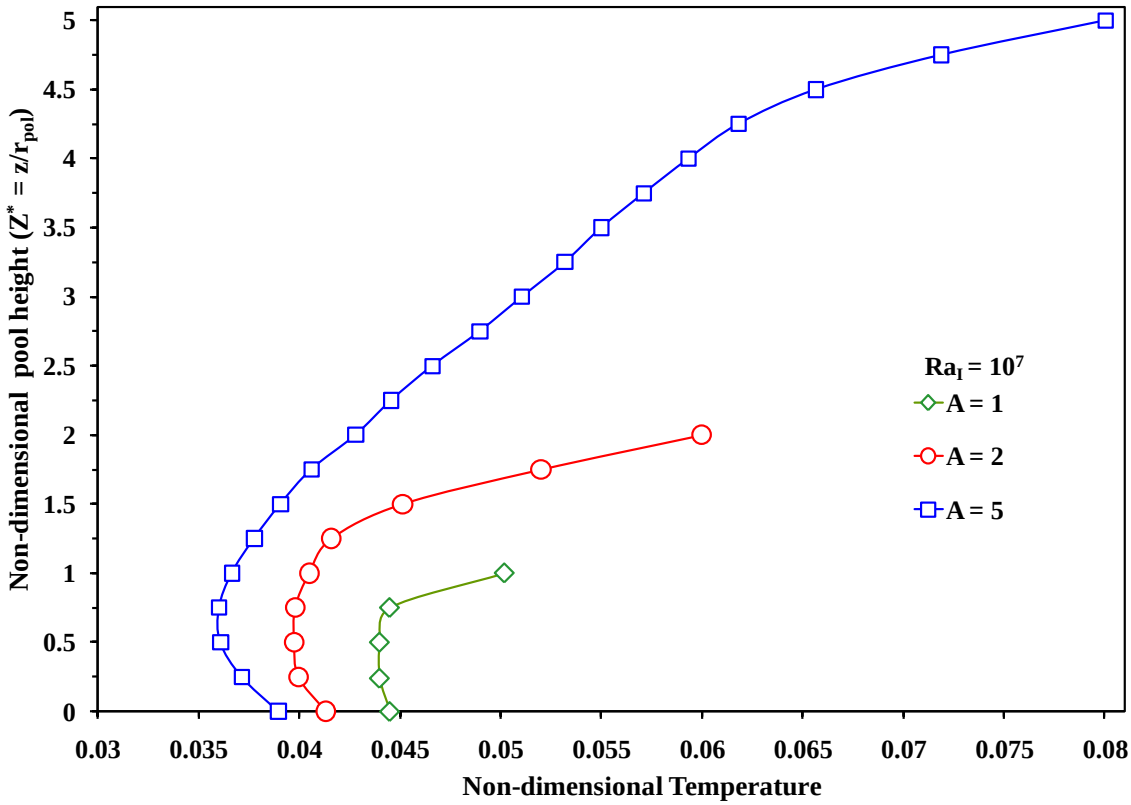

Fig. 4.7. Dimensionless temperature variation along the centerline of the pool for different values of aspect ratios.

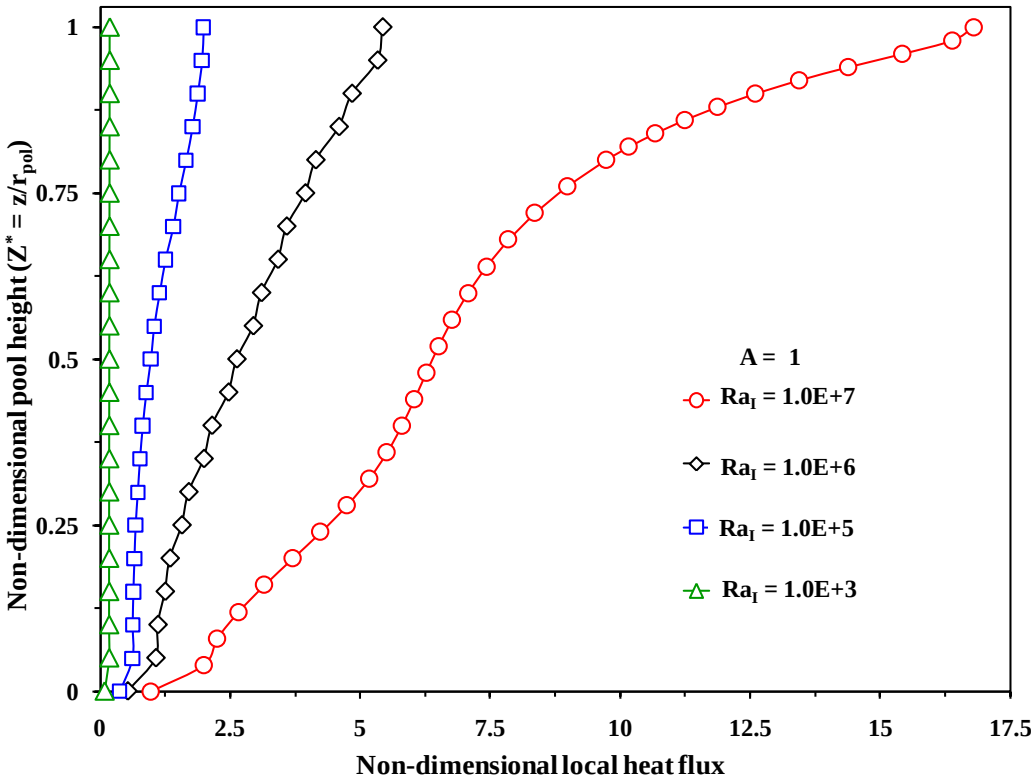

Fig. 4.8a. Dimensionless local heat flux variation along the hexcan wall with different values of aspect ratios of the pool for A = 1.

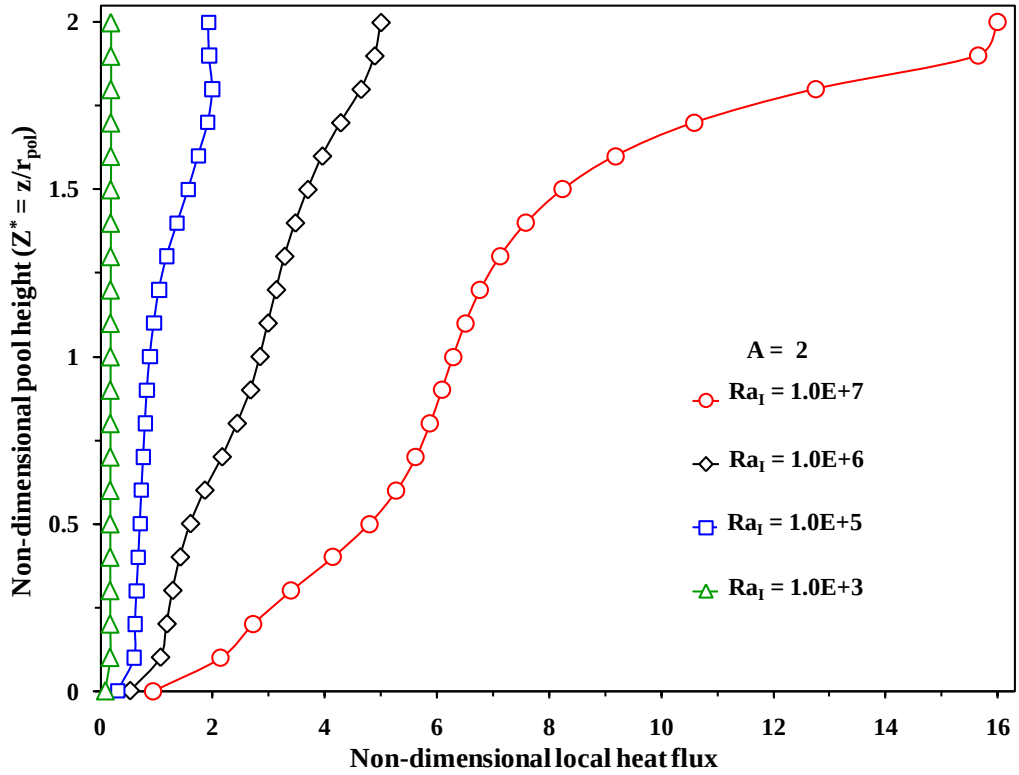

Fig. 4.8b. Dimensionless local heat flux variation along the hexcan wall with different values of aspect ratios of the pool for A = 2.

The variation of the dimensionless bulk temperature of the pool with Ra_I for different aspect ratios considering natural convection and considering only conduction is depicted in Fig. 4.9. It is noted that dimensionless bulk temperature considering only conduction, $T_{bulk,cond}$ is neither affected by the aspect ratio nor by Ra_I as expected. But, the dimensionless bulk temperature considering convection $T_{bulk,conv}$ has considerable variation with both the aspect ratio as well as the Ra_I. The temperature decreases as Ra_I increases due to enhanced convection and hence good mixing. The temperature is high if cavity is tall due to thermal stratification effects.

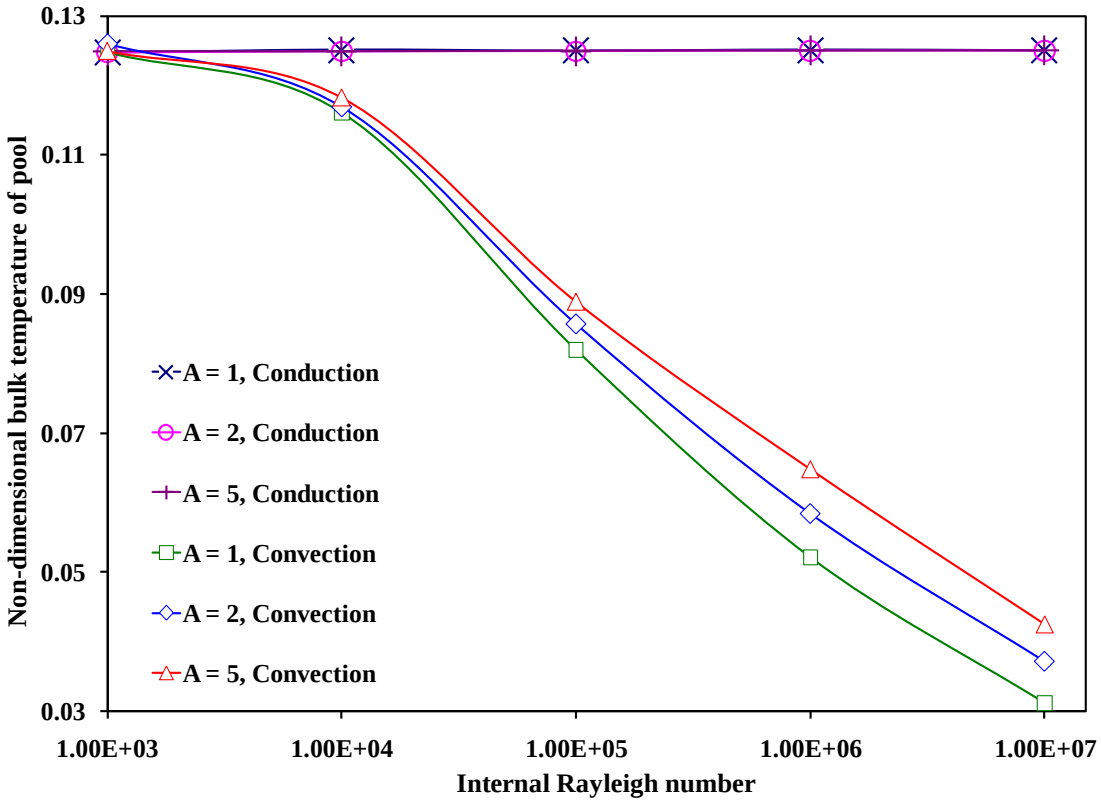

Fig. 4.9. Variation of dimensionless bulk temperature of pool with Ra_I for different values of aspect ratio.

Natural convection in the heat generating pool is affected by parameters such as q''' and A. Hence, Ra_I, which is a function of these parameters, is correlated with factor (CF) as suggested by Bol'shov et al. (2001):

$$CF = a\,(Ra_I)^b \tag{4.22}$$

The values of coefficient *a* and exponent *b* are determined by carrying out detailed parametric studies for various values of Ra_I and *A*. These are presented in Table 4.3. The variation of the factor (*CF*) with Ra_I, for different aspect ratios is depicted in Fig. 4.10. These results form input for the analysis described in the next section, viz., 'rate of hexcan melting'.

Table 4.3. Values of *a* and *b* for laminar and turbulent regimes.

Ra_I	$A = 1$		$A = 2$		$A = 5$	
	a	*b*	*a*	*b*	*a*	*b*
Laminar ($Ra_I \leq 10^4$)	0.3653	0.1425	0.4038	0.1308	0.4181	0.1239
Turbulent ($10^5 \leq Ra_I \leq 10^{10}$)	0.12312	0.1786	0.2926	0.1564	0.2823	0.1548

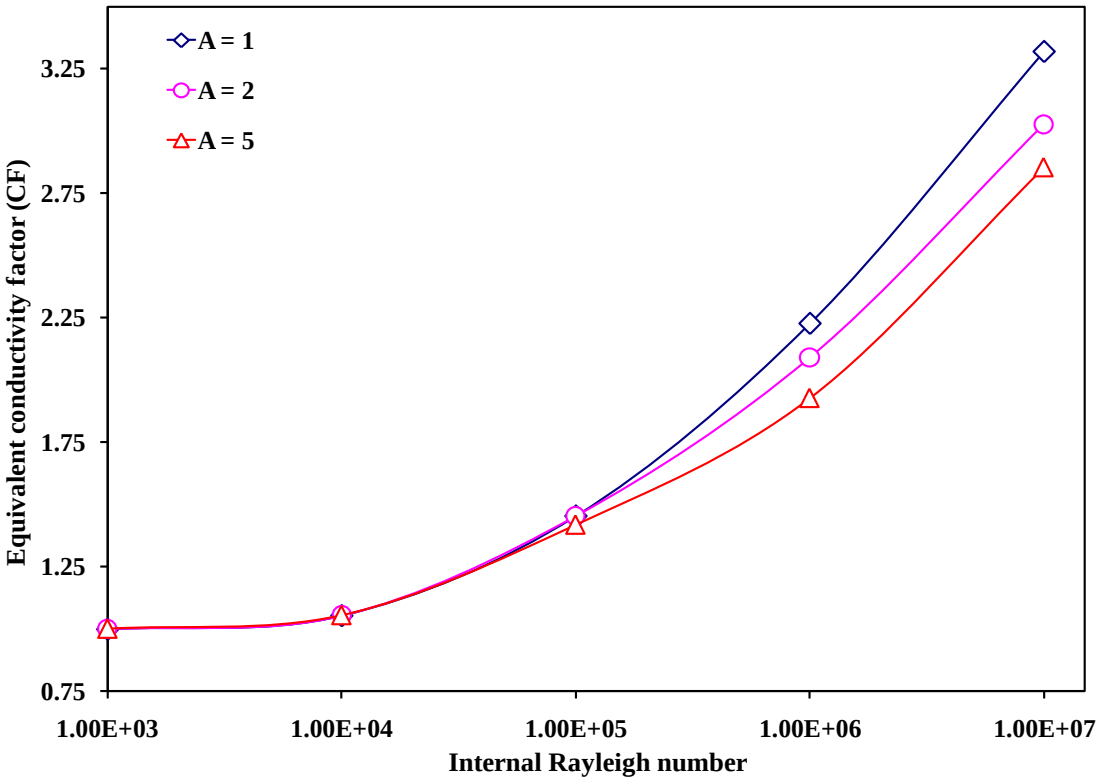

Fig. 4.10. Equivalent conductivity factor for various values of aspect ratio.

4.3.2 STEP-2: INVESTIGATION OF HEXCAN MELTING

During molten fuel attack, the hexcan of the neighboring subassemblies in contact with the molten fuel starts melting layer by layer from inner side and its outer surface is exposed to flowing sodium. Heat flux leaving the hexcan surface is affected by thermal resistance of hexcan which decreases with time due to reduction in its thickness by melting. The melting speed of the hexcan wall is a strong function of heat flux and the fuel-hexcan interface temperature which in turn depends on the heat transfer mechanism. The effect of natural convection in the fuel pool is accounted by considering the equivalent thermal conductivity in the heat balance model described in step-2 of section 4.1.2. The aspect ratio of pool formed in the case of a prototype fuel subassembly with 217 pins (Chetal et al., 2006) is 5 and the Ra_I *is* ~ 3×10^7, for full power condition. The equivalent conductivity factor estimated for this case using Eqn. (4.22) is 4. For the same case, if the natural convection in the fuel pool is neglected then CF = 1 (pure conduction). Evolutions of temperature in the pool and hexcan for CF = 1 and 4 are depicted in Figs. 4.11a and 4.11b respectively. It is observed that for the pure conduction case (CF = 1), a time duration of several seconds is required for the interface temperature to rise before start of the hexcan melting. The first element of the hexcan completes melting by 8.8 s and about 45% of the hexcan wall completes melting by 35 s (see, Fig. 4.11a). On the other hand when natural convection in the fuel pool is considered (CF = 4), it takes only about 0.4 and 1 s respectively after molten fuel attack (see, Fig. 4.11b), highlighting that the natural convection in the fuel pool enhances the melting speed of the hexcan.

The temperature rise in neighboring subassembly sodium and the corresponding residual thickness of hexcan wall for CF=1 and 4 are depicted in Fig. 4.12. It is seen that when natural convection in the fuel pool is considered ($Ra_I = 3\times10^7$ and CF = 4), the residual thickness of the hexcan at the end of 35 s is less than 5%.

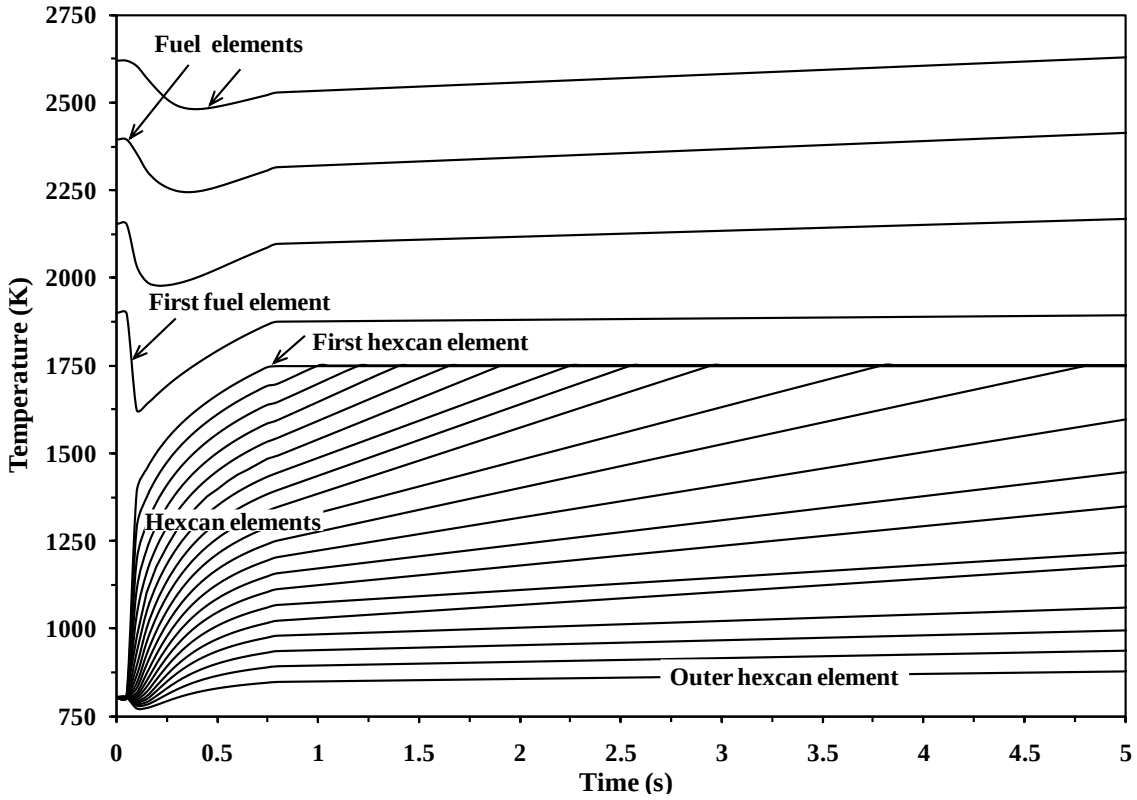

Fig. 4.11a. Evolution of affected SA fuel and neighboring SA hexcan temperatures during molten fuel attack for *CF* = 1.

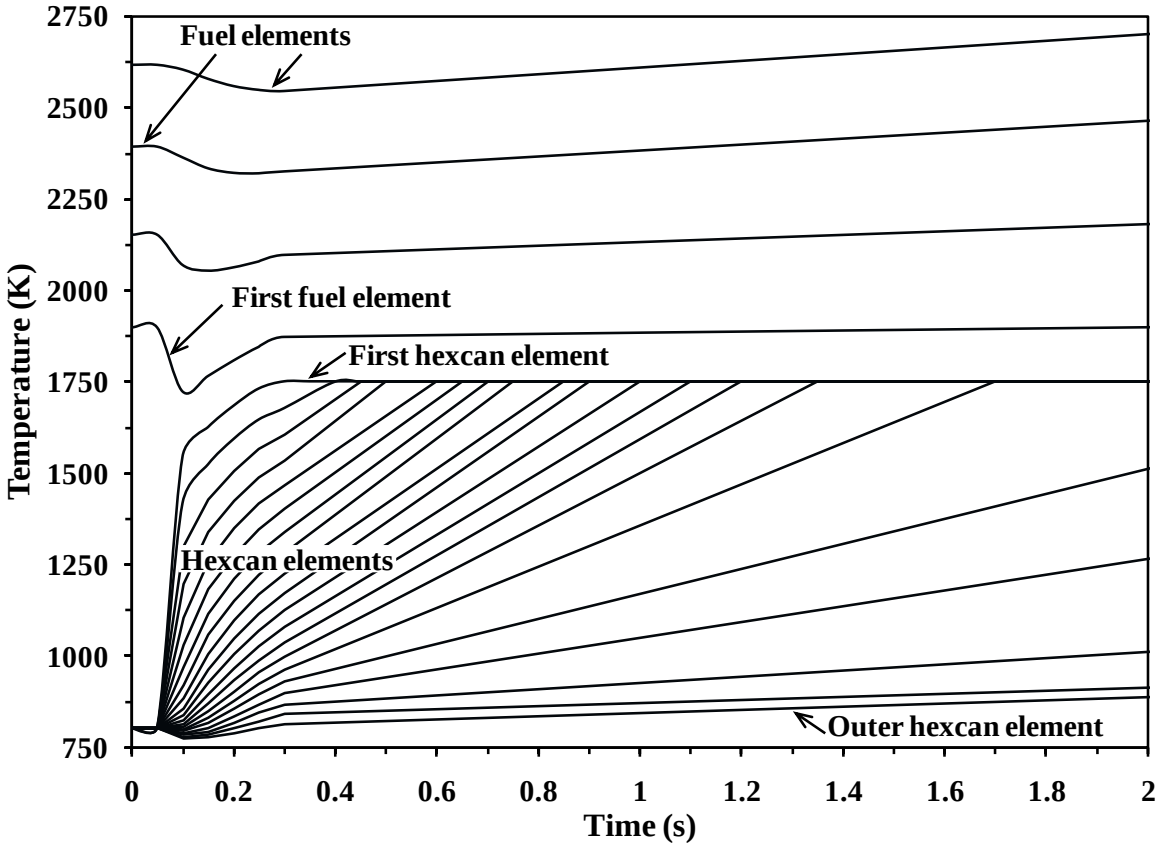

Fig. 4.11b.Evolution of affected SA fuel and neighboring SA hexcan temperatures during molten fuel attack for *CF* = 4.

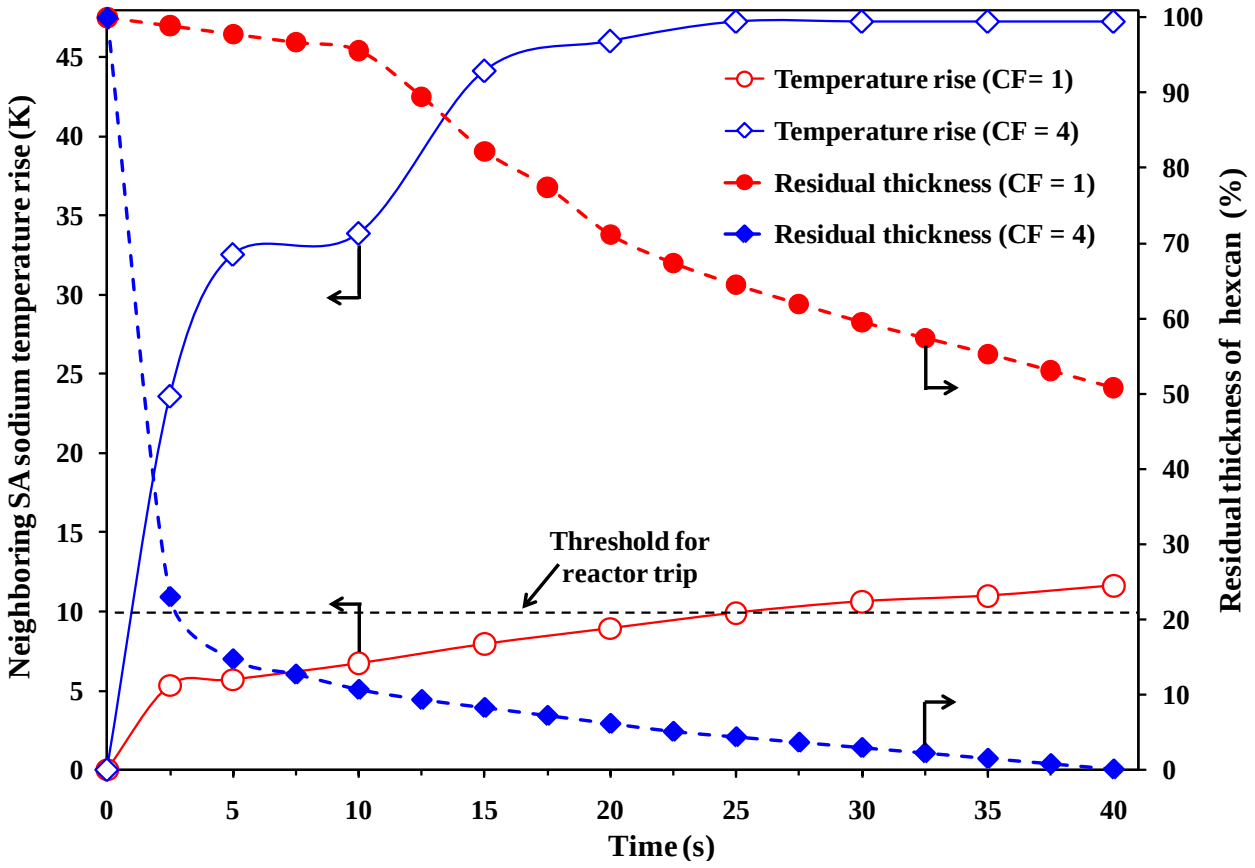

Fig. 4.12. Time dependent temperature rise of neighboring subassembly sodium during molten fuel attack as a function of conductivity factor.

On the other hand when only conduction is considered in the fuel pool (*CF* = 1), the residual thickness at the end of the same instant is 55%, highlighting that as the value of *CF* increases the melting speed of the hexcan wall also increases. One of the critical information relevant to the current study is rise in sodium outlet temperature from the neighboring subassembly, which is continuously monitored for safety action. It is seen that when the neighboring subassembly sodium temperature rises by 10 K the corresponding residual thickness of hexcan is ~ 65% for all the values of *CF*. Interestingly, the residual thickness value is found to be insensitive to the value of *CF*. However, the rapid rise in temperature of neighboring SA sodium as well as melting speed of hexcan, noticed during natural convection in fuel pool seem to be highly conservative in nature. For example, at *CF* = 1, time taken for the temperature rise of 10 K in the neighboring SA

sodium is ~ 35 s and the residual thickness of hexcan at this instant is 55%, whereas in case of *CF* = 4, it takes just 1.25 s for the same temperature rise. These drastic variations are because of assuming fully established natural convection in the pool. It is known that establishment of natural convection within the pool takes a finite time. But, in the present study, an equivalent conductivity factor corresponding to fully established natural convection is implemented in the heat balance model, which leads to conservative results. Hence, transient natural convection in the fuel pool has to be considered to predict the realistic inter-subassembly heat transfer rate and the melting speed of the hexcan.

The thermocouple located at SA outlet to monitor the sodium temperature have a finite response time, due to which, the thermocouples do not read the instantaneous sodium temperature, as explained earlier (Section 3.2.1). The response time for typical thermocouple is 8 s. The estimated time required for temperature rise of 10 K in the neighboring SA sodium is ~ 1.25 s, which is quit smaller than the response time of the thermocouple.

Thus, it is clear that the natural convection within fuel pool leads to enhanced melting speed of the hexcan and hence speeds up the core damage propagation. It is also seen that the extent of damage to hexcan per degree temperature rise in the neighboring subassembly sodium remains nearly unaffected. However, considering fully developed natural convection leads to unrealistic damage progression and inter-subassembly heat transfer. Hence, transient natural convection in the fuel pool has to be accounted.

4.4 CLOSURE

It is found that natural convection within the pool formed during TIB in a fuel SA leads to quicker melting of the hexcan wall, suggesting the effect of natural convection in fuel pool should be accounted while modeling stage-III. Further, the residual thickness of neighboring SA hexcan is found to be insensitive to the presence/absence of natural convection in the fuel pool at

the time of 10 K temperature rise in neighboring SA sodium. However, considering fully established natural convection in fuel pool leads to unrealistic rate of heat transfer and melting speed of neighboring hexcan. As a consequence of this it appears that the core monitoring thermocouple, having a finite response time, cannot detect the TIB in the fuel SA. Hence, it can concluded that for a realistic prediction of heat transfer rate and speed of damage progression during stage-III, the transient natural convection in the fuel pool has to be considered instead of fully established natural convection. This is the focus of the next Chapter.

CHAPTER 5

DEVELOPMENT OF INTEGRATED 2-D MODEL AND INVESTIGATION OF DAMAGE PROGRESSION

5

5.0 INTRODUCTION

The enthalpy based 1-D transient model discussed earlier is a simplified thermal model, based on uniform heat generation in the pin which was found to be efficient to carry out parametric studies. It is to be noted that the heat generation in the fuel pins follows a cosine profile along the fuel pin axis with peaking at the center of the core, which cannot be represented by 1-D models. The axial variation in temperatures of fuel, clad and sodium during TIB is one of the important parameters that affect the initiation of damage, which cannot be captured in 1-D model. Further, natural convection that sets-in within the molten fuel pool formed during stage-III enhances the radial heat transfer to the neighboring SA leading to enhanced melting speed of the neighboring SA hexcan. Establishment of natural convection within the pool takes a finite time. Assuming a fully established natural convection leads to unrealistic damage propagation. Hence, knowledge of transient natural convection heat transfer that takes place in the heat generating fuel pool is essential. The effect of transient natural convection on core damage propagation is not accounted in 1-D model.

Towards implementing these features, an integrated 2-D thermal hydraulic model has been developed by coupling all three stages of the TIB accident scenario. The model accounts for the above factors and considers an explicit representation of all the rows of the fuel pins in the

blocked SA for a realistic prediction of time and location of damage initiation and the sequence of damage progression. This 2-D model is used to carry out detailed parametric study to evaluate the effects of thermocouple time constant on possible early detection of TIB. Further, the present study attempts to bring out the relative importance of implementing the transient natural convection model over pure conduction model for investigating the heat transfer and damage progression during stage-III.

5.1 MODELING

5.1.1 GEOMETRIC MODELING

The integration of three discrete stages of the TIB in a fuel SA is carried out by imposing the interface conditions between the various stages, which are based on the findings of the experimental studies reported in open literature. These interface conditions play an important role in deciding initial conditions for the subsequent stage. It is learnt from the SCRABEE BE+3 experiment (Kayser et al., 1998) that the liquid steel draining downward during clad melting forms steel blockage at the bottom of active blanket region. On top of this blockage a tight fuel pool is formed within the blocked SA. This forms the interface condition between stage - I and stage-II. Similarly, after melting of blocked SA hexcan, the molten steel blocks the inter-wrapper gap and creates an enclosure for formation of molten fuel pool. This forms the interface condition between stage-II and stage-III. The structure of the code system developed and their interface conditions are presented in Fig. 5.1. A prototype hexagonal fuel subassembly of 217 pins with triangular pitch of 8.28 mm arranged in 8 rows is geometrically modeled by an equivalent 2-D axi-symmetric circular domain whose diameter is calculated by respecting the area of prototype subassembly. The flow and geometric details of the fuel SA are presented in the Table 5.1.

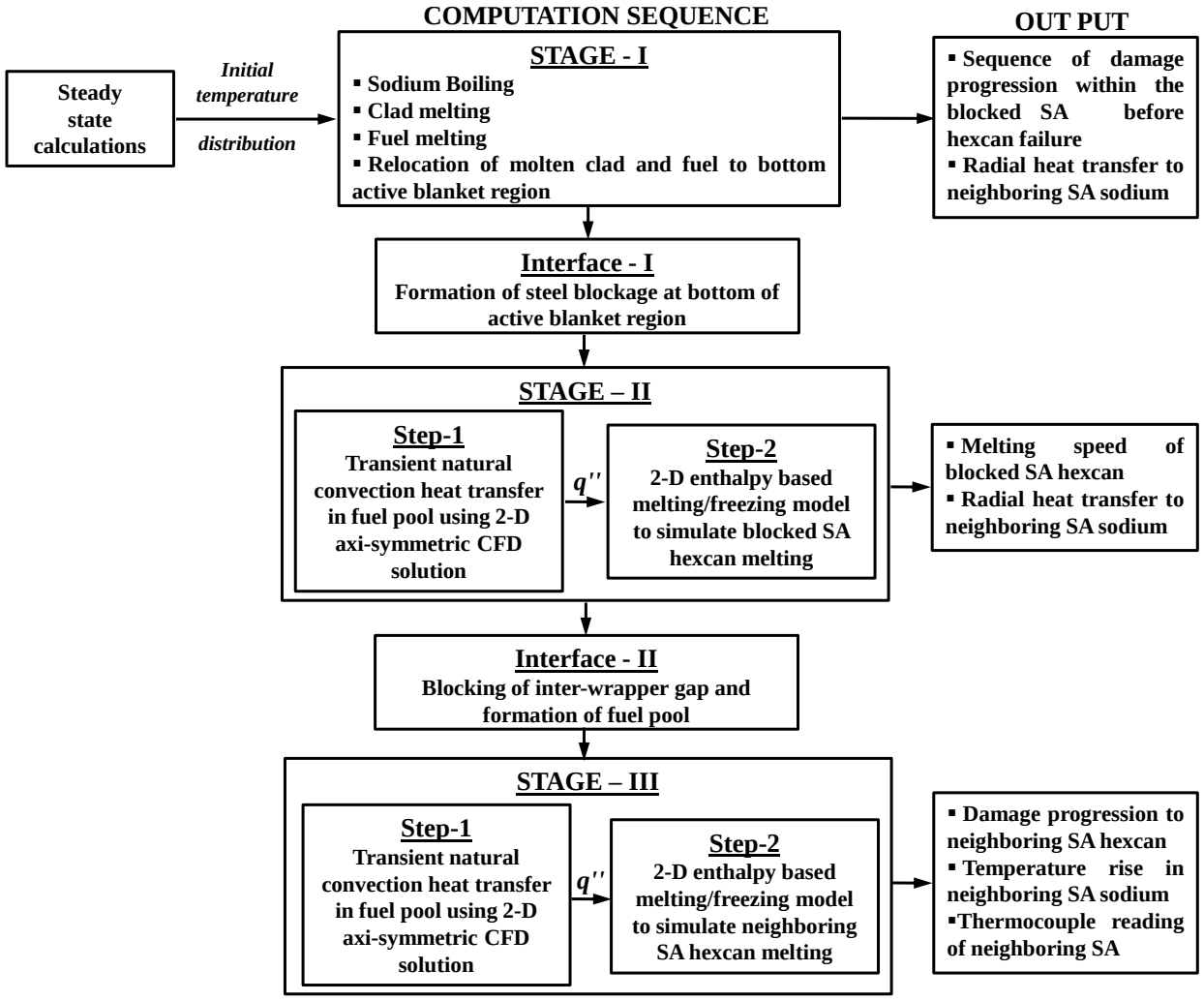

Fig. 5.1. Structure of the code for integrated study with various stages and interface conditions (q'' wall heat flux).

The geometrical modeling represents central (blocked) SA, inter-wrapper sodium, and neighboring SA hexcan in axi-symmetric model. The central SA is divided into 12 concentric zones as depicted in Fig. 5.2. The first 9 zones represent 217 fuel pins (one central pin region with associated sodium channel and 8 rows of pins with associated sodium channels). Other 3 zones (10, 11 and 12) represent central SA hexcan, inter-wrapper sodium and neighboring SA hexcan respectively. Each of first 9 zones representing the pins are further divided into 4 circular rings representing inner cladding, fuel, outer cladding and sodium. Thus, the whole domain consisting of blocked SA, inter-wrapper sodium and neighboring SA is divided into 38 radial

rings (Fig. 5.3). Each of these rings can be divided in the radial direction for further grid refinement. The total number of grids required in radial and axial directions is decided based on the grid independence study discussed in Section 5.2.1. It may be indicated that during initial steady state, the sodium flow rate through the central SA is 35.8 kg/s. Subsequently, the flow rate to the central SA is brought to zero, leading to an instantaneous blockage.

Table 5.1.Geometric parameters of the fuel subassembly.

Parameters	**Value**
Triangular pitch of pin arrangement (mm)	8.28
Fuel pin inner diameter (mm)	1.8
Fuel pin outer diameter (mm)	6.6
Clad thickness (mm)	0.45
Fissile height of fuel pin (mm)	1000
Lower axial fertile height (mm)	300
Upper axial fertile height (mm)	300
Outer-width across flat of hexcan (mm)	131.3
Hexcan thickness (mm)	3.4
Number of fuel pins in a subassembly	217
Number of rows of pins in a subassembly	8
Total power of the subassembly (MW)	8
Initial flow rate of sodium in a subassembly (kg/s)	35.8
Inlet sodium temperature (K)	673
Inter-wrapper flow sodium velocity (m/s)	0.5

Axial power distribution in the fuel pin is assumed to be a cosine profile as exhibited in Fig. 5.4. The axial fuel power distribution and total power of the central SA as well as neighboring SA are assumed to be identical.

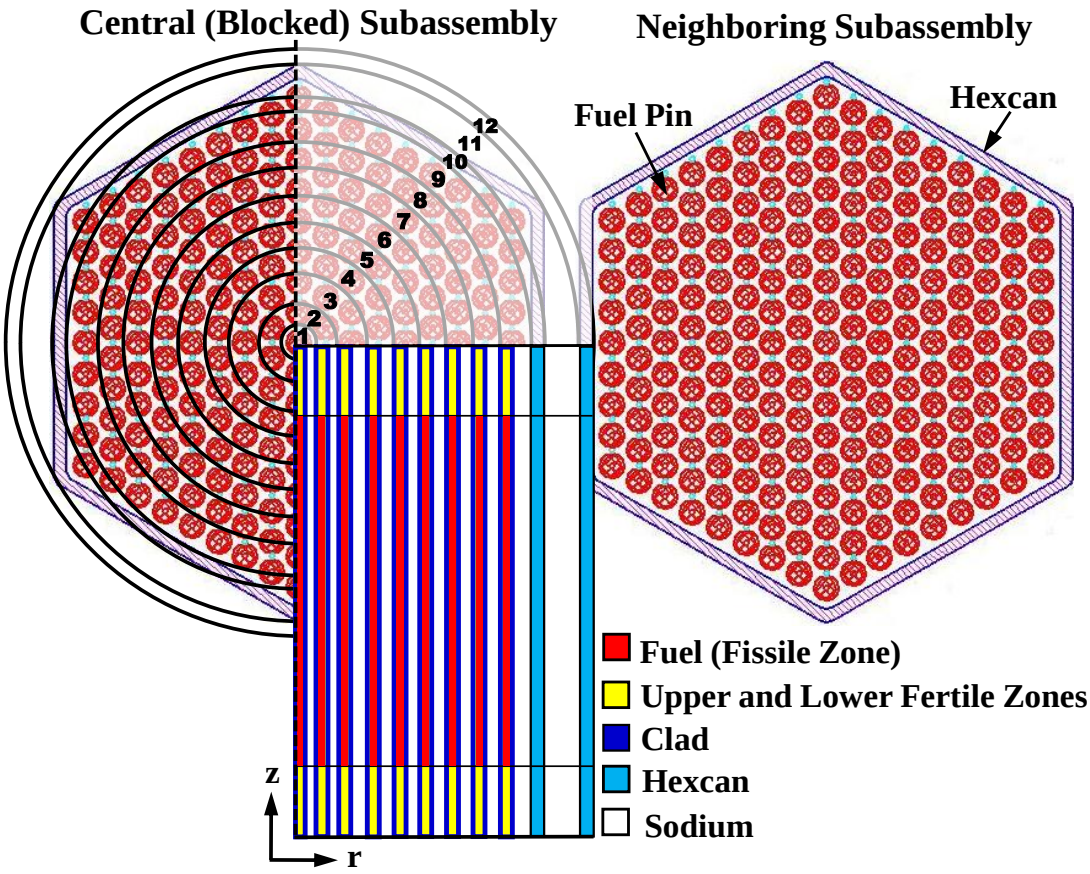

Fig. 5.2. Sectional view of central (blocked) SA and one of the six neighboring SA.

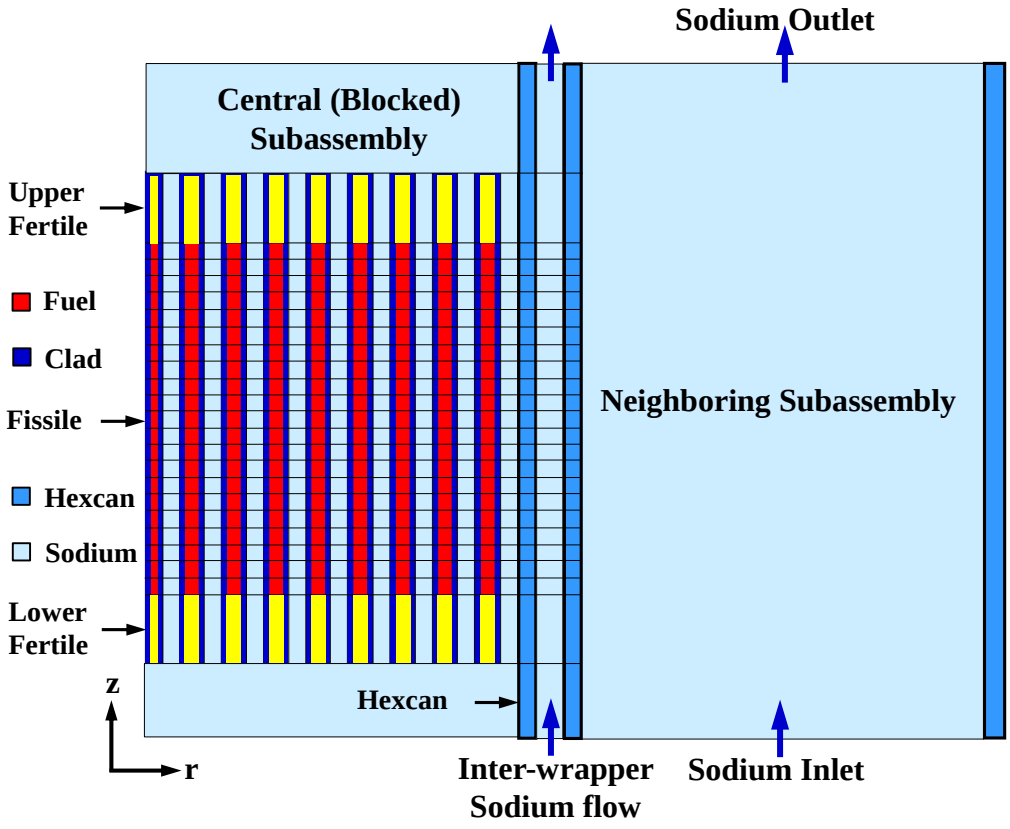

Fig. 5.3. Geometrical model with mesh for central (blocked) SA with neighboring SA.

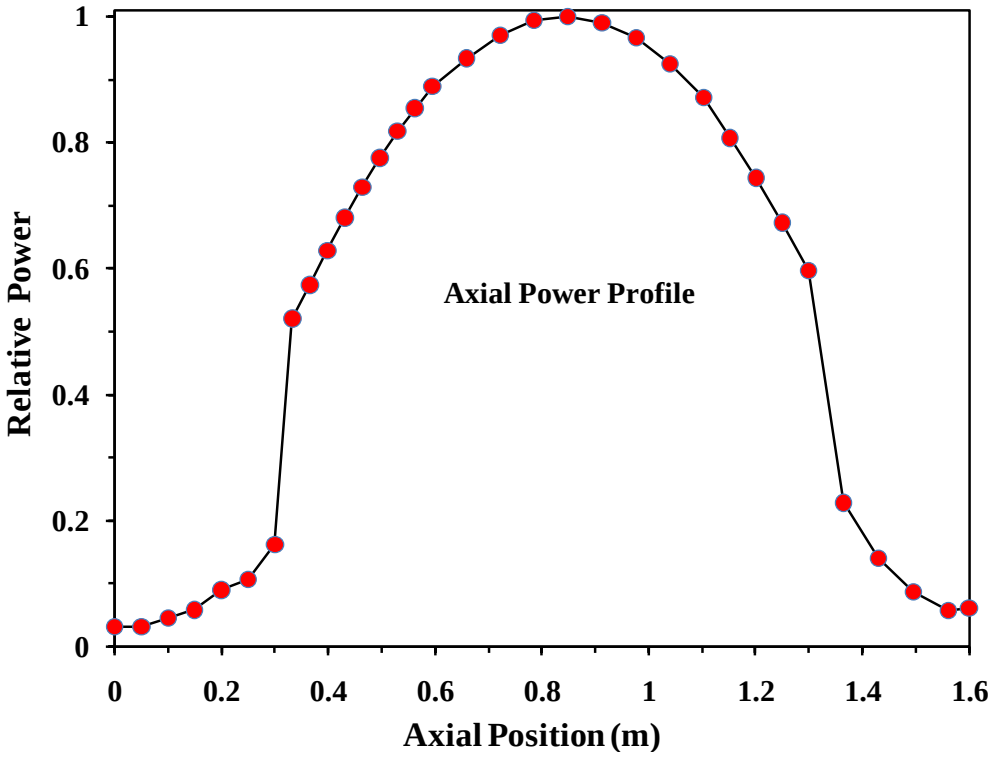

Fig. 5.4. Power variation along the active length of the fuel pin.

5.1.2 MATHEMATICAL MODELING

Initial Steady State Calculations

Initial steady state calculations are carried out before conducting transient analysis to determine the steady state temperature distribution in fuel, clad, sodium and hexcan of central SA as well as the neighboring SA, which are imposed as the initial conditions to initiate the transient analysis. SA power, fuel pin power distribution, sodium inlet temperature and sodium mass flow rate required for steady state calculations are obtained from basic heat balance. The steady state temperature distribution in the fuel pin, clad, sodium and hexcans of central and neighboring SA are obtained by numerically solving the following non-linear 2-D transient energy equations for time duration long enough to attain the steady state solution (Chen et al., 1979). It may be indicated that in the steady state analysis with pins intact, no momentum

equation is solved and the axial velocity of sodium is taken uniform throughout the cross-section of the SA.

Fuel:

$$\rho C \frac{\partial T}{\partial t} = \nabla \left[K(\nabla T) \right] + q''' \tag{5.1}$$

Clad and Hexcan:

$$\rho C \frac{\partial T}{\partial t} = \nabla \left[K(\nabla T) \right] \tag{5.2}$$

Sodium flow:

$$\rho C \frac{\partial T}{\partial t} + \rho C \nabla (U T) = \nabla \left[K(\nabla T) \right] \tag{5.3}$$

The effective conductance (G) between the nodal points of clad and fuel elements in the calculations are evaluated using the general expression for radial heat flow across a hollow cylinder as expressed in Eq. (3.10). The effective conductance between the wall and sodium flow, viz., clad and flowing sodium, hexcan and inter-wrapper sodium flow and also between the hexcan and the neighboring SA sodium are evaluated by:

$$G_{ws} = \frac{a_w}{\left(\frac{\delta_w}{2K_w} + \frac{1}{h_{ws}} \right)} \tag{5.4}$$

Where G_{ws} is effective conductance between the wall and the forced sodium flow, a_w is surface area of wall exposed to sodium flow, δ_w is thickness of wall, K_w is thermal conductivity of wall material and h_{ws} is heat transfer coefficient on wall surface due to forced sodium flow. For fuel clad and hexcan wall on the inner faces exposed to forced sodium flow, the heat transfer coefficient is calculated using the correlation proposed by Kazimi and Carelli (1976),

$$Nu = 4 + 0.33\left(\frac{P_t}{D_c}\right)^{3.8}\left(\frac{Pe}{100}\right)^{0.86} + 0.16\left(\frac{P_t}{D_c}\right)^{5} \tag{5.5}$$

For hexcan wall on the outer faces exposed to inter-wrapper flow, the heat transfer coefficient is calculated using the correlation (Cengel, 2007),

$$Nu = 6.3+0.0167\, Re^{0.85}\, Pr^{0.93} \tag{5.6}$$

Transient Calculations

The transient phase corresponds to the scenario of sudden and complete blockage of sodium flow to the affected SA operating at nominal power. Transient calculations are initiated by imposing zero flow velocity boundary condition at SA inlet. During transient, various components of the SA undergo temperature change as well as phase change. To model these complex phenomena, the enthalpy formulation is adopted which is described below:

Fuel:

$$\rho\frac{\partial}{\partial t}\left(H_{spe}\right) = \nabla\left[K\left(\nabla \mathrm{T}\right)\right] + q''' \tag{5.7}$$

Stagnant sodium, clad and hexcan:

$$\rho\frac{\partial}{\partial t}\left(H_{spe}\right) = \nabla\left[K\left(\nabla T\right)\right] \tag{5.8}$$

It may be mentioned that Eq. 5.8 refers to stage-I, when fuel pool is yet to form. Natural convection in fuel pool is accounted in stage-III. However natural convection in sodium during sodium boiling is not accounted because, the hydraulic diameter of the sub-channel is very small (~3 mm). Further, the pin bundle is provided with helically wound spacer wires. These features offer significant resistance for flow.

Sodium flow in the inter-wrapper gap:

$$\rho C \frac{\partial}{\partial t}\left(H_{spe}\right)+\rho C \nabla\left(U T\right)=\nabla\left[K\left(\nabla T\right)\right]+\text{heat exchaange with hexcan} \tag{5.9}$$

The discretised forms of the above heat balance equations for phase change of an element with radial and axial positions indicated by subscripts '*m*' and '*n*' respectively in the computational domain during the transients are expressed as below.

Fuel:

$$\frac{dH}{dt}=q+G_{m-1,m}\left(T_{m-1}-T_m\right)+G_{n-1,n}\left(T_{n-1}-T_n\right)-G_{m,m+1}\left(T_m-T_{m+1}\right)-G_{n,n+1}\left(T_n-T_{n+1}\right) \tag{5.10}$$

Stagnant sodium, clad and hexcan:

$$\frac{dH}{dt}=G_{m-1,m}\left(T_{m-1}-T_m\right)+G_{n-1,n}\left(T_{n-1}-T_n\right)-G_{m,m+1}\left(T_m-T_{m+1}\right)-G_{n\ ,n+1}\left(T_n-T_{n+1}\right) \tag{5.11}$$

Inter-wrapper sodium:

$$\frac{dH}{dt}=G_{sxr}\left(T_{xb}-T_{sr}\right)-G_{sxr}\left(T_{sr}-T_{xn}\right)-m_{sr}C_s\left(T_{sno}-T_{sni}\right) \tag{5.12}$$

In the above equations, q is rate of heat generation in fuel element. The effective thermal conductance (G) between the nodal points is calculated using Eqs. (3.10) and (5.4). The estimation of melting and solidification rates using analytical methods is limited to semi infinite regions and constant material properties (Epstein, 1973). In the present study, finite thickness of fuel and hexcan elements are considered and the variation in thermo-physical properties of sodium, steel and fuel material due to temperature changes are accounted by implementing the property equations suggested by Chawla et al. (1984), Carbajo et al. (2001), Morita and Fischer, (1998), Morita et al. (1998) and Fink and Leibowitz, (1995) (see, Appendix for property values and equations for coolant, clad, fuel, and thermo-physical properties). The variation in temperature of (i) coolant and (ii) fuel, clad and hexcan materials during their phase change

process are monitored using Eqns. 3.17 and 3.19 respectively. The solidus and liquidus temperatures for clad and hexcan material (steel) are taken as 1720 K and 1750 K respectively. For fuel material (MOX) the solidus and liquidus temperatures are taken as 3070 K and 3090 K respectively (Carbajo et al., 2001).

It is to be noted that using enthalpy formulation for modeling melting/freezing of steel and fuel elements during transient is associated with the problem of unrealistic oscillations in the temperature field due to dynamic deletion of molten elements from the computational domain. However, this problem is tackled in the present study by implementing the Voller's algorithm, which is a technique of variable time step and fixed space grid keeping phase front always on a node point, known as node jumping scheme (Voller, 1987).

The transient natural convection in the fuel pool formed during TIB is geometrically modeled as a volumetric heat generating fluid enclosed in a cylindrical enclosure (see Fig. 4.2). The flow and heat transfer during transient natural convection in the molten fuel pool are governed by the following transient, mass, momentum and energy equations (Hughes and Gaylord, 1964) along with conservation equations for turbulent kinetic energy and turbulent dissipation rate (Sharma et al., 2009 and Henkes, 1990):

Continuity:

$$\frac{1}{r}\frac{\partial(ru)}{\partial r}+\frac{\partial v}{\partial z}=0 \tag{5.13}$$

Radial momentum:

$$\frac{\partial(\rho u)}{\partial t}+\frac{\partial(\rho uu)}{\partial r}+\frac{\partial(\rho uv)}{\partial z}=-\frac{\partial p}{\partial r}+\frac{1}{r}\frac{\partial}{\partial r}\left(r\,\mu_{eff}\frac{\partial u}{\partial r}\right)+\frac{\partial}{\partial z}\left(\mu_{eff}\frac{\partial u}{\partial z}\right)-\mu_{eff}\frac{u}{r^2} \tag{5.14}$$

Axial momentum:

$$\frac{\partial(\rho v)}{\partial t}+\frac{\partial(\rho uv)}{\partial r}+\frac{\partial(\rho vv)}{\partial z}=-\frac{\partial p}{\partial z}+\frac{1}{r}\frac{\partial}{\partial r}\left(r\,\mu_{eff}\frac{\partial v}{\partial r}\right)+\frac{\partial}{\partial z}\left(\mu_{eff}\frac{\partial v}{\partial z}\right)+g\rho\beta\left(T-T_{ref}\right) \tag{5.15}$$

Energy:

$$\frac{\partial(\rho CT)}{\partial t}+\frac{\partial(\rho CTu)}{\partial r}+\frac{\partial(\rho CTv)}{\partial z}=\frac{1}{r}\frac{\partial}{\partial r}\left[rK_{eff}\frac{\partial T}{\partial r}\right]+\frac{\partial}{\partial z}\left[K_{eff}\frac{\partial T}{\partial z}\right]+q''' \tag{5.16}$$

Turbulent kinetic energy:

$$\frac{\partial(\rho k)}{\partial t}+\frac{\partial(\rho uk)}{\partial r}+\frac{\partial(\rho vk)}{\partial z}=\frac{1}{r}\frac{\partial}{\partial r}\left[r\left(\mu+\frac{\mu_t}{\sigma_k}\right)\frac{\partial k}{\partial r}\right]+\frac{\partial}{\partial z}\left[\left(\mu+\frac{\mu_t}{\sigma_k}\right)\frac{\partial k}{\partial Z}\right]+P_k+B_k-\rho\varepsilon \tag{5.17}$$

Turbulent dissipation rate:

$$\frac{\partial(\rho\varepsilon)}{\partial t}+\frac{\partial(\rho u\varepsilon)}{\partial r}+\frac{\partial(\rho v\varepsilon)}{\partial z}=\frac{1}{r}\frac{\partial}{\partial r}\left[r\left(\mu+\frac{\mu_t}{\sigma_\varepsilon}\right)\frac{\partial \varepsilon}{\partial r}\right]+\frac{\partial}{\partial z}\left[\left(\mu+\frac{\mu_t}{\sigma_\varepsilon}\right)\frac{\partial \varepsilon}{\partial z}\right]+\left[C_{\varepsilon 1}\left(P_k+C_{\varepsilon 3}B_k\right)-C_{\varepsilon 2}\varepsilon\right]\frac{\varepsilon}{k} \tag{5.18}$$

Where

$$P_k=\mu_t\left[2\left(\frac{\partial u}{\partial r}\right)^2+2\left(\frac{\partial v}{\partial z}\right)^2+\left(\frac{\partial u}{\partial z}+\frac{\partial v}{\partial r}\right)^2+2\left(\frac{u}{r}\right)^2\right],\ B_k=-g\beta\frac{\mu_t}{\sigma_T}\frac{\partial T}{\partial r}$$

$$\mu_{eff}=\mu+\mu_t,\ \mu_t=C_\mu\frac{\rho k^2}{\varepsilon},\ K_{eff}=K+K_t,\ K_t=\frac{\mu_t C}{\sigma_T}$$

Values of turbulence model constants used are:

σ_ε = 1.3, σ_T = 0.9, σ_k = 1.0, $C_{\varepsilon 1}$ = 1.44, $C_{\varepsilon 2}$ = 1.92, $C_{\varepsilon 3}$ = tanh (u/v) and C_μ = 0.09. The turbulence model constants for the present calculation have been adopted from Henkes (1990). He has studied various versions of turbulence models including standard k-ε model and low Reynolds number version of k-ε model, for turbulent natural convection in rectangular enclosures driven by vertical walls. His study indicated that the standard k-ε model without wall function provides accurate and stable results compared to other models. Based on the success of Henkes (1990), Sharma et al. (2009) have used the same model along with the similar constants for simulating

natural convection in cylindrical enclosures with internal heat sources. Thus, usage of these constants for the present condition of turbulent natural convection in heat generating fuel pool is justified. The molten fuel is assumed to be Newtonian and incompressible with constant thermo-physical properties except for density in the buoyancy term, which follows the Boussinesq approximation. Solution to the above set of partial differential equations is obtained numerically by using a Finite Volume Method (FVM), wherein a non-uniform structured grid is employed. The size of the grid is taken fine enough near the boundary and coarse away from the wall, such that the first grid from the boundary wall lies within the viscous sub-layer during the turbulent flow. The pressure-velocity coupling is resolved by using the SIMPLE algorithm proposed by Patankar and Spalding, (1972).

5.2 CODE VALIDATION

The present computational model is used to predict the sequence and time of occurrence of various principal events as well as the associated heat transfer during TIB in a prototype fuel subassembly. The present results are compared against experimental and numerical results reported in the open literature.

5.2.1 GRID SENSITIVITY STUDY

Extensive tests were carried out to ascertain the grid size and time interval by adopting various values. The effect of grids on the instant of occurrences of various key events during TIB in a prototype fuel subassembly with 217 pins is studied as depicted in Fig. 5.5. The results of the study indicate that a minimum of 3500 grids and time step of 10^{-5} s are to be adopted to obtain mesh-independent solution.

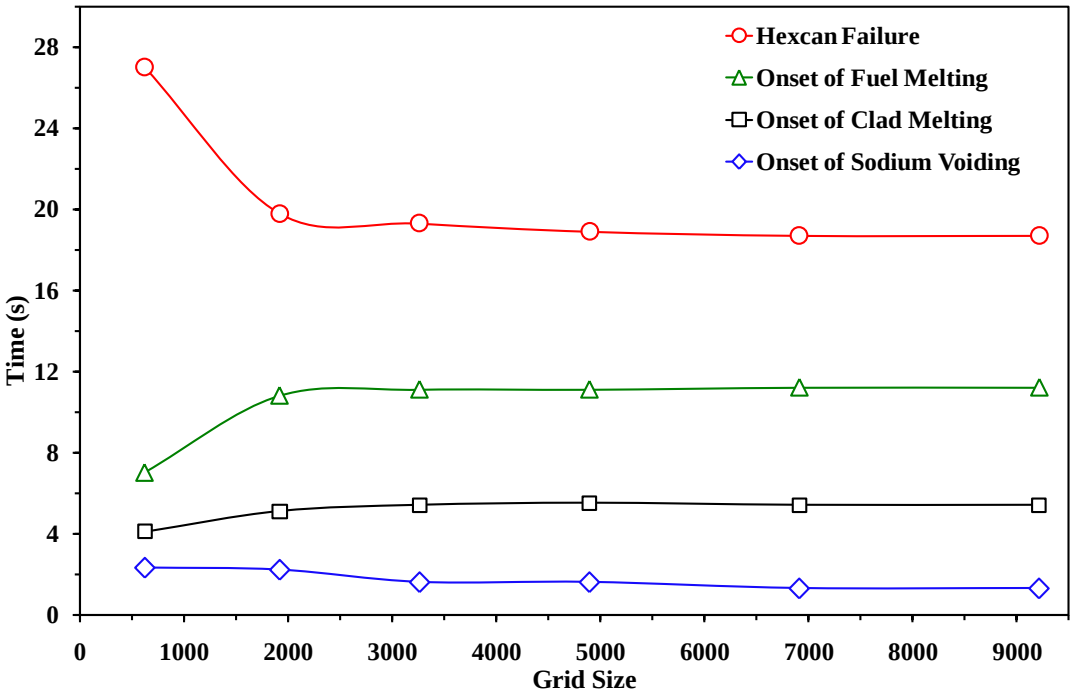

Fig. 5.5. Effect of grids on time of occurrence of principal events during TIB.

5.2.2 ACADEMIC BENCHMARK

The computational model in the present study is used to predict the transient natural convection in heat generating fluid in a cylindrical enclosure. Due to the lack of standard benchmark results for transient natural convection in cylindrical enclosures, the present computational model is validated against the benchmark numerical results of Shim and Hyun, (1997). They have carried out numerical studies to understand evolution of time-dependent natural convection in a heat generating fluid enclosed in a square cavity with the two vertical side walls maintained isothermally at different temperatures. The flow and the associated heat transfer are characterized by the externally controlled Rayleigh number (Ra_E) and by internal heat generation rate represented by internal Rayleigh number (Ra_I) expressed as:

$$Ra_E = \frac{g\ \beta\ \Delta T\ z_{cav}^3}{\upsilon\alpha} \text{ and } Ra_I = \frac{g\beta q''' z_{cav}^5}{\upsilon\alpha K} \tag{5.19}$$

Where, ΔT is temperature difference between the hot and cold walls of the cavity ($\Delta T = T_{hot} - T_{cold}$), z_{cav} is height of the cavity, β is volumetric expansion coefficient of fluid, g is acceleration due to gravity, q''' is volumetric heat generation rate, v is kinematic viscosity, α is thermal diffusivity and K is the thermal conductivity. The Ra_E is varied as a function of temperature difference between the vertical hot and cold walls of the cavity, whereas Ra_I is varied by changing the volumetric heat generation rate of the fluid. The hot and cold walls of the cavity are maintained at nondimesionalized temperatures ϕ = 0.5 and -0.5 respectively, where, ϕ *is* non-dimensional temperature defined as:

$$\phi = \frac{T - \left(T_{hot} + T_{cold}\right)/2}{\left(T_{hot} - T_{cold}\right)} \tag{5.20}$$

The non-dimensional time t^* is defined as:

$$t^* = \frac{t\upsilon}{z_{cav}^2} \tag{5.21}$$

The streamlines and isotherms predicted by the present model for $Ra_E = 10^5$ and $Ra_I = 10^7$ at various non-dimensional instants, viz., t^* = 0.0001, 0.005, 0.01 and 0.1, are compared with the results of Shim and Hyun, (1997) in Fig. 5.6. It can be seen that during initial stages (at $t^* <$ 0.005) the flow is under the influence of the external heating and a large part of the cavity is occupied by a single clockwise circulating cell. In the intermediate stages (at t^* = 0.005 - 0.01), the impact of the internal heating begins and an additional differential buoyancy is produced. As a result of this, a small sized counter clock wise circulation emerges. As the time passes, the relative effect of internal heating dominates over the external heating and finally at t^* = 0.1, the whole cavity is occupied by two counter circulating cells. It can be seen that the present results compare satisfactorily with the benchmark data. The time dependent non-dimensional peak temperature variation of fluid in the cavity is compared against the published data in Table 5.2 and the comparison is highly satisfactory.

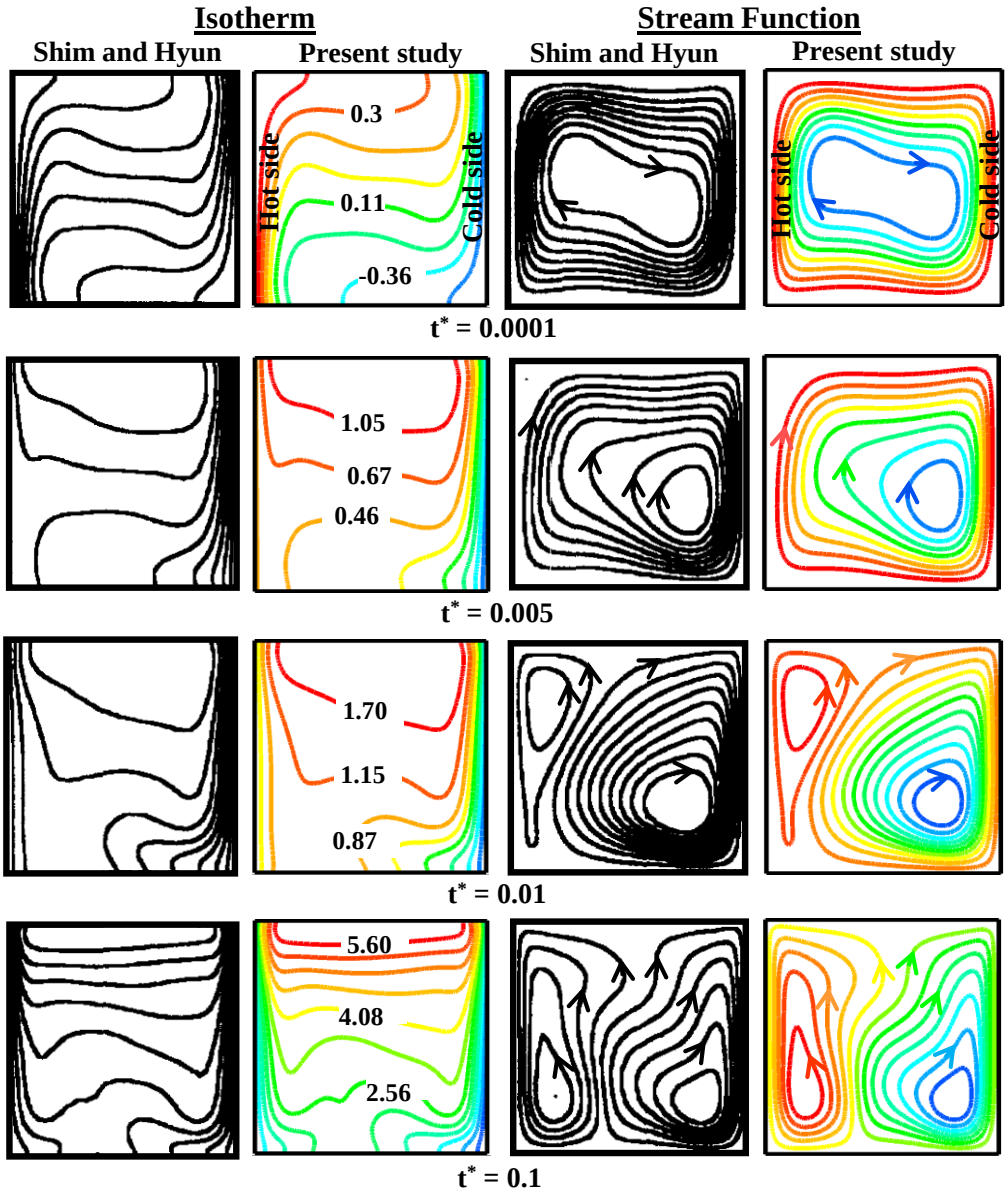

Fig. 5.6. Comparison of stream function and isotherm for a square cavity at $Ra_E = 10^5$ and $Ra_I = 10^7$ against results of Shim and Hyun, (1997).

Table 5.2. Comparison of predicted non-dimensional peak temperature in the square cavity at $Ra_E = 10^5$ and $Ra_I = 10^7$ with Shim and Hyun, (1997).

Temperature (ϕ_{max})		
t^*	Present	Shim and Hyun, (1997)
0.0001	0.5	0.5
0.005	1.04	1.05
0.01	1.70	1.71
0.1	5.59	5.54

5.2.3 APPLICATION BENCHMARK

Validating the Model against the Numerical Results

The sequence and time of occurrence of principal events during TIB in a fuel subassembly predicted in the present study are presented in Table-5.3. The numerical results of TIB analysis reported for prototype fuel subassemblies of CEFR (Wang and Cao, 2007), Phenix (Cadiou and Louvet, 2006) and Superphenix (Murin et al., 1982) are also presented in the same table. It is clear that the present results compare satisfactorily with the reported data, generated using advanced versions of the SIMMER code. It may be highlighted that various results presented in Table-5.3 are not for identical subassemblies or power. However, the results indicate that the duration of various instants are nearly insensitive to the power of the subassembly. The rise in neighboring SA thermocouple reading during TIB in a fuel SA predicted using the present 2-D model is compared with the Superphenix calculations (Murin et al., 1982) in Fig. 5.7. Comparing Figs 3.8 and 5.7, it is clear that the rate of temperature rise is faster when natural convection in fuel pool is considered. Again satisfactory comparison is noticed justifying the acceptability of the present model.

Table 5.3. Instants of occurrence of various events during a TIB.

Process	Time (s)			
	PFBR (Present)	Phenix	Superphenix	CEFR
Start of TIB	0.0	0.0	0.0	0.0
Start of sodium boiling	0.5	0.5	-	1.0
End of sodium boiling	4.0	2.5	3.1	2.5
Start of clad melting	4.3	2.5	5.3	2.5
End of clad melting	8.5	6.0	8.3	6.0
End of fuel melting	16.0	-	21.8	15.0
End of blocked hexcan melting	18.0	18.5	22.3	16.6

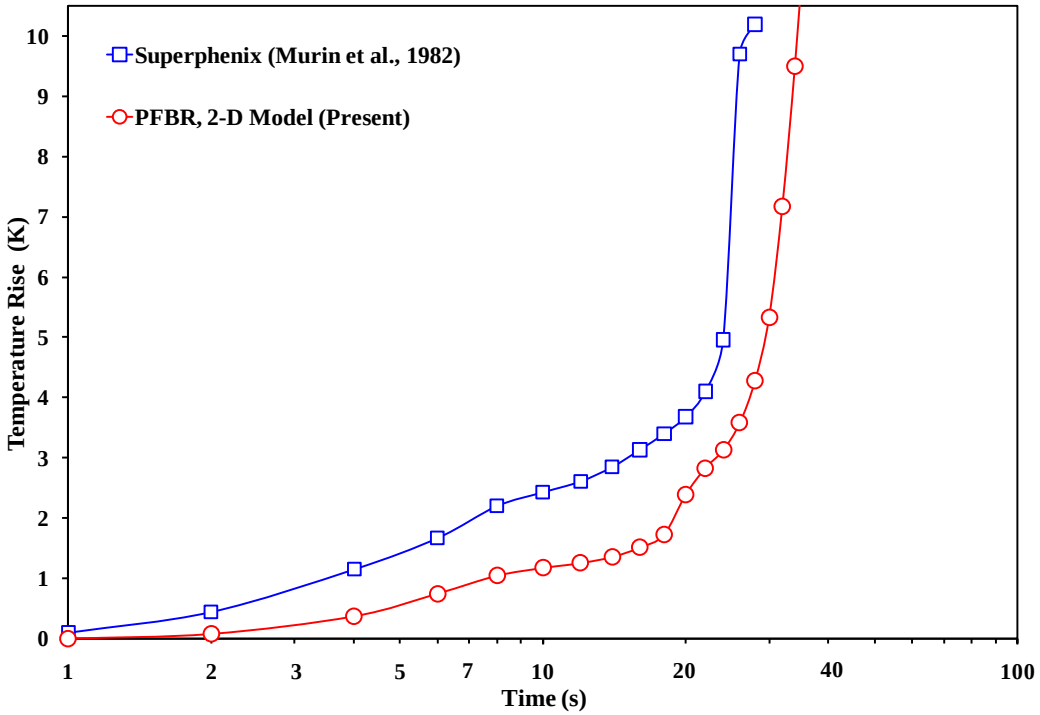

Fig. 5.7. Temporal variation in the neighboring SA thermocouple reading (τ = 4 s) during TIB in a fuel SA.

Validating the Model against the Experimental Results

The results predicted by the present model are compared against the SCARABEE BE+3 experimental results. This experiment was carried out using 37 pin bundle in the SCARABEE in-pile test reactor (Kayser et al., 1998 and Papin, 1989). The fissile height of the pin is 600 mm and the upper and lower blanket heights are 100 mm each. The hollow fuel has pellet inner and outer diameters of 2 mm and 7.1 mm respectively. Clad has inner and outer diameters of 7.37 mm and 8.5 mm respectively. The fuel pins are surrounded by multiple layers. The first layer is a steel wall (called hexcan TH1) of 1 mm thickness followed by an insulating argon gas gap of 1mm, thick steel wall of 5.5 mm (called hexcan TH2), inter-subassembly sodium gap of 1.5 mm, third steel wall of 1 mm thickness (called hexcan TH3), insulating layer and a pressure tube as depicted in Fig. 5.8. The width across the flats of the hexcan TH1 is 62 mm. The pin power and flow details of the test SA are tabulated in the Tables 5.4 and 5.5 respectively.

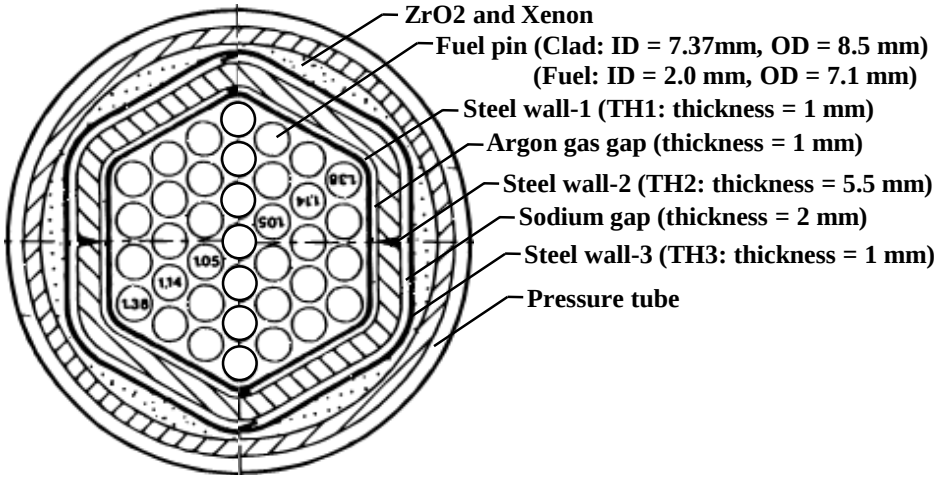

Fig. 5.8. Sectional view of SCRABEE BE+3 test arrangement

Table 5.4. Power details of the SCRABEE BE+3 test setup.

Parameters	Row Number			
	1	2	3	4
No. of pins	1	6	12	18
Average linear power, W/cm	281	289	319	389
Normalized power	1.0	1.032	1.136	1.385

Table 5.5. Flow details of the SCRABEE BE+3 test setup.

Parameter	Value	
	Before TIB	During TIB
SA sodium flow rate, m^3/s	0.00725	0
SA sodium velocity, m/s	6.0	0
SA inlet sodium temperature, K	623	-
Inter SA sodium flow rate, m^3/s	0.00125	0.0018
Inter SA sodium velocity, m/s	2.2	3.2
Inter SA inlet sodium temperature, K	623	623

The test SA is geometrically modeled by an equivalent 2-D axi-symmetric circular domain with 6 radial and 80 axial meshes. The 37 pins arranged in 4 rows are represented by four zones (one central pin region with the associated sodium channel and 3 rows of pins with the associated

sodium channels). The hexcan walls TH1, TH2 and argon gas gap represent the fifth zone. The inter-wrapper sodium and TH3 hexcan wall represent the sixth zone as shown in Fig. 5.9. The steady state temperature distribution in the pin bundle is calculated before carrying out the transient calculations. In experiment, thermocouples TC15, TC17 and TC19 represent cladding temperatures, whereas TC16 and TC18 represent the sodium temperatures. In the calculation, the temperature of sodium, clad, fuel and hexcan walls are represented by their respective mesh number.

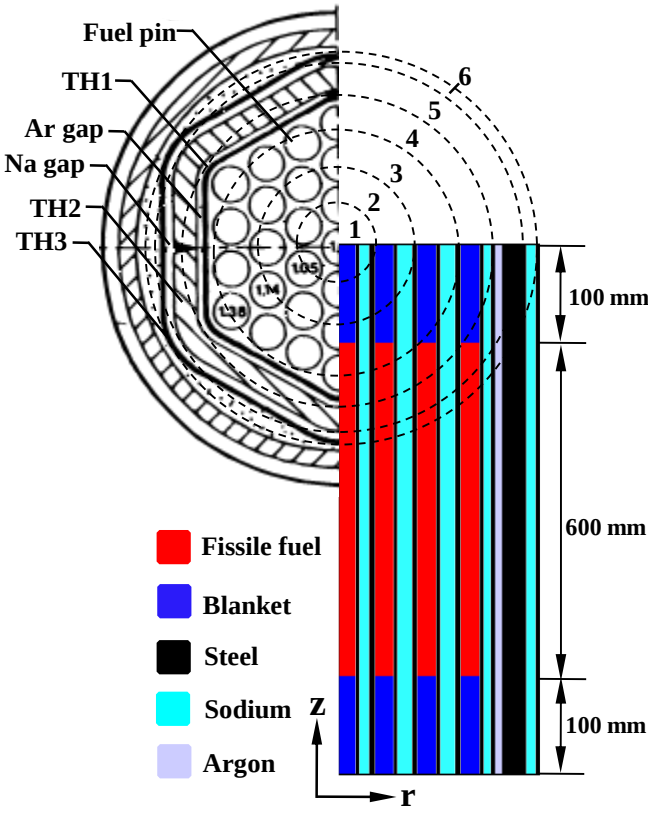

Fig. 5.9. Geometric model of SCRABEE BE+3 test arrangement.

The calculated steady state temperature distribution in the axial direction of sodium and clad are compared with experimental data in Figs. 5.10 and 5.11 respectively. The calculated sodium temperature distribution is in good agreement with the experimental data except for the outer ring (4^{th} ring), where the calculated temperature is over estimated. This is because of radial

power profile in BE+3 test section, which has higher power at the peripheral region than in the core region. However, in the experiment, sodium temperatures at central and peripheral regions are nearly identical. This is because the cross-sectional sodium flow area per pin in peripheral region is more than in central region which enhances the cooling at peripheral region, nullifying the effect of enhanced heating at peripheral region (Yamano et al., 2014). But in the present calculation the flow cross-section area per pin is maintained same throughout the pin bundle, which is the reason for overestimation of temperature at peripheral region. However these variations do not have any significant effect on the overall results of the present study.

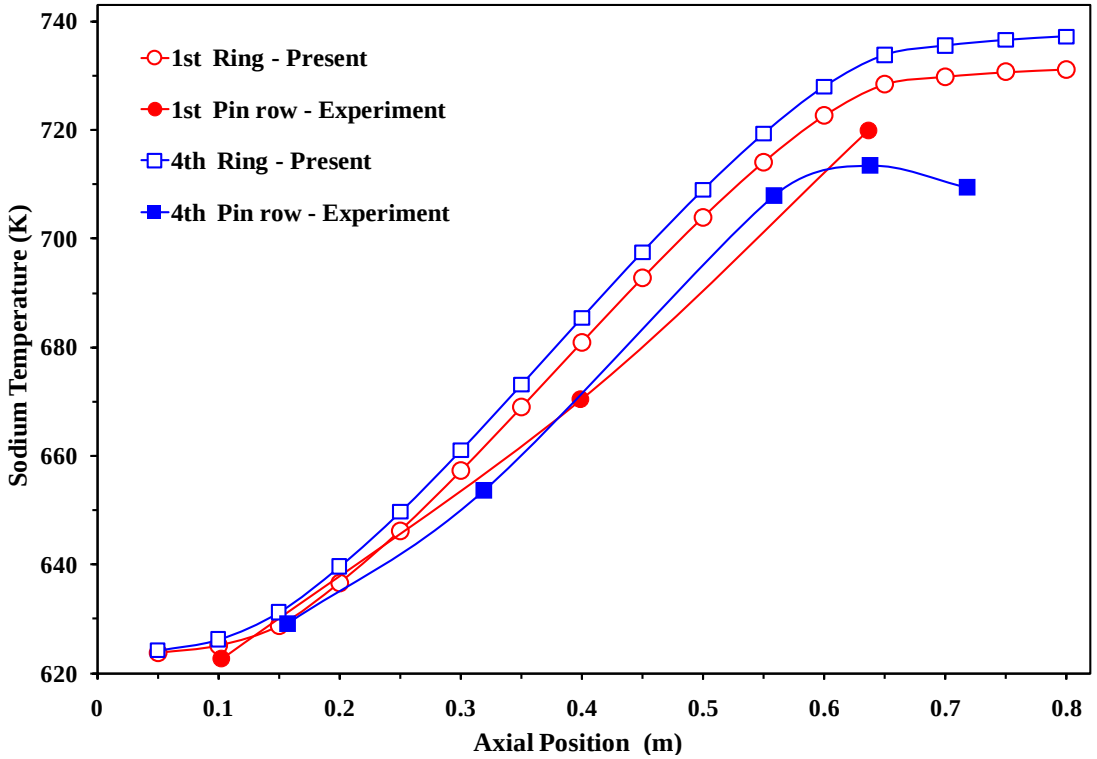

Fig. 5.10. Comparison of calculated sodium temperature distribution along the axial direction with the experimental data before TIB.

In Fig. 5.11, it can be seen that the calculated cladding temperatures along the axial direction are higher than the experimental values which are very close to sodium temperature. This is because the thermocouples measuring the clad temperatures were mounted near the outer

surface of cladding which reads the temperature of outer surface of cladding (Yamano et al., 2014). But the present model gives the temperature calculated at mid wall of the cladding. The temperature difference across the thickness is expected to be ~ 62 K. Considering this fact, the comparison is good.

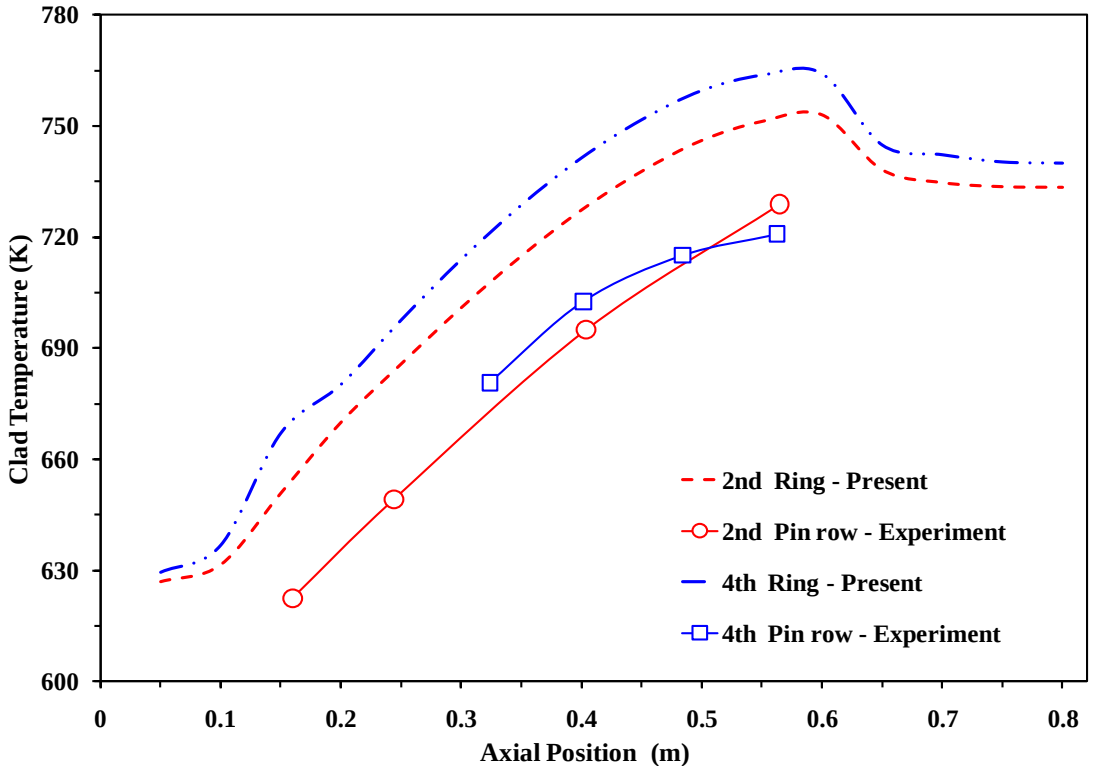

Fig. 5.11. Comparison of calculated cladding temperature distribution along axial direction with the experimental data before TIB.

Transient was initiated in the experiment by completely stopping the sodium flow to the pin bundle. The calculated steady state temperature distribution of pin bundle with sodium flow was the initial condition to initiate the transient in the calculation. During transient, various components of the pin bundle undergo temperature change as well as phase change. The calculated temperature variations of sodium and clad in the third ring of the pin bundle at mid-plane (3, 40) are compared with the experimental results in Fig. 5.12. Sodium boiling is noticed

early in the calculation at about 1.8 s and completes at about 4.5 s. The cladding temperature increases gradually during early transient and remains almost constant during sodium boiling. After sodium dry-out, the clad temperature starts rising and attains melting point at about 5.5 s resulting in clad failure. The sequence and time of occurrence of various events such as start and end of sodium boiling, and clad melting predicated in the present calculations showed the same tendency as observed in the experiment.

The calculated TH1 wall temperatures at 200 mm, 300 mm and 450 mm above the core bottom are compared with corresponding thermocouple readings TC41, TC42 and TC43 in Fig. 5.13. The TH1 wall temperature gradually rises during early transients and remains constant during sodium boiling. After sodium dry out, temperature of TH1 wall starts rising gradually due to heat transfer from the molten steel, draining down after clad melting. At a calculated time of about 9.5 s, failure of TH1 wall is noticed at the distance of about 200 mm above the core bottom due to molten steel attack. After start of TH1 wall melting, the thermocouple TC41 is expected to lose contact with molten steel. Due to this, the temperature of TC41 decreases. However, decrease in temperature is observed in thermocouples TC42 and TC43 before start of TH1 wall melting. This may be due to sodium voiding, which decreases the heat transfer rate between the fuel pins and TH1 wall. Further, these thermocouples do not come in contact with molten fuel as they are located at higher elevation. The calculated TH1 wall failure position is in good agreement with the experimental data. The calculated TH1 wall failure time of 9.5 s is very close to experimental time of 9.1 s. Therefore, calculated time and position of TH1 wall failure are in good agreement with the experimental data, demonstrating the acceptability of the present model.

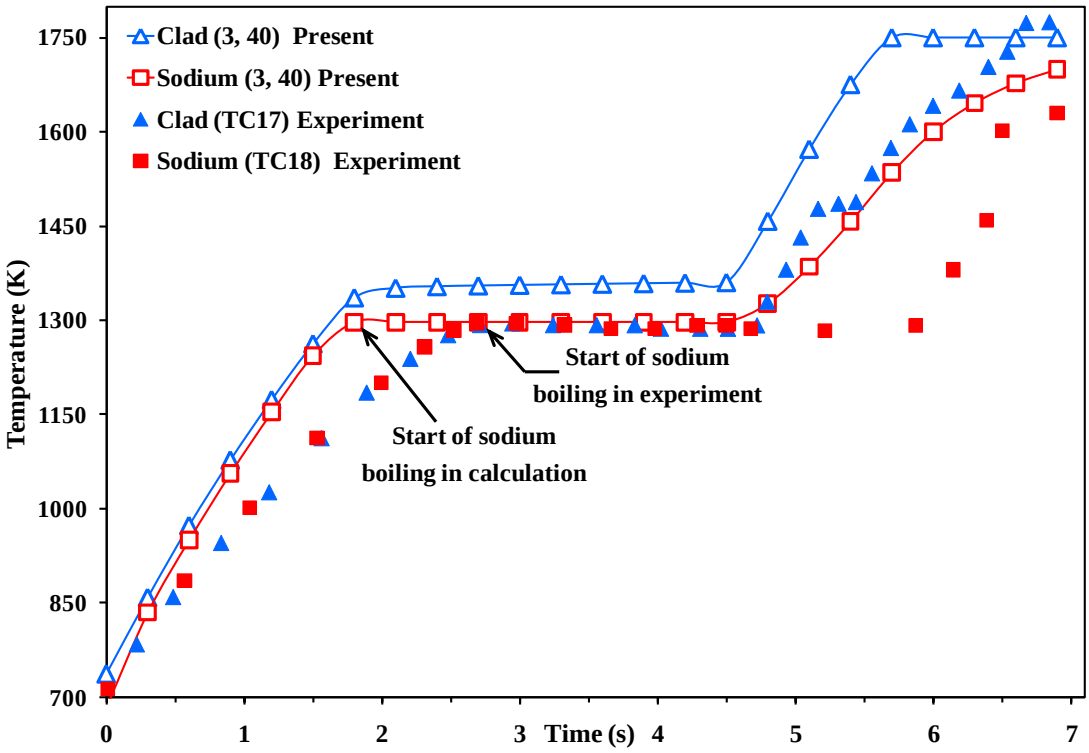

Fig. 5.12. Comparison of calculated temperature of sodium and cladding in third ring with the experimental data during TIB.

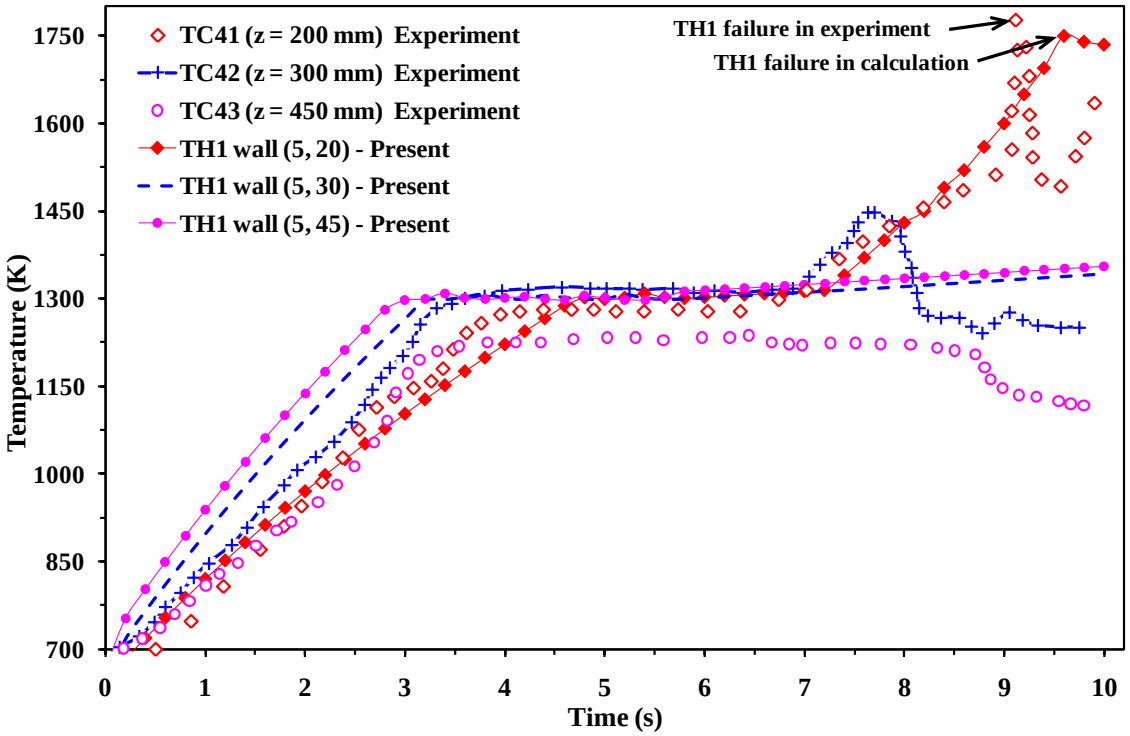

Fig. 5.13. Comparison of calculated TH1 wall temperature with the experimental data during TIB.

5.3 RESULTS AND DISCUSSION

Detailed investigation of TIB accident scenario in a single fuel SA of a 500 MW sodium cooled fast reactor is carried out. The fuel SA with 217 fuel pins has a thermal power of 8 MW at normal operation. The initial sodium mass flow rate is 35.8 kg/s. Temperature of sodium at inlet and outlet of the SA are 673 and 849 K respectively. Flow and geometric details are tabulated in Table 5.1. Before initiating the actual transient calculations, the temperature distribution in fuel, clad, sodium and hexcan of central and neighboring SA operating at normal reactor operation condition are calculated. Calculated steady state temperatures are imposed as initial condition to initiate the transient analysis.

5.3.1 STEADY STATE ANALYSIS

Transient calculations are carried out using reactor data obtained from the basic core calculations without any perturbation. After ~60 s of transient duration, the steady condition is reached. The calculated steady state temperature variation of sodium in the axial direction during normal operation (before initiation of TIB) is depicted in the Fig. 5.14.

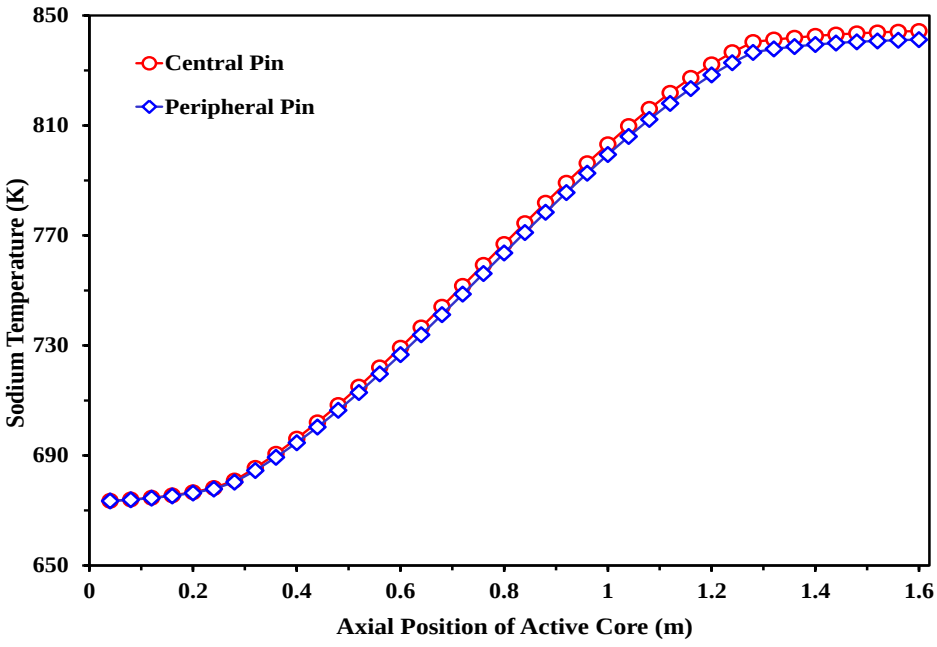

Fig. 5.14. Initial temperature variation of sodium along the axial direction of the active region before TIB.

Sodium at central and peripheral regions of the SA experience nearly similar temperature variation. Calculated steady sodium temperature at the SA outlet is ~ 845 K, which is in line with the energy balance calculations. Further, the calculated steady state temperature of sodium and clad at various axial positions of the pin are compared with 3-D computational Fluid Dynamics results of Naveen and Velusamy (2016) in Table 5.6. The comparison is satisfactory, justifying the acceptance of the steady results arrived from a transient route.

Table 5.6. Comparison of calculated steady state results with 3-D Computational Fluid Dynamic results (Naveen and Velusamy, 2016).

Parameters	Vertical position	Mean Temperature (K)	
		Present calculations	3-D CFD results (Naveen and Velusamy, 2016)
Sodium in active region	Top (z = 1600 mm)	846	842
	Middle (z = 800 mm)	760	753
	Bottom (z = 0.00 mm)	673	670
Clad in active region	Top (z = 1600 mm)	853	851
	Middle (z = 800 mm)	780	766
	Bottom (z = 0.00 mm)	673	670

A gradual rise in clad temperature is observed along the axial direction of central and peripheral pins. The clad attains peak temperature at just below the top of the active region and starts decreasing over rest of the length (Fig. 5.15). From Figs. 5.14 and 5.15, it is observed that the temperatures of clad and sodium for the peripheral row are lower than that for central row. It may be highlighted here that the cross-sectional area of the coolant channel per pin is maintained same for all the rows, but the peripheral region is colder than other region. This is due to the external cooling effect caused by inter-wrapper forced coolant flow. As expected, similar difference is also noticed in the peak temperatures of central and peripheral fuel pellets, depicted in Fig. 5.16.

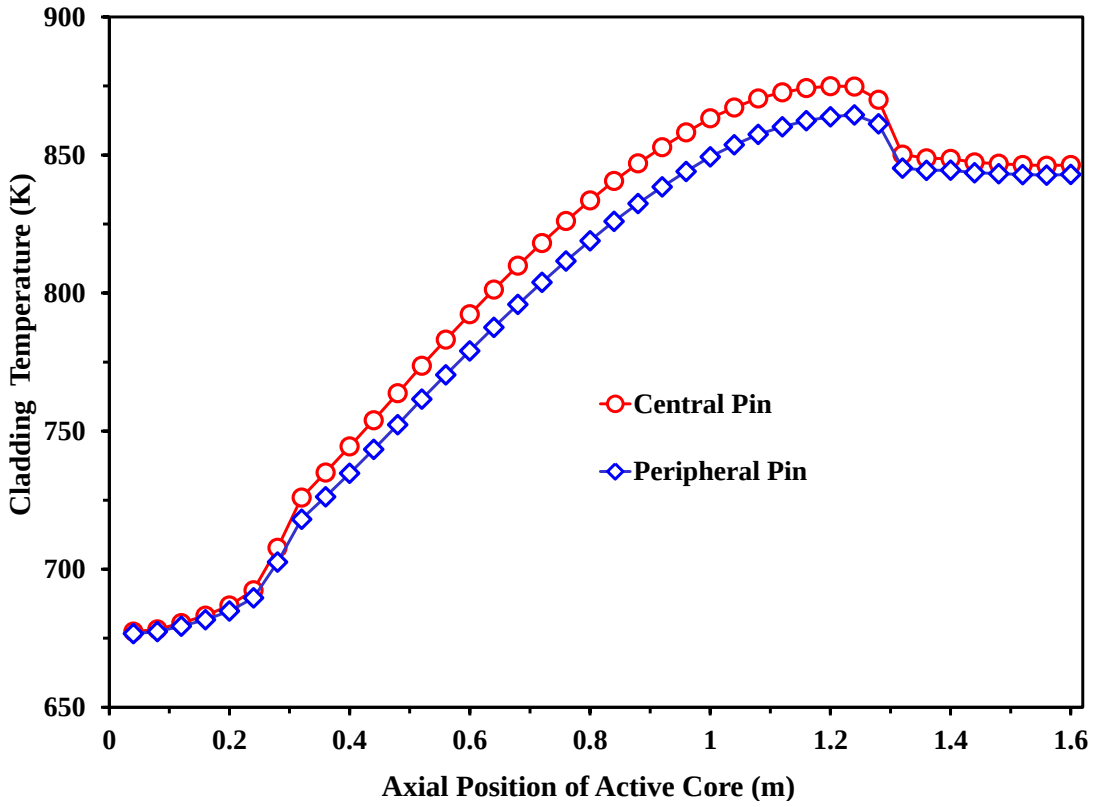

Fig. 5.15. Initial temperature variation along axial direction of the cladding before TIB.

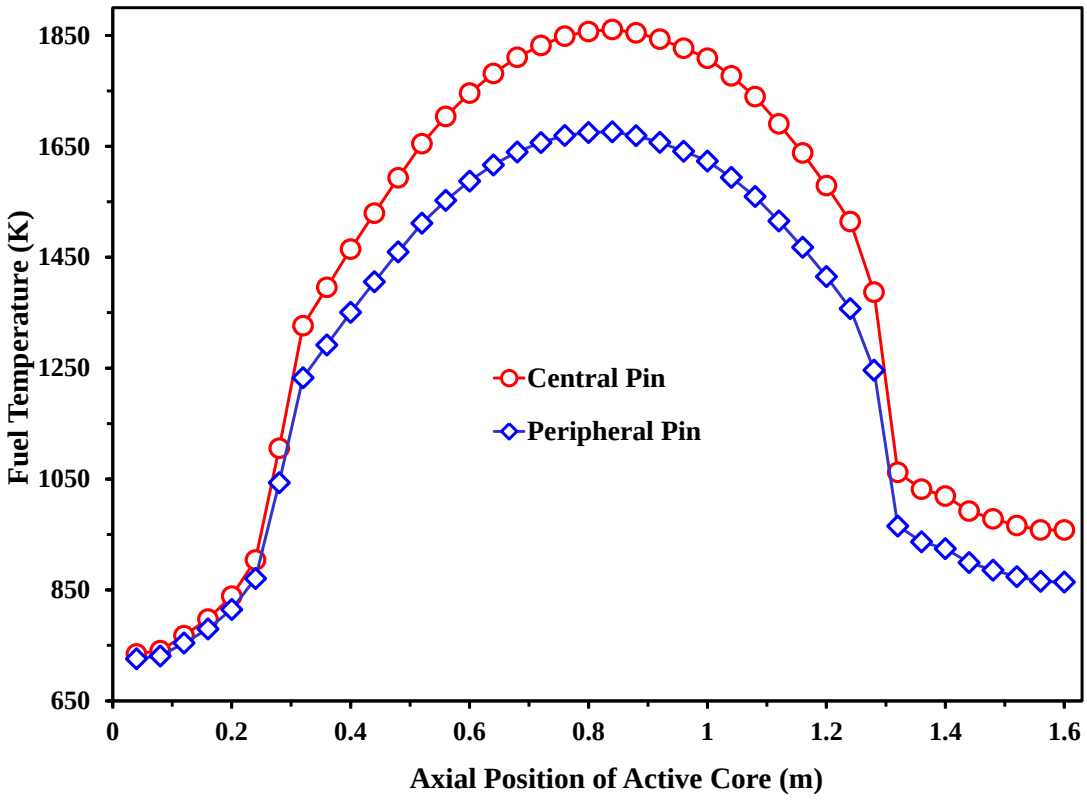

Fig. 5.16. Initial temperature variation along axial direction of the fuel pellet before TIB.

The calculated steady state temperature variation of inter-wrapper sodium flow and hexcans of central SA and neighboring SA along the axial position of the active region are depicted in Fig. 5.17. The hexcan walls of central and neighboring SA experience nearly identical temperature variation before initiation of TIB.

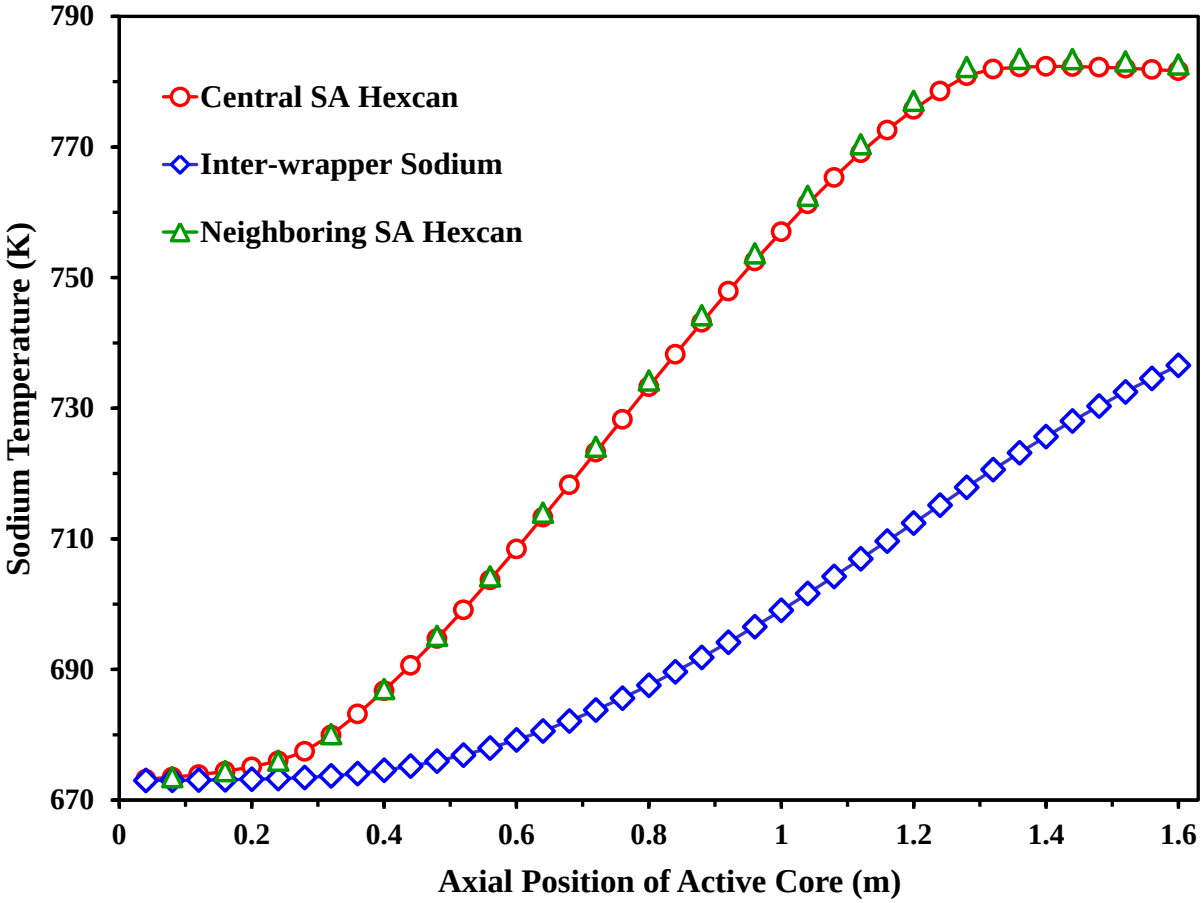

Fig. 5.17. Initial temperature variation in the hexcans and inter-wrapper sodium along the axial direction of the active region before TIB.

The inter-wrapper sodium, which receives nearly the same amount of heat from the central and neighboring SAs has a continuous rise in its temperature in the axial direction and attains peak value at the top of active region, which is less than the peak temperature of the sodium flowing inside the SA. The temperature distribution predicted in various parts of the SA during normal operation is depicted in the Fig. 5.25a (at t = 0 s).

5.3.2 TRANSIENT ANALYSIS

The transient phenomenon due to total instantaneous blockage in a SA operating at full power is initiated by reducing the SA sodium mass flow rate to zero instantaneously. During the transient, temperature of the blocked SA starts rising, followed by sodium boiling. The temperature distribution along the axial direction for (i) fuel, clad and sodium in the central pin region of the blocked SA and (ii) hexcan of blocked SA, inter-wrapper sodium and neighboring SA hexcan before TIB and 2 s after TIB are as shown in Figs 5.18 and 5.19 respectively. In Fig. 5.18, it can be noticed that there is large increase in sodium and clad temperatures to the tune of ~400 K, 2 s after the initiation of TIB. However, the temperature rise in fuel is only about 100 K during the corresponding instant. This is due to the fact that the thermal capacity of fuel is much higher than that of clad and sodium. It may be noted that the ratio of heat capacity of fuel pin compared to that of clad is around 4, indicating the validity of the results. In Fig. 5.19, it is observed that during normal operation, the hexcan temperatures of the central and neighboring SA peak at the outlet. This is due to the forced cooling of the SA by sodium flow along the axial direction. But, during initial stage of the TIB, the heat removal from the blocked SA is only by phase changes of the materials inside the SA and inter-subassembly heat transfer. Due to this imbalance between heat generation and heat removal, a continuous rise in temperature of fuel, clad and sodium within the blocked SA takes place. Thus the temperature difference between center and peripheral regions of the SA increases leading to enhanced inter-subassembly heat transfer. As the power distribution in a pin is highly non-uniform with peaking at the center, radial heat flux also peaks at the center of the active region. This leads to gradual shift in the location of peak temperature from the exit of the SA towards the center of the active region in the blocked SA. But, due to continued cooling of the neighboring hexcan, its maximum temperature occurs near the outlet during TIB.

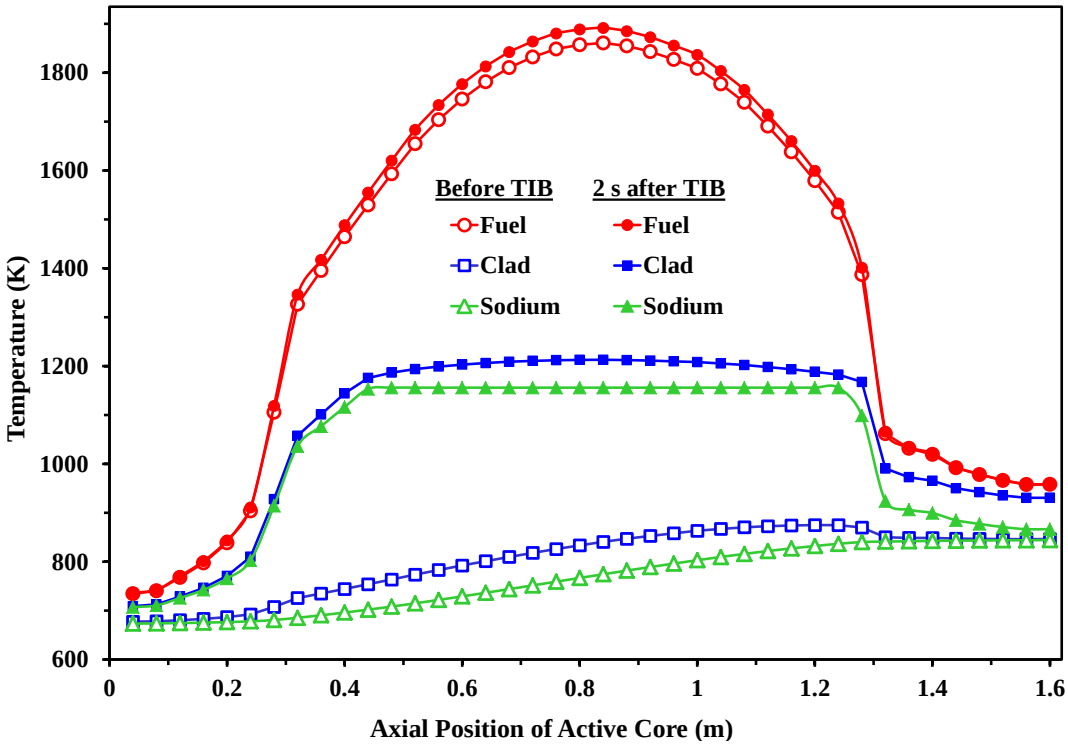

Fig. 5.18. Temperature evolution of fuel, clad and sodium in the center region of the central (blocked) SA along the axial direction of the active region before TIB and 2 s after TIB

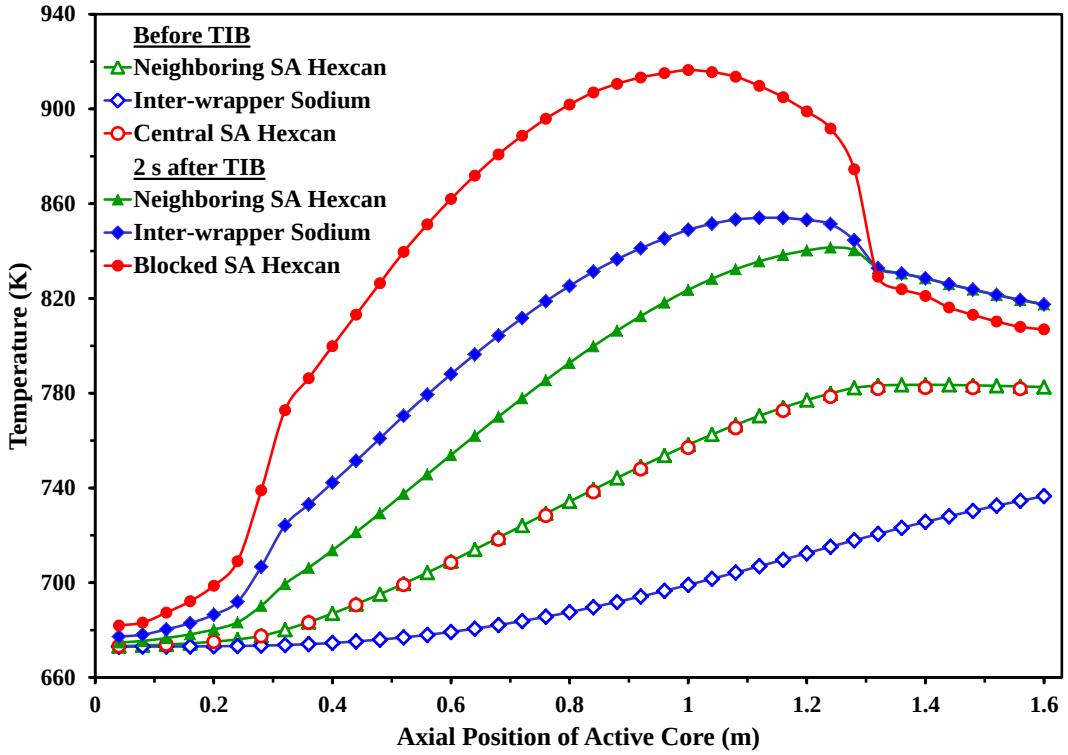

Fig. 5.19. Temperature evolution of central SA hexcan, inter-wrapper sodium and the neighboring SA hexcan along the axial direction before TIB and 2 s after TIB.

Sodium boiling is first observed at ~0.5 s after TIB, in the central pin region at the top of the active zone (Fig. 5.20). Further, boiling propagates rapidly in both axial and radial directions and reaches the peripheral region at about 0.8 s after initiation of the TIB as seen in Fig. 5.20. Sodium voiding in the blocked SA starts at about 2 s in the central region of the SA (see Fig. 5.25a, at t =2 s) and propagates rapidly inducing sodium dry-out at about 4 s after start of TIB.

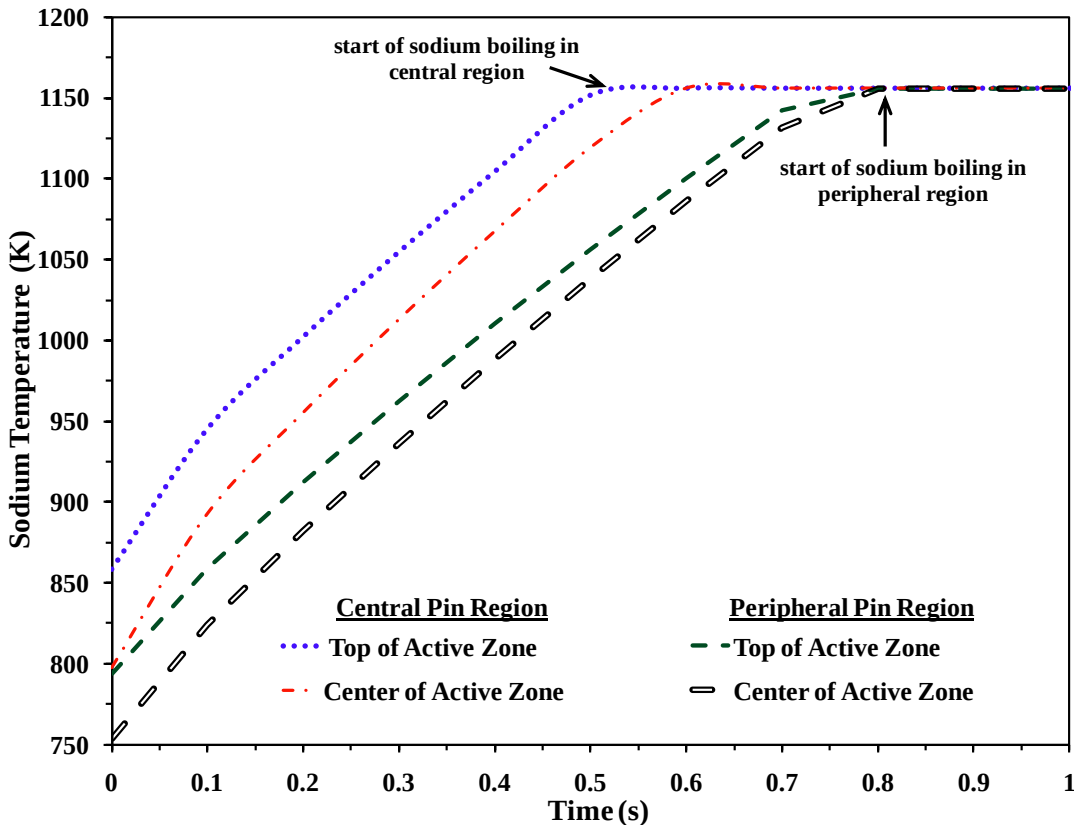

Fig. 5.20. Temperature evolution in sodium at different planes of the blocked SA during TIB.

Sodium dry-out in the blocked SA is immediately followed by clad melting. Sodium vapor in the SA creates adiabatic environments around the cladding surface, causing sudden rise in clad temperature. Clad failure is first noticed in the central pin at the mid of the active height at about 4.2 s after TIB (see Figs. 5.21 and 5.25a). Further, clad in the peripheral region starts melting at mid of the active height at about 4.9 s. The clad melting in the blocked SA completes by ~8.5 s after start of TIB. The evolution of temperature from sodium void to clad melting and start of fuel break-up can be observed in Figs. 5.25a and 5.25b.

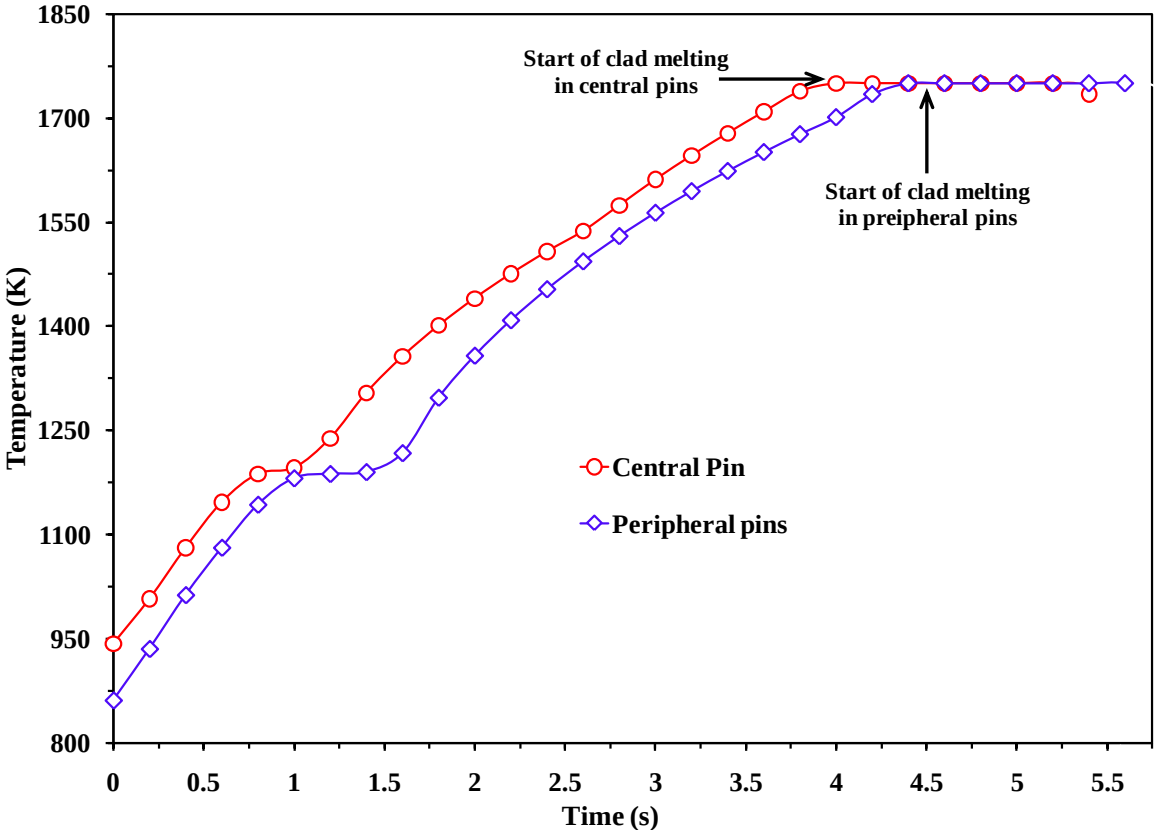

Fig. 5.21. Temperature evolution in clad at mid-plane of the blocked SA during TIB.

Fuel break-up is first noticed in the central pin at the center of the active zone at about 11.2 s and proceeds further to neighboring rows. Peripheral row fuel break-up is observed at about 13.5 s after TIB as can be seen in Figs. 5.22 and 5.25b. The fuel melting and the formation of the fuel pool over the steel blockage in the blocked SA completes within ~17 s after the initiation of the TIB.

The continuous rise in the temperature of fuel, clad and sodium during TIB in the SA results in the inter-subassembly heat transfer through the blocked SA hexcan, inter-wrapper sodium and neighboring SA hexcan. The hexcan wall, exposed to blocked SA sodium on one side and inter-wrapper sodium on the other side experiences monotonic temperature rise as seen in Fig. 5.23. In the same figure, it can be seen that there is a dip in the temperature of hexcan at planes z = 0.8 m and z = 0.46 m at about 7 s and 10.5 s respectively after the commencement of the TIB.

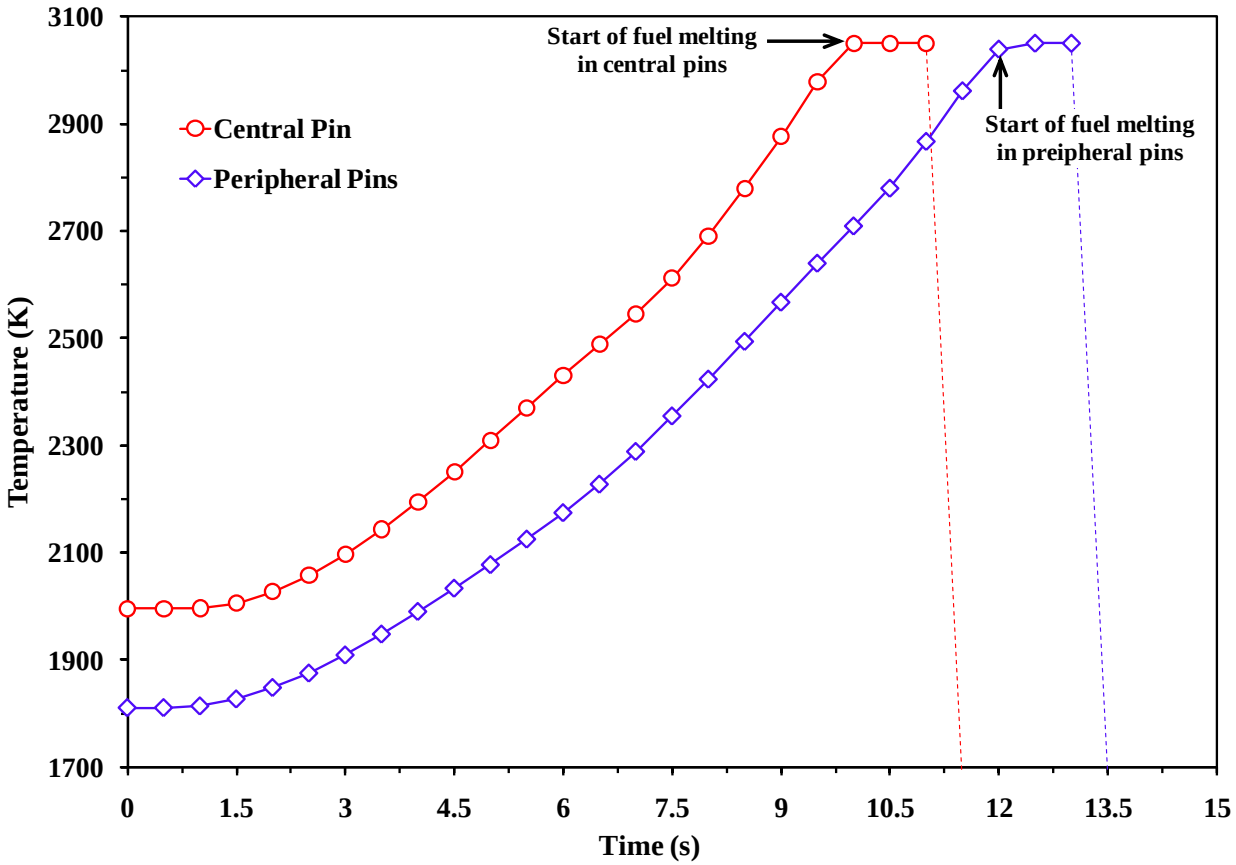

Fig. 5.22. Temperature evolution in fuel at mid-plane of the blocked SA during TIB.

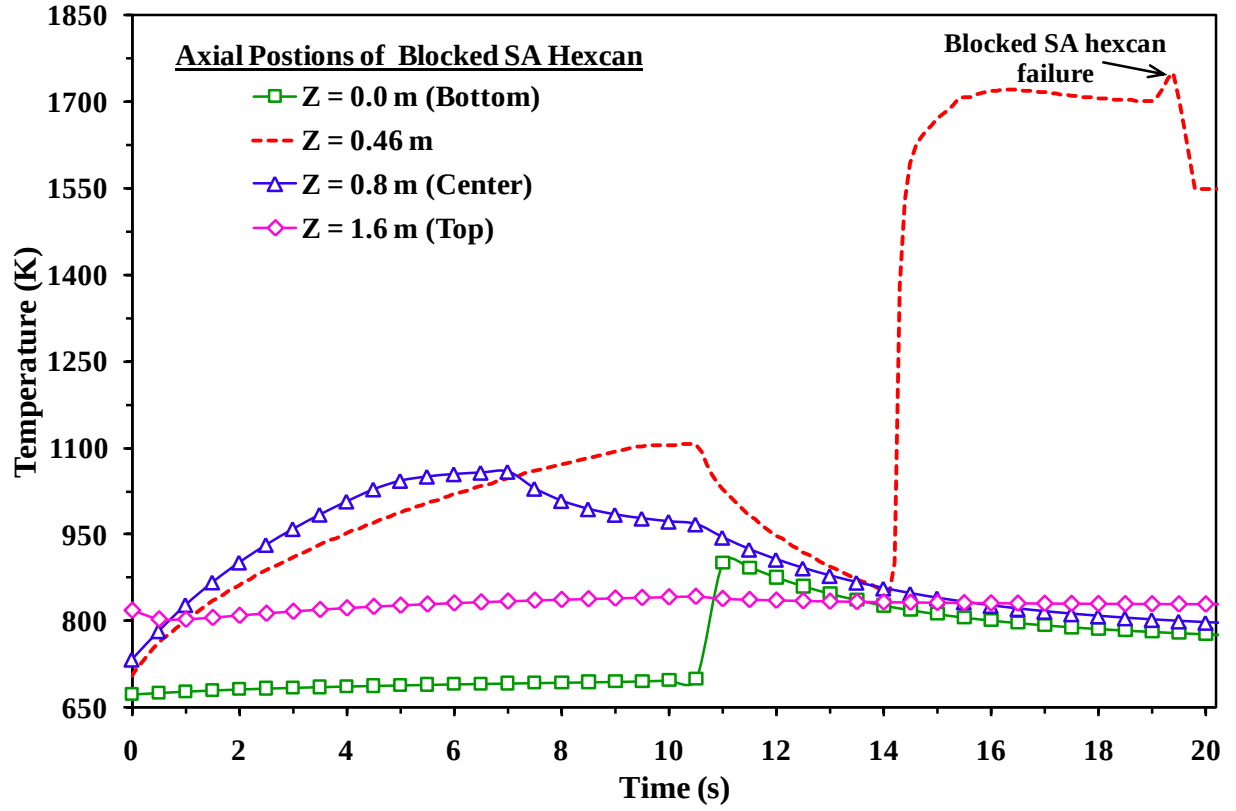

Fig. 5.23. Temperature evolution of blocked SA hexcan at various axial positions during TIB.

This is due to local sodium voiding at peripheral region, adjacent to blocked SA hexcan. Further, sodium dry out in peripheral region is immediately followed by clad melting. The molten steel draining down towards the lower axial blanket comes in contact with blocked SA hexcan, which leads to sudden rise in temperature at lower region of hexcan (z = 0.0 m) at about 10.5 s (see, Fig. 5.23). During the molten pool formation, the hexcan of the blocked SA comes in contact with molten fuel, which leads to sudden rise in its temperature as seen in Fig. 5.23 at plane z = 0.46 m at about 14.2 s. This leads to melting of hexcan wall layer by layer and later at about 18.7 s after start of the TIB, the blocked SA hexcan fails at just above lower axial blanket region (z = 0.46 m) as seen in Figs. 5.23 and 5.25b (t = 18.7 s).

After the failure of blocked SA hexcan, the melt front advances radially towards the neighboring SA. The molten steel resulting from the hexcan melting enters the inter-wrapper region and blocks the inter-wrapper gap which prevents the escape of molten fuel through inter-wrapper gap as seen in Fig. 5.25b (at t =18.7 s). As a consequence of this, an enclosed fuel pool is formed which is surrounded by six neighboring SA (Fig. 5.25b, at t =20.1 s). A thin layer of fuel in the melt front undergoes cooling and solidification due to sufficient heat loss during advancement towards the neighboring SA. Further, a fuel crust is formed when melt front comes in contact with relatively cold neighboring hexcan wall. The resulting fuel crust at the surface of the hexcan acts as thermal insulator due to its poor thermal conductivity and delays the melting of hexcan, and increases the temperature of the fuel pool. When the pool attains a bulk temperature of 3200 K, the natural convections is initiated. The instantaneous temperature field and material distribution during natural convection within in the fuel pool are depicted in Fig. 5.24. It is observed that a major circulation cell driven by large temperature difference between the core and side wall of the pool is formed at the bottom of the pool and is followed by formation of secondary rolls in the upper region, exhibiting development of natural convection currents within in the pool. However, large thermal stratification effects can be seen in the pool,

with hot liquid settling at the top and increasing the local heat flux along the pool height. As a consequence of this, the neighboring SA hexcan starts melting at the top and proceeds towards bottom as seen in Fig. 5.25b (at t = 38 s). The heat flux emerging from the pool increases with the time, intensifying the melting speed of hexcan at the top of the SA. The variation in the residual thickness of hexcan at the top of neighboring SA during TIB is depicted in Fig. 5.26.

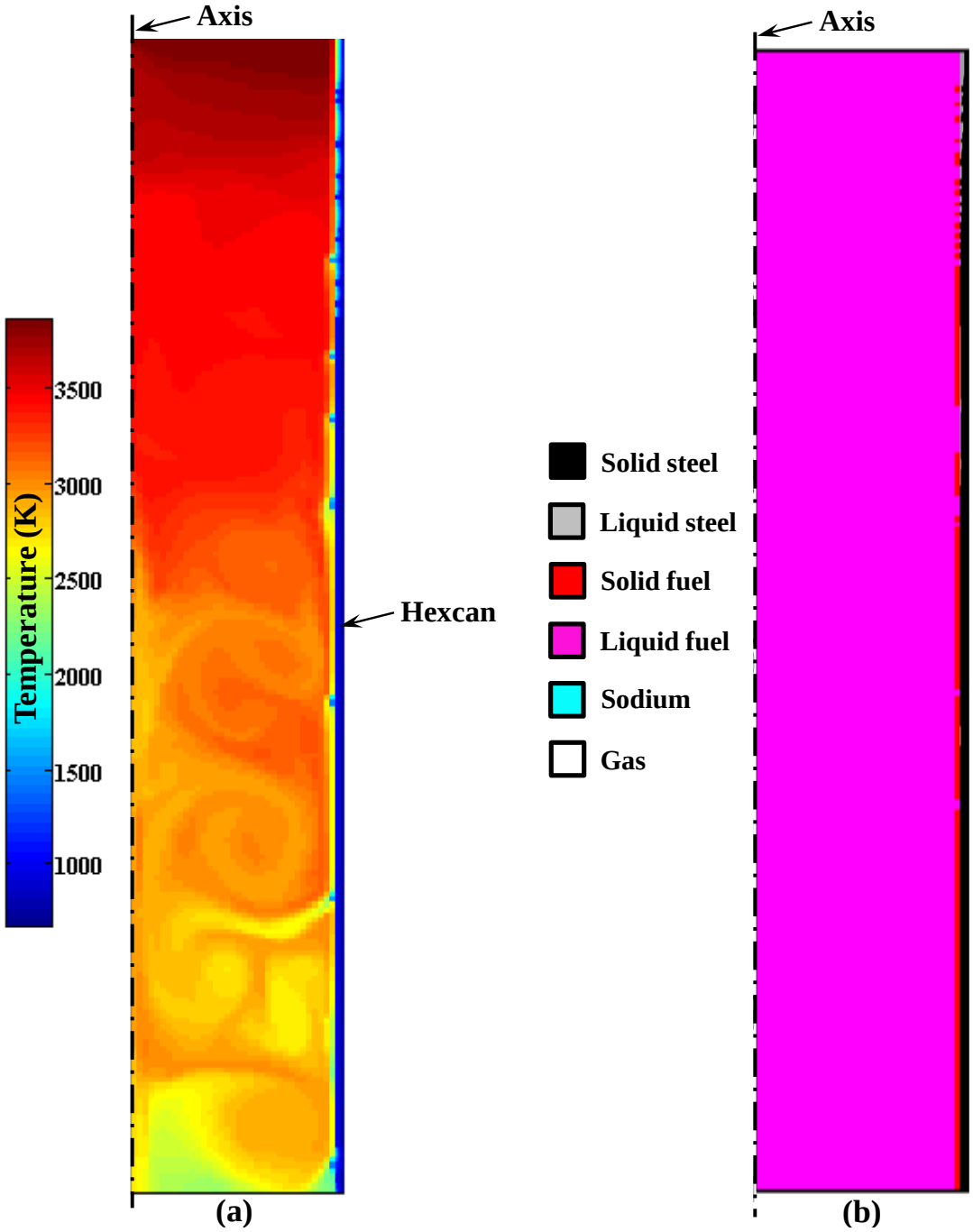

Fig. 5.24. Instantaneous (a) temperature field and (b) material distribution during molten fuel attacking neighboring SA hexcan (at t = 26.3 s).

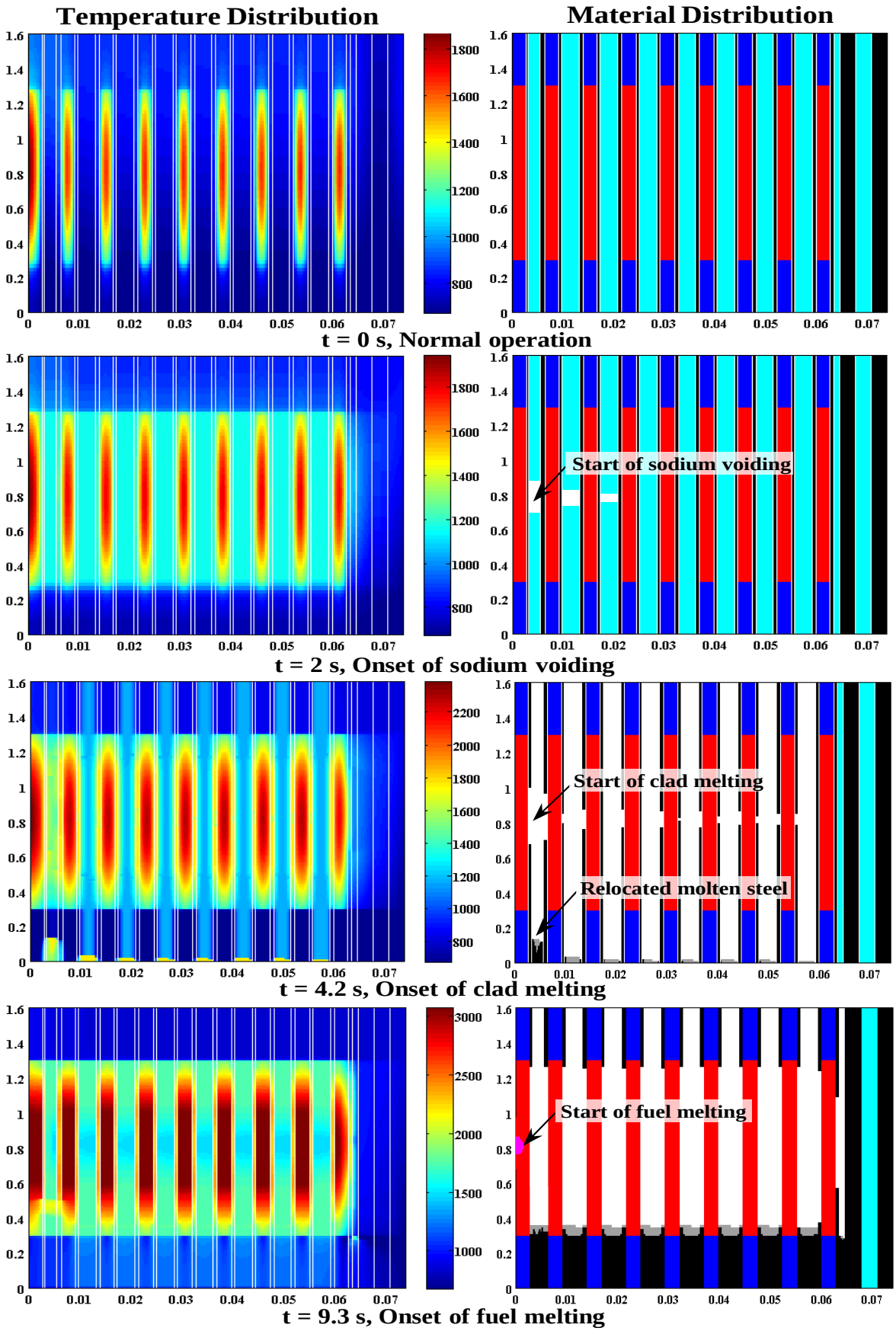

Fig. 5.25a. Temperature and material distributions (see, the legend of Fig. 5.24b) during TIB before fuel pool formation (height of the fuel pin is ordinate and radial distance from center of the SA is abscissa).

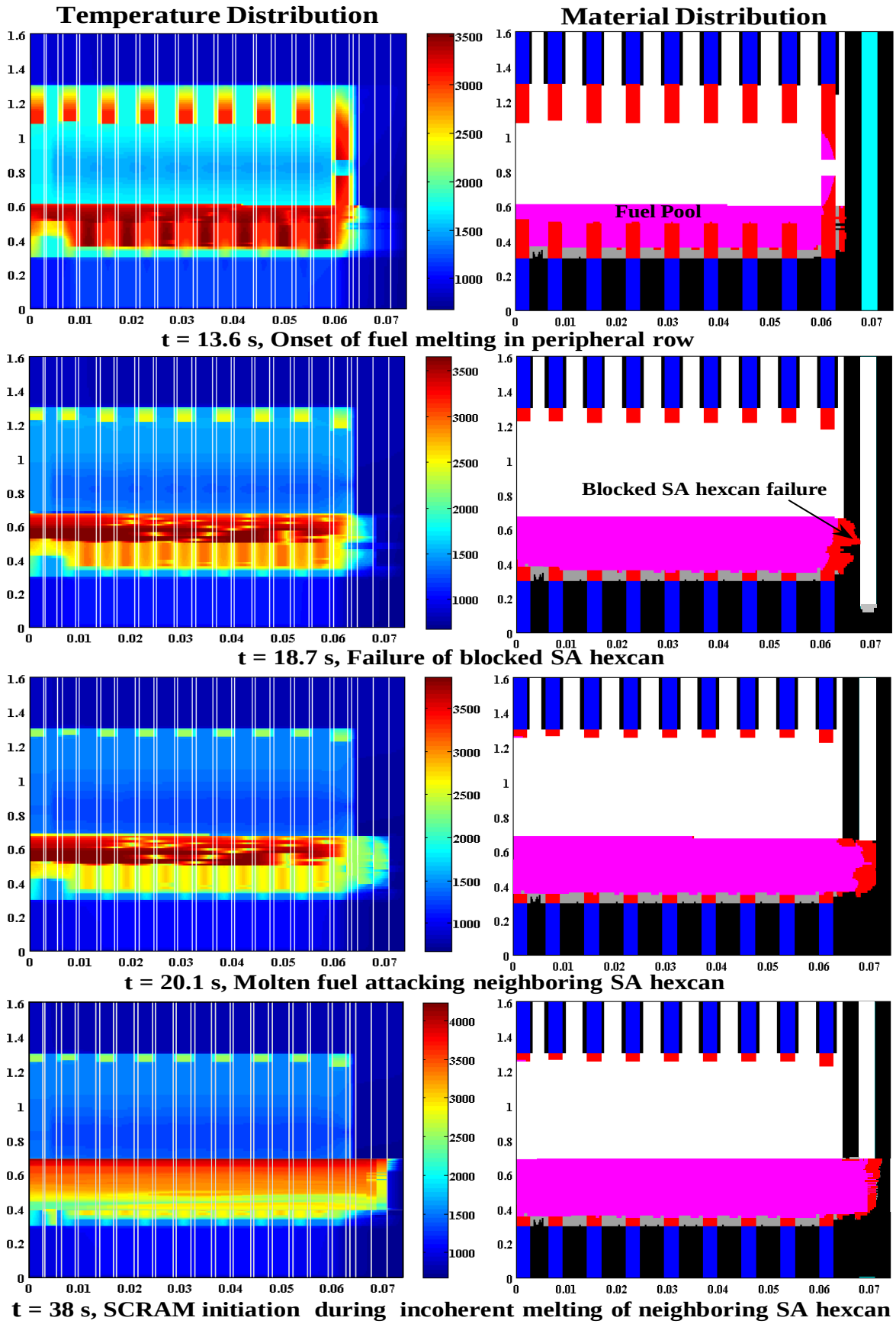

Fig. 5.25b. Temperature and material distributions (see, the legend of Fig. 5.24b) during fuel pool formation (height of the fuel pin is ordinate and radial distance from center of the SA is abscissa).

The temperature rise of neighboring SA sodium is gradual for a few seconds after the start of TIB (Fig. 5.26, thermocouple time constant (τ) = 0.0 s), and it starts falling later at about 6.5 s due to sodium dry-out in the blocked SA. Further, no considerable rise in temperature is noticed till failure of blocked SA hexcan. Later at about 19 s there is rapid rise in temperature, which is due to high heat flux on the neighboring SA hexcan during initial contact of fuel pool. However, the rate decreases after ~ 21 s due to freezing of fuel layers. Following this, a gradual increase in sodium temperature is noticed, which is due to increase in heat transfer consequent to developing natural convection within in the pool. The thermocouple reading due to temperature rise of sodium flowing in the neighboring SA is calculated considering various thermocouple time constants. It can be seen in Fig. 5.26, a thermocouple temperature rise of 10 K (threshold for reactor SCRAM) is recorded at ~ 38 s after start of TIB for τ = 8 s. The corresponding residual thickness of neighboring hexcan is 52% indicating that the TIB occurrence can be detected during molten fuel attacking the neighboring SA hexcan by monitoring the neighboring SA sodium outlet temperature. It is to be noted here that in the present study damage assessment is done by considering only the thermal effect. The effect of creep and internal pressure are not accounted while assessing the damage to SA.

Effect of Thermocouple Time Constant

The thermocouples located at SA outlet to monitor the sodium temperature, have a finite response time as explained earlier (Chapter 3, Section 3.1.1). The effect of thermocouple response time, viz., 0.0, 2.0, 4.0, 6.0 and 8.0 s on early detection of TIB is analyzed in this section. Study has been carried out with fuel pool of 8 MW thermal power. For nil response time, thermocouple reads 10 K at 32 s after start of TIB and the residual thickness of neighboring hexcan at this instant is ~ 90%. Whereas for 6 s response time, neighboring SA thermocouple

reads temperature rise 10 K at about ~36 s with neighboring hexcan residual thickness of ~ 67% demonstrating that thermocouple with low response time plays a very significant role in early detection of TIB with better residual thickness of hexcan (Fig. 5.26). It is to be noted here that above demonstration also highlights one of the limitations of 1-D model over 2D model in bringing out the significance of thermocouple response time on early detection of TIB.

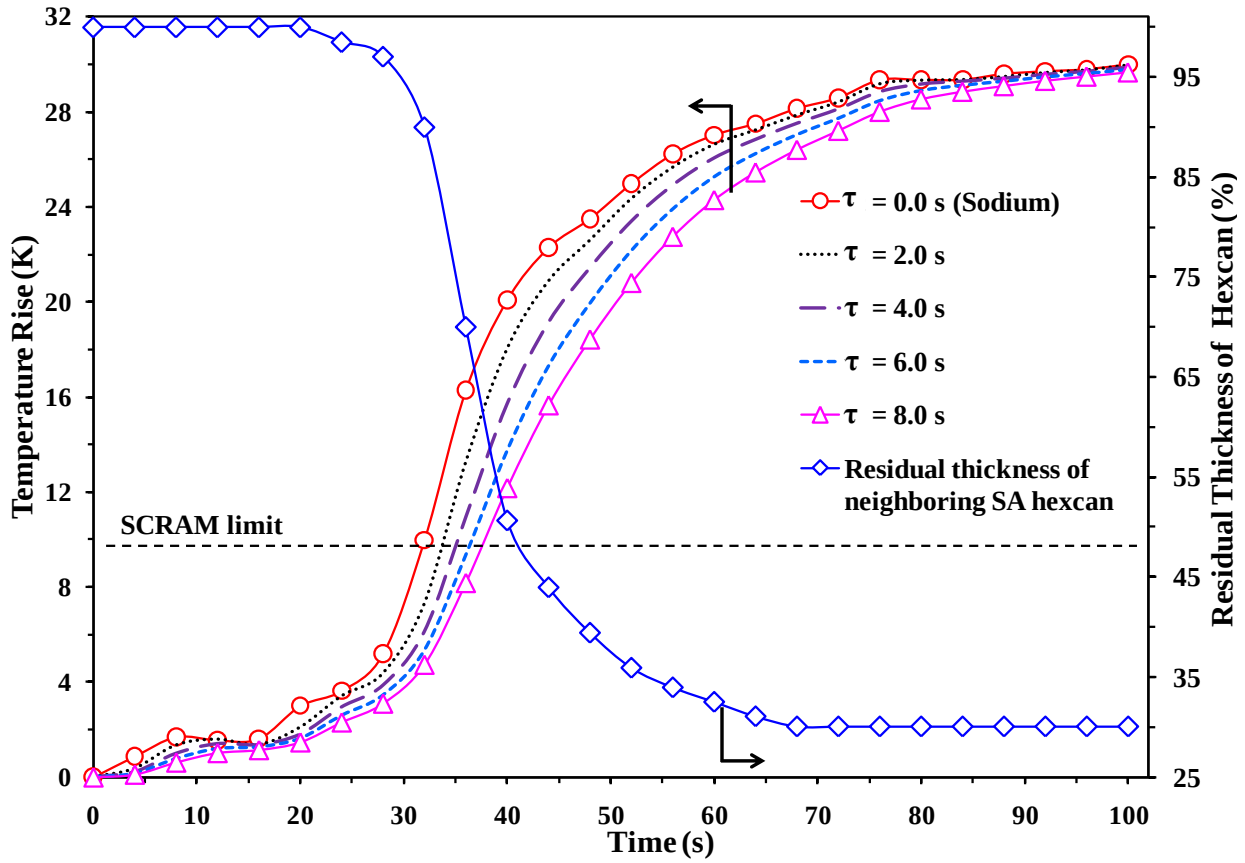

Fig. 5.26. Evolution of neighboring SA thermocouple reading as a function of thermocouple time constant and residual thickness of neighboring hexcan during TIB.

Effect of Transient Natural Convection in Fuel Pool

The rate and extent of damage propagation to hexcan wall depend on (i) heat transfer mechanisms involved during melting of hexcan wall by molten fuel attack, (ii) the resulting heat flux and (iii) the fuel-steel interface temperature. In the simulation of molten fuel attack on neighboring SA hexcan, two models have been used for the fuel pool to understand their effect

on damage propagation. In the first model, a stagnant pool is assumed (which is referred as 'conduction' model) and in the second model, natural convection within the pool is considered by CFD simulations (which is referred as 'convection' model). In the first approach, heat transfer and damage progression during molten fuel attack on hexcan is modeled considering the enthalpy based pure conduction model (discused in Chapter-3). In the second approach, the coupled calculation procedure is employed for a realistic evaluation of heat transfer and melting speed of hexcan by accounting for the effect of natural convection in the fuel pool. The results of these two approaches are compared in Fig. 5.27.

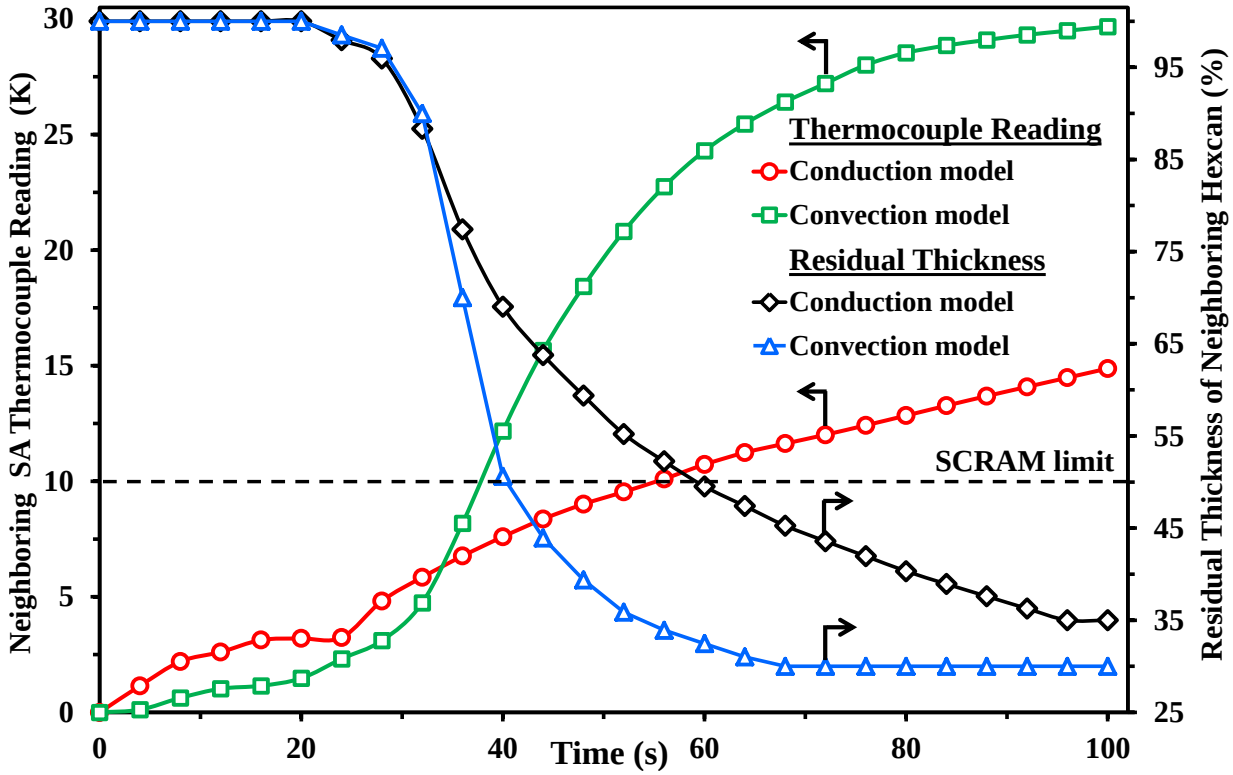

Fig. 5.27. Comparison of conduction model with convection model for time dependent temperature rise of thermocouple (time constant = 8 s) and corresponding residual thickness of the neighboring SA hexcan.

Natural convection within the fuel pool increases the rate of heat transfer to the neighboring SA. As a consequence of this, the rate of damage to hexcan wall and the rate of increase in the thermocouple reading are accelerated. Due to these two factors, a temperature rise of 10 K is

registered by neighboring SA thermocouple at 38 s after start of TIB. The instantaneous hexcan residual thickness at this instant is ~ 54 %. These are as per the predictions of natural convection model. The corresponding predictions of the conduction model are 55 s and 51 % respectively. Interestingly the residual thickness value is found to be insensitive to the heat transfer model adopted. Thus, it is clear that the transient natural convection within fuel pool leads to enhanced melting speed of the hexcan and hence speeds up the core damage propagation. However, the extent of damage to hexcan per degree temperature rise in the neighboring subassembly sodium was found to be nearly unaffected.

5.4 CONCLUSIONS

The integrated 2-D thermal hydraulics model predicts a faster damage progression than the 1-D model. However, the residual thickness of the neighboring SA hexcan at the time of reactor trip is found to be nearly same as that predicted by the 1-D model. The thermocouple time constant which had less significant role on early TIB detection in 1-D model is found to be a sensitive parameter for early detection of the TIB in the integrated 2-D model. By detailed parametric studies, it is established that the damage is restricted to seven SA in the event of TIB for a medium size fast reactor. During early transients, no significant inter-subassembly heat transfer takes place which could help in early detection of this event (before neighboring subassembly is damaged). Other major conclusions of the study are:

- Non-uniform power distribution in fuel pin leads to early start of sodium boiling, clad melting and fuel melting during TIB in a fuel SA.
- Vigorous natural convection is observed within the fuel pool that leads to enhanced heat transfer to the neighboring SA resulting in quicker melting of neighboring SA hexcan and

hence speeds up core damage progression. But, the residual thickness of the neighboring SA hexcan at time of reactor SCRAM is nearly independent of natural convection.

- Thermocouple with low response time plays a very significant role in early detection of TIB with better residual thickness of hexcan.
- A temperature rise of 10 K in the neighboring SA thermocouple is registered at about 38 s after the initiation of TIB with a thermocouple time constant of 8 s. The residual thickness of hexcan at this instant is about 52%.
- Further, since the damage initiated by TIB does not propagate beyond seven subassemblies, the thermal load on core catcher due to a TIB event is the decay heat from 7 fuel subassemblies.

CHAPTER 6

CONCLUSIONS AND SCOPE FOR FUTURE RESEARCH

6

6.0 CONCLUSIONS

As a part of this research, a simplified transient 1-D model and an integrated transient 2-D model have been developed for the purpose of thermal hydraulic investigation of total instantaneous blockage in a fuel subassembly. The focus of the study has been to understand the thermal hydraulics of damage progression during TIB and to estimate the extent of damage progression and total thermal load on core catcher at the time of reactor trip. The thermal-hydraulics models developed are based on enthalpy formulation to suit the phase change phenomena. The natural convection that sets in the heat generating fuel pool formed during TIB have been investigated by solving energy and momentum conservation equations employing finite volume method. Detailed grid independent test and validation studies have been carried out for the developed computational models. Using the developed models, TIB in a full scale prototype fuel SA with 217 pins have been analyzed and the results of the study are discussed in Chapters 3-5. In the present chapter, the major observations and conclusions drawn from the results of Chapters 3 to 5 are summarized:

6.0.1 DEVELOPMENT OF A 1-D MODEL AND INVISTIGATION OF DAMAGE PROGRESSION

- During TIB in a fuel SA operating at nominal power condition, thermal damage propagates to only one row of SA indicating that the associated thermal load on core-

catcher during the event is decay power of seven SA.

- Complete melting of the blocked SA occurs within ~20 s.
- Further, reactor SCRAM from neighboring SA thermocouple takes place at 55 s after the TIB and the residual thickness of hexcan wall at the time of reactor SCRAM is 51%.
- At low power conditions of the reactor (and hence at low SA power ratings) detection capability improves and the residual thickness of neighboring hexcan during reactor SCRAM also increases.
- Thicker hexcan does not enhance early detection.
- Increase in thermal conductivity of hexcan material enhances early detection of the event and improves the residual thickness at the time of SCRAM.
- Reduction in time constant of thermocouple does not significantly help in early detection of TIB event.

6.0.2 NATURAL CONVECTION IN FUEL POOL AND ITS IMPACT ON DAMAGE PROGRESSION

- Natural convection within the pool formed during TIB in a fuel SA leads to quicker melting of the hexcan wall, suggesting the effect of natural convection in fuel pool should be accounted while modeling the molten fuel attack on neighboring SA hexcan.
- The residual thickness of neighboring SA hexcan is found to be insensitive to the presence/absence of natural convection in the fuel pool at the time of reactor trip.
- However, considering fully established natural convection in fuel pool leads to unrealistic rate of heat transfer and melting speed of neighboring hexcan. As a consequence of this

the core monitoring thermocouple, having a finite response time, cannot detect the TIB in the fuel SA.

6.0.3 DEVELOPMENT OF INTEGRATED 2-D MODEL AND INVESTIGATION OF DAMAGE PROGRESSION

- The integrated 2-D thermal hydraulics model predicts a faster damage progression than the 1-D model. However, the residual thickness of the neighboring SA hexcan at the time of reactor trip is found to be nearly same as that predicted by the 1-D model.
- By detailed parametric studies, it is established that the damage is restricted to seven SA in the event of TIB for a medium size fast reactor.
- Thermocouple with low response time plays a very significant role in early detection of TIB with better residual thickness of hexcan.
- Non-uniform power distribution in fuel pin leads to early start of sodium boiling, clad melting and fuel melting during TIB in a fuel SA.
- A temperature rise of 10 K in the neighboring SA thermocouple is registered at about 38 s after the initiation of TIB with a thermocouple time constant of 8 s. The residual thickness of hexcan at this instant is about 52%. This demonstrates that the damage initiated by TIB does not propagate beyond seven subassemblies.

6.1 SCOPE FOR FUTURE RESEARCH

- It is reported in open literature that the phenomena such as sodium voiding, clad and fuel relocation and pool formation can significantly affect the core reactivity and reactor power. The present model does not account for the reactivity changes. Hence, the present thermal hydraulics model can be coupled with reactor physics model.

- The high heat flux and temperature on the hexcan and other SA components during TIB accident reduces their mechanical resistance and may lead to early mechanical failure rather than failure due to pure thermal load. Hence, the effect of thermal stress induced due to thermal transients and change in mechanical properties of the SA components are to be accounted in the computational model to analyze their thermo-mechanical behavior and to predict the exact time and extent of damage progression before reactor SCRAM.
- The molten material relocation (draining down) during clad and fuel melting is modeled in the present study by adopting a simplified technique of detaching the molten element by dynamic node deletion from the computational domain. For a realistic prediction of this phenomenon, suitable molten material draining model can be adopted.
- The core damage progression in radial direction is assumed to be symmetric in the present study. But it is reported in BE +3 and BE+3bis test results that a slight azimuthal asymmetries will prevent the occurrence of failure condition of all the six sides of the hexcan at the same instant. Hence, the study of asymmetric damage progression is advisable to be taken up in the future studies.
- Above the active core (see, Fig. 1.4) there are axial blanket, mixing plenum, steel/B_4C shielding and blockage adopter. These provisions offer ample scope for mixing of sodium from varies subassemblies. Considering these points, sodium from neighboring subassembly is assumed to be well mixed in the present study. However, prediction of sodium outlet temperature distribution, calls for transient, 3-D CFD analysis of neighboring SA flow characteristics. Hence, this is taken as scope for future studies.

APPENDIX

In the present study, finite thickness of fuel and hexcan elements are considered and the variations in thermo-physical properties of coolant, clad and fuel material due to temperature changes are accounted by implementing the property equations suggested by Chawla et al. (1984), Carbajo et al. (2001), Morita and Fischer, (1998), Morita et al. (1998) and Fink and Leibowitz, (1995). The property values and equations of properties for various materials used in the present study are as follows:

Thermo-physical properties of MOX fuel

Phase	Physical Property	Property Equation/Value
Solid	Density (ρ), kg/m^3	$\rho = \left(10.97\times10^{3}\right)\times \left(1.0056-1.6324\times10^{-5}T-8.3281\times10^{-9}T^{2}+2.0176\times10^{-13}T^{3}\right)$
	Specific Heat at constant pressure (C), J/kg K	For $298\,\text{K}\le T\le 2670\,\text{K}$, $C = 3.70392\times\left[\frac{c_1\theta^2 e^{\theta/T}}{T^2\left(e^{\theta/T}-1\right)^2}+2c_2T+c_3ke^{-E_a/kT}\left(1+\frac{E_a}{kT}\right)\right]$ For $2670\,\text{K}\le T\le 3120\,\text{K}$, $C = 618.60$ where $c_1 = 78.215, c_2 = 3.8609\times10^{-3}, c_3 = 3.4250\times10^{8}$, $E_a = 1.9105, \theta = 516.12$, and $k = 8.6144\times10^{-5}$
	Thermal conductivity (K), w/m K	For $298\,\text{K}\le T\le 2670\,\text{K}$, $K = 3.70392\times\left[\frac{1}{a+bT+cT^2}+dTe^{-e/kT}\right]$ For $2670\,\text{K}\le T\le 3120\,\text{K}$, $K = 4.1486-2.2673\times10^{-4}T$ where $a = 6.8337\times10^{-2}, b = 1.6693\times10^{-4}, c = 3.1186\times10^{-8}$, $d = 1.2783\times10^{-1}, e = 1.1608$ and $k = 8.6144\times10^{-5}$
	Melting Point (T_{mp}), K	Solidus temperature (T_{Sol}) = 3070 K Liquidus temperature (T_{Liq}) = 3090K

	Latent heat of fusion (L_{fu}), J/kg	$L_{fu} = 2.5\times10^{5}$
Liquid	Density (ρ), kg/m^3	$\rho = 8.86\times10^{3}–0.916\ (T-3120)$
	Volumetric thermal expansion coefficient (β), K^{-1}	$\beta = \left[\dfrac{9.16\times10^{-4}}{8.86-9.16\times10^{-4}(T-3120)}\right]$
	Specific Heat at constant pressure(C), J/kg K	For $3120\ \text{K} \le T \le 4500\ \text{K}$, $C = 0.931-4.9215\times10^{9}/T^{2}$
	Thermal conductivity (K), w/m K	$K = 5.5$
	Viscosity (μ), kg/s m	$\mu = 0.988\times10^{-3}–e^{(4620/T)}$

Thermo-physical properties of Stainless steel type 316

Phase	Physical Property	Property Equation/Value
Solid	Density (ρ), kg/m^3	$\rho = 8.084\times10^{3}-4.209\times10^{-1}T-3.894\times10^{-5}T^{2}$
	Specific heat at constant pressure (C), J/kg K	For $T \le 1700\ \text{K}$, $C = 462.656+0.1338\,T$
	Thermal conductivity (K), w/m K	For $T \le 1700\ \text{K}$, $K = 9.248-1.571\times10^{-2}T$
	Melting Point (T_{mp}), K	$T_{mp} = 1700$ K
	Latent heat of fusion (L_{fu}), J/kg	$L_{fu} = 2.7033\times10^{5}$
Liquid	Density (ρ), kg/m^3	$\rho = 7.433\times10^{3}+3.934\times10^{-2}T-1.801\times10^{-4}T^{2}$
	Specific heat at constant pressure (C), J/kg K	$C = 776.2$
	Thermal conductivity (K), w/m K	$K = 12.41+3.729\times10^{-3}T$
	Viscosity (μ), kg/s m	$\mu = 0.2536\times10^{-3}–e^{(5492.2/T)}$

Thermo-physical properties of Sodium

Phase	Physical Property	Property Equation/Value
Liquid	Density (ρ), kg/m^3	For $371\,\text{K} \le T \le 1644\,\text{K}$, $\rho = 1011.8 - 0.22054T - 1.9226\times10^{-5}T^2 + 5.6371\times10^{-9}T^3$
	Specific heat at constant pressure (C), J/kg K	$C = 1.5314\times10^3 - 6.1343\times10^{-1}T + 3.3551\times10^{-4}T^2 + 5.4056\times10^6/T^2$
	Thermal conductivity (K), w/m K	$K = 105.78 - 5.1767\times10^{-2}T + 4.8696\times10^{-6}T^2$
	Boiling point (T_{bp}), K	T_{bp} = 1156 K
	Latent heat of vaporization (L_{va}), J/kg	For $371\,\text{K} \le T \le 2503.7\,\text{K}$, $L_{va} = 393.37\times10^3\left(1-\frac{T}{T_{cri}}\right) + 4398.6\times10^3\left(1-\frac{T}{T_{cri}}\right)^{0.29302}$ where T_{cri} is critical temperature of sodium = 2503.7 K, For $T_{bp} = 1156\,\text{K}$ at atmospheric pressure, $L_{va} = 3986.2\times10^3$
Vapor	Thermal conductivity (K), w/m K	$K = -3.5509\times10^{-2} + 1.5167\times10^{-4}T - 5.4376\times10^{-8}T^2$

REFERENCES

Aberle, J., Romer, O., Schleisiek, K., Schmuck, I., 1994. Conclusion from MOL &C/6 on local faults in irradiated mixed oxide fuel subassembly. Proc. Int. Topical Meeting on Sodium Cooled Fast Reactor Safety, Obninsk, Russia, 2, 156-165

Acharya, S., and Goldstein, R. J., 1985. Natural convection in an externally heated vertical or inclined square box containing internal heat sources. ASME Journal Heat Transfer. 107(4), 855–866.

Alvarez, D., Malterre, P., Seiler, J.M., 1986. Natural convection in volume heated liquid pools-the BAFOND experiment: Proposal for new correlations. In: Proc. of Int. Con. on Science and Technology of Fast Reactor Safety, Guernsey, United Kingdom, May 12-16, 1986, Vol. I. British Nuclear Energy Society, pp. 331-336.

Alexanderson, E.P., 1979. Fermi-I: New age for nuclear power. LaGrange Park, IL: American Nuclear Society.

Anzieu, P., Le Gouez, J.M., Pourcheresse, C., Carlier, S., Filppi, G., 1986. SURFASS a computer code describing the consequences of total instantaneous blockage of a subassembly on the RNR 1500. In: Proc. of lnt. Con. on Science and Technology of Fast Reactor Safety, Vol 1, Guernesey, United Kingdom, May 12-16, 1986, Vol. I. British Nuclear Energy Society, pp. 447-450.

Anzieu, P., Van Dorsselaere, J.P., 1990. Total Instantaneous Blockage Calculations with the SURFASS Code for Fast Reactor Subassemblies. In: Proc. of Con. on Fast Reactor Core and Fuel Structural Behavior, Inverness 4-6 June 1990, British Nuclear Energy Society, pp. 105-111.

Bede, M., Perret, C., Pretrel, H., Seiler, J.M., 1993. One component, volume heated, boiling pool thermalhydraulics. In: Proc. of the 6th Int. Topical Meeting on Nuclear Reactor Thermal Hydraulics (NURETH-6), Grenoble, France, October 5-8, 1993.

Bol'shov, L.A., Kondratenko, P.S., Strizhov, V.F., 2001. Natural convection in heat generating fluids. Physics-Uspekhi. 44 (10), 999-1016.

Berthoude, G., Duret, B., 1989. The freezing of molten fuel: reflections and new results. In: Proc. of 4th Int. Topical Meeting on Nuclear Reactor Thermal Hydraulics (NURETH-4), Karlsruhe, Germany, October 10-13, 1989, pp. 675-681.

Bohl, W. R., Wilhelm, D., 1992. The advanced fluid dynamics model program: Scope and accomplishment. Nuclear Technology. 99(3), 366-373.

Bohl, W.R., Wilhelm, D., Parker, F.R., Berthier, J., Goutagny, L, Ninokata, H., 1990. AFDM: An Advanced Fluid-Dynamics Model, Volume I: Scope, Approach, and Summary. LA-11692-MS, Vol. I, Los Alamos National Laboratory.

Cadiou, T., Louvet, J., 2006. Evaluation of the accident scenario initiated by a total instantaneous blockage in a Phenix sub-assembly. Nuclear Technology. 153 (3), 256-263.

Cahalan, J.E., Wei, T. Y. C., 1990. Modeling Developments for the SAS4A and SASSYS Computer Codes. In: Proc. of Int. Reactor Safety Meeting, Snowbird, Utah, August 12-16, 1990.

Cahalan, J.E., Tentner, A.M., Morria, E.E., 1994. Advanced LMR Safety Analysis Capabilities in the SASSYS-1 and SAS4A Computer Codes. In: Proc. of the Int. Topical Meeting on Advanced Reactors Safety, Pittsburgh, PA, April 17-21, 1994, American Nuclear Society.

Carbajo, J.J., Yoder, G.L., Popov, S.G., Ivanov, V.K., 2001. A review of the thermophysical properties of MOX and UO_2 fuels. Journal of Nuclear Materials. 299, 181–198.

Cengel, A.C., 2007. Heat and Mass Transfer. McGraw-Hill, New York.

Chang, W.P., Ha, K.S., Suk, S.D., Jeong, H.Y., 2011. A comparative study of the MATRA-LMR–FB calculation with the SABRE result for the flow blockage accident in the sodium cooled fast reactor. Nuclear Engineering and Design. 241, 5225-5237.

Chawla, T. C., Chasanov, M. G., Pedersen, D. R., Baker, L., Jr., and Bingle, J.D., 1984. Thermo physical properties of MgO, UO_2, their eutectic solution and slurry of liquid-solid mixtures, concrete, sodium, stainless steel and debris beds for use in molten pool penetration of MgO substrate. Nuclear Engineering and Design. 80(1), 65–77.

Chen, W.L., Ishii, M., Grolmes, M.A., 1979. The application of the simple fuel pin transient and melting model to thermal-hydraulics in LMFBR subassembly. Nuclear Engineering and Design. 53, 321–388.

Chen, X., Li, R., Rineiski, A., Jager, W., 2015. Macroscopic Pin Bundle Model and its Blockage Simulations. Energy Conversion and Management. 91, 93-100.

Cheng, S., Matsuba, K., Isozaki, M., Kamiyama, K., Suzuki, T., Tobita, Y., 2015. SIMMER-III Analyses of Local Fuel-Coolant Interactions in a simulated Molten Fuel Pool: Effect of Coolant Quantity, Science and Technology of Nuclear Installations, Volume 2015, Article ID 964327, 14 pages.

Chetal, S.C., Balasubramaniyan, V., Chellapandi, P., Mohanakrishnan, P.,Puthiyavinayagam, P., Pillai, C.P., Raghupathy, S., Shanmugham, T.K.,Sivathanu Pillai, C., 2006. The design of the prototype fast breeder reactor. Nuclear Engineering and Design. 236, 852–860.

Chetal, S.C., Chellapandi, P., Puthiyavinayagam, P., Raghupathy, S.,Balasubramaniyan, V., Selvaraj, P., Mohanakrishnan, P., Baldev Raj, 2011.Current status of fast reactors and future plans in India. Energy Proc. 7, 64–73.

Dadillon, J., Chaudat, J.P., Schwaz, M., Tategrain, A., Heusener, G., Kuczera, B.,Kussmaul, G., Wolff, J., 1979. The CABRI test facility experimental fuel pin programme. Its objectives and present results. In: Proc. Int. Mtg. Fast Reactor Safety Technology, Seattle, Washington, August 19–23, 1979, vol. II.

Dadillon, J., Kussmaul, G., Agaisse, R., Augier, G., Bensoussan, P., Butement, A.W.,Fabrega, S., Haessler, M., Hoppe, P., Mitsuki, S., Philipponneau, Y., Rongier, P., Steinbock, L., Wolff, J., 1982. The CABRI project-recent progress and present status. In: Proc. LMFBR Safety Topl. Mtg, Lyon, France, July 19–23, 1982, vol.II. European Nuclear Society/American Nuclear Society, pp. 177-188.

Di Piazza, I., Magugliani, F., Tarantino, M., Alemberti, A., 2014. A CFD analysis of flow blockage phenomena in ALFRED LFR demo fuel assembly. Nuclear Engineering and Design. 276, 202-215.

Doerner, R.C., Bauer, T.H., Morman, J.A., Holland, J.W., 1992. Features of postfailure fuel behavior in transient overpower and transient undercooled/overpower test in the transient reactor test facility. Nuclear Technology. 98(1), 124-136.

Duret, B., Bonnard, J.C., 1988. Crust instability criteria during transient freezing on a liquid film. In: Proc. of the ASME Winter Annual Meeting, Chicago, Illinois, November 27-December 2, 1988.

Edwards, A.J., Bird, M.J., Denham, M.K., 1992. Molten fuel propagation in sodium-filled fast reactor subassembly geometries. Nuclear Technology. 4, 70-78.

Epstein, M., 1973. Heat conduction in the UO_2-cladding composite body with simultaneous melting and solidification. Nuclear Science and Engineering. 51, 84-87.

Fieg, G., Moschke, M., Werle, H., 1992. Freezing phenomena of ceramic alumina melts flowing in pin bundles. Nuclear Technology. 99, 309-317.

Fink, J.K., Leibowitz, L., 1995. Thermodynamic and transport properties of sodium liquid and vapor, Argonne National Laboratory Report, USA, ANL/RE-95/2.

Fukano, Y., 2015. SAS4A Analysis on hypothetical total instantaneous flow blockage in SFRs based on in-pile experiments. Annals of Nuclear Energy. 77, 376-392.

Gabor, J.D., Baker, L., Cassulo, J.C., Erskine, D.J., Warner, J.G., 1980. Heat transfer to curved surfaces from heat generating pools. Journal of Heat Transfer. 102 (3), 519-524.

Guyot, M., Gubernatics, P., Suteau, C., 2014. On the multiple-pin modeling of the fuel bundle for the simulation of the initiating phase of a severe accident in a sodium fast reactor. Nuclear Science and Engineering.178, 202-224.

Henkes, R.A.W.M., 1990. Natural Convection Boundary Layers (Ph.D. thesis). Delft University of Technology, The Netherlands.

Hossain, M.K., Himuro,Y., Morita, K., Nakagawa. K., Matsumoto, T., Fukuda,K., Maschek, W., 2009. Simulation of molten metal penetration and freezing behavior in a seven-pin bundle experiment. Journal of Nuclear Science and Technology. 46 (8) 799-808.

Hughes, W.F., Gaylord, E.W., 1964. Basic Equations of Engineering Science. McGraw-Hill, New York.

Jones, B.G., Spencer, B.W., Henry, R.E., 1978. Interaction of molten UO_2 with stainless steel cladding under TOP accident conditions. Transactions of the American Nuclear Society. 28, 447-448.

Kaiser, K., Peppler, W and Will, H., 1994. SIMBATH 1976-1992, Seventeen years of experimental investigation of key issues concerned with severe reactor accident. In: Proc. of IAEA/IWGFR Technical Committee Meeting on Evaluation of Material Coolant Interaction and Material Movement and Relocation in Liquid Metal Reactors, O-arai Engineering Center, Japan, June10, 1994.

Kakodkar, A., 2008. Evolving Indian Nuclear Program: Rationale and Perspectives. Lecture at Indian Academy of Sciences, Bangalore, July 4, 2008 (http://www.dae.gov.in/Lecture.html).

Kasahara, F., Endo, H., 1992. QUASAR-A computer code for analyzing subassembly accidents in liquid-metal fast breeder reactors. Nuclear Technology. 99(3), 301-308.

Kasahara, F., Ninokata, H., 2000. The multi-fluid multi-phase subchannel analysis code KAMUI for subassembly accident analysis of an LMFR. Journal of Nuclear Science and Technology. 37(8), 654-669.

Kayser, G., Stansfield, R., 1994. SCARABEE experimental expertise on failure mechanisms of stainless steel walls attacked by molten oxide. In: Proc. Int. Topical Meeting on Advanced

Reactors Safety (ARS'94), Pittsburgh, USA, April 17-21, 1994, Vol. 2. American Nuclear Society, pp. 768-775.

Kayser, G., Charpenel, J., Jamond, C., 1998. Summary of the SCARBEE-N subassembly melting and propagation test with an application to a hypothetical total instantaneous blockage in a reactor. Nuclear Science and Engineering. 128, 144-185.

Kazimi., M.S., Carelli, M.D., 1976. Heat Transfer Correlation for Analysis of CRBRP Assemblies. Report CRBRP-ARD-0034, Westinghouse.

Kondo, Sa., 1994. Current R&D status on material motion and interactions relevant to core disruptive accidents. In: Proc. of IAEA/IWGFR Technical Committee Meeting on Evaluation of Material Coolant Interaction and Material Movement and Relocation in Liquid Metal Reactors, O-arai Engineering Center, Japan, June10, 1994.

Konishi, K., Toyooka, J., Kamiyama, K., Sato, I., Kubo, S., Kotake, S., Koyama, K., Vurim, A.D., Gaidaichuk, V.A., Pakhnits, A.V., Vassiliev, Y.S., 2007. The results of a wall failure in-pile experiment under the EAGLE Project. Nuclear Engineering and Design. 237, 2165-2174.

Kriventsev, V., Rineiski, A., Maschek, W., 2014. Application of safety analysis code SIMMER-IV to blockage accidents in FASTEF subcritical core. Annals of Nuclear Energy. 64, 114-121.

Liu, P., Chen, X., Rineiski, A., Maschek, W., 2010. Transient analyses of the 400MWth-class EFIT accelerator driven transmuter with the multi-physics code: SIMMER-III. Nuclear Engineering and Design. 240(10), 3481-3494.

Livolant, M., Dadillon, J., Kayser, G., Moxon, D., 1990. SCARABEE: a test reactor and programe to study fuel melting and propagation in connexion with local faults, objectives, and results. In: Proc. Int. Fast Reactor Safety Meeting 1990, Snowbird, Utah, vol. II, pp. 177-186.

Macdougall, J. D., Lillington, J. N., 1984. The SABRE code for fuel rod cluster thermohydraulics. Nuclear Engineering and Design. 82(2), 171-190.

Maity, R.K., Velusamy, K., Selvaraj, P., Chellapandi, P., 2011. Computational fluid dynamic investigations of partial blockage detection by core-temperature monitoring system of a sodium cooled fast reactor. Nuclrar Engineering and Design. 241, 4994–5008.

Marie, N., Marrel. A., Seiler, J.M., Bertrand,F., 2015. Physico-statistical Approach to Assess the Core Damage Variability Due to a Total Instantaneous Blockage of SFR Fuel Sub-assembly. Nuclear Engineering and Design. (In Press).

Martinez-Martinez, S., Messai, N., Jeannot, J. P., Nuzillard, D., 2015. Two Neural Network Based Strategies for the Detection of a Total Instantaneous Blockage of a Sodium-Cooled Fast Reactor. Reliability Engineering & System Safety. 137, 50-57.

Maschek, W., Rineiski, A., Suzuki, T., Chen, X., Mori, Mg., Wang, S., Tobita, Y., Kondo, Sa., Yamano, H., Fujita, S., Cadiou, T., Coste, P., 2003. The SIMMER-III and SIMMER-IV code family: 2-D and 3-D mechanistic simulation tools for reactor transients and accidents. In: Proc. of Technical Meeting on Progress in Development and Use of Coupled Codes for Accident Analysis, Vienna, Austria, November 26-28, 2003, IAEA-TECDOC-1539.

Meyer-Heine, A., Kayser, G., Moxon, D., Aujollet, J.M., Sureau, M., Justin, M., 1986. The SCARABEE program and the PHYSURA-GRAPPE code-A Phenomenological approach for subassembly accidents. In: Proc. of Science and Technology of Fast Reactor Safety. Guernsey, United Kingdom, May 12-16, 1986, Vol. I. British Nuclear Energy Society, pp. 251-256.

Morita, K., Fischer, E.A., 1998. Thermodynamic properties and equations of state for fast reactor safety analysis. Part I: analytic equation-of-state model. Nuclear Engineering and Design. 183, 177-191.

Morita, K., Fischer, E.A., Thurnay, K., 1998. Thermodynamic properties and equations of state for fast reactor safety analysis. Part II: properties of fast reactor materials. Nuclear Engineering and Design. 183, 193–211.

Morita, K., Zhang, S., Koshizuka, S., Tobita, Y., Yamano, H., Shirakawa, N., Inoue, F., Yugo, H., Naitoh, M., Okada, H., Yamamoto, Y., Himi, M., Hirano, E., Shimizu, S., Oue, M., 2011. Detailed analyses of key phenomena in core disruptive accidents of sodium-cooled fast reactors by the COMPASS code. Nuclear. Engineering and Design. 241, 4672-4681.

Murin, Mireau, Arslan, Balloffet, Magnon, 1982. Creys Malville-sub-assembly accident analysis. In: Proc. LMFBR Safety Topl. Mtg. Lyon, France, Vol. II. European Nuclear Society/American Nuclear Society, pp. 375-382.

Natesan, K., Kasinathan, N., Velusamy, K., Selvaraj, P., Chellapandi, P., 2012. Plant dynamics studies towards design of plant protection system for PFBR. Nuclear Engineering and Design. 250, 339-350.

Naveen Raj, M., Velusamy, K., 2016. Characterization of velocity and temperature fields in a 217 pin wire wrapped fuel bundle of sodium cooled fast reactor. Annals of Nuclear Energy. 87 (2), 331-349.

Ninokata, H., Okano, T. A., 1990. SABENA: Subassembly boiling evolution numerical analysis. Nuclear Engineering and Design. 120(2), 349-367.

Papin, J., 1989. The SCARABEE test program: Objectives and main issues of the BE1and BF Series. Proc. CCE Seminar on Nuclear Research Safety, Varese, Italy, November 20-24, 1989.

Park, R.J., Kim, S.B., Kim, H.D., Choi, S.M., 1999. Natural convection heat transfer with crust formation in the molten metal pool. Nuclear Technology. 127, 66-80.

Patankar, S. V., and Spalding, D. B., 1972. A calculation procedure for heat mass and momentum transfer in three dimensional parabolic flows. International Journal of Heat and Mass Transfer. 15(10), 1787-1806.

Paumel, K., Jeannot, J.P., Jeanne, T., Laffont, G., Vanderhaegen, M., Massacret, N., 2013. R&D on early detection of the Total Instantaneous Blockage for 4th Generation Reactors - inventory of non-nuclear methods investigated by the CEA. In: The 4th Int. Con. on Advancements in Nuclear Instrumentation Measurement Methods and their Applications, Marseille, June 23–2, 2013, IEEE, ISBN: 978-1-4799-1046-5.

Sawada, T., Ninokata, H., Shimizu, A., 1995. Analysis of an out-of-pile experiment for materials redistribution under core disruptive accident condition of fast breeder reactors. Journal of Nuclear Science and Technology. 32(6), 584-595.

Schwarz, M., Kayser, G., Jamond, c., The SCRABEE PV-A test for melt propagation of a boiling pool into a neighboring pin bundle. In: Proc. Int. Mtg. Sodium Cooled Fast Reactor Safety, Obninsk, Russia, October 1994.

Scott, R.L., 1971. Fuel-melting incident at the Fermi reactor on Oct. 5, 1966. Nuclear Safety. 12 (2).

Seiler, J.M., Kayser, G., Wilhelm, D., Synthesis of research on boiling pool thermalhydraulics at CEA and KFK. In: Proc. Int. Atomic Energy Agency Mtg., Oarai, Japan, June 1994.

Sharma, A. K., Velusamy, K., and Balaji, C., 2009, Turbulent natural convection of sodium in a cylindrical enclosure with multiple internal heat sources: A conjugate heat transfer Study. International Journal of Heat and Mass Transfer. 52 (11-12), 2858-2870.

Shim, Y. M., and Hyun, J. M., 1997. Transient confined natural convection with internal heat generation. International Journal of Heat and Fluid Flow. 18(3), 328-333.

Spencer, B.W., Wilson, R.J., Vetter, D.L., Erickson, E.G., Dewey. G., 1985. Results of recent reactor-material tests on dispersal of oxide fuel from a disrupted core. In: Proc. of ANS/ENS Fast Reactor Safety Meeting, Knoxville, Tennessee (USA), April 21-24, 1985, CONF-850410-VO1.2, DE85 018108, pp. 877-882.

Srinivasan, G., Suresh Kumar, K.V., Rajendran, B., Ramalingam, P.V., 2006. The fast breeder test reactor design and operating experiences. Nuclear Engineering Design. 236 (7-8), 796-811.

Suresh, Ch.S.Y., Sundararajan, T., Venkateshan, S.P., Sarit, K.Das., Thansekhar, M.R., 2005. Heat transfer from a totally blocked fuel subassembly of a liquid metal fast breeder reactor. Nuclear Engineering Design. 235, 897-912.

Tenchine D., 2010. Some thermal hydraulic challenges in sodium cooled fast reactors. Nuclear Engineering and Design. 240, 1195-1217.

Velusamy K., Chellapandi P., Chetal S.C., Raj B., 2010. Overview of pool hydraulic design of Indian Prototype Fast Breeder Reactor. Sadhana, 35(2), 97-128.

Velusamy, K., Natesan, K., Ram Kumar Maity., Asokkumar, M., Arul Baskar, R., Rajendrakumar, M., Partha Sarathy, U., Selvaraj, P., Chellapandi, P., Senthil Kumar, G., Jebaraj, C., 2015. Primary system thermal hydraulics of future Indian fast reactors. Nuclear Engineering and Design. 294, 170-182.

Voller, V. R., 1987. An implicit enthalpy solution for phase change problems: with application to binary alloy solidification. Applied Mathematical Modelling. 11(2), 110-116.

Wang, Z., Cao, X.W., 2007. Preliminary thermal-hydraulic phenomena investigation during total instantaneous blockage accident for CEFR. Nuclear Engineering Design. 237, 1550-1559.

Yamano, H., Fujita, S., Tobita, Y., Kamiyama, K., Kondo, Sa., Morita, K., Fischer, E.A., Brear, D.J., Shirakawa, N., Cao, X., Sugaya, M., Mizuno, M., Hosono, S., Kondo, T.,Maschek, W., Kiefhaber, E., Buckel, G., Rineiski, A., Flad, M., Suzuki, T., Coste, P.,Pigny, S., Louvet, J., Cadiou, T., 2003. SIMMER-III: A Computer Program for LMFR Core Disruptive Accident Analysis. Japan Nuclear Cycle Development Institute, JNC TN9400 2003-071.

Yamano, H., Onoda, Y., Tobita, Y., Sato, I., 2009. Transient heat transfer characteristics between molten fuel and steel with steel boiling in the CABRI-TPA2 Test. Nuclear Technology. 165 (2), 145-165.

Yamano, H., Tobita, Y., 2014. Experimental analyses by SIMMER-III on duct-wall failure and fuel discharge/relocation behavior. Mechanical Engineering Journal. 1(4), TEP 0028.

NOMENCLATURE

English Symbols

a	effective heat transfer area, m^2
A	aspect ratio, z_{pol}/r_{pol}
B_k	buoyancy production of turbulent kinetic energy, kg/m s^3
B_k^*	dimensionless buoyancy production of turbulent kinetic energy
C	specific heat, J/kg K
$C_{\varepsilon 1}$ to $C_{\varepsilon 3}$	turbulence model constants
CF	equivalent conductivity factor
D	diameter, m
e	emissivity
F	view factor
g	acceleration due to gravity, m/s^2
G	effective thermal conductance, W/K
Gr	Grashoff number
h	heat transfer coefficient, W/m^2K
H	enthalpy, J
H_{spe}	specific enthalpy, J/kg
k	turbulent kinetic energy, m^2/s^2
k^*	dimensionless turbulent kinetic energy
K	thermal conductivity, W/m K
K_e	equivalent thermal conductivity, W/m K

K_{eff}	effective thermal conductivity, W/m K
K_t	turbulent thermal conductivity, W/m K
l	length, m
L	latent heat, J/kg
m_s	subassembly sodium flow rate, kg/s
m_{sr}	inter-wrapper sodium flow rate, kg/s
N_f	number of fuel elements
N_{fh}	sum of fuel and hexcan elements
Nu	Nusselt number
p	pressure, N/m^2
p^*	dimensionless pressure
P_k	shear production of turbulent kinetic energy, $kg/m\ s^3$
P_k^*	dimensionless shear production of turbulent kinetic energy
P_t	triangular pitch of fuel pins, m
Pe	Peclet number
Pr	Prandtl number
Pr_{eff}	effective Prandtl number
Pr_t	turbulent Prandtl number
q	heat generation rate, W
q"	local heat flux, W/m^2
q"*	dimensionless local heat flux
q"'	volumetric heat generation rate, W/m^3
Q	total heat transfer rate, W
r	radius, m

r^*	dimensionless radius
r_i	inner radius, m
r_o	outer radius, m
Ra	Rayleigh number
Ra_c	critical internal Rayleigh number
Ra_E	external Rayleigh number
Ra_I	internal Rayleigh number
Re	Reynolds number
S	conduction shape factor, m
t	time, s
t^*	dimensionless time
T	temperature, K
T^*	dimensionless temperature
T_{hot}	Temperature of hot wall, K
T_{cold}	Temperature of cold wall, K
u	radial velocity component, m/s
u^*	dimensionless radial velocity component
U	resultant velocities, m/s
v	axial velocity component, m/s
v^*	dimensionless axial velocity component
z	vertical height, m
z^*	dimensionless height

Greek symbols

α	thermal diffusivity, m^2/s
β	thermal expansion coefficient, K^{-1}
θ	phase change factor
δ	thickness, m
σ	Stefan-Boltzmann constant, $W/m^2\ K^4$
σ_ε, $\sigma_{k,}$ and σ_T	turbulence Prandtl number
ε	turbulent dissipation rate, m^2/s^3
ε^*	dimensionless turbulent dissipation rate
μ	dynamic viscosity, Ns/m^2
μ_{eff}	effective viscosity, Ns/m^2
μ_t	turbulent viscosity, Ns/m^2
ν	kinematic viscosity, m^2/s
ρ	density, kg/m^3
τ	thermocouple time constant, s
ϕ	dimensionless temperature of cavity
ΔT	temperature difference between vertical walls of the cavity, K
Δt	time step, s

Subscripts

bp	boiling point
c	clad
cav	cavity

ci	inner clad
co	outer clad
cond	conduction
conv	convection
cso	clad and sodium at outer region of blocked subassembly
cxo	clad and hexcan at outer region of blocked subassembly
f	fuel
fci	fuel and clad at inner region of blocked subassembly
fco	fuel and clad at outer region of blocked subassembly
fu	fusion
fi	inner fuel
fo	outer fuel
fxo	fuel and hexcan at outer region of blocked subassembly
lp	liquid phase
Liq	liquidus
mp	melting point
mpf	melting point of fuel
mph	melting point of hexcan
pol	pool
ref	reference
s	sodium
si	inner sodium column
sio	sodium column at inner and outer regions of blocked subassembly
so	outer sodium column

sp	solid phase
sr	inter-wrapper sodium
sn	neighboring subassembly sodium
sni	neighboring subassembly sodium inlet
sno	neighboring subassembly sodium outlet
sxo	sodium column and hexcan at outer region of blocked subassembly
sxr	sodium and hexcan at inter-wrapper region
sxn	sodium and hexcan of neighboring subassembly
Sol	solidus
tr	thermocouple reading
va	vaporization
vp	vapor phase
w	wall
ws	wall and sodium
xb	blocked subassembly hexcan
xbn	blocked hexcan and neighboring hexcan at inter-wrapper region
xe	hexcan element
xn	neighboring subassembly hexcan

Abbreviations

AFDM	Advanced Fluid Dynamics Model
AHWR	Advanced Heavy Water Reactor
CDA	Core Disruptive Accident

CEFR	China Experimental Fast Reactor
CFD	Computational Fluid Dynamics
CSR	Control and Safety Rod
CRBR	Clinch River Breeder Reactor
CRGT	Control Rod Guide Tube
DHRS	Decay Heat Removal System
DSR	Diverse Safety Rod
DND	Delay Neutron Detector
FBR	Fast Breeder Reactor
FBTR	Fast Breeder Test Reactor
FCI	Fuel Coolant Interaction
FVM	Finite Volume Method
IHX	Intermediate Heat Exchanger
JSFR	Japanese Sodium cooled Fast Reactor
LMFBR	Liquid Metal Fast Breeder Reactor
MFCI	Molten Fuel Coolant Interaction
OGDHRS	Operation Grade Decay Heat Removal System
PFBR	Prototype Fast Breeder Reactor
PHWR	Pressurized Heavy Water Reactor
PSP	Primary Sodium Pump
SA	Subassembly
SCRAM	Safety Control Rod Accelerated Movement
SFR	Sodium Cooled Fast Reactor
SG	Steam Generator

SGDHRS	Safety Grade Decay Heat Removal System
SIMPLE	Semi-Implicit Method for Pressure Linked Equations
SPX	Super PheniX
TIB	Total Instantaneous Blockage
ULOFA	Unprotected Loss of Flow Accident
UTOPA	Unprotected Transient Overpower Accident